Abstract of "Mechanics of Elastic Contact and Adhesion of Rough Surfaces" by Weilin Deng, Ph.D., Brown University, October 2019.

Adhesion originated from van der Waals interactions becomes predominant over bulk properties of elastic solids at small length scales. A fundamental understanding of the mechanics of elastic contact and adhesion of rough surfaces is of paramount importance due to its wide applications in various engineering and biological fields from avoiding stiction failure of micro-electromechanical systems to achieving optimal adhesion capability of gecko-inspired micro-fibrillar adhesives. This dissertation focuses on several critical problems of frictionless adhesive elastic contact with particular emphasis on the interplay of surface roughness and adhesion. Based on the Maugis-Dugdale theory and Nayak's theory of rough surface, we propose a new mechanics model of adhesive elastic contact to study the depth-dependent hysteresis and energy loss during a contact cycle in the regime of large surface roughness. We develop an effective, nonlinear body force based approach to simulate adhesive elastic contact using the realistic molecular potential. It is shown that the surface roughness can either enhance or reduce the effective work of adhesion required to separate two contacting surfaces, depending on the magnitude of roughness. The continuum simulations reveal that the mechanism of adhesion enhancement and depth-dependent hysteresis observed in adhesive contact experiments is attributed to the small-scale surface imperfection induced mechanical instabilities. Through analyzing the quasi-static peeling of an elastic thin film from a rough substrate, we demonstrate that the effective work of adhesion can be significantly improved by surface roughness, resulting in an apparent interface toughening. Moreover, we examine the principle of contact splitting for biological fibrillar structures and investigate the effects of fibril's stiffness and surface's roughness and correlation length on adhesion of the fibrillar structure. We also present an analytical model of adhesive elastic contact that accounts for the effect of machine stiffness, which explains experimentally measured contact force-indentation depth curves better than the Johnson-Kendall-Roberts theory. These comprehensive results highlight the importance of surface topography and material properties in adhesive elastic contact and can guide future work on attuning effective adhesive and tribological properties through designing small-scale surface architectures.

Mechanics of Elastic Contact and Adhesion of Rough Surfaces

by
Weilin Deng
B.Eng., Engineering Mechanics, Tianjin University, 2010
M.Eng., Solid Mechanics, Tianjin University, 2013

Submitted in partial fulfillment of the requirements
for the Degree of Doctor of Philosophy in
Solid Mechanics at Brown University

Providence, Rhode Island
October 2019

This dissertation by Weilin Deng is accepted in its present form by
the School of Engineering as satisfying the dissertation requirement
for the degree of Doctor of Philosophy.

Date _____ _____

Haneesh Kesari, Ph.D., Advisor

Recommended to the Graduate Council

Date _____ _____

Pradeep Guduru, Ph.D., Reader

Date _____ _____

Vikas Srivastava, Ph.D., Reader

Approved by the Graduate Council

Date _____ _____

Andrew G. Campbell, Ph.D.
Dean of the Graduate School

Curriculum Vitæ

Weilin Deng was born in Gaoan, Jiangxi, China. He attended Tianjin University in 2006. Later he received his B.Eng. degree in Engineering Mechanics in 2010 and M.Eng. degree in Solid Mechanics in 2013. He graduated with honors from both Tianjin University and Tianjin Municipal Commission of Education. He began his doctoral studies in the Solid Mechanics program at Brown University in January, 2014.

Refereed Journal Publications

Deng WL and Kesari H. Molecular statics study of depth-dependent hysteresis in nano-scale adhesive elastic contacts. *Modelling and Simulation in Materials Science and Engineering*, 25(5): 055002, 2017.

Deng WL and Kesari H. Depth-dependent hysteresis in adhesive elastic contacts at large surface roughness. *Scientific Reports*, 9(1): 1639, 2019.

Deng WL and Kesari H. Effect of machine stiffness on interpreting contact force–indentation depth curves in adhesive elastic contact experiments. *Journal of the Mechanics and Physics of Solids*, 131:404-423, 2019.

Deng WL and Kesari H. Surface roughness enhanced adhesion in adhesive elastic contact: Finite element simulation and analysis. *Journal of the Mechanics and Physics of Solids*, In submission, 2019.

Deng WL and Kesari H. Interface toughening in thin film peeling from wavy substrates. *Journal of Applied Mechanics*, In submission, 2019.

Conference Proceedings

(1 = talk, 2 = poster)

Deng WL and Kesari H, "Surface roughness dependent adhesion: Finite element modelling and analysis," ASME's International Mechanical Engineering Congress and Exposition (IMECE), Pittsburgh, PA, 2018.[1]

Deng WL and Kesari H, "Surface roughness induced adhesion enhancement," 9th New England Workshop on Mechanics of Materials and Structures, Brown University, Providence, RI, 2018.[1]

Deng WL and Kesari H, "Surface roughness dependent adhesion: Finite element modelling and analysis," 18th U.S. National Congress for Theoretical and Applied Mechanics–Jointly Organized with the Chinese Society of Theoretical and Applied Mechanics, Chicago, IL, 2018.[1]

Deng WL and Kesari H, "Theoretical modelling of depth-dependent hysteresis in adhesive elastic contact," 54th Annual Technical Meeting of the Society of Engineering Science (SES), Northeastern University, Boston, MA, 2017.[1]

Deng WL and Kesari H, "Depth-dependent hysteresis in adhesive elastic contacts for large surface roughness," 53rd Annual Technical Meeting of the Society of Engineering Science (SES), University of Maryland, College Park, MD, 2016.[1]

Deng WL and Kesari H, "Molecular statics simulations of depth-dependent hysteresis in adhesive elastic contacts," 7th New England Workshop on Mechanics of Materials and Structures, Harvard University, Cambridge, MA, 2016.[2]

Teaching Experience at Brown

Graduate

Mathematical Methods in Engineering and Physics I, TA (Fall 2014)

Undergraduate

Advanced Engineering Mechanics, TA (Spring 2018, Spring 2019)

Acknowledgements

I am sincerely grateful to my advisor Haneesh Kesari and have been very fortunate to be trained by him. Over the last five years, he has given me an abundance of intellectual freedom, patience, encouragement, and understanding while we come up with some fresh ideas and concreted them into scientific knowledge together. Through the discussions we had he has exemplified the true spirits of an original and bold thinker as an independent scientist—observant mind and critical thinking. From his abilities to distill a complex problem to its essence and to explain it with crystal clear clarity, I learned that a good scientist should also be a good story-teller. I was also fully influenced by his pure enthusiasm for science and research and his optimism in difficult situations. Through all these he had made my academic journey very much enjoyable and memorable.

Besides my advisor, I would like to specifically thank my dissertation committee members (Pradeep Guduru and Vikas Srivastava) for taking the time to read my dissertation and providing their insightful comments and valuable suggestions. I am thankful to Prof. Guduru, an expert in adhesive elastic contact, for his crucial remarks during my progress review presentation. I am also grateful to Prof. Srivastava for agreeing to serve on my dissertation committee. In addition, I would like to express my gratitude to Prof. Huajian Gao for accepting me to Brown and providing kind support to my first-year study.

The members of the Kesari group have contributed immensely to my personal and professional time at Brown. The group of smart people with diverse backgrounds has been a source of friendships as well as good advice. I am especially grateful to Michael Monn, Kaushik Vijaykumar, and Wenqiang Fang for their willingness to help whenever I have had questions and doubts. I acknowledge other past and present group members that I have had the great pleasure to work with: gradate students Jarod Ferreira, Jianzhe Yang, Wenbo Sun, Sayaka kochiyama, and post-doc Md Masiur Rahaman. I will cherish every 'Aha!' moment and exhilarating experience with them all the time.

My time at Brown was made enjoyable in large part due to my peer students in Solids Mechanics program and many wonderful friends in Providence. They provided not only support for my research but also enjoyment in living a balanced life. Among them, I gratefully acknowledge the assistance of Corrie Mook. She helped me a lot with much patience to improve the writings of my manuscript about the effect of machine stiffness on adhesive elastic contact. I also thank her and her generous family for the hospitality I received in the Thanksgiving Eve. I would like to thank my great friends in the badminton and basketball clubs. I will never forget the many fun activities we have done together. Special thanks to Xinye Lin, for all the happy moments we enjoyed in and the difficult times we came through together. Those have become unforgettable memories in my life.

Last and most importantly, I am deeply grateful to my parents for their sacrifices, endless love, and encouragement. Accomplishment of this dissertation would not be possible without their unconditional support. I love them forever.

DEDICATED TO MY PARENTS

Table of Contents

List of Tables

List of Illustrations

Chapter 1

Introduction

1.1 Motivation and background

Mechanics of adhesion and contact between elastic solids is important to many fields including engineering, physics, and biology. In engineering, for instance, as the design and production of structures being pushed down to micrometer and nanometer scales (e.g., micro/nano-electromechanical systems (MEMS/NEMS)), the surface adhesive forces between solids become predominant over the solid's bulk elastic properties [1]. These adhesive forces cause MEMS/NEMS devices to fail by having their parts inadvertently get stuck together, which limits their developments and applications [2]. Moreover, in the micro- and nano-fabrication of flexible and stretchable inorganic electronics, transfer printing is an emerging assembly technique that enables heterogeneous integration of separately fabricated objects into functional systems [3, 4]. The successful retrieval and printing of fabricated objects rely on fundamental understanding of the mechanism of tunable and reversible adhesion. Adhesion and contact also play a critical role in the physical mechanisms that underlie friction and wear at the sub-micrometer scale [5, 6]. Contact between hard solids, such as metals and ceramics, primarily takes place at the surfaces' asperities. Adhesion firmly welds the asperities, and thus the two solids. In order to move or slide the solids over one another, significant frictional force must be generated in order to break the asperities apart or rupture the asperities from their respective solids, contributing to wear. In biology, the mechanics of biological contact play a fundamental role in cell adhesion and insect and lizard locomotions. For example, cells interact with their environment

through mechanical forces for their mobility, division, and assembly. These mechanical forces are transmitted to the underlying substrate through "focal adhesion" sites [7]. Furthermore, it has been found that many insects and lizards possess fibrillar structures on their foot pads that, through adhesion, allow them to adeptly scale vertical surfaces [8]. Extensive efforts have been made to the study of biological adhesive systems as well as attempts at design and micro-fabrication of bio-inspired adhesive surfaces [9–12].

1.1.1 Classical elastic contact theories

Several classical contact theories, such as the Hertz [13], Johnson–Kendall–Roberts (JKR) [14], Derjaguin–Muller–Toporov (DMT) [15], and Maugis-Dugdale (MD) [16] theories, have been developed to analyze the contact behavior between elastic solids. It is assumed in those contact models that the solids' surfaces are smooth and the roughness effect is ignored. Among them, the Hertz theory does not consider adhesive interaction in the contact model, while the others do. The difference among the JKR, DMT, and MD theories lies in the way of modeling adhesive interaction in contact.

The frictionless, elastic contact problem was first solved by Hertz [13] in 1882, who considered the adhesiveless contact between two elastic spheres and approximated the shape of spheres near contacting point as paraboloid. The resulting indentation depth, h, and contact force, P are, respectively, given as

$$\begin{aligned} h &= \frac{a^2}{R}, \\ P &= \frac{4E^* a^3}{3R}, \end{aligned} \tag{1.1}$$

where a is the contact radius, $1/R = 1/R_1 + 1/R_2$, $1/E^* = (1-\nu_1^2)/E_1 + (1-\nu_2^2)/E_2$, R_1 and R_2 are the radii of the contacting spheres, E_i and ν_i $(i = 1,2)$ are, respectively, the Young's moduli and Poisson's ratios of the contacting spheres. A necessary condition for the Hertz theory to hold is that the contact radius should be much less than the sphere radius, i.e., $a \ll R$. A plot of the contact force–indentation depth (P–h) curve as per the Hertz theory is shown in Figure 1.1.

The seminal work of including surface adhesive interaction in elastic contact is the analytical model proposed by Johnson *et al.* [14] in 1975. In the JKR theory, the adhesive interaction is treated by including an adhesion energy term in the system's total potential energy, and the contact region

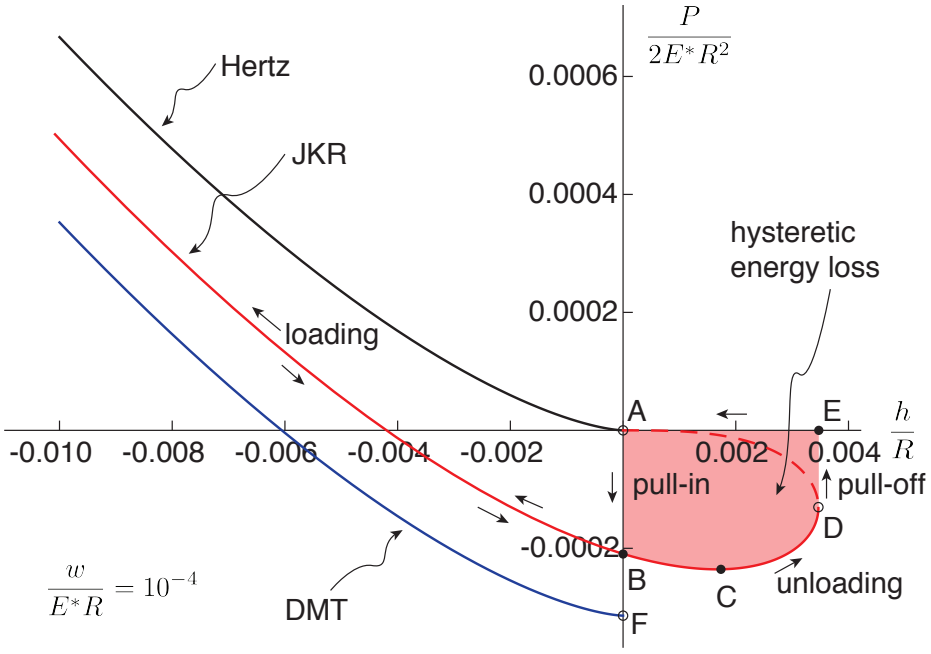

Figure 1.1: The contact force–indentation depth curves predict by the Hertz theory (black), the JKR theory (red), and the DMT theory (blue). The pull-in ($A \to B$) and pull-off ($D \to E$) instabilities for the JKR theory are marked along the curves, where the circle and dot indicate the unstable and stable states, respectively. The adhesive forces for the JKR and DMT theories are achieved at point C and F, respectively.

is determined by stipulating that the contact radius locally minimizes the total potential energy. Conceptually, it is identical to Griffith's theory of fracture. That is, the variation of elastic strain energy per unit area as the contact region changes is equal to the work of adhesion, w. For the adhesive contact between two elastic spheres, the indentation depth and contact force predicted by the JKR theory are

$$\begin{aligned} h &= \frac{a^2}{R} - \sqrt{\frac{2\pi a w}{E^*}}, \\ P &= \frac{4E^* a^3}{3R} - \sqrt{8\pi a^3 w E^*}. \end{aligned} \tag{1.2}$$

As per the JKR theory, the two solids would jump into contact unstably with a pull-in instability when approaching to each other (loading phase), and would jump out of contact with a pull-off instability during separation (unloading phase), see Figure 1.1. After the pull-instability, the formed contact area, indentation depth, and resulting contact force are, respectively,

$$a_B = \left(\frac{2\pi R^2 w}{E^*}\right)^{1/3}, \quad h_B = 0, \quad P_B = -\frac{4}{3}\pi w R. \tag{1.3}$$

The contact area, indentation depth, and contact force at the pull-off instability are, respectively,

$$a_D = \left(\frac{\pi R^2 w}{8E^*}\right)^{1/3}, \quad h_D = -\left(\frac{27\pi^2 R w^2}{64E^{*2}}\right)^{1/3}, \quad P_D = -\frac{5}{6}\pi w R. \tag{1.4}$$

The adhesive force, defined as the most negative contact force during contact, occurs at point C, where

$$a_C = \left(\frac{9\pi R^2 w}{8E^*}\right)^{1/3}, \quad h_C = -\left(\frac{3\pi^2 R w^2}{64E^{*2}}\right)^{1/3}, \quad P_C = -\frac{3}{2}\pi w R. \tag{1.5}$$

The measured P–h curves during a contact cycle form a closed loop due to the pull-in and pull-off instabilities, whose enclosed area indicates the hysteretic energy loss and is equal to

$$\mathscr{H}_{\mathrm{JKR}} = 7.092\left(\frac{R^4 w^5}{E^{*2}}\right)^{1/3}. \tag{1.6}$$

This energy loss is independent on the maximum indentation depth, which we refer to as depth-independent hysteresis.

Later on, Derjaguin *et al.* [15] proposed another adhesive elastic contact model, in which they assume that the stress and displacement fields remain the same as the Hertz theory but the adhesive interaction just outside contact region results an additional adhesive force. Derjaguin *et al.* [15] did not obtain an analytical P–h relation. However, if one ignores the elastic deformation due to the adhesive interaction, then the indentation depth of the DMT theory is the same as that of the Hertz theory, and the contact force of the DMT theory is the sum of the contact force given by Hertz theory and the adhesive force, i.e.,

$$\begin{aligned} h &= \frac{a^2}{R}, \\ P &= \frac{4E^* a^3}{3R} - 2\pi w R. \end{aligned} \tag{1.7}$$

A plot of the P–h curve as per the DMT theory is shown in Figure 1.1. The adhesive force predicted by the DMT theory is $-2\pi w R$, which occurs at $a = 0$.

An apparent contradiction between the JKR and DMT theories is their predictions of adhesive force. Tabor argued both theories are correct in a sense that the elastic contact with surface adhesive

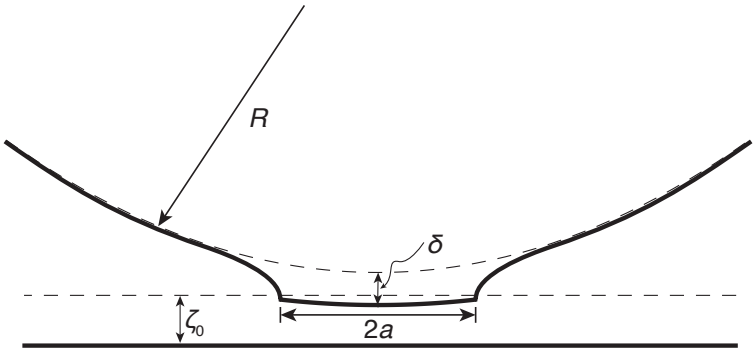

Figure 1.2: The comparison of the interatomic equilibrium separation with the localized height on the sphere due to adhesion within the contact region.

interaction is indeed governed by a dimensionless parameter [17]

$$\mu_{\mathrm{T}} = \left(\frac{Rw^2}{E^{*2}\zeta_0^3} \right)^{1/3}, \tag{1.8}$$

which is now referred to as Tabor parameter. Here ζ_0 is the interatomic equilibrium separation. The Tabor parameter represents the ratio of the localized height on the sphere due to adhesion within the contact region, δ [which is in the order of $(Rw^2/E^{*2})^{1/3}$], to the adhesive length scale, ζ_0, see Figure 1.2. Muller *et al.* [18] numerically showed that the JKR and DMT theories, respectively, hold for large μ_{T} ($\mu_{\mathrm{T}} > 5$) and small μ_{T} ($\mu_{\mathrm{T}} < 0.1$), and observed a smooth transition from DMT to JKR for $0.1 < \mu_{\mathrm{T}} < 5$. By using the *Dugdale cohesive zone* to model the adhesive interaction at the contact edge, Maugis [16] obtained an analytical solution for the adhesive elastic contact and showed the continuous transition from DMT to JKR as the μ_{T}-related parameter increases. In fact, the MD theory [16] assumes a finite range of adhesive interaction, while the JKR theory and the DMT theory consider the range of adhesive interaction to be infinitesimal short and infinite, respectively, compared with the length scale of the solid's elastic deformation. Thus, the JKR theory and the DMT theory can be derived as two opposite asymptotic limits of the MD theory, see detailed discussion in Chapter 3.

1.1.2 Effect of roughness on adhesion

The classical contact theories (Hertz, JKR, DMT, and MD) model the contact of solids whose surfaces are smooth, and are not applicable for real surfaces that are known to possess roughness—local

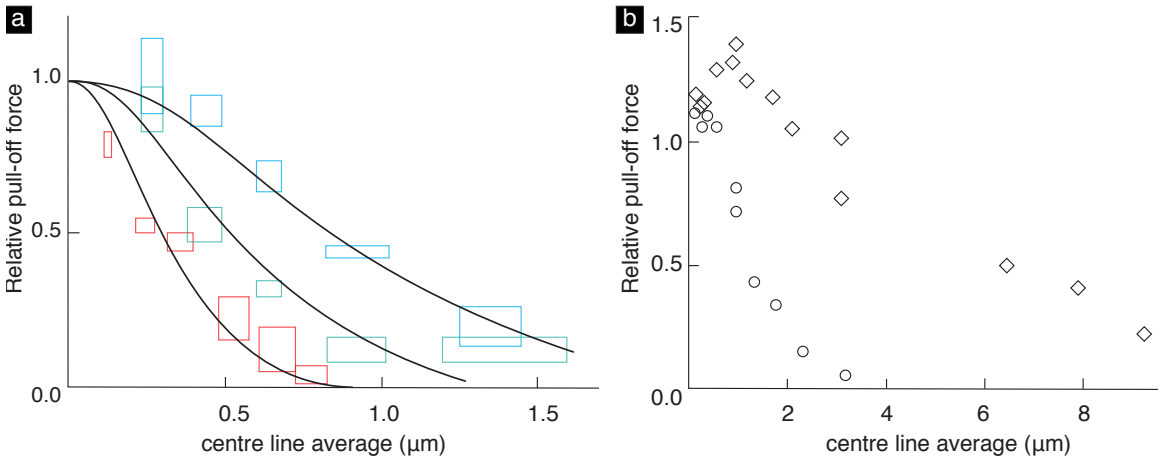

Figure 1.3: Relative pull-off force of a smooth rubber surface in contact with a Perspex surface as a function of the roughness of the Perspex. The pull-off force is normalized by that of a nominally smooth Perspex surface. (a) Experimental measurements by Fuller and Tabor [19]. Red–Rubber modulus: 2.4 MPa; Green–0.68 MPa; Blue–0.22 MPa. (b) Experimental measurements by Briggs and Briscoe [23]. ○–Rubber modulus: 487 kPa; ◇–67kPa.

imperfections and deviations from ideal flatness. Therefore, understanding the role of roughness on adhesive elastic contact is of paramount importance.

Surface roughness has been shown to significantly affect the adhesive contact between elastic solids. There are several experimental observations in which surface roughness has been typically shown to reduce the adhesion when separating two contacting surfaces. For example, Fuller and Tabor [19] measured the adhesive force between a smooth rubber sphere and a hard rough substrate (Perspex). They found that the small-scale surface roughness of magnitude at a few micrometers could lead to an extremely large reduction in adhesion, see Figure 1.3a. Similar observations have also been made by Levins *et al.* [20], Quon *et al.* [21], and Rabinovich *et al.* [22]. The reduction effect of roughness is often attributed to the decrease in the true contact area because of the fact that only asperity contacts occur on the contacting interface. In the energy point of view, the decrease in the total free energy due to the formation of adhesive contacting interface is offset by the relatively large elastic energy penalty needed to bring the two rough surfaces into contact.

To explain the reduction of adhesion by roughness, Fuller and Tabor [19] developed an adhesive contact theory of rough surfaces based on the Greenwood and Williamson's *multiple non-interacting asperity contact model* (GW model) [24] and the JKR theory [14]. Figure 1.4a shows the GW model which considers the adhesiveless contact of an elastic rough surface with an ideally flat rigid surface. The mean plane of asperity heights is taken as the datum and the distance between the rigid

flat surface and the datum is referred to as the separation d. All the asperities are assumed to be spherical shape with a constant radius R. The asperity height is denoted as z_s and has a distribution function $\phi(z_s)$, which express the probability of finding an asperity of height z_s lying in the interval z_s to $z_s + dz_s$. The asperity height's distribution function is often assumed to be Gaussian,

$$\phi(z_s) = \frac{1}{\sqrt{2\pi}\sigma_{\text{rms}}} e^{-\frac{z_s^2}{2\sigma_{\text{rms}}^2}}, \tag{1.9}$$

where σ_{rms} is standard deviation of asperity heights. If there are N asperities within the nominal contact area in all, then the number of contacting asperities is

$$n = N \int_d^\infty \phi(z_s) dz_s. \tag{1.10}$$

Fuller and Tabor [19] extended the GW model by using the JKR theory to describe the contact behavior between the asperities and the rigid flat surface. According to [19], we rewrite the P–h relation of the JKR theory for the individual asperity contact as

$$\frac{h}{h_o} = \begin{cases} (3\chi - 1)\left[\frac{1}{9}(1+\chi)\right]^{1/3}, & \chi \geq 0, \\ -(3\chi + 1)\left[\frac{1}{9}(1-\chi)\right]^{1/3}, & 0 \leq \chi \leq \frac{2}{3}, \end{cases} \tag{1.11}$$

where

$$\chi = \left(1 + \frac{P}{P_o}\right)^{1/2}, \tag{1.12}$$

$h_o = h_D$, and $P_o = P_C$. The expressions of H_D and P_C are given in the JKR theory. Hence from (1.11) we obtain the relation

$$\frac{P}{P_o} = F\left(\frac{h}{h_o}\right). \tag{1.13}$$

Let $h = z_s - d$ denotes the indentation depth. Then the total contact force can be computed as a sum of the contact force from each asperity contact,

$$P(d) = NP_o \int_d^\infty F\left(\frac{z_s - d}{h_o}\right) \phi(z_s) dz_s = NP_o \int_L^\infty F\left(\frac{h}{h_o}\right) \phi(h+d) dh. \tag{1.14}$$

The value of the lower limit of integration in (1.14) is different for the loading and unloading phases.

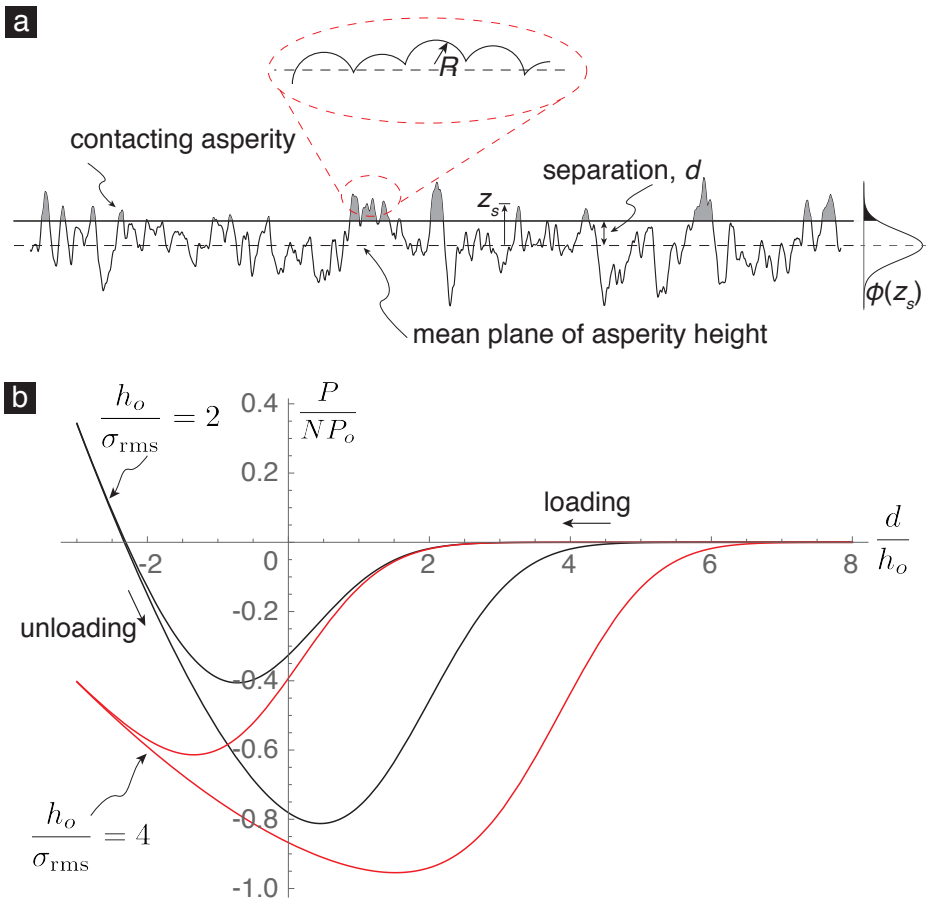

Figure 1.4: (a) The GW model showing contact between an elastic rough surface and a rigid flat surface. The asperities are simply identical spheres with radius R and their heights have a Gaussian distribution. (b) The effect of roughness on contact force–separation curves as per Fuller and Tabor's theory.

During the loading phase, $L = 0$. However, when the unloading phase starts from the minimum separation $d_{\min}$, it is necessary to account for the fact that the asperities, which already made contact with the flat surface during loading, would be extended and not break contact until their extensions exceed h_o. Therefore, during unloading, the value of L is determined by

$$L = \begin{cases} -h_o, & d - d_{\min} \geq h_o, \\ d_{\min} - d, & d - d_{\min} \leq h_o. \end{cases} \tag{1.15}$$

As per Fuller and Tabor's theory, the adhesion is reduced as the roughness increases. This can be clearly seen from Figure 1.4b, which shows the contact force–separation curves for two different $\sigma_{\rm rms}$ values. It is found that both the adhesive force and the energy loss decrease as $\sigma_{\rm rms}$ increases.

Despite the widely observed reduction of adhesion by roughness, experimental evidences showing adhesion enhancement of rough surfaces are not uncommon. For example, Briggs and Briscoe [23] reported the increase of adhesive force for very small roughness before it decreases as the roughness becomes larger in the contact of a roughened Perspex and a smooth rubber surface, see Figure 1.3b. Later on, Fuller and Roberts [25] performed a rolling experiment involving a very soft rubber and a Perspex surface and confirmed the enhancement effect of surface roughening on adhesion. They further argued that neither Briggs and Briscoe's explanation [23] in terms of energy loss at isolated asperities nor the rate-independent and -dependent peel energy models is not able to produce adhesion enhancement. Instead, they showed that the adhesion enhancement is resulted from the increase of real contact area, since the viscoelasticity and relaxation of the rubber allows the soft rubber to conform the Perspex's rough surface without building up high interfacial stress. Kim and Russell [26] studied the effect of surface roughness on the adhesion with artificially roughened surfaces and crosslinked poly(dimethylsiloxane) (PDMS) and found that the work of adhesion increases with the surface roughness before decreasing. Kesari *et al.* [27] conducted atomic force microscopy (AFM) contact experiments between a glass bead and PDMS slabs with various root-mean-square (RMS) roughness (Figure 1.5a). They concluded that the hysteretic energy loss during a contact cycle initially increases with the RMS roughness, reaches a maximum and then decreases (Figure 1.5b). More recently, surface wrinkles driven by elastic instabilities and other techniques provide an approach to form periodic surface roughness with various patterns of tunable surface topography [28]. Many studies demonstrated that the adhesion of a soft material could be controlled with desirable properties such as on-demand increase and decrease by tuning the dimension and morphology of wrinkles patterned on the surface [29–33], as shown in Figure 1.5c.

The understanding of the mechanisms of adhesion enhancement due to roughness remains open. One plausible argument for the enhanced adhesion due to roughness observed in experiments might be attributed to the increase in real contact area based on the fact that the soft elastic solid can deform conformably to the rough surface [25, 33]. Another explanation for the enhanced adhesion due to roughness comes from the theoretical work by Guduru [34], Kesari and Lew [35], and Li and Kim [36]. Guduru [34] considered the axisymmetric adhesive contact problem between a wavy elastic half-space and a rigid solid as a model to study to the roughness effect on adhesion. Guduru's

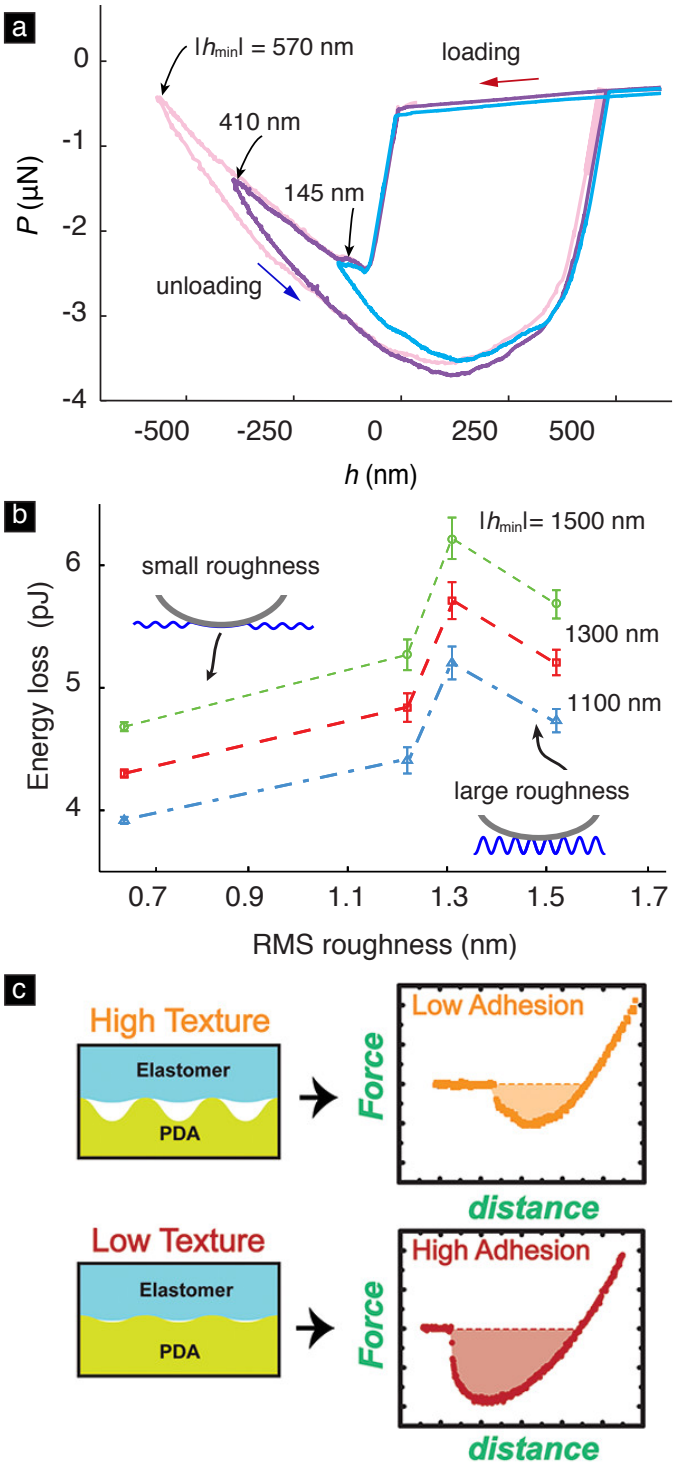

Figure 1.5: (a) Representative *P*–*h* curves measured in the AFM contact experiments between a glass bead and a PDMS substrate. The loading and unloading curves during a contact cycle are not overlapped with each other and the size of the hysteresis loop increases with $|h_{\min}|$. (b) The variation of total energy loss as a function of the RMS roughness in the experiments. (a–b) are modified from [27] and see experiment details therein. (c) The adhesion of soft material can be tuned by controlling the amplitude of the surface wrinkles [33].

theory predicts enhanced hysteretic energy loss and pull-off force of the wavy surface comparing with that of the adhesive contact of a flat surface by the JKR theory, which is confirmed by Guduru and Bull's experiment [37]. Kesari and Lew [35] generalized Guduru's wavy adhesive contact problem by considering the contact between an elastic half-space and an axisymmetric, rigid wavy punch. They also obtained an effective contact force–indentation depth relation in the limit of small roughness, i.e., the wavy amplitude is much smaller than the characteristic size of the punch. Li and Kim [36] considered the adhesive contact problem between two solids using the homogenized cohesive zone, in which one of them was an elastic half-space and the other was a rigid solid with two-dimensional sinusoidal undulations on its surface. The theoretical argument for adhesion enhancement by roughness is attributed to the fact that the surface roughness could create surface mechanical instabilities and consequently lead to an effective adhesive toughening of the contact interface [34–36].

1.1.3 Depth-dependent hysteresis in adhesive elastic contact

An important phenomenon associated with the surface roughness dependent adhesion is the depth-dependent hysteresis (DDH) observed in many adhesive contact experiments involving soft materials [27, 33, 38–40]. In such experiments, the contact force at a given indentation depth differs depending on whether the experiment is in a loading or an unloading phase, see Figure 1.5a. Moreover, the force in the unloading phase depends on the maximum indentation depth $|h_{\min}|$, which is the indentation depth at the beginning of the unloading phase in a contact cycle. Therefore, the hysteretic energy loss is different from one contact cycle to another depending on $|h_{\min}|$. In addition, the energy loss is found to increase with roughness at small roughness regime but to decrease as the surface becomes rougher, see Figure 1.5b. It is noted that the DDH phenomenon can not be captured by the classical adhesive contact theories.

The DDH has traditionally been attributed to various mechanisms including the interdigitation of tethered chains [38], the meniscus effect of ambient moisture [40], the formation of hydrogen bonds [41], and the viscoelastic and plastic deformations of materials [42, 43], etc. However, Kesari *et al.* [27] reported that the DDH persists while the aforementioned mechanisms can be reasonably excluded. Furthermore, Kesari and Lew [35] proposed a continuum model of adhesive contact

involving an elastic half-space and a rigid rough punch, in which the small-scale roughness is represented by the wavy undulations on the punch's surface. Based on this model, they suggested an alternative mechanism for DDH. That is, the DDH is an emergent property from contact between rough surfaces which originates as the smeared out effect of a series of mechanical instabilities created by the small-scale surface asperities. The instabilities are similar to the pull-in and pull-off instabilities as seen in the classical adhesive contact theories, but are at the asperity level and numerous, leading to extensive energy loss. In addition, their model predicts that the energy of DDH increases with the small-scale surface roughness in the small roughness regime.

1.2 Outline of the dissertation

The main objectives of this dissertation are to develop analytical and computational models for adhesive elastic contact between rough surfaces and analyze the effects of bulk and surface material properties and surface topography on adhesive elastic contacts. The researches carried out in this dissertation aim to provide fundamental understanding of the mechanics of elastic contact and adhesion of rough surfaces. The results of this dissertation have direct implications in various fields including MEMS devices, bio-inspired adhesive structures, and interfacial toughening for soft material. The dissertation is organized as follows.

In Chapter 2, we study an axisymmetric mechanics problem involving the adhesive, frictionless contact between an elastic half-space and a rigid tip with general surface profile to investigate the effect of machine stiffness on interpreting contact force–indentation depth curves in adhesive elastic contact experiments. The JKR theory has been exceptionally successful in interpreting contact force–indentation depth measurements and explaining adhesive, elastic contact phenomena, such as the pull-in and pull-off instabilities. However, in many cases the JKR theory predicts a lower magnitude for the pull-off force than what is experimentally measured, and it does not capture the finite changes in the indentation depth that occur during the pull-in and pull-off instabilities. We believe that these discrepancies occur because the classical JKR theory ignores the machine stiffness—which, in the case of AFM-type instruments, is the stiffness of the mechanical structure that connects the tip to the translation stage. Our model explains the experimental data better than

the JKR theory in the cases where the JKR theory displays the aforementioned discrepancies.

In Chapter 3, we present a randomly rough surface model of adhesive elastic contact to analyze DDH at large surface roughness. Although Kesari and Lew [35] proposed a mechanics model based on the occurrence of adhesion and roughness related small-scale instabilities to explain DDH, their model only applies in the regime of infinitesimally small surface roughness, and consequently it does not capture the decrease in energy loss with surface roughness at the large roughness regime, as shown in Figure 1.5b. Our new mechanics model, which is a non-interacting asperity type contact model, applies in the regime of large surface roughness. The primary difference between the model presented in [35] and the new model herein is that the contact region in the former is simply connected whereas in the latter it is multiply connected. Our model is based on the MD theory of adhesive elastic contact and Nayak's theory of rough surface. In it, the surface asperities come into and out of contact with the tip through small-scale surface mechanical instabilities. The number of instabilities depends on the roughness of the contact surface and the maximum indentation depth. Larger maximum indentation depth results in more surface features participating in the contact process, leading to larger hysteretic energy losses. The model captures the trend of decreasing energy loss with increasing roughness. It also captures the experimentally observed dependencies of energy loss on the maximum indentation depth, and bulk and surface material properties.

In Chapter 4, we propose an effective, nonlinear body force based approach to simulate adhesive elastic contact and investigate the effect of surface roughness on adhesion. We specifically study the contact between an axisymmetric elastic tip and a rigid half-space. The adhesive interaction is modeled as an effective body force on the tip due to its interaction with the half-space, which is governed by the generalized Lennard-Jones (LJ) potential. For the contact between a smooth tip and the half-space, we find the occurrence of contact instabilities is controlled by the Tabor parameter. The most notable feature of the study is that it is able to capture the mechanism of DDH and the adhesion enhancement by surface roughness observed in many adhesive contact experiments. Our simulations provide a critical evidence to the small-scale contact instability mechanism as a plausible explanation for DDH. Our simulations reveal that DDH originates from small-scale contact instabilities at the surface asperity level. Both maximum adhesive force and hysteretic energy

loss first increase then decrease as the surface roughness increases. The adhesion enhancement effect of rough surfaces is resulted from the increased contact area in the small roughness regime. Furthermore, our simulations give other interesting insights into the mechanics of adhesive contact between rough surfaces. It is found that the change in the trend of roughness effect on adhesion correlates with the transition of contact region from being simply connected to multiply connected. The interactions between surface asperities become weaker and the contact becomes asperity type as roughness increases. These new findings cannot be captured by theoretical contact models.

In Chapter 5, we explore the principle of contact splitting for biological fibrillar structures and investigate their adhesion on rough surfaces through a multiple spring model. Many animals such insects, spiders, and lizards have developed an alternate strategy—fibrillar structures on their attachment pads—to achieve remarkable adhesion and easy release for locomotion on natural rough surfaces. The biological fibrillar structures allow individual fibril to deform more easily to conform with the rough surface, resulting increased contact area, which gives strong adhesion for relative stiff biological materials. The detachment of a single fibril is unable to trigger the next fibril to detach from the substrate. The additional energy needed for crack re-initiation of each fibril manifests as a better adhesion of the fibrillar structure. We investigate the effects of fibril stiffness and surface roughness and correlation length of rough surface on the adhesion of fibrillar structures.

In Chapter 6, we present a model of peeling an elastic soft thin film from a rigid substrate with a periodic, rough surface. The peeling force is obtained by minimizing the total potential energy of the system and the equilibrium path is discussed based on stability analysis. It is found that there exist snap-through instabilities during the peeling of thin film, resulting in an apparent toughening of the interface between thin film and substrate. Furthermore, it is shown that the effective peeling force and work of adhesion for rough substrates can be increased significantly compared to that of the flat case by increasing the aspect ratio of the surface. Asymptotic limits of effective peeling force and work of adhesion are obtained in the limit of large aspect ratio of the wavy substrate's surface. The theoretical results suggest that the adhesion of interface can be enhanced by designing the interfacial topography.

Finally, in Chapter 7 we conclude the dissertation with a summary of main findings of the work and a outlook of related future directions.

Chapter 2

Effect of machine stiffness on interpreting contact force–indentation depth curves in adhesive elastic contact experiments

Note: A version of this chapter is accepted for publishing in *Journal of the Mechanics and Physics of Solids*. Data and figures have been used with all co-authors' consent.

Deng WL and Kesari H. Effect of machine stiffness on interpreting contact force–indentation depth curves in adhesive elastic contact experiments. Journal of the Mechanics and Physics of Solids, Accepted, 2019.

2.1 Introduction

Van der Waals (dipole-dipole) and Coulombic interactions between molecules can give rise to attractive forces between solids [44, 45]. These attractive forces can make a pair of contacting surfaces adhesive even when they are not connected by any liquid bridges. The effect of these attractive forces, termed *dry adhesion*, operates at all scales but is dominant at μm–nm lengths (Figure 2.1a).

Dry adhesion has been found to play an important role in many fields, including biology, engineering, and physics. Many insects, spiders, and reptiles, for example, possess fibrillar structures on their foot pads that, through adhesion, allow these animals to adeptly scale vertical surfaces [8,46–50] (Figure 2.1b). In MEMS engineering, adhesion-induced device failure is a pervasive problem that limits its continued development. In MEMS devices, such as comb drive accelerometers, slender, micrometer-sized structures are aligned in parallel rows in close proximity to one another (Figure 2.1c). During the device's fabrication stage or later in its operation, these structures can unintentionally come into contact with each other or the substrate and remain permanently adhered, leading to device failure [2]. Adhesion also plays a role in the physical properties that underlie friction and wear at the sub-micrometer scale [6, 51]. Contact between hard solids, such as metals and ceramics, primarily takes place at the surfaces' asperities. Adhesion firmly welds the asperities, and thus the two solids. In order to move or slide the solids over one another, significant frictional force must be generated in order to break the asperities apart or rupture the asperities from their respective solids, contributing to wear (Figure 2.1d).

An important metric for quantifying dry adhesion between two contacting solids is the Dupré's work of adhesion,

$$w := \gamma_1 + \gamma_2 - \gamma_{12}, \tag{2.1}$$

where γ_1 and γ_2 are the surface energies of the two solids and γ_{12} is the contact interface's energy per unit area [1]. Adhesion can be measured through a variety of tests and experiments, including thin film peeling [53–55], blister tests [56,57], and normal contact experiments [27,58–64]. Among these techniques, normal contact experiments distinguish themselves for two reasons: firstly, they can provide information about the materials' elastic properties; and secondly, they can spatially map out a material's surface adhesive and bulk elastic properties at the μm–nm length scales, making it the preferred test for evaluating adhesion and the elasticity of a solid.

Normal contact experiments are typically performed using an AFM [27,58–61] or an instrument modeled after it. In these experiments, a sample of the material whose properties are to be examined is prepared in the form of a rectangular or circular slab. This slab is most commonly referred to as the substrate. The substrate is placed under a rigid tip, which is connected to a stage via a passive mechanical structure, such as the cantilever in an AFM (Figure 2.2a). The instrument

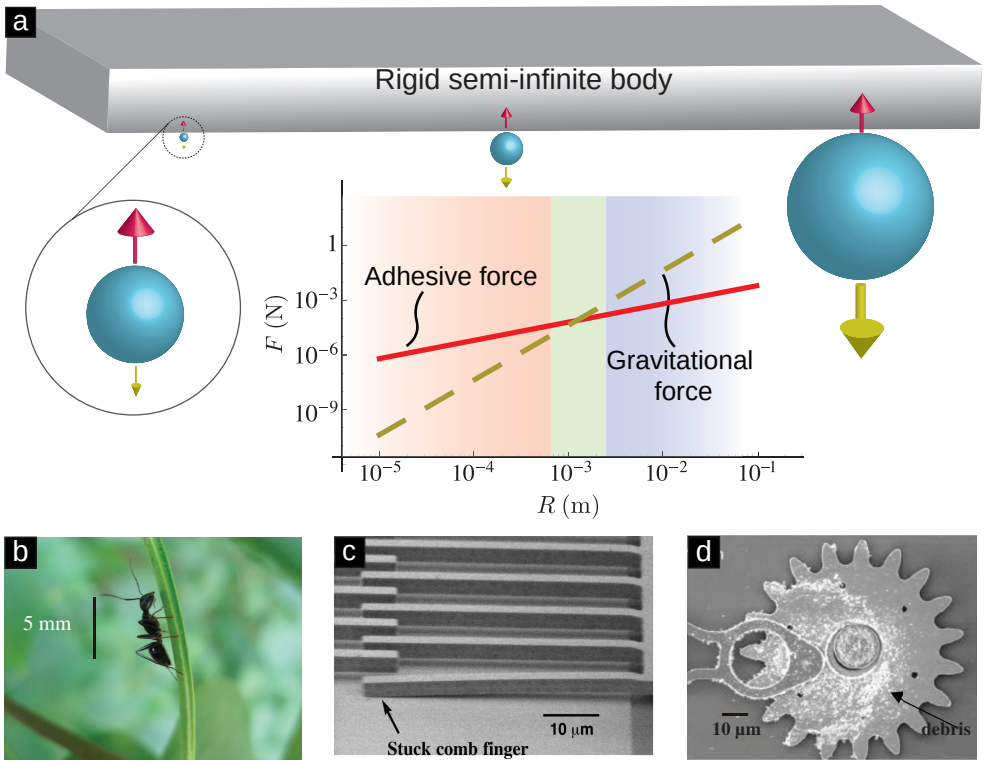

Figure 2.1: (a) Adhesion dominates at small scales. Bradley [52] considered the adhesive force between a rigid sphere and a rigid semi-infinite body. He assumed that the adhesive interaction between two molecules of the solids, with centers a distance d apart, is proportional to $1/d^n$ where n is an integer. The adhesive force is found to be $2\pi wR$, where w is the work of adhesion and R is the radius of the sphere. At the same time, the gravitational force on the sphere is $4\pi\rho gR^3/3$ where ρ is the density of the material of which the sphere is composed. For most engineering materials, w and ρ are of the order of 10 mJ/m^2 [1] and 10^3 kg/m^3, respectively. (b) An ant climbs on a plant stem, showcasing that adhesive forces overcomes the gravitational forces at small length scales. (c) A comb finger of a drive actuator is stuck to the substrate due to adhesion [2]. (d) Wear debris accumulates on the surface of the gear of a microengine [2] as a result of adhesion.

controls the position of the stage and brings the tip and substrate into and out of contact. Mechanical properties are measured at a given location on a substrate's surface by carrying out one or more contact cycles. Each contact cycle begins with a loading phase, when the stage moves towards the substrate, followed by an unloading phase, when the stage moves away from the substrate. During contact cycles, the deformation of the mechanical structure that connects the stage to the tip is often small, resembling an elastic spring. The stiffness of this spring is referred to as the *machine stiffness*. In AFM contact experiments, the mechanical structure that connects the tip to the stage is a cantilever. The cantilever's shape, size, and material composition then dictate the machine stiffness.

In the experiments, the contact force that arises between the two solids is measured as a function of the indentation depth which is the distance from the undeformed substrate's surface to the tip. The properties of the substrate are obtained from the contact force–indentation depth data based

on a classical adhesive contact theory such as the JKR theory [14]. According to the JKR theory, the tip would jump into contact with the substrate unstably in the loading phase, resulting in an abrupt decrease in the contact force. Similarly, in the unloading phase, the tip would jump out of contact with the substrate spontaneously, resulting in a sudden increase in contact force. The phenomena of the tip jumping into and out of contact with the substrate unstably are called *pull-in* and *pull-off* instabilities, respectively. There are two important experimental results that differ from the JKR predictions. First, the indentation depth just before and after the pull-in and pull-off instabilities do not change as per the JKR theory, see Figure 2.2b. However, in many adhesive contact experiments the indentation depth just before and after the pull-in and pull-off instabilities are different [27,58,59,61], see Figure 2.2c. Second, the JKR theory predicts the contact force at the pull-off instability, i.e. the pull-off force, to be $-5\pi wR/6$, where R is the radius of curvature of the tip; whereas the measured pull-off force in experiments is different from that value (see §2.4). The work of adhesion would be inaccurate if it were calculated using the pull-off force given by the JKR theory. The reason for this difference is due to the machine stiffness, whose effect is overlooked in the JKR theory.

In this work, we show that machine stiffness is an important factor in adhesive contact. Our problem is a model for a class of contact experiments that are conducted using an AFM-type instrument. We consider an axisymmetric mechanics problem involving the adhesive, frictionless contact between two solids to study the effect of machine stiffness. Both the tip's symmetry axis and the stage's translational directions are normal to the substrate's surface that faces the tip. We assume that the contact region is simply connected and hence is a disk that has its center on the tip's symmetry axis. Just as in the JKR model [14], adhesion in our problem is modeled as an infinitesimal interaction—albeit its origins from the van der Waals and Coulombic interactions are finite-ranged. More specifically, Johnson *et al.* [14] treated adhesive elastic contact by including an adhesion energy term in the system's total potential energy, and then determined the contact region by stipulating that the contact radius locally minimizes the potential energy. We adopt the same methodology as Johnson *et al.* [14], and additionally include an elastic energy term that results from the deformation of the instrument's mechanical structure into the total potential energy calculation of our model. We use a variational approach in the study of our adhesive contact problem and derive

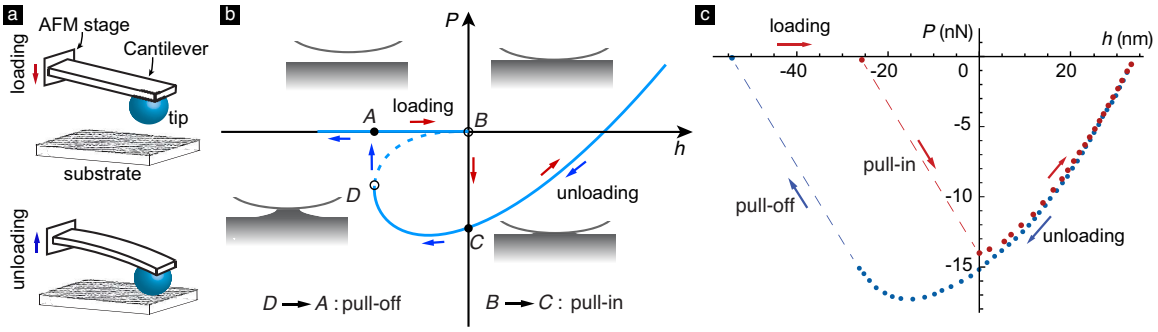

Figure 2.2: (a) A schematic of an AFM contact experiment. The instrument brings the tip and substrate into and out of contact by controlling the position of the stage, which is connected to the tip by an elastic cantilever. (b) The contact force–indentation depth curve according to the JKR theory. The pull-in instability ($B \to C$) and pull-off instability ($D \to A$) are marked along with corresponding contact configurations. (c) The measured contact force–indentation depth data from the contact experiments between a glass bead and a Polydimethylsiloxane (PDMS) substrate [58].

the necessary and sufficient conditions on the solutions to our problem. We remark that Takahashi *et al.* [65] and Yang [66] analyzed the effect of machine stiffness on the adhesive contact between a paraboloidal tip and an elastic half-space. They too use a variational approach. However, our approach is different from that of Takahashi *et al.* and Yang in that they only consider the first order necessary conditions on the solutions to their problems, while in our model we further consider the second order sufficiency conditions on the solutions. Second order sufficiency conditions have previously been used to study the stability of the equilibrium configurations in adhesive elastic contact problems by Kesari and Lew [35], Argatov *et al.* [67], Willert *et al.* [68], and Popov *et al.* [69], among others.

The outline of the work is as follows. First, we formulate our contact problem using the variational approach and derive the solutions in §2.2. In §2.3 we consider two tip geometries, spherical and conical, as examples to illustrate the results derived in §2.2. In this section, we also study the dependence of the pull-in and pull-off instabilities and the resulted hysteretic energy loss on the machine stiffness. We compare the theoretical predictions of our model with experimental measurements and discuss some potential sources for the discrepancies between our model and experiments in §2.4.

2.2 Adhesive elastic contact model

2.2.1 Geometry

Figure 2.3 shows the geometry of our contact mechanics problem. Our problem has the three-dimensional Euclidean point space $\mathbb{E}^3$ as its backdrop. We identify points in $\mathbb{E}^3$ using the set of Cartesian coordinates $\{x, y, z\}$ that correspond to a fixed, orthonormal set of vectors $\{\hat{\boldsymbol{e}}_x, \hat{\boldsymbol{e}}_y, \hat{\boldsymbol{e}}_z\}$ that span the vector space $\mathcal{V}$ associated with $\mathbb{E}^3$.

The tip in the class of experiments that we model in this work is usually composed of materials that are much stiffer than that of the substrate. Thus, we model the tip as a rigid solid. Recall that in the experiments we model, the tip's geometry has continuous rotational symmetry. Therefore, we take the tip to be a solid of revolution whose symmetry axis is a fixed line that is parallel to $\hat{\boldsymbol{e}}_z$ and passes through the fixed point O, which is the origin of $\mathbb{E}^3$. In the reference configuration of our problem (Figure 2.3a), the tip's surface facing the substrate is the region

$$\partial\mathcal{T}_0 := \{\mathscr{P}_t = O + r\hat{\boldsymbol{e}}_r(\theta) + f(r)\hat{\boldsymbol{e}}_z \in \mathbb{E}^3 \mid \theta \in [0, 2\pi) \text{ and } r \in [0, \infty)\},$$

where the tip's radial profile $f : [0, \infty) \to (-\infty, 0]$ is a sufficiently smooth function such that $f(0) = 0$, the vector $\hat{\boldsymbol{e}}_r(\theta) := \cos\theta\hat{\boldsymbol{e}}_x + \sin\theta\hat{\boldsymbol{e}}_y$, and r and θ are, respectively, the radial and polar coordinates of $\mathscr{P}_t$.

We model the instrument's stage as a material point and the structure connecting the tip and the stage as a linear elastic spring. In the reference configuration of Figure 2.3a, the spring is unstretched. In the class of experiments we model, the size of the contact region is typically much smaller than the dimensions of the substrate. In the reference configuration, the substrate occupies the region $z \geq 0$, which we refer to as the half-space $\mathcal{S}_0$. We refer to the surface of $\mathcal{S}_0$ that faces the tip as $\partial\mathcal{S}_0$. In the reference configuration, there is no contact between the tip and substrate and the substrate is stress-free. We discuss in more detail what it means for the tip and substrate to be in contact later in this section.

Figure 2.3b shows the deformed configuration of our problem. In it, the stage and tip have been moved by amounts of $\Delta\hat{\boldsymbol{e}}_z$ and $h\hat{\boldsymbol{e}}_z$, respectively, from where they were located in the reference

configuration. We call Δ the stage displacement and $h \in (-\infty, +\infty)$ the indentation depth. In the deformed configuration, the tip's surface facing the substrate occupies the region

$$\partial \mathscr{T}_t := \{o + r\hat{\boldsymbol{e}}_r(\theta) + \tilde{u}_z(r;h)\hat{\boldsymbol{e}}_z \in \mathbb{E}^3 \mid \theta \in [0, 2\pi) \text{ and } r \in [0, \infty)\},$$

where $\tilde{u}_z(\cdot, h) : [0, \infty) \to (-\infty, +\infty)$ is defined as

$$\tilde{u}_z(r;h) := h + f(r). \tag{2.2}$$

As is standard in continuum mechanics, we identify material particles that belong to the tip or substrate by the spatial points in the reference configuration $\mathbb{E}^3$ where they originate. We say that a substrate's surface material particle $\mathcal{S} \in \partial \mathscr{S}_0$ is a contact particle if there exists a tip material particle $\mathcal{Q} \in \partial \mathscr{T}_0$ such that $\mathcal{S}$ and $\mathcal{Q}$ occupy the same spatial point in the deformed configuration. We refer to the set of all contact particles as the contact region Γ_c and to the measure of Γ_c as the contact area. We define the tip and substrate to be in contact if the contact area is strictly positive. As previously noted, our problem is axisymmetric and the contact region in it is simply connected. Therefore, we can always write $\Gamma_c = \{\mathcal{S} \in \partial \mathscr{S}_0 \mid r \leq a\}$, where r is $\mathcal{S}$'s radial coordinate and $a \geq 0$ is Γ_c's contact radius.

Let $\mathscr{P} \in \mathscr{S}_0$ be a substrate material particle. The displacement of $\mathscr{P}$ is the vector $\boldsymbol{u}(\mathscr{P})$ that is defined such that $\mathscr{P} + \boldsymbol{u}(\mathscr{P}) = p$, where p is $\mathscr{P}$'s location in the deformed configuration. In our problem we only consider displacement fields $\boldsymbol{u} : \mathscr{S}_0 \to \mathscr{V}$ for which p has the same θ coordinate as $\mathscr{P}$. Therefore, $\boldsymbol{u}(\mathscr{P})$ can be expressed as $u_r(r,z)\hat{\boldsymbol{e}}_r(\theta) + u_z(r,z)\hat{\boldsymbol{e}}_z$, where r, θ, and z are $\mathscr{P}$'s cylindrical coordinates and $u_r(\cdot,\cdot),\ u_z(\cdot,\cdot) : [0,\infty) \times [0,\infty) \to (-\infty, \infty)$.

Let $\mathcal{S} \in \partial \mathscr{S}_0$ be a contact particle that is in contact with a tip particle $\mathcal{Q} \in \partial \mathscr{T}_0$. Because $\mathcal{S}$ and $\mathcal{Q}$ occupy the same spatial point in the deformed configuration, it follows that

$$(r_{\mathcal{S}} + u_r(r_{\mathcal{S}}, 0))\hat{\boldsymbol{e}}_r(\theta_{\mathcal{S}}) + u_z(r_{\mathcal{S}}, 0)\hat{\boldsymbol{e}}_z = r_{\mathcal{Q}}\hat{\boldsymbol{e}}_r(\theta_{\mathcal{Q}}) + \tilde{u}_z(r_{\mathcal{Q}};h)\hat{\boldsymbol{e}}_z, \tag{2.3}$$

where $r_{\mathcal{S}}$, $\theta_{\mathcal{S}}$ and $r_{\mathcal{Q}}$, $\theta_{\mathcal{Q}}$ are the radial and polar coordinates of $\mathcal{S}$ and $\mathcal{Q}$, respectively. It follows

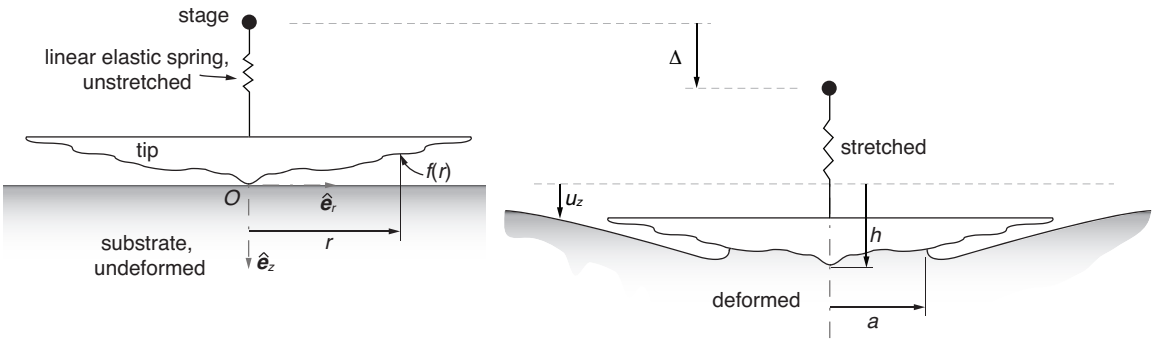

Figure 2.3: (a) and (b), respectively, show the reference and a deformed configuration of the contacting solids in our problem, see §2.2.1.

from (2.3) that $\theta_S = \theta_Q$, $r_S + u_r(r_S,0) = r_Q$, and

$$u_z(r_S,0) = \tilde{u}_z(r_S + u_r(r_S,0);h). \tag{2.4}$$

Imposing the boundary condition (2.4) on the substrate's displacement field leads to a problem for which obtaining an analytical solution is quite challenging. In our problem, we impose the boundary condition

$$u_z(r_S,0) = \tilde{u}_z(r_S;h), \tag{2.5}$$

which is an approximation of (2.4) on the substrate's displacement field.

2.2.2 Variational formulation of the adhesive elastic contact problem

We use a variational perspective in the study of our contact mechanics problem. That is, for a given stage displacement Δ, we posit that the experimentally observed configuration of the spring, tip, and half-space is one in which the system's total energy is locally minimized with respect to a, h, and $\boldsymbol{u}$. Thus, we allow for the possibility of there being more than one configuration that is experimentally observable at a given Δ. We assume that the type of solutions we seek can be obtained by first minimizing the potential energy with respect to $\boldsymbol{u}$ alone, while holding a and h fixed, and then minimizing this partially minimized potential energy with respect to a and h.

The potential energy in our problem consists of three terms: the energy stored in the spring because of its stretching, the energy stored in the contact region due to the adhesive interactions

between the tip and the substrate, and the energy stored in the substrate due to its deformation. The potential energy stored in the spring that connects the tip to the stage is $k_s(\Delta - h)^2/2$, where $k_s \in (0,\infty)$ is the spring's stiffness. As previously noted, we model adhesion between the tip and the substrate using the JKR theory. According to this theory, the potential energy from the adhesive interactions between the tip and substrate is $-\pi w a^2$. We model the substrate as a homogeneous, isotropic, linear elastic material with Young's modulus E and Poisson's ratio ν. Therefore, the potential energy stored in the substrate is

$$\frac{1}{2}\int_{\mathscr{S}_0} \boldsymbol{\sigma} : \boldsymbol{\epsilon}\, d\mathscr{S}_0, \tag{2.6}$$

where

$$\boldsymbol{\sigma} = \frac{E}{(1+\nu)}\left[\boldsymbol{\epsilon} + \frac{\nu}{(1-2\nu)}\mathrm{Tr}\,(\boldsymbol{\epsilon})\,\mathbf{I}\right] \tag{2.7}$$

is the Cauchy stress tensor and

$$\boldsymbol{\epsilon} = \frac{1}{2}\left(\nabla \boldsymbol{u} + \nabla \boldsymbol{u}^{\mathsf{T}}\right) \tag{2.8}$$

is the small strain tensor. The symbol : in (2.6) denotes double contraction. In (2.7), the symbol $\mathbf{I}$ denotes the second rank identity tensor and $\mathrm{Tr}(\cdot)$ denotes the trace operator. In (2.8) the operators $\boldsymbol{\nabla}(\cdot)$ and $(\cdot)^{\mathsf{T}}$ denote the gradient and transpose operators, respectively.

It follows from (2.5) that the displacement field always needs to satisfy the essential boundary condition

$$u_z(r,0) = \tilde{u}_z(r;h) \quad \text{on} \quad \Gamma_c. \tag{2.9}$$

When Δ, a, and h are held fixed, it can be shown that among the displacement fields that satisfy (2.9), the one that minimizes the system's potential energy is the one that satisfies the equation and boundary conditions

$$\mathrm{Div}(\boldsymbol{\sigma}) = \boldsymbol{o} \quad \text{in} \quad \mathscr{S}_0, \tag{2.10a}$$

$$\boldsymbol{\sigma}\hat{\boldsymbol{e}}_z = \boldsymbol{o} \quad \text{on} \quad \partial\mathcal{S}_0 \backslash \Gamma_c, \tag{2.10b}$$

$$(\boldsymbol{I} - \hat{\boldsymbol{e}}_z \otimes \hat{\boldsymbol{e}}_z)\boldsymbol{\sigma}\hat{\boldsymbol{e}}_z = \boldsymbol{o} \quad \text{on} \quad \Gamma_c, \tag{2.10c}$$

where Div$(\cdot)$ is the divergence operator, $\boldsymbol{o}$ is the null vector in $\mathcal{V}$, and $\hat{\boldsymbol{e}}_z \otimes \hat{\boldsymbol{e}}_z$ is the tensor product of $\hat{\boldsymbol{e}}_z$ and itself. It is also required that the components of $\boldsymbol{u}$ and $\boldsymbol{\sigma}$, respectively, be asymptotic to $(r^2+z^2)^{-1/2}$ and $(r^2+z^2)^{-1}$ as $(r^2+z^2)^{1/2} \to \infty$.

The solution to the mixed boundary value problem defined by (2.9)–(2.10) was given by Sneddon [70]. (For a concise derivation of this solution using Betti's reciprocity theorem, see [71].) Using that solution, it can be shown that for any given Δ and h and a positive a, the partially minimized potential energy of the system is

$$\frac{\pi^2 E}{4(1-\nu^2)} \int_0^a \chi(\tilde{a};h)^2 \, d\tilde{a} + \frac{1}{2} k_s (\Delta - h)^2 - \pi w a^2, \tag{2.11}$$

where

$$\chi(\tilde{a};h) = \frac{2}{\pi} \left[h + \tilde{a} \int_0^{\tilde{a}} \frac{\tilde{u}_z'(r;h)}{\sqrt{\tilde{a}^2 - r^2}} \, dr \right] \quad \text{for} \quad \tilde{a} > 0. \tag{2.12}$$

Because of the boundary condition (2.9), the mixed boundary value problem defined by is not well posed when $a = 0$ and $h \neq 0$. The value of the expression (2.11) equals the system's partially minimized potential energy only when $a > 0$ or when $a = 0$ and $h = 0$. When $a = 0$ and $h \leq 0$, the tip and the half-space are not in contact. In this case, the partially minimized potential energy only results from the stretching or compression of the spring. It is not possible for $a = 0$ and $h > 0$ because the tip cannot move into the region that is occupied by the unstressed half-space without forming any contact area with the half-space. Therefore, we conclude that the variational solution we seek will remain unaltered if we take the partially minimized potential energy of the system to be given by the value of the function $\Pi(\cdot,\cdot;\Delta) : \mathcal{D} \subset \mathbb{R}^2 \to \mathbb{R} \cup +\infty$, where

$$\Pi(a,h;\Delta) := \begin{cases} \frac{\pi^2 \mathcal{E}}{4} \int_0^a \chi(\tilde{a};h)^2 \, d\tilde{a} + \frac{1}{2} k_s (\Delta - h)^2 - \pi w a^2, & a > 0,\ h \in (-\infty, +\infty), \\ \frac{1}{2} k_s (\Delta - h)^2, & a = 0,\ h \leq 0, \\ +\infty, & a = 0,\ h > 0, \end{cases} \tag{2.13}$$

with the domain

$$\mathcal{D} := [0,\infty) \times (-\infty, +\infty), \tag{2.14}$$

and the plane strain Young's modulus $\mathcal{E} := E/(1-\nu^2)$. We next locally minimize $\Pi(\cdot,\cdot;\Delta)$ with

respect to a and h. More precisely, we seek the solution point $(a^*, h^*) \in \mathcal{D}$ for which there exists a positive number δ such that

$$\Pi(a^*, h^*; \Delta) \leq \Pi(a, h; \Delta), \quad \forall (a,h) \in B(a^*, h^*, \delta), \tag{2.15}$$

where $B(a^*; h^*; \delta) := \{(a,h) \in \mathbb{R}^2 | \, \|(a^*, h^*) - (a,h)\| < \delta\}$. The solution point is also said to be the stable equilibrium configuration of the adhesive elastic contact.

2.2.3 Solutions

Contact radius and indentation depth

The solutions defined by (2.15) can lie either in the interior of the domain or on its boundary. We name the points in the interior of $\mathcal{D}$ *interior points* and on the boundary of $\mathcal{D}$ *boundary points*. We denote the boundary of $\mathcal{D}$ as $\text{int}(\mathcal{D})$ and the interior of $\mathcal{D}$ as $\partial\mathcal{D}$. It follows from the definition of $\mathcal{D}$ that the interior and boundary points are simply the points $(a,h) \in \mathbb{R}^2$ with $a > 0$ and $a = 0$, respectively. We show in Appendix A.1 that the boundary contains solutions only when $\Delta < 0$, and that those solutions are of the form $(0, \Delta)$. In the remainder of this section, we only discuss solution points that lie in $\text{int}(\mathcal{D})$. We begin by defining and characterizing the stationary points that are relevant for our discussion of interior solution points.

Stationary points A stationary point (a°, h°) is an interior point that satisfies the first order conditions

$$\frac{\partial \Pi}{\partial h}(a^\circ, h^\circ; \Delta) = 0, \tag{2.16a}$$

$$\frac{\partial \Pi}{\partial a}(a^\circ, h^\circ; \Delta) = 0. \tag{2.16b}$$

The stationary point is also referred to as the equilibrium configuration of the adhesive elastic contact. At all interior points (a,h) it follows from (2.13) that

$$\frac{\partial \Pi}{\partial h}(a,h;\Delta) = \frac{\pi^2 \mathcal{E}}{2} \int_0^a \chi(\tilde{a};h) \frac{\partial \chi(\tilde{a};h)}{\partial h}\, d\tilde{a} - k_s(\Delta - h), \tag{2.17a}$$

$$\frac{\partial \Pi}{\partial a}(a,h;\Delta) = \frac{\pi^2 \mathcal{E}}{4} \chi(a;h)^2 - 2\pi a w. \tag{2.17b}$$

At any interior point (a,h) it follows from (2.12) that $\partial \chi(a;h)/\partial h = 2/\pi$. Thus, after substituting $\partial \chi(\tilde{a};h)/\partial h$ with $2/\pi$ in (2.17a) and simplifying, we find that

$$\frac{\partial \Pi}{\partial h}(a,h;\Delta) = \pi \mathcal{E} \int_0^a \chi(\tilde{a};h)\, d\tilde{a} - k_s(\Delta - h). \tag{2.18}$$

Equations (2.16a) and (2.18) imply that

$$\pi \mathcal{E} \int_0^{a^\circ} \chi(\tilde{a};h^\circ)\, d\tilde{a} - k_s(\Delta - h^\circ) = 0. \tag{2.19}$$

Equations (2.16b) and (2.17b) imply that $\chi(a^\circ;h^\circ)$ is equal to $\pm\sqrt{8a^\circ w/(\pi\mathcal{E})}$. However, we show in Appendix A.2 that only the negative square root is physically meaningful, i.e.,

$$\chi(a^\circ;h^\circ) = -\sqrt{\frac{8a^\circ w}{\pi \mathcal{E}}}. \tag{2.20}$$

Equivalently, the stationary point (a°,h°) is a root of the function

$$(a,h) \mapsto \chi(a;h) + \sqrt{\frac{8aw}{\pi \mathcal{E}}}. \tag{2.21}$$

It follows from (2.12) and (2.21) and the *implicit function theorem* that there exists a function $\hbar$ that is defined on a neighborhood of a° such that

$$h^\circ = \hbar(a^\circ). \tag{2.22}$$

We derive $\hbar$ for contact experiments involving a spherical and conical tip in §2.3.1 and §2.3.2, respectively.

First order necessary condition It can be shown that $\Pi(\cdot,\cdot;\Delta)$ is continuously differentiable on $\text{int}(\mathcal{D})$. Consequently, if (a^*,h^*) is an interior solution point, then it must also be a stationary point. Therefore, an interior solution point (a^*,h^*) is also a root of the function (2.21) and it satisfies the equation $h^* = \hbar(a^*)$.

Second order necessary condition We discuss the second order conditions in Appendix A.3. A consequence of those conditions is that the value of the function $g : [0,\infty) \to \mathbb{R}$, where

$$g(a) := \hbar'(a) - \frac{\sqrt{8\pi a\mathcal{E}w}}{2a\mathcal{E}+k_s} \tag{2.23}$$

at an interior solution point's abscissa should be non-negative. The derivative of $\hbar$ is denoted as $\hbar'$.

Second order sufficient condition We show in Appendix A.3.3 that a stationary point (a°,h°) is a solution point if

$$g(a^\circ) > 0. \tag{2.24}$$

Equation (2.24) is the second order sufficiency condition (A.3.12) written in terms of the function g, which we introduced in (2.23).

Contact force

In our contact problem, the contact force between the tip and the substrate can be written as $P\hat{e}_z$. When P in non-negative (resp. non-positive), we say that the contact force is compressive (resp. attractive). The contact force corresponding to the solution point (a^*,h^*) is denoted as P^*.

As we discussed in §2.2.3, the solution points (a^*,h^*) belonging to $\partial\mathcal{D}$ are of the form $(0,\Delta)$, where $\Delta < 0$. In the solutions corresponding to those points, the spring is unstretched, the substrate is undeformed, and the tip and the substrate are not in physical contact. (See Appendix A.1 for details.) Therefore, the contact force $P^* = 0$ in those solutions.

When (a^*,h^*) belongs to the $\text{int}(\mathcal{D})$ it follows from the results presented by Snedddon [70]

and [71, 5.10] that the contact force P^* is

$$P^* = \mathcal{P}(a^*, h^*), \tag{2.25a}$$

where $\mathcal{P} : \mathscr{D} \to \mathbb{R}$ and

$$\mathcal{P}(a,h) := \pi \mathcal{E} \int_0^a \chi(r;h)\, dr. \tag{2.25b}$$

As we discussed in §2.2.3, by necessity an interior solution point is also a stationary point. Thus, we can replace a° and h° with, respectively, a^* and h^* in (2.19) and (2.20), and then, from (2.25), substitute $\pi \mathcal{E} \int_0^{a^*} \chi(\tilde{a};h^*)\, d\tilde{a}$ with P^* in the first of the resulting equations to get

$$\Delta = \frac{P^*}{k_s} + h^* \tag{2.26}$$

and

$$\chi(a^*;h^*) = -\sqrt{\frac{8a^* w}{\pi \mathcal{E}}}. \tag{2.27}$$

We determine the solution contact radius, indentation depth, and contact force, i.e., a^*, h^*, and P^*, through simultaneously solving the equations (2.25a)–(2.27). We illustrate this in §2.3.1 and §2.3.2, respectively, where we consider tips having spherical and conical shapes.

2.3 Applications

2.3.1 Spherical tip

Theory

In AFM-type contact experiments involving a substrate that is especially delicate, such as a gel or a biological tissue, it is customary to use a spherical glass or polystyrene bead as the tip [27, 58–60]. The radial profile of the spherical tip can be written as

$$f(r) = R(1 - r^2/R^2)^{1/2},$$

where $0 \leq r < R$ and R is the sphere's radius, see Figure 2.4a. For this particular f on calculating $\tilde{u}_z$ from (2.2) and substituting it into (2.12), we get

$$\chi(\tilde{a};h) = \frac{2}{\pi}\left[h - \tilde{a}\tanh^{-1}\left(\frac{\tilde{a}}{R}\right)\right]. \tag{2.28}$$

From (2.28), it follows that in the limit $\tilde{a}/R \to 0$

$$\frac{\chi(\tilde{a};h)}{R} = \frac{2}{\pi}\left[\frac{h}{R} - \left(\frac{\tilde{a}}{R}\right)^2\right] + O\left(\frac{\tilde{a}^4}{R^4}\right). \tag{2.29}$$

Generally, when measuring compliant materials, the contact radius must be made large enough that the contact force is measurable. Because of this, during some stages of the experiments the contact radius a is not substantially smaller than the bead radius R. Despite that, in order to simplify some of the ensuing calculations in this section, we assume that the contact radius during the experiment is much smaller than R. That is, we ignore the fourth order term in (2.29) and simply take

$$\chi(\tilde{a};h) = \frac{2}{\pi}\left(h - \frac{\tilde{a}^2}{R}\right). \tag{2.30}$$

Substituting (2.30) in (2.19) and (2.20), we find that the points (a°, h°) satisfy the equations

$$h^\circ = \hbar(a^\circ), \tag{2.31a}$$

where

$$\hbar(a^\circ) = \frac{a^{\circ 2}}{R} - \sqrt{\frac{2\pi a^\circ w}{\mathcal{E}}} \tag{2.31b}$$

and

$$\Delta = \frac{\mathcal{P}(a^\circ, h^\circ)}{k_s} + h^\circ, \tag{2.32a}$$

where

$$\mathcal{P}(a^\circ, h^\circ) = 2a^\circ h^\circ \mathcal{E} - \frac{2a^{\circ 3}\mathcal{E}}{3R}. \tag{2.32b}$$

Recall from §2.2.3 that a stationary point (a°, h°) is a solution point if it satisfies the condition (2.24). We can compute the derivative of the function $\hbar$ given in (2.31b) and substitute it into (2.23) to determine the function g, and then substitute g in (2.24). In doing this, we find that (a°, h°) is a solution point if

$$g(a^\circ) = \frac{2a^\circ}{R} - \sqrt{\frac{\pi w}{2a^\circ \mathcal{E}}} - \frac{\sqrt{8\pi a^\circ \mathcal{E} w}}{2a^\circ \mathcal{E} + k_s} \tag{2.33}$$

is positive.

The non-dimensional variables and parameters $\bar{\mathcal{P}}(\bar{a}^\circ, \bar{h}^\circ) := \mathcal{P}(a^\circ, h^\circ)/\hat{P}$, $\bar{\hbar}(\bar{a}^\circ) := \hbar(a^\circ)/\hat{h}$, and $\bar{\Delta} = \Delta/\hat{h}$, where $\bar{a}^\circ = a^\circ/\hat{a}$, $\bar{h}^\circ = h^\circ/\hat{h}$, $\hat{P} := 3\pi w R/2$, $\hat{a} := \left(9\pi w R^2/8\mathcal{E}\right)^{1/3}$, and $\hat{h} := (\hat{a}^2/R)$ allow equations (2.31)–(2.32) to be written as, respectively,

$$\bar{h}^\circ = \bar{\hbar}(\bar{a}^\circ), \tag{2.34a}$$

where

$$\bar{\hbar}(\bar{a}^\circ) = \bar{a}^{\circ 2} - \frac{4}{3}\bar{a}^{\circ 1/2} \tag{2.34b}$$

and

$$\bar{\Delta} = \frac{4}{3\alpha}\bar{\mathcal{P}}\left(\bar{a}^\circ, \bar{h}^\circ\right) + \bar{h}^\circ, \tag{2.35a}$$

where

$$\bar{\mathcal{P}}\left(\bar{a}^\circ, \bar{h}^\circ\right) = \frac{3}{2}\bar{a}^\circ \bar{h}^\circ - \frac{1}{2}\bar{a}^{\circ 3}. \tag{2.35b}$$

Defining $\bar{g}(\bar{a}^\circ) := \bar{a}^{\circ 1/2} g(\bar{a}^\circ \hat{a})/(3\pi w/(8\mathcal{E}R))^{1/3}$ and with the non-dimensional parameters $\hat{a}$ and α,

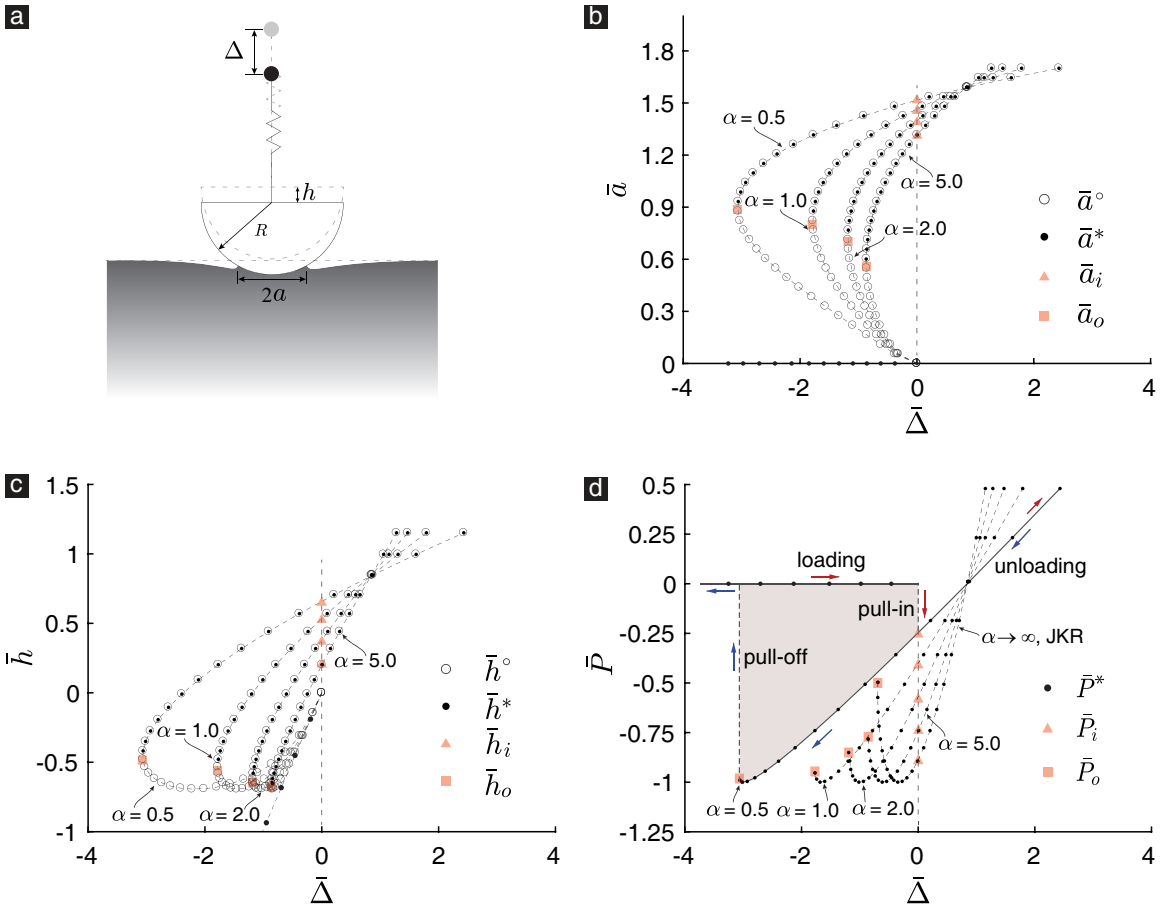

Figure 2.4: (a) Geometry of the spherical-tip contact problem. In (b)–(d) we denote the different tip-substrate configurations as points. A configuration's abscissa gives its prescribed state displacement $\bar{\Delta}$. In (b) and (c) the ordinate of each configuration gives its contact radius and indentation depth, respectively. The configurations whose contact radii and indentation depths corresponding to stationary points are marked as circles, while those corresponding to solution points are marked as dots. In (d) the ordinate of a configuration gives its contact force $\bar{P}^*$. The configurations just after the occurrence of the pull-in instability are marked by triangles, while the configurations just before the occurrence of the pull-off instability are marked by squares.

we get from (2.33) that

$$\bar{g}(\bar{a}^\circ) = 3\bar{a}^{\circ 3/2} - \frac{4\bar{a}^\circ}{2\bar{a}^\circ + \alpha} - 1. \tag{2.36}$$

The parameter α in (2.35a) and (2.36) is the ratio of the machine stiffness k_s to the contact interface's characteristic stiffness $\hat{k}_s := \left(9\pi w \mathcal{E}^2 R^2/8\right)^{1/3}$.

Numerical calculation of pull-in and pull-off forces and hysteretic energy loss

We numerically computed the stationary points for a range of $\bar{\Delta}$ values using (2.34)–(2.35). The results from these calculations are shown in Figure 2.4b–c. It follows from the discussion in Appendix A.1 that the pull-in instability occurs when $\bar{\Delta} = 0$. The contact radius just after the pull-in instability, $\bar{a}_i$, is the abscissa of the stationary point that satisfies (2.34)–(2.35) for $\bar{\Delta}$=0. We define the pull-off contact radius $\bar{a}_o$ to be $\arg\inf\,\{\bar{a}^\circ \mid \bar{g}(\bar{a}^\circ) > 0\}$. The indentation depths just prior to the pull-in instability and pull-off instability are, respectively, $\bar{h}_i = \bar{h}(\bar{a}_i)$ and $\bar{h}_o = \bar{h}(\bar{a}_o)$, where $\bar{h}$ for the spherical tip is given in (2.34b). We marked $\bar{a}_i$ and $\bar{a}_o$ in Figure 2.4b, and $\bar{h}_i$ and $\bar{h}_o$ in Figure 2.4c.

We define a non-dimensional solution point to be $(\bar{a}^*, \bar{h}^*) := (a^*/\hat{a}, h^*/\hat{h})$. A stationary point $(\bar{a}^\circ, \bar{h}^\circ)$ qualifies as a non-dimensional solution point if its abscissa satisfies the sufficiency condition that $\bar{g}(\bar{a}^\circ)$ in (2.36) is positive. We show the abscissa and ordinate of several of these solution points in Figure 2.4a and b, respectively, using solid symbols. In addition to the solution points that we have from the set of stationary points, it follows from the discussion of §2.2.3 that when $\bar{\Delta} < 0$ we have additional solution points on the boundary $\partial\mathcal{D}$ that are of the form $(0, \bar{\Delta})$. The abscissa and ordinate of these points are also marked in Figure 2.4b and c, respectively.

For each of the solution points $(\bar{a}^*, \bar{h}^*)$ shown in Figure 2.4b–c, we computed the non-dimensional contact force $\bar{P}^* := P^*/\hat{P}$ as $\bar{\mathcal{P}}(\bar{a}^*, \bar{h}^*)$, where $\bar{\mathcal{P}}$ for the spherical tip is given in (2.35b). We show these force values in Figure 2.4d. The contact forces corresponding to the solution points of the form $(0, \bar{\Delta})$, which are actually all zero, are also shown in that figure.

We denote the contact force and the stage displacement just prior to the occurrence of the pull-in (resp. pull-off) instability as $\bar{P}_i^*$ (resp. $\bar{P}_o^*$) and $\bar{\Delta}_i$ (resp. $\bar{\Delta}_o$). Recall that $\bar{\Delta}_i = 0$. It follows from (2.35a) that

$$\bar{\Delta}_o = \frac{4}{3\alpha}\bar{\mathcal{P}}(\bar{a}_o, \bar{h}_o) + \bar{h}_o.$$

The pull-in and pull-off contact forces, i.e. $\bar{P}_i^*$ and $\bar{P}_o^*$, can be calculated as $\bar{\mathcal{P}}(\bar{a}_i, \bar{h}_i)$ and $\bar{\mathcal{P}}(\bar{a}_o, \bar{h}_o)$, respectively, where $\bar{\mathcal{P}}$ for the spherical tip is given in (2.35b). We have marked the points $(\bar{\Delta}_i, \bar{P}_i^*)$ and $(\bar{\Delta}_o, \bar{P}_o^*)$ in Figure 2.4d.

We show the contact forces $\bar{P}_i^*$ and $\bar{P}_o^*$ as a function of α in Figure 2.5a. Through an analysis of (2.34) and (2.35), we found that as $\alpha \to 0$ the contact forces $\bar{P}_i^*$ and $\bar{P}_o^*$ tend to 0 and -1,

respectively. And as $\alpha \to \infty$, the contact forces $\bar{P}_i^*$ and $\bar{P}_o^*$ tend to $-8/9$ and $-5/9$, respectively. With the aid of these asymptotic results we were able to construct the functions $\bar{\mathcal{P}}_i^*$, $\bar{\mathcal{P}}_o^* : (0,\infty) \to (-\infty, 0)$, where

$$\bar{\mathcal{P}}_i^*(\alpha) = -\frac{8}{9}\left(1 - \frac{1}{1+0.83\alpha^{1.12}}\right) \tag{2.37a}$$

and

$$\bar{\mathcal{P}}_o^*(\alpha) = -\frac{1}{9}\left(5 + \frac{4}{1+0.21\alpha^{1.32}}\right). \tag{2.37b}$$

These provide excellent approximations for $\bar{P}_i^*$ and $\bar{P}_o^*$ for a wide range of α values. (See Figure 2.5a.)

As can be noted from Figure 2.4b and c, there exist two solution points for some $\bar{\Delta}$ values. For those same values, unsurprisingly, there are also two force values. Which of these two force values are actually measured in an experiment depends on the contact cycle employed in that experiment. For example, for the typical contact cycle discussed in §2.1, the experiment will measure the force values that we have marked using right and left arrows in Figure 2.4d during the loading and the unloading phases, respectively.

The hysteretic energy loss during a contact cycle can be computed as $(R^4 w^5/\mathcal{E}^2)^{1/3}\bar{H}$, where

$$\bar{H} = \frac{4}{3\alpha}\int_{\bar{a}_o}^{\bar{a}_i} \bar{\mathcal{P}}(\bar{a}^*, \bar{h}(\bar{a}^*))\left[\bar{\mathcal{P}}_{,1}(\bar{a}^*, \bar{h}(\bar{a}^*)) + \bar{\mathcal{P}}_{,2}(\bar{a}^*, \bar{h}(\bar{a}^*))\bar{h}'(\bar{a}^*) + \frac{3\alpha}{4}\bar{h}'(\bar{a}^*)\right] d\bar{a}^*, \tag{2.38}$$

in which $\bar{\mathcal{P}}_{,1}$ and $\bar{\mathcal{P}}_{,2}$ are the partial derivatives of $\bar{\mathcal{P}}$ with respect to its first and second arguments, respectively. It can be shown that as $\alpha \to 0$ the hysteretic energy loss $\bar{H} \to \infty$, and as $\alpha \to \infty$ the hysteretic energy loss $\bar{H} \to (\pi^{5/3} + 3\,(2\pi)^{5/3})/10\,(\approx 7.092)$. With the aid of these asymptotic results, we constructed the function $\bar{\mathcal{H}} : (0,\infty) \to (0,\infty)$, where

$$\bar{\mathcal{H}}(\alpha) = 7.092 + \frac{7.657}{\alpha^{0.99}}. \tag{2.39}$$

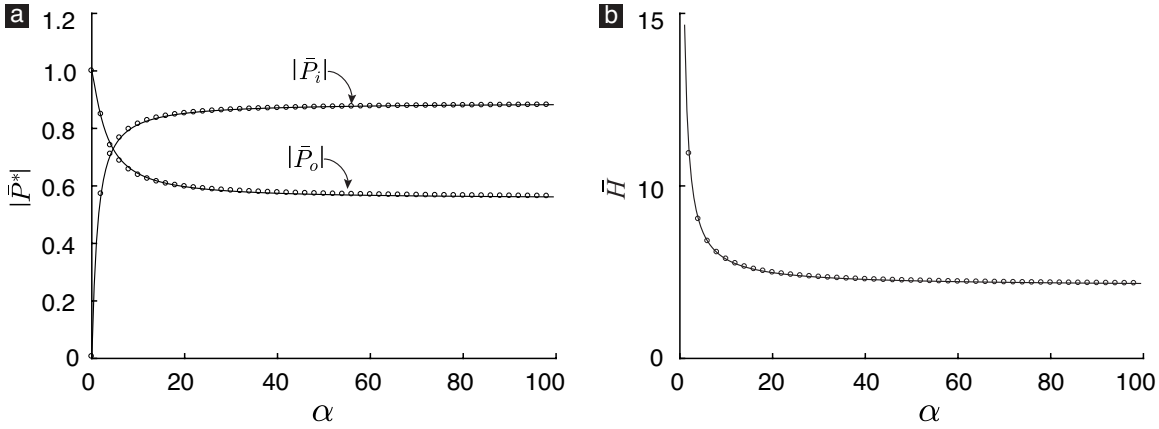

Figure 2.5: The spherical-tip case. (a) The exact (circles) and approximate (solid line) values of $|\bar{P}_i|$ and $|\bar{P}_o|$ as a function of α. The exact values are computed using the procedure outlined in §2.3.1. The approximate values are given by the functions $\bar{\mathcal{P}}_i$ and $\bar{\mathcal{P}}_o$ defined in (2.37). (b) The exact (circles) and approximate (solid line) values of $\bar{H}$ as a function of α. The exact values are computed using (2.38), while the approximate values are given by the function $\bar{\mathcal{H}}$ defined in (2.39).

The values of $\bar{\mathcal{H}}$ are very close to $\bar{H}$ for a wide range of α values, see Figure 2.5b.

2.3.2 Conical tip

Theory

In this section, we consider a conical tip whose radial profile $f(r) = -r\tan\theta$, where $\theta \in (0, \pi/2)$ is shown marked in Figure 2.6a. Calculating $\tilde{u}_z$ from (2.2) for this radial profile and substituting it into (2.12) results in

$$\chi(\tilde{a};h) = \frac{2}{\pi}\left(h - \frac{\pi}{2}\tilde{a}\tan\theta\right). \tag{2.40}$$

As we did in the case of the spherical tip (§2.3.1), by substituting (2.40) in (2.19)–(2.20) we obtain that the points (a°, h°) satisfy the equations

$$h^\circ = \hbar(a^\circ), \tag{2.41a}$$

where

$$\hbar(a^\circ) = 2a^\circ h^\circ \mathcal{E} - \frac{1}{2}\pi a^{\circ 2}\mathcal{E}\tan\theta \tag{2.41b}$$

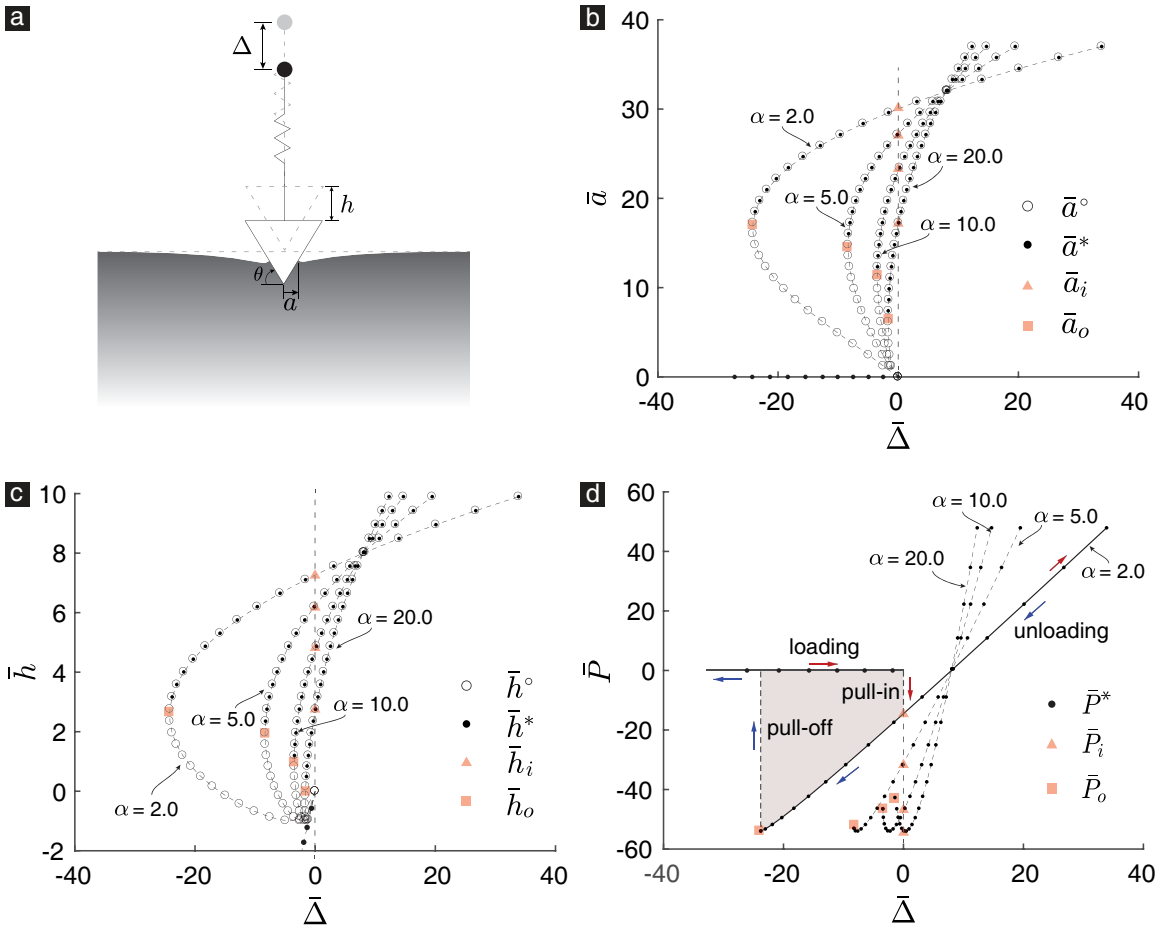

Figure 2.6: (a) Geometry of the conical-tip contact problem. In (b)–(d) we denote the different tip-substrate configurations as points. A configuration's abscissa gives its prescribed state displacement $\bar{\Delta}$. In (b) and (c) the ordinate of each configuration gives its contact radius and indentation depth. The configurations whose contact radii and indentation depths corresponding to stationary points are marked as circles, while those that corresponding to solution points are marked as dots. In (d) the ordinate of a configuration gives its contact force $\bar{P}^*$. The configurations just after the occurrence of the pull-in instability are marked by triangles, while the configurations just before the occurrence of the pull-off instability are marked by squares.

and

$$\Delta = \frac{\mathcal{P}(a^\circ, h^\circ)}{k_s} + h^\circ, \tag{2.42a}$$

where

$$\mathcal{P}(a^\circ, h^\circ) = 2a^\circ h^\circ \mathcal{E} - \frac{1}{2}\pi a^{\circ 2} \mathcal{E} \tan\theta. \tag{2.42b}$$

From (2.23) and (2.41b), it follows that the function g for the case of conical tip is

$$g(a^\circ) = \frac{\pi}{2}\tan\theta - \sqrt{\frac{\pi w}{2a^\circ \mathcal{E}}} - \frac{\sqrt{8\pi a^\circ \mathcal{E} w}}{2a^\circ \mathcal{E} + k_s}. \tag{2.43}$$

The functions with non-dimensional values and non-dimensional variables $\bar{\mathcal{P}}(\bar{a}^\circ, \bar{h}^\circ) := \mathcal{P}(a^\circ, h^\circ)/\hat{P}$, $\bar{h}(\bar{a}^\circ) := h(a^\circ)/\hat{h}$, and $\bar{\Delta} := \Delta/\hat{h}$, where $\bar{a}^\circ := a^\circ/\hat{a}$, $\bar{h}^\circ := h^\circ/\hat{h}$, $\hat{P} := w^2/(\pi\mathcal{E}\tan^3\theta)$, $\hat{a} := w/(\pi\mathcal{E}\tan^2\theta)$, and $\hat{h} := w/(\mathcal{E}\tan\theta)$, allow (2.41)–(2.42) to be written as, respectively,

$$\bar{h}^\circ = \bar{h}(\bar{a}^\circ), \tag{2.44a}$$

where

$$\bar{h}(\bar{a}^\circ) = \frac{\bar{a}^\circ}{2} - (2\bar{a}^\circ)^{1/2} \tag{2.44b}$$

and

$$\bar{\Delta} = \frac{1}{\alpha}\bar{\mathcal{P}}\left(\bar{a}^\circ, \bar{h}^\circ\right) + \bar{h}^\circ, \tag{2.45a}$$

where

$$\bar{\mathcal{P}}\left(\bar{a}^\circ, \bar{h}^\circ\right) = 2\bar{a}^\circ\bar{h}^\circ - \frac{1}{2}\bar{a}^{\circ 2}. \tag{2.45b}$$

The parameter α in (2.45a) is the ratio of the machine stiffness k_s to the contact interface's characteristic stiffness $\hat{k}_s := w/(\pi\tan^2\theta)$. Defining $\bar{g}(\bar{a}^\circ) := (2\bar{a}^\circ)^{1/2} g(\bar{a}^\circ\hat{a})/(\pi\tan\theta)$, we find from (2.43) and the definitions of α and $\hat{a}$ that

$$\bar{g}(\bar{a}^\circ) = \frac{\sqrt{2\bar{a}^\circ}}{2} - \frac{4\bar{a}^\circ}{2\bar{a}^\circ + \alpha} - 1. \tag{2.46}$$

Numerical calculation of the pull-in and pull-off forces and the hysteretic energy loss

We numerically computed the stationary points $(\bar{a}^\circ, \bar{h}^\circ)$ for a range of $\bar{\Delta}$ values using (2.44)–(2.45). The solution points $(\bar{a}^*, \bar{h}^*)$ are those stationary points $(\bar{a}^\circ, \bar{h}^\circ)$ for which $\bar{g}(\bar{a}^\circ) > 0$, with $\bar{g}$ being given in (2.46). When $\bar{a}^* > 0$ then $\bar{P}^* = \bar{\mathcal{P}}(\bar{a}^*, \bar{h}^*)$, where $\bar{\mathcal{P}}$ is given in (2.45b). When $\bar{a}^* = 0$, then $P^* = 0$. We show the abscissa (resp. ordinate) of the stationary and solution points as a function of $\bar{\Delta}$ in Figure 2.6b (resp. c), and show $\bar{P}^*$ in Figure 2.6d.

We employed the same procedure that we used in §2.3.1 to identify the contact radii $\bar{a}_i$ and $\bar{a}_o$, indentation depths $\bar{h}_i$ and $\bar{h}_o$, and contact forces $\bar{P}_i$ and $\bar{P}_o$ to identify those quantities in the case of conical tip (Figure 2.6b–d). We found that as $\alpha \to 0$ the contact forces $\bar{P}_i^*$ and $\bar{P}_o^*$ approach 0 and -54, respectively. And as $\alpha \to \infty$, the contact forces $\bar{P}_i^*$ and $\bar{P}_o^*$ approach -32 and -6, respectively. With the aid of these asymptotic results, we were able to construct the functions $\bar{\mathcal{P}}_i^*$ and $\bar{\mathcal{P}}_o^* : (0,\infty) \to (-\infty, 0)$, where

$$\bar{\mathcal{P}}_i^*(\alpha) = -32\left(1 - e^{-0.12\alpha}\right)\left(1 + 2.05e^{-0.123\alpha^{0.665}}\right) \tag{2.47a}$$

and

$$\bar{\mathcal{P}}_o^*(\alpha) = -6 - \frac{48}{1 + 0.00158\alpha^{2.285}} \tag{2.47b}$$

whose values approximate, respectively, $\bar{P}_i^*$ and $\bar{P}_o^*$ very closely for a wide range of α (Figure 2.7a).

We computed the hysteretic energy loss during a contact cycle as $w^3\bar{H}/(\pi\mathcal{E}^2\tan^4\theta)$, where

$$\bar{H} = \frac{1}{\alpha}\int_{\bar{a}_o}^{\bar{a}_i} \bar{\mathcal{P}}(\bar{a}^*, \bar{h}(\bar{a}^*))\left[\bar{\mathcal{P}}_{,1}(\bar{a}^*, \bar{h}(\bar{a}^*)) + \bar{\mathcal{P}}_{,2}(\bar{a}^*, \bar{h}(\bar{a}^*))\bar{h}'(\bar{a}^*) + \alpha\bar{h}'(\bar{a}^*)\right] d\bar{a}^*, \tag{2.48}$$

in which $\bar{h}$ and $\bar{\mathcal{P}}$ are given in (2.44b) and (2.45b), respectively. We found that as $\alpha \to 0$ the hysteretic energy loss $\bar{H} \to \infty$, and as $\alpha \to \infty$ the hysteretic energy loss $\bar{H} \to 22$. With the aid of

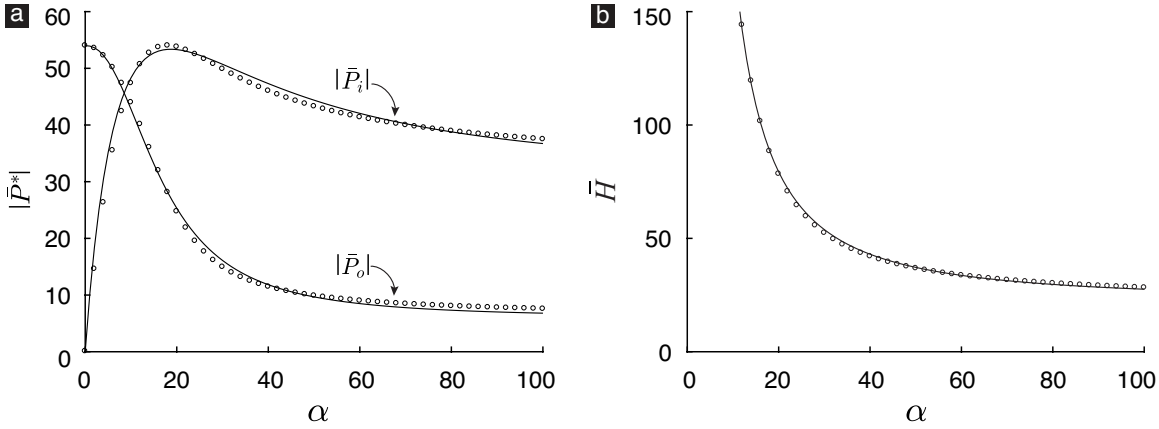

Figure 2.7: The conical-tip case. (a) The exact (circles) and approximate (solid line) values of $|\bar{P}_i|$ and $|\bar{P}_o|$ as a function of α. The exact values are computed using the procedure outlined in §2.3.2. The approximate values are given by the functions $\bar{\mathcal{P}}_i$ and $\bar{\mathcal{P}}_o$ defined in (2.47). (b) The exact (circles) and approximate (solid line) values of $\bar{H}$ as a function of α. The exact values are computed using (2.48), while the approximate values are given by the function $\bar{\mathcal{H}}$ defined in (2.49).

these asymptotic results we were able to construct the function $\bar{\mathcal{H}} : (0,\infty) \to (0,\infty)$, where

$$\bar{\mathcal{H}}(\alpha) = 22 + \frac{4383.87}{\alpha^{1.4478}}, \tag{2.49}$$

whose value is very close to $\bar{H}$ for a wide range of α (Figure 2.7b).

2.4 Experimental comparison and discussion

2.4.1 Experimental comparison

In this section, we compare our model to the experiments reported by Sun *et al.* [58] and Notbohm *et al.* [59]. Both experiments involved adhesive elastic contact between a PDMS slab and an AFM tip. The AFM tip in Sun *et al.*'s experiments was a Si_3N_4 bead of radius $R = 58$ nm. In Notbohm *et al.*'s experiments the AFM tip was a glass bead with $R = 2.5\,\mu$m.

In Figure 2.8a we show the contact force–indentation depth data from a representative contact cycle in Sun *et al.*'s experiments as gray dots. In that same figure, we show the best fit of our model, specifically (2.31b) and (2.32b), as blue curves and the JKR model as red curves. For both models, we use $\mathcal{E}$ and w as the fitting parameters. (See Appendix A.4 for details.) These parameters come out to be 6.39 MPa and 63.2 mJ/m^2, respectively, in the best fit of both our model and the JKR

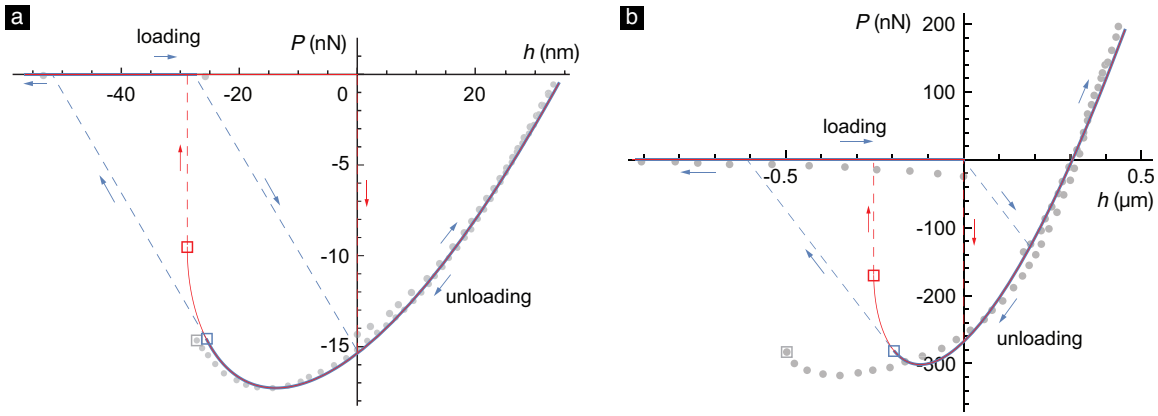

Figure 2.8: Comparison of the contact force–indentation depth curves predicted by our (blue lines) and the JKR (red lines) models with experimental data (gray dots). The data in (a) and (b) are, respectively, from the experiments performed by Sun *et al.* [58] and Notbohm *et al.* [59]. In each of the curves and data sets, the configuration just before the occurrence of the pull-off instability is marked with a square.

model. Sun *et al.* [58] report the stiffness of the AFM cantilever in their experiments to be $k_s = 0.66$ N/m. Using this value, the best fit of our model predicts the pull-off force to be -14.73 nN, whereas the best fit of the JKR model predicts it to be $-5\pi wR/6 = -9.59$ nN. As can be seen in Figure 2.8a, the experimental pull-off force is -14.8 nN. Thus, the prediction of the pull-off force from our model is much closer to the experimental value than the prediction of the JKR model.

An important experimental feature that is uniquely captured by our model is that in the experiments, the indentation depth changes by a finite amount during the pull-in and pull-off instabilities. For example, in the data shown in Figure 2.8a, the indentation depth changes by 26.7 nm and 26.9 nm during the pull-in and pull-off instabilities, respectively. In alignment with these observations, the best fit of our model predicts the indentation depth during the instabilities to change by 27.4 nm and 26 nm, respectively. In distinct contrast, the JKR model always predicts there to be no change in the indentation depth during either of the instabilities.

Figure 2.8b shows the contact force–indentation depth data from a representative contact cycle in Notbohm*et al.*'s experiments as gray dots. The best fits of our model and the JKR model are shown in Figure 2.8b as blue and red curves, respectively. In the best fits of both our model and the JKR model, $\mathcal{E}$ and w come out to be 0.65 MPa and 25.7 J/m^2, respectively. The AFM cantilever's stiffness in Notbohm *et al.*'s experiments was $k_s = 0.642$ N/m. Using this value for the machine stiffness, we find the pull-off contact force in the best fit of our model to be -281.5 nN. This value is remarkably close to the experimental pull-off force value, which is -281.6 nN. In contrast, the

pull-off force in the best fit of the JKR theory is $-5\pi wR/6 = -167.5$ nN, which is significantly greater than the experimental value. The changes in the indentation depth during the occurrence of the pull-in and pull-off instabilities in the experiments are 0.17 μm and 0.41 μm, respectively. These changes in the best fit of our model are, respectively, 0.19 μm and 0.42 μm, which are very close to the experimental values.

2.4.2 Discussion

There is a significant discrepancy between the best fits of our model, the JKR model, and the experiments towards the end of the unloading phase. (See Figure 2.8b.) Notbohm *et al.* [59] argue that the discrepancy between their data and the JKR model towards the end of the unloading phase was due to the nonlinear deformation behavior of the AFM cantilever. We believe this discrepancy requires further investigation.

There is also a discrepancy between the best fits of our model, the JKR model, and Notbohm *et al.*'s experimental data just prior to the occurrence of the pull-in instability. Prior to the occurrence of the pull-in instability, there is no contact force in either our model or the JKR model. However, as can be noted in Figure 2.8b, in Notbohm *et al.*'s experiments there are some small, but non-negligible, negative contact forces prior to the occurrence of the pull-in instability. We believe that this discrepancy is due to the assumption in our model that the interbody adhesive interactions are infinitesimally short ranged. As we discussed in §2.1, dry adhesion mostly originates from van der Waals and Coulombic type interactions, which have a finite interaction range. The finite ranged interactions can give rise to negative forces between the tip and the substrate even prior to the occurrence of the pull-in instability. This view is supported by molecular statics simulations of adhesive elastic contact [72], in which the interbody interactions are taken to have a finite range and the contact forces in them are seen to be non-zero prior to the occurrence of the pull-in instability.

A further implication of our assumption that the interbody adhesive interactions are infinitesimally short ranged is that our model's prediction that the pull-in instability occurs when $\Delta = 0$ is also quite likely to be inconsistent with experiments. In experiments, the pull-in instability is likely to occur when $\Delta < 0$, although it might be difficult to experimentally demonstrate this fact since identifying the datum of Δ is quite challenging in adhesive elastic contact experiments.

Chapter 3

Depth-dependent hysteresis in adhesive elastic contacts at large surface roughness

Note: A version of this chapter is published in *Scientific Reports*. Data and figures have been used with all co-authors' consent.

Deng WL and Kesari H. Depth-dependent hysteresis in adhesive elastic contacts at large surface roughness. Scientific Reports 9(1): 1639, 2019.

3.1 Introduction

A clear understanding of adhesive contact mechanics is critical for spatially mapping out a material's mechanical properties using, for example, nanoindentation- and contact mode AFM-based techniques [63, 73]. Typically, material properties are measured by fitting contact force vs. indentation depth (P–h) measurements to a contact mechanics theory. Some of the most popular theories for modeling adhesive elastic contact include the JKR [14], the DMT [15], and the MD [16] theories. These classical contact theories predict that when the solids are in physical contact, the force is uniquely determined by the indentation depth and is independent of the history of the contact

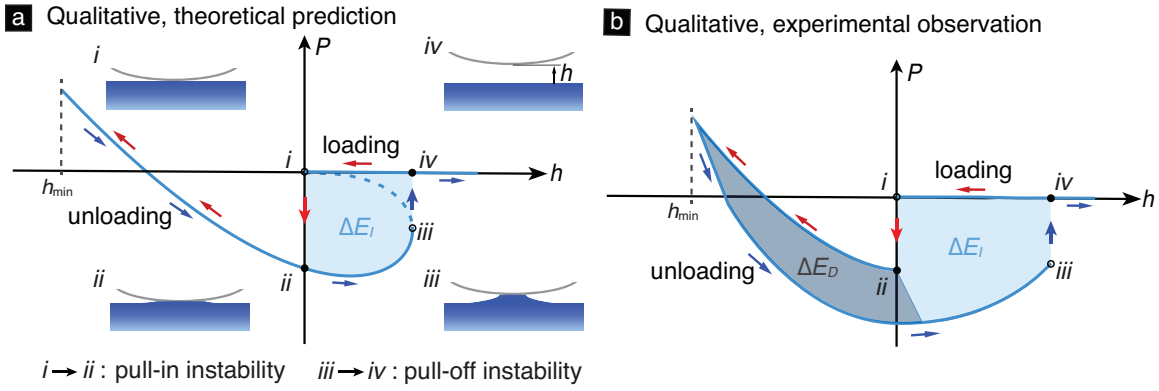

Figure 3.1: (a) The schematic of the *P*–*h* curve as per the JKR theory. The "pull-in" ($i \rightarrow ii$) and "pull-off" ($iii \rightarrow iv$) instabilities are marked along with the corresponding contact configurations. Closed and open symbols (circles) mark stable and unstable states on the *P*-*h* curve, respectively. A contact cycle includes the loading (red arrows) and unloading (blue arrows) phases. The size of the hysteresis loop formed in a contact cycle due to the instabilities (*i.e.*, the shaded area ΔE_I) denotes the hysteretic energy loss, which is depth independent. (b) The schematic of the *P*-*h* curve observed in some experiments [*e.g.*, see Figure 3.2a] which shows that the contact forces differ between the loading and unloading phases. The total hysteretic energy loss includes depth-independent part ΔE_I and depth-dependent part ΔE_D.

process [see Figure 3.1a]. However, in many experiments it is found that the contact forces depend on the contact process history. A typical contact experiment consists of one or more contact cycles, each of which consisting of a loading and an unloading phase. In those phases the solids are, respectively, being moved towards and away from each other [Figures 3.1a–b and 3.2a]. It is found that, at a given indentation depth, the contact force differs depending on whether the experiment is in a loading or an unloading phase [see Figures 3.1b and 3.2a]. For example, Kesari *et al*. [27] reported AFM-based contact experiments between a glass bead and a PDMS substrate, which shows that the contact forces differ between the loading and unloading phases [Figure 3.2a]. The force during the unloading phase was also observed to depend on the maximum indentation depth $|h_{\min}|$ [Figure 3.2a]. Kesari *et al*. termed this phenomenon depth-dependent hysteresis (DDH). The maximum indentation depth in a contact experiment is the indentation depth at the beginning of its unloading phase.

Depth-dependent hysteresis has also been observed in a number of other contact experiments, which span various length scales from μm to cm and involve different soft materials such as gelatin, PDMS, and poly(n-butyl acrylate) (PNBA) [40, 62, 74]. When the solids are in contact, the classical contact theories predict a single *P*–*h* curve [Figure 3.1a], whereas in the presence of DDH the experimental measurements display a different *P*–*h* branch for the loading and unloading phases

[Figures 3.1b and 3.2a], respectively. The estimates for the material properties are different depending on which branch is chosen to be fitted to a classical contact theory. For example, fitting the unloading and loading branches of the *P–h* curves shown in Figure 3.2a to the JKR theory yields values of 20 and 30 mJ/m^2, respectively, for the Dupré's work of adhesion w. Here $w = \gamma_1 + \gamma_2 - \gamma_{12}$, where γ_1 and γ_2 are the surface energies of the two solids, respectively, and γ_{12} is the interfacial energy [1]. In some experiments, the ambiguity in the estimated values for w can be quite dramatic. For example, the *P–h* measurements reported by Guduru *et al*. [37] for contact between a polycarbonate punch and a gelatin slab display significant DDH, with the measurements falling into distinct loading and unloading branches. Fitting the loading branch of those measurements to the JKR theory yields a value of 8 mJ/m^2 for w, whereas fitting the unloading branch yields a value of 220 mJ/m^2.

Depth-dependent hysteresis has been attributed to various mechanisms, such as the meniscus effect of ambient moisture [40], the entanglement and interdigitation of tethered chains [41], the formation of hydrogen bonds [38], and the inelastic behaviors of materials (viscoelasticity [42] and plasticity [43]). However, Kesari *et al*. [27] showed that DDH persists even when the aforementioned mechanisms can be reasonably excluded. Motivated by the observation of overlapping hysteresis loops during consecutive load-unload cycles both in air and underwater, they hypothesized that DDH was due to the occurrence of a series of small-scale surface, mechanical instabilities that are created due to surface roughness, adhesion, and the large compliance of the soft materials involved [35]. Our recent static molecular simulations showed that this mechanism can operate in adhesive elastic contacts [72]. The surface instabilities through which small-scale roughness gives rise to DDH in the work of Kesari *et al*. [27] and Kesari and Lew [35] are the same as those through which surface undulations cause adhesive toughening in the work of Li and Kim [36] and Guduru [34].

The area enclosed by the *P-h* curves in a contact cycle, ΔE, is a measure of the energy lost during that cycle. It was found experimentally that ΔE initially increases and then later decreases with the surface roughness [23, 27], *e.g.*, see Figure 3.2b. Kesari *et al*. [27, 35] presented a model for DDH that captures many of the salient features of DDH, including the initial increase of ΔE with the RMS roughness σ_{rms}. However, that model does not capture the later decreases of ΔE with σ_{rms}. Kesari

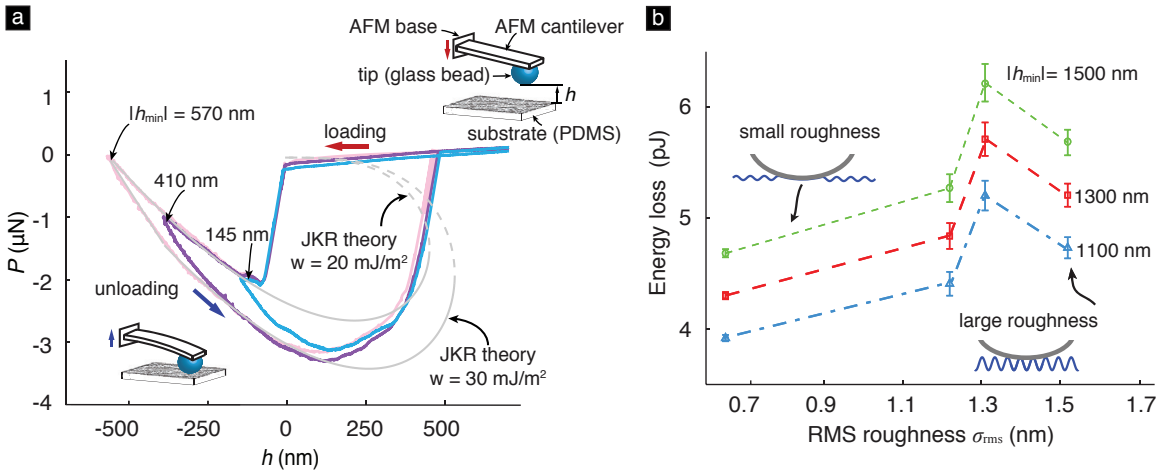

Figure 3.2: (a) Representative P–h curves measured in AFM contact experiments between a glass bead and a PDMS substrate [27]. The glass bead was of diameter $\approx 50\ \mu$m. The PDMS sample was cast on a silicon wafer having a RMS roughness ≈ 1.3 nm. As can be noted, the measured P–h curves for the loading and unloading phases of the experiment are different. The size of the hysteresis loop increases with the maximum indentation depth, $|h_{\min}|$. The gray dashed curves are the fit of the loading and unloading branches of the measured P–h data to the JKR theory. (b) A plot showing the variation of total energy loss as function of the RMS roughness in the experiments. The RMS roughness refers to the surface roughness of the silicon wafer on which the PDMS substrates were cast. The indenting rate in the experiments corresponding to all data points shown in the plot was 1000 nm/s. See Ref. [27] for experimental details.

et al. and we believe that this fact is due to the model's assumption that the contact region is simply connected [top inset, Figure 3.2b]. The contact region between two flat, perfectly smooth surfaces would be simply connected. It is likely to remain so even if infinitesimally small undulations were superimposed onto the flat surfaces. This would be especially true if the solids were composed of compliant materials, such as hydrogels or nonmineralized, biological tissues. However, irrespective of the compliance of the materials, as the height of the undulations is increased and the surface becomes rougher, the contact region will eventually become multiply connected [bottom inset in Figure 3.2b].

In this work, we focus on the regime of large surface roughness where the contact region is multiply connected, and present a new model that captures the trend of ΔE decreasing with σ_{rms}. This model is based on the MD theory of adhesive elastic contacts (Figures 3.3–3.5) and Nayak's theory of rough surfaces [75]. The mechanism of energy loss in this model is similar to the one in the model presented by Kesari and Lew *et al.* [35], in which the energy loss arises as a consequence of small-scale surface mechanical instabilities. The primary difference between the model presented in [35] and the new model herein is that the contact region in the former is simply connected whereas in the latter it is multiply connected.

Our new model involves adhesive elastic contact between a smooth, rigid paraboloid (tip) and a rough, semi-infinite, deformable solid (substrate) [see Figure 3.6a]. The substrate's surface facing the tip is nominally flat but contains a random distribution of asperities. There are two major types of models used for studying contact between rough surfaces. The first type is based on the *non-interacting asperity contact model* pioneered by Greenwood and Williamson [24], which is widely used for studying the effect of roughness on adhesion [19, 76], particle adhesion [77], elasto-plastic contact [78], and friction [79]. The second type is related to the *self-affine fractal contact model* put forward by Persson [80]. Ours is a non-interacting asperity type contact model, in which we assume that each substrate asperity interacts with the tip as though it were the only one interacting with it.

The energy loss ΔE was found experimentally to scale affinely with $|h_{\min}|$, with its minimum value corresponding to the case $|h_{\min}| = 0$. Furthermore, it was found that ΔE can be partitioned into two parts: a fixed part ΔE_I that only depends on the geometry and mechanical properties of the contacting solids and not on $|h_{\min}|$ and a variable part ΔE_D that in addition to the solids' geometric and mechanical properties also depends on $|h_{\min}|$ [see Figure 3.1b]. The depth-independent part ΔE_I is a consequence of two surface mechanical instabilities that occur at the large-scale. These large-scale instabilities correspond to the initial sudden drop in the contact force [*i.e.*, the transition from state (i) to (ii) in Figure 3.1b] and the final abrupt increase in contact force [*i.e.*, the transition from state (iii) to (iv) in Figure 3.1b]. These instabilities are generally referred to as "pull-in" and "pull-off" instabilities. It was observed in the experiments [27] that each of these large-scale instabilities always occurred once and only once in a contact cycle. Therefore, ΔE_I is the fixed, minimum amount of energy that gets dissipated in every contact cycle. Consequently, ΔE_I can be computed as the total energy dissipated in the contact cycle with $|h_{\min}| = 0$.

After the occurrence of the large-scale "pull-in" instability, as the solids are moved towards one another, more and more surface asperities will come into contact. We assume that those surface asperities will come into contact through small-scale surface mechanical instabilities, as done in Ref [27, 35]. Consequently, we refer to the asperities that come into contact during the loading phase after the occurrence of the large-scale "pull-in" instability as the *depth-dependent asperities*. Classical contact theories, which ignore roughness, predict that the contact radius prior to the occurrence of the large-scale "pull-off" instability is smaller than after the occurrence of the large-scale

"pull-in" instability. We assume that that prediction holds true even in the presence of roughness and therefore that during the unloading phase there will be a point when the contact region has receded back—in a nominal (large-scale) sense—to the one formed just after the occurrence of the large-scale "pull-in" instability. This implies that all the depth-dependent asperities would go out of contact before the occurrence of the large-scale "pull-off" instability. We assume that the detachment of the depth-dependent asperities takes place through the occurrence of small-scale instabilities, too. Thus, the energy loss ΔE_D consists of the energy lost during the instabilities through which the depth-dependent asperities come into and go out of contact. Since the larger the $|h_{\min}|$ the larger will be the number of depth-dependent asperities, the loss ΔE_D increases with $|h_{\min}|$.

This work is organized as follows. First, we evaluate the energy loss corresponding to the pair of small-scale "pull-in" and "pull-off" instabilities by using the MD theory. Second, based on Nayak's theory of rough surfaces, we estimate the number of depth-dependent asperities and the depth-dependent energy loss ΔE_D during a contact cycle. Furthermore, we discuss the comparisons of the theoretical prediction of ΔE_D based on our model with the experimental measurements. Finally, we conclude by discussing the limitations of our model.

3.2 Theory

3.2.1 Energy loss per asperity using the Maugis-Dugdale theory

The MD theory describes the axisymmetric contact between two isotropic, homogeneous, linear elastic solids of Young's moduli and Poisson's ratios E_i and ν_i ($i = 1, 2$), respectively [see Figure 3.3a]. The adhesive interactions are introduced using the *Dugdale cohesive zone* model [81]. As per this model, a surface material point experiences a traction only if its distance from the other solid in the direction normal to the surface is less than Z_0. Thus Z_0 denotes the range of the inter-body adhesive forces, which are thought to arise from van der Waals-type interactions between the surfaces. When the normal distance of the material point is less than Z_0 but non-zero, then the traction it experiences is purely tensile and of a fixed magnitude of σ_0 [see Figure 3.3b–c].

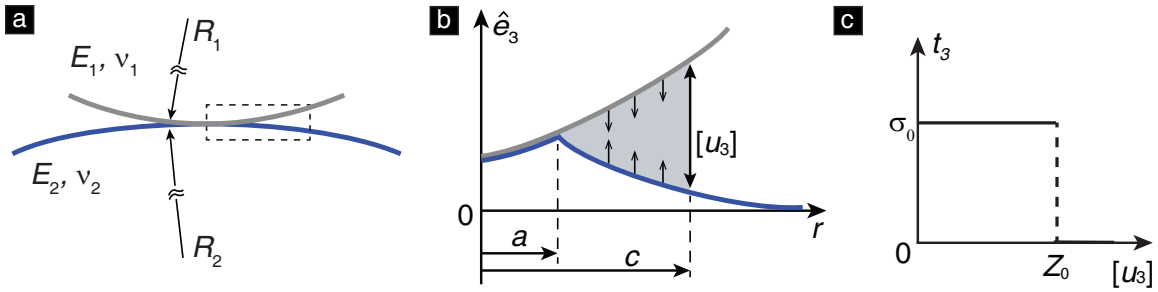

Figure 3.3: The MD model of adhesive elastic contact. (a) Geometry of the contacting solids. (b) The Dugdale cohesive zone, which is assumed to be present at the contact periphery (marked by the dashed box in (a)) as per the MD theory. The vector $\hat{\boldsymbol{e}}_3$ belongs to the set of Cartesian unit basis vectors, $\{\hat{\boldsymbol{e}}_i\}_{i=1,2,3}$, which is defined in Figure 3.6a. The symbol r denotes the radial coordinate in the plane spanned by $\hat{\boldsymbol{e}}_1$, $\hat{\boldsymbol{e}}_2$. The datum of r lies on the axial symmetry axis of the contacting solids. (c) A schematic diagram showing the traction distribution t_3 as a function of the separation $[u_3]$. The traction $t_3 = \hat{\boldsymbol{e}}_3 \cdot (\boldsymbol{\sigma}\,\hat{\boldsymbol{e}}_3)$, where $\boldsymbol{\sigma}$ is the Cauchy stress tensor. The parameters Z_0 and σ_0 are defined in the text.

The contact process is governed by the two dimensionless parameters

$$\ell = \frac{\pi w}{E^* R} \tag{3.1}$$

and

$$\chi = \frac{w}{E^* Z_0}, \tag{3.2}$$

where $1/R = 1/R_1 + 1/R_2$ is the sum of the mean curvatures of the contacting solids at their respective points of contact, and $1/E^* = (1-\nu_1^2)/E_1 + (1-\nu_2^2)/E_2$. In terms of these non-dimensional parameters, the magnitude of the contact force P and the indentation depth h at equilibrium are related as

$$\begin{aligned}
\bar{P} &= \begin{cases} \frac{2}{3}\bar{a}^3 - \chi\bar{a}^2\left(\sqrt{m^2-1} + m^2\tan^{-1}\sqrt{m^2-1}\right), & \bar{a} > 0, \\ -\frac{\pi}{2}\chi\bar{c}^2, & \bar{a} = 0, \end{cases} \\
\bar{h} &= \begin{cases} -\bar{a}^2 + 2\chi\bar{a}\sqrt{m^2-1}, & \bar{a} > 0, \\ 2\chi\bar{c} + \bar{h}_g, & \bar{a} = 0, \end{cases} \\
\ell &= \begin{cases} \bar{a}^2\left[\sqrt{m^2-1} + (m^2-2)\tan^{-1}\sqrt{m^2-1}\right] & \\ \quad + 4\bar{a}\chi^2\left[\sqrt{m^2-1}\tan^{-1}\sqrt{m^2-1} - m + 1\right], & \bar{a} > 0, \\ \frac{\pi}{2}\chi\bar{c}^2 + 2(\pi-2)\chi^2\bar{c} + \pi\chi\bar{h}_g, & \bar{a} = 0, \end{cases}
\end{aligned} \tag{3.3}$$

where $\bar{P} = P/(2E^*R^2)$, $\bar{h} = h/R$, $\bar{h}_g = h_g/R$, $\bar{a} = a/R$, $\bar{c} = c/R$ and $m = c/a$. The parameter c is defined such that all surface points whose radial coordinate in the undeformed configuration r is less than or equal to c experience a non-zero traction force [see Figure 3.3b]. The coordinate

system corresponding to r is defined in Figure 3.3. The parameter a is defined such that there is no separation, $[u_3]$, between the solids' surfaces in the region $r \leq a$. The separation $[u_3]$ is defined in Figure 3.3b and is usually referred to as the *crack opening displacement* [1]. The parameter h_g is the separation between the solids' surface points at $r = 0$ when $a = 0$. Due to the finite range of the inter-body surface adhesive interactions, the surface tractions in the MD theory do not vanish when $\bar{a} \to 0$, which is the case in the JKR and Hertz theories. For this reason we refer to c as the contact radius. The cases $\bar{a} > 0$ and $\bar{a} = 0$ in (3.3) were, respectively, derived by Maugis [16] and Kim *et al.* [82]

Figure 3.4 shows the representative equilibrium P–h curves for different combinations of parameters χ and ℓ according to (3.3). When $\ell > 0$, the MD theory asymptotes to the JKR and DMT theories, respectively, as $\chi \to \infty$ and 0 [Figure 3.4a]. The JKR theory applies to compliant materials having a large work of adhesion, while the DMT theory applies to stiff materials having a small work of adhesion. When χ is any finite, fixed value, then as $\ell \to 0$ the MD theory asymptotes to the Hertz theory [Figure 3.4b].

When $\ell > 0$, the MD theory predicts that the solids will come into and go out of contact through the well-known mechanical instabilities termed the "pull-in" and "pull-off" instabilities during a contact cycle. The schematic of a typical equilibrium P–h curve predicted by the MD theory is shown in Figure 3.1a. In that schematic, the "pull-in" and "pull-off" instabilities, respectively, correspond to the initial sudden drop in the contact force [state (i) to (ii)] and the final sudden increase in the contact force [state (iii) to (iv)]. In a displacement controlled experiment, the measured P–h curve will be the envelope of the equilibrium P–h curve. The energy lost during a contact cycle, ΔE_{md}, due to the "pull-in" and "pull-off" instabilities, is equal to the area enclosed by the P–h curves measured during that cycle. It is denoted as the shaded area in Figure 3.4.

The energy loss can be computed from the $\bar{P}$–$\bar{h}$ curves, which are defined by (3.3) as

$$\Delta E_{\text{md}} = (2E^* R^3)\Delta \bar{E}_{\text{md}}, \tag{3.4a}$$

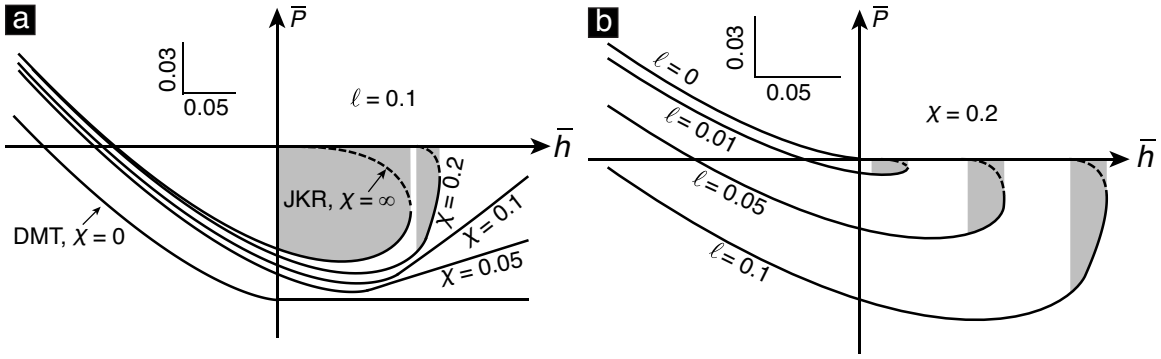

Figure 3.4: (a) The equilibrium P-h curves predicted by the MD theory for different χ values, with ℓ being held fixed at 0.1. The JKR and DMT limits are achieved when $\chi \to \infty$ and $\chi \to 0$, respectively. (b) The curves for different ℓ values, with χ being held fixed at 0.2. The Hertz limit is achieved when $\ell \to 0$. In both plots, the solid and dashed segments denote stable and unstable equilibrium states, respectively. The shaded area indicates the energy loss of the hysteresis loop.

where

$$\Delta\bar{E}_{\mathrm{md}} = \int_{r_i}^{r_o} \bar{P}(r)\frac{\partial \bar{h}(r)}{\partial r}\,dr. \tag{3.4b}$$

The limits of integration r_i and r_o in (3.4b) are the contact radii at the instances just after and prior to the occurrence of the "pull-in" and "pull-off" instabilities, respectively. We refer to $\Delta\bar{E}_{\mathrm{md}}$ as the normalized energy loss. Since the $\bar{P}$–$\bar{h}$ curves are completely defined by χ and ℓ, the energy loss $\Delta\bar{E}_{\mathrm{md}}$ only depends on these two parameters, too. We could not find a closed form expression for $\Delta\bar{E}_{\mathrm{md}}$ by evaluating the integral in (3.4b) analytically for arbitrary values of χ and ℓ. However, we were able to obtain closed form expressions in three special cases. When $\chi \to \infty$, with ℓ held fixed, we find that

$$\Delta\bar{E}_{\mathrm{md}} \sim 0.5262\ell^{5/3}. \tag{3.5a}$$

On the other hand, when $\chi \to 0$ with ℓ held fixed we obtain that

$$\Delta\bar{E}_{\mathrm{md}} \sim 5.8483\chi^{5}, \tag{3.5b}$$

as shown in Figure 3.5a. Finally, when $\ell \to 0$ with χ held fixed, the energy loss $\Delta\bar{E}_{\mathrm{md}} \to 0$.

We numerically compute $\Delta\bar{E}_{\mathrm{md}}$ for a wide range of χ and ℓ values (see Figure 3.5). As can

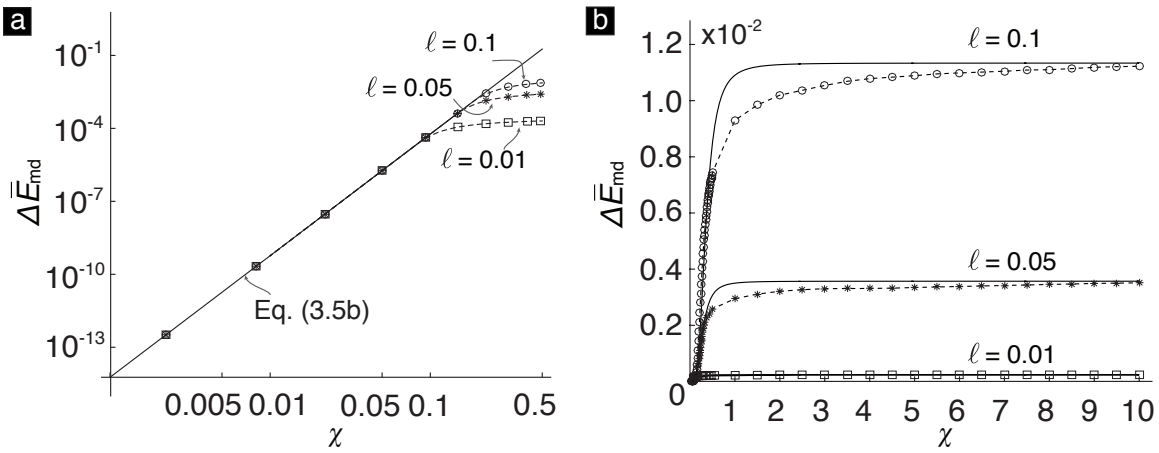

Figure 3.5: (a) The plot of the (3.5b) and the numerically computed $\Delta\bar{E}_{\text{md}}$ for different ℓ when χ is very small. (b) The comparison of exact dashed line with symbols) with approximate (solid line) values of $\Delta\bar{E}_{\text{md}}$ for different χ and ℓ. The exact values are computed numerically using eqs. (3.3)–(3.4b). The approximate values are computed from (3.6).

be seen, $\Delta\bar{E}_{\text{md}}$ increases with both χ and ℓ. By analyzing the numerical data shown in Figure 3.5, we find that the dependence of $\Delta\bar{E}_{\text{md}}$ on χ and ℓ can be well approximated by the values of the empirical function

$$\Delta\tilde{E}_{\text{md}}(\chi,\ell) = \frac{c_1\chi^5}{\left[c_2\left(\chi^3/\ell\right)+1\right]^{5/3}}, \tag{3.6}$$

where $c_1 = 5.8483$ and $c_2 = 4.2415$. A comparison of the approximate values of $\Delta\bar{E}_{\text{md}}$ given by (3.6) with its exact values computed numerically is shown in Figure 3.5b. A notable aspect of the empirical function $\Delta\tilde{E}_{\text{md}}$ is that it gives the exact values of $\Delta\bar{E}_{\text{md}}$ in the limit $\chi \to 0$ and $\chi \to \infty$, while holding ℓ fixed, and also in the limit $\ell \to 0$, while holding χ fixed. The differences between $\Delta\bar{E}_{\text{md}}$ and $\Delta\tilde{E}_{\text{md}}$ are more noticeable at intermediate values of χ. However, we found those differences to be less than 15% for the data shown in Figure 3.5. Therefore, we will approximate $\Delta\bar{E}_{\text{md}}$ with $\Delta\tilde{E}_{\text{md}}$ in our remaining analysis.

3.2.2 Depth-dependent energy loss due to the asperity level instabilities

In this section we present a rough surface contact model, and use that model to compute the depth-dependent part of the energy loss, ΔE_D, as the product of the total number of depth-dependent asperities and the mean energy loss per asperity.

In our rough surface contact model, the tip is a paraboloid with the radial profile $\tilde{u}_3 = h + r^2/2R_t$, $r \in [0, R_t]$. We describe the geometry of our model using the Cartesian coordinates x_i, $i = 1,\ 2,\ 3$,

whose corresponding basis vectors, $\hat{e}_i$, are shown in Figure 3.6a.We describe the substrate's surface topography using the function $z : \mathbb{R}^2 \to \mathbb{R}$, which gives the height (x_3 coordinate) of the substrate's surface points as a function of their x_1, x_2 coordinates. The datum of the $\hat{e}_3$ direction is chosen such that $\int_{\mathbb{R}^2} z(x_1,x_2)\,dx_1dx_2 = 0$. That is, the set of points $x_3 = 0$ form the mean plane of the substrate's rough surface [see Figure 3.6c]. The datums of the $\hat{e}_1$, $\hat{e}_2$ directions are chosen such that the coordinate system's origin is the point where the tip's rotational symmetry axis intersects the mean plane.

Consider a region in the mean plane having an area of unit magnitude. We say that this unit region contains an asperity whose apex has the coordinates $(x_1,x_2,z(x_1,x_2))$, if it contains the point $(x_1,x_2,0)$. The unit region will, in general, contain a large number of asperities. A number of surface topography measurements have shown that the variation of a rough surface's geometric features can be well described using stochastic models [83, 84]. Motivated by those results, we model the variation of the different geometric characteristics of the asperities belonging to the unit region using the probability density functions (PDFs) given by Nayak [75]. In our current model, we assume that, in a statistical sense, the substrate's surface roughness is homogeneous and isotropic. That is, the PDFs characterizing the different geometric features of the asperities do not depend on the location or the orientation of the unit region. For this special case, Nayak [75] gives the joint PDF of the heights and curvatures of the asperities belonging to the unit region to be

$$p(\xi,t) = \frac{\sqrt{3C_1}}{2\pi} e^{-C_1\xi^2} \left(t^2 - 2 + 2e^{-\frac{t^2}{2}}\right) e^{-\frac{C_1t^2+C_2t\xi}{2}}, \tag{3.7}$$

where $\xi \in (-\infty,\infty)$ is the asperity height normalized by the surface's RMS roughness σ_{rms} [see Figure 3.6c], $t = -\sqrt{3/m_4}k_m$, and the asperity curvature $k_m \in (0,\infty)$ is the surface's mean curvature at the apex of an asperity [see Figures 3.6c–d]. The constants C_1, C_2 in (3.7) are defined as $C_1 := \alpha/(2\alpha-3)$ and $C_2 := C_1\sqrt{12/\alpha}$, where α is an important parameter called Nayak's parameter. It is defined as $\alpha := m_0m_4/m_2^2$, where m_0, m_2, and m_4 are the surface's spectral moments. These moments can be computed from the equation

$$m_n = \frac{2\sqrt{\pi}\Gamma((1+n)/2)}{\Gamma(1+n/2)} \int_0^\infty q^{n+1} C^{\text{iso}}(q)\,dq \tag{3.8}$$

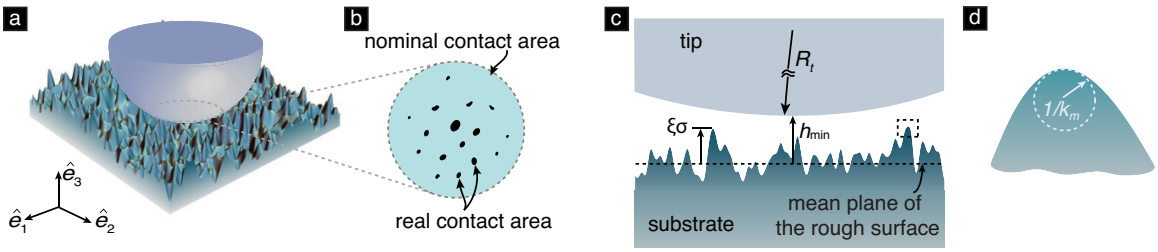

Figure 3.6: (a) The schematic of contact between a smooth rigid tip and a rough elastic substrate. (b) The schematic of nominal and real contact areas. (c) The section-view of the rough contact model shown in (a). (d) An asperity with radius of curvature $1/k_m$ at its apex as indicated by the dashed box in (c).

by setting $n = 0$, 2 and 4, respectively, where Γ is the gamma function, the function $C^{\text{iso}} : \mathbb{R} \to \mathbb{R}$ is the isotropic surface's power spectral density (PSD). It is determined by the surface's topography z. See Appendix B for its complete definition.

We assume in our model that the contact between the tip and the substrate takes place only at the asperities. Consequently, in our model the real contact region is smaller than the nominal contact region. We define the nominal contact region to be a circular region in the mean plane that contains all the contacting asperities [Figure 3.6b]. The nominal contact region is also referred to as the apparent contact region in the literature, since at the large-scale it is the region over which the solids appear to be in contact. The nominal contact region grows and recedes during the loading and the unloading phases of the contact cycle, respectively. The evolution of the real contact region is much more complicated. The definition of the nominal contact region, by itself, does not imply that all asperities contained within it are in contact with the tip. Indeed, it is possible that many asperities never make contact despite belonging to the nominal contact region during some instance of the contact cycle. However, as part of our model, we assume that all asperities within a nominal contact region make and break contact with the tip as that region forms and unforms. As a consequence of this assumption, the total number of depth-dependent asperities can be computed as the product of the asperity density and the area of the nominal contact region that forms after the occurrence of the large-scale "pull-in" instability during the remainder of the contact cycle's loading phase. The asperity density is the total number of asperities contained in a nominal contact region of unit area. Nayak [75] gives the total number of asperities contained in a region of the mean plane of unit area to be

$$\eta = \frac{m_4}{6\pi\sqrt{3}m_2}. \tag{3.9}$$

Recall that the nominal contact region is part of the mean plane. Therefore, η is in fact equal to the asperity density. We compute the area of the nominal contact region formed after the occurrence of the large scale "pull-in" instability as

$$\Delta A_c = A_c^{h_{\min}} - A_c^0, \tag{3.10}$$

where A_c^0 and $A_c^{h_{\min}}$ are areas of the nominal contact region at the large-scale "pull-in" instability point (*i.e.*, $h = 0$, marked as state *ii* in Figure 3.1b) and at the maximum indentation depth (*i.e.*, $h = h_{\min}$, see Figure 3.1b), respectively. Our rough contact does not provide predictions for the nominal contact region. In many contact experiments the nominal contact region is measured as part of the experiment (*e.g.*, see Guduru and Bull [37]). In such cases, the total number of depth-dependent asperities can be estimated by using the measured nominal contact area values in conjunction with eqs. (3.9) and (3.10). In other situations, where such measurements are unavailable we believe that the best alternative is to estimate the nominal contact region using a classical adhesive elastic contact theory. For example, in the next section, we estimate the nominal contact region in the experiments of Kesari *et al*. using the JKR theory.

We estimated the energy loss for a single depth-dependent asperity, ΔE_{md}, using the MD theory. That energy loss is not constant between the asperities, but varies between them depending on their curvature. Using (3.7), we find that the variation of curvatures in the population of all asperities contained in any unit region of the mean plane to be

$$p_\kappa(t) = \sqrt{\frac{3}{4\pi}} \left(t^2 - 2 + 2e^{-\frac{t^2}{2}} \right) e^{-\frac{(8C_1^2 - C_2^2)t^2}{16C_1}}. \tag{3.11}$$

Recall that the nominal contact region belongs to the mean plane. Therefore, the PDF (3.11) also applies to the population of all the asperities contained in any nominal contact region of unit area. Since the depth-dependent asperities are the total number of asperities contained in the nominal contact region formed after the occurrence of the large scale "pull-in" instability, the PDF (3.11) also applies to the population of all depth-dependent asperities. Thus, the mean energy loss per

depth-dependent asperity can be computed as

$$\langle \Delta E_{\mathrm{md}} \rangle = \int_{-\infty}^{0} \Delta E_{\mathrm{md}} p_{\kappa}(t)\, dt. \tag{3.12}$$

Writing ΔE_{md} in (3.12) in terms of $\Delta \bar{E}_{\mathrm{md}}$ using (3.4a), and then approximating $\Delta \bar{E}_{\mathrm{md}}$ with $\Delta \tilde{E}_{\mathrm{md}}$ defined in (3.6), we get

$$\langle \Delta E_{\mathrm{md}} \rangle \approx 2E^{*} \int_{-\infty}^{0} \Delta \tilde{E}_{\mathrm{md}}(\chi, \ell(t)) p_{\kappa}(t) R^{3}(t)\, dt, \tag{3.13}$$

where

$$\ell(t) = \frac{\pi w}{E^{*} R(t)}, \tag{3.14a}$$

$$R(t) = \left(\frac{1}{R_t} - \sqrt{\frac{m_4}{3}} t \right)^{-1}. \tag{3.14b}$$

Equation (3.14a) follows from noting that in (3.1) the second argument, ℓ, of the function $\Delta \tilde{E}_{\mathrm{md}}$ depends on the effective mean curvature $1/R$, which is the sum of mean curvatures of the solids at their respective points of contact. We assume that at all contact points the tip's curvature equals $1/R_{\mathrm{t}}$ and that the asperity's curvature at the contact point is the same as its curvatures k_m at its apex. The (3.14b) follows these assumptions and the fact that $k_m = -\sqrt{m_4/3}t$.

Multiplying the mean energy loss per depth-dependent asperity with the total number of those asperities we get

$$\Delta E_D = \eta \Delta A_c \langle \Delta E_{\mathrm{md}} \rangle, \tag{3.15}$$

where η, ΔA_c, and $\langle \Delta E_{\mathrm{md}} \rangle$ are, respectively, given by (3.9), (3.10), and (3.13).

3.3 Comparison with experiments

In this section, we use (3.15) to estimate ΔE_D in the glass bead–PDMS contact experiments reported by Kesari *et al*. [27] and compare the estimates with measured values. The experiments involved contact between a spherical glass bead and PDMS substrates. The geometry of the contacting solids

in the experiments is shown in the insets of Figure 3.2a. In the experiments, both the substrate and the tip are rough [see Figures 3.7a–c]. However, in our model only the substrate is rough. This makes the quantitative comparison of our model with the experiments challenging. Nevertheless, we still attempt to compare our model's predictions with the experiments by taking our model's surface topography function to be a scalar multiple of that of the substrate so that the substrate's roughness in our model stands in for the roughness of both the tip and the substrate in the experiments. Despite its crude nature, we hope that some knowledge can yet be gained about the utility of our model from this comparison.

To calculate ΔE_D from (3.15), we need to know the asperity density η, the mean energy loss per asperity $\langle \Delta E_{\mathrm{md}} \rangle$, and the nominal contact area ΔA_c in the context of the experiments. To calculate the first two of these quantities we need to know the C^{iso} function. Given a substrate surface topography function, we are able to numerically compute $C^{\mathrm{iso}}(q)$, where q is the wavenumber magnitude, using the method presented in Ref. [85], see §1 of Appendix B for details. We take the surface topography function in our model to be a scaled version of the surface topography function of the substrate in the experiments.

Kesari *et al.* reported that it was difficult to measure the PDMS substrates' surface topography directly because of their low stiffness. As an alternative, they assumed that a substrate's topography function was the same as that of the Si mold on which it was cast. For the purposes of the current comparison, we make the same assumption. However, as we discuss in §Conclusion, the validity of this assumption needs further investigation.

The PDMS substrates were cast on four different Si molds having different surface topographies. The RMS roughness of those topographies ranged between 0.65 nm and 1.52 nm [see, *e.g.*, Figure 3.2b]. Since our model applies to the large surface roughness regime, we only consider the experiments on the substrate with the largest roughness, namely 1.52 nm. Figure 3.7c shows the surface topography of the Si mold corresponding to this substrate. We use that topography data to construct the surface topography function for the substrate in the experiments. The values of C^{iso} corresponding to this surface topography function are shown in Figure 3.7d. As can be seen, the values of C^{iso} are approximately constant at small wavenumber magnitudes, and fall off rapidly at large wavenumber magnitudes. This behavior is similar to that of a power-law PSD function. To be

specific, consider the PSD function

$$q \mapsto \frac{1}{C_0} \frac{e^{-q/q_0} L_c^2 \sigma_{\text{rms}}^2}{(1+L_c^2 q^2)^n}, \tag{3.16}$$

where

$$C_0 = 2\pi \int_0^\infty \frac{e^{-q/q_0} L_c^2 q}{(1+L_c^2 q^2)^n} \, dq,$$

and L_c, q_0, and n are parameters referred to as the correlation length, cut-off wavenumber, and the power-law index, respectively. The PSD function (3.16) is a modified version of the k-correlation, or *ABC* model, which has been shown to be applicable to a large variety of surface topographies [86, 87]. We found that the PSD function (3.16) matches the C^{iso} function whose values are shown in Figure 3.7d remarkably well for the parameter values

$$\sigma_{\text{rms}} = 1.45 \text{ nm}, \quad L_c = 20.1 \text{ nm}, \quad n = 3.28, \quad \text{and} \quad q_0 = 1.0 \times 10^8 \text{ m}^{-1}. \tag{3.17}$$

(The values for σ_{rms}, L_c, and n were obtained by minimizing a measure of the difference between the C^{iso} values shown in Figure 3.7d and the values given by the PSD function (3.16). The value for q_0 was chosen independently before performing the minimization.) Therefore, we take the PSD function (3.16) with the values for the parameters in it given by (3.17) to be an analytical representation of the C^{iso} function that corresponds to the surface topography of the substrate in the experiments.

To account for the roughness of the tip in the experiments in our model, in which the tip is always smooth, we take the surface topography function of the substrate in our model to be a scaled version of that of the substrate in the experiments. Specifically, if in the experiments the height of a substrate surface point is $z(x_1, x_2)$ then in our model we take the height of that point to be $kz(x_1, x_2)$, where $k \geq 1$. Taking $k = 1$ would amount to simply ignoring the roughness of the tip-in-the-experiments in our model. We perform our comparison for a range of k values, which—as we shall discuss shortly—we selected by taking into consideration the measured roughness of the tip-in-the-experiments. It follows from §1 of Appendix B that if the isotropic PSD function corresponding to z is C^{iso}, then that corresponding to kz is $k^2 C^{\text{iso}}$. Therefore, we take the C^{iso} function in our model to be k^2 times the PSD function (3.16) with the values for the parameters in it still being

given by (3.17).

Knowing the C^{iso} function in our model, we numerically evaluate the integrals in (3.8) for the cases $n = 0,\ 2$ and 4 to get

$$m_0 \approx 2.1k^2 \text{ nm}^2, \quad m_2 \approx 1.3k^2 \times 10^{-3}, \quad \text{and} \quad m_4 \approx 4.3k^2\ \mu\text{m}^{-2}. \tag{3.18}$$

Substituting the values for the spectral moments given in (3.18) in (3.9) we get the asperity density $\eta \approx 101.4\,\mu\text{m}^{-2}$.

The mean energy loss $\langle \Delta E_{\text{md}} \rangle$ can be computed from (3.13)–(3.14) on knowing the values of R, ℓ, and p_κ for any given $t < 0$ and the parameter χ. We calculate the values of R from (3.14b), in which we take R_t to be 25 μm, as that was the radius of the glass bead (tip) in the experiments, and m_4's value to be that which was given in (3.18). Knowing R, we calculate the values of ℓ from (3.14a). In (3.14a), as well as in the remainder of this comparison, we take the material properties E^* and w to be, respectively, 0.75 MPa and 26 mJ/m^2, since these were the values measured for them in the experiments. We calculate α from the values for the spectral moments given in (3.18) and then use it to calculate the parameters C_1 and C_2. Knowing these parameters, we calculate the values of p_κ from (3.11). Having knowledge of E^* and w the parameter χ can be computed from (3.2) once we have knowledge of Z_0. However, we could not find a clear way to identify Z_0 in the experiments. Therefore, we treat Z_0 as a fitting parameter in our comparison.

Unfortunately, neither Kesari *et al.* reported measurements of ΔA_c in their experiments nor does our model give predictions for it. For a lack of a better alternative, we use the JKR theory to estimate ΔA_c in the experiments. The JKR theory is the most widely used model for adhesive elastic contact, which only applies to contact between smooth surfaces. Kesari and Lew [35] presented a generalization of the JKR theory that applies to contact between rough surfaces and gives a prediction for the nominal contact area. However, as we discussed in the introduction, that model only applies in the regime of small surface roughness. Employing the JKR theory we find that ΔA_c in the experiments is approximately equal to $4R_t|h_{\min}|$. See §2 of Appendix B for details.

The experimentally measured ΔE_D values reported by Kesari *et al.* are shown in Figure 3.8a. As the final step for making the comparison, we need to choose appropriate values for k. Recall that we

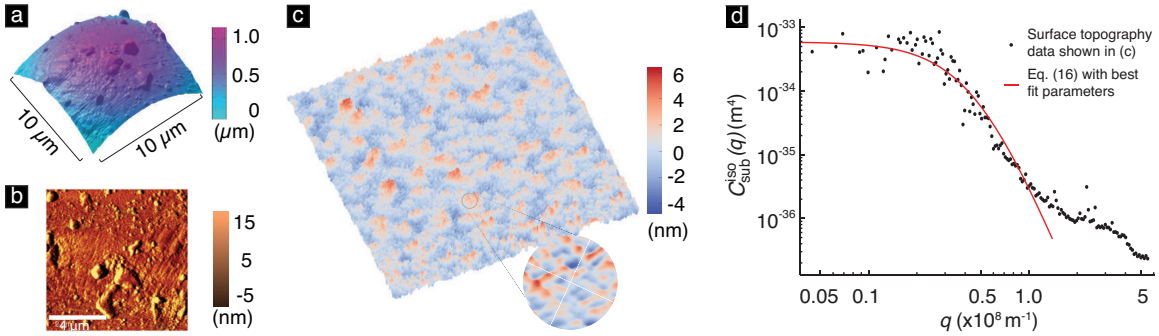

Figure 3.7: (a) The curved shape of the tip (which is a glass bead) and (b) its surface topography after subtracting the curvature effect. The RMS roughness of this bead is 12.14 nm. See Table 1 in Appendix B for details about the glass bead roughness. (c) The surface topography of the Si mold scanned over a area of 2 μm $\times$ 2 μm with a total of 256 points in each direction. The measured RMS roughness σ_{rms} is 1.52 nm. (d) The power spectrum of the Si mold's surface topography, and the corresponding fitting to the PSD function (3.16) with best fitting parameters $\sigma_{\text{rms}} = 1.45$ nm, $L_c = 20.1$ nm and $n = 3.28$.

introduced the scaling parameter k to account for the roughness of the tip in the experiments in our model, in which the tip is smooth. The tip in the experiments was a spherical glass bead. Table 1 in Appendix B gives the RMS roughness of four glass beads that were sampled from the same source as the glass bead used in the experiments. As can be noted from the table, the RMS roughness of these beads ranges from 2.59 nm to 12.14 nm. Since the roughnesses of the tip and the substrate are not expected to be correlated, it is reasonable to require that the substrate's roughness in our model be equal to the value obtained by adding together the squares of the RMS roughnesses of the tip and the substrate in the experiment and then taking the square root of that sum. As per this criteria, an appropriate range for the roughness of the substrate in our model is 3 nm to 12.2 nm, which implies that a reasonable range for k is $(1.97,\ 8.03)$. We show the estimates for ΔE_D from our model for the cases when $k = 1.97$ ($\sigma_{\text{rms}} = 3$ nm) and $k = 8.03$ ($\sigma_{\text{rms}} = 12.2$ nm) in Figure 3.8a. While making these estimates we used Z_0 as a fitting parameter. For the cases $k = 1.97$ and 8.03 we got the best fit values for Z_0 to be 96 nm and 24 nm, respectively. As can be seen in Figure 3.8a, the estimates from our model for the two cases $k = 1.97$ and 8.03 are almost indistinguishable. In fact, we found that the estimates for other cases in which k (resp. σ_{rms}) varied between 1.97 (resp. 3 nm) and 8.03 (resp. 12.2 nm) were also indistinguishable from the ones shown in Figure 3.8a. In each of those

Table 3.1: Estimates for the range of Z_0 from literature

Materials	Geometry	Range
Silica–Silica [88]	Sphere (of radius 3.8 μm)–Plate	10 nm
Polystyrene–Glass [89]	Sphere (of radius 6 μm)–Plate	20–100 nm

cases we again used Z_0 as a fitting parameter. The best fit values for Z_0 in these other cases varied between 96 nm and 24 nm [Figure 3.8c]. Recall that the parameter Z_0 is a measure of the distance of the inter-body cohesive forces and that we were unable to clearly identify it in the experiments of Kesari *et al.* [27]. However, the parameter Z_0 has been found in other experiments to range from 10 nm to 100 nm (see Table 3.1). Thus, the best fit values for Z_0 in our comparison lie well within the experimentally reasonable range.

Consider the quantity

$$\overline{\Delta E}_D = \frac{\Delta E_D}{\Delta A_c} \approx \frac{\Delta E_D}{4R_t|h_{\min}|}, \tag{3.19}$$

which is the depth-dependent energy loss per unit nominal contact area. This quantity is a constant in our model, since in it ΔE_D depends linearly on $|h_{\min}|$ on account of ΔE_D depending linearly on ΔA_c, and ΔA_c depending linearly on $|h_{\min}|$. Figure 3.8b shows the values of $\overline{\Delta E}_D$ in the experiments at different $|h_{\min}|$. We computed these values using the data shown in Figure 3.8a. As can be seen, $\overline{\Delta E}_D$ is essentially a constant equal to $0.0241\ \mathrm{J/m^2}$ in the experiments. Thus, our model's prediction that ΔE_D varies linearly with $|h_{\min}|$ is in good agreement with experimental measurements.

3.4 Effect of roughness and adhesive interaction range on energy loss

Figure 3.8c shows the contour plot $\overline{\Delta E}_D$ of as a function of Z_0 and σ_{rms} based on our model's prediction. It can be noted from the figure that at a fixed Z_0, $\overline{\Delta E}_D$ and hence ΔE_D decreases and approaches zero as σ_{rms} increases. This behavior is in agreement with the trend of ΔE decreasing with roughness at large surface roughness regime reported by Kesari *et al.* and others, as discussed in the Introduction. Also can be seen in Figure 3.8c is the trend that, for a fixed σ_{rms}, $\overline{\Delta E}_D$ and hence ΔE_D decrease as the adhesive interaction length-scale Z_0 increases. We are unaware of any experimental data that can be used to check the validity of this theoretical prediction of our model. However, this trend is consistent with the numerical results reported by Song *et al.* [76], in which the strength of adhesion decreases as the adhesive interaction length-scale increases.

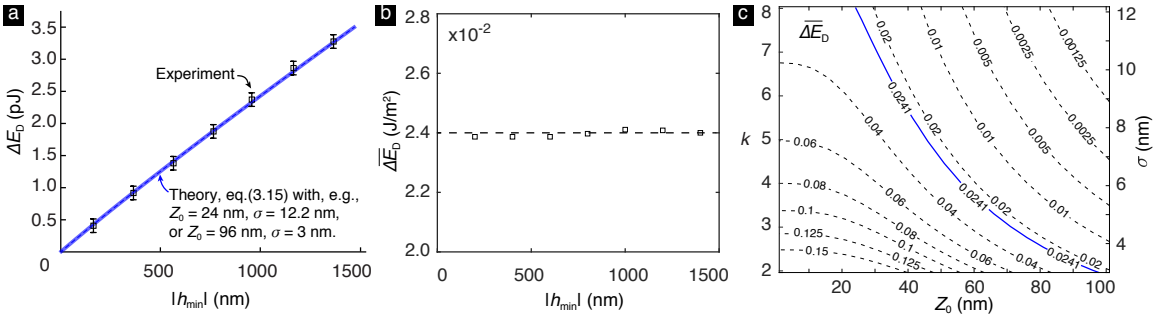

Figure 3.8: (a) The comparison of the depth-dependent energy loss ΔE_D measured in the experiment [27] (squares) with the estimations based on the theoretical model according to (3.15) with $Z_0 = 24$ nm, $\sigma_{\text{rms}} = 12.2$ nm (thick, solid line) and $Z_0 = 96$ nm, $\sigma_{\text{rms}} = 3$ nm (thin, dashed line). The error bars indicate the standard deviation of the measurements of hysteretic energy loss taken at five locations on the PDMS substrates in the experiments. (b) The plot of depth-dependent energy loss per unit nominal contact area $\overline{\Delta E}_D$ with $|h_{\text{min}}|$. It is essentially a constant equal to 0.0241 J/m^2 (dashed line). (c) The contour plot of $\overline{\Delta E}_D$ as a function of Z_0 and σ_{rms}. The contour of the experimental value of $\overline{\Delta E}_D$ is shown as a solid blue line. Also, while making the comparison if we choose the value of k (equivalently σ_{rms}) to be the ordinate of a point lying on the blue line then the best fit value for Z_0 in the comparison is the abscissa of that point.

3.5 Concluding remarks

We generated predictions from our model in the context of the experiments reported by Kesari *et al.* In general, however, it is challenging to determine *a priori* whether or not it is reasonable to apply our model to a particular contact scenario. The reason is that we assumed in our model that the contact region is multiply connected and that there is no interaction between neighboring asperities. These are reasonable assumptions only if the size of the contact region formed at each asperity is much smaller than the separation between neighboring asperities. However, we are not aware of any general criteria/models that can be used to gather information in this regard without actually solving for the complex stress and displacement fields at the contact interface. Therefore, a general theory of the type developed by Johnson [90] that yields information about the topology of the contact region would form a valuable supplement to our model.

Kesari *et al.* [27] and we assume that the PDMS substrates' RMS roughness is proportional to that of their respective Si molds. Kesari *et al.* used the soft-lithography technique developed by Hua *et al.* [91] to cast their PDMS substrates. Hua *et al.* demonstrated that their technique was capable of copying surface features as small as 3 nm from a Si mold onto a PDMS substrate. However, it has been argued that in soft-lithography it can be challenging to replicate features due to surface stress flattening out features having high curvature [92–94]. This raises the question of how justified it is to assume that the PDMS substrates' RMS roughness is proportional to that of

their respective Si molds. Some preliminary insight into addressing this question can be obtained by considering the model presented by Style *et al.* [94] in which the surface topography of a compliant solid is taken to have a sinusoidal profile with wavelength λ in a single direction. As per their model, the surface stress would flatten out the sinusoidal surface if $\lambda \ll \ell_{\text{ec}}$, where $\ell_{\text{ec}} := \gamma/E$ is the elasto-capillarity length, and γ and E are, respectively, the surface stress and Young's modulus of the complaint solid. Assuming that PDMS' Poisson's ratio is 0.5 we get that E in Kesari *et al.*'s experiments is ≈ 0.6 MPa. Kesari *et al.* do not report the surface stress of the PDMS they use in their experiments [27]. In other experiments, however, the surface stress of PDMS was found to lie in the 15 to 50 mN/m range [95–97]. If we assume that PDMS' surface stress in Kesari *et al.*'s experiments too lies in this range then we get that in their experiments ℓ_{ec} lies in the 25–80 nm range. We found that the average distance between each asperity and its nearest neighbor on the Si mold surface shown in Figure 3.7b is ≈ 17 nm (See §4 of Appendix B for details). Thus, at least as per the sinusoidal surface stress model, it is justified to question the validity of the assumption that a Si mold's topography is faithfully reproduced in the PDMS substrate cast on it in Kesari *et al.*'s experiments. Thus, this preliminary analysis of the flattening effect of surface stress adds to the importance of using direct measurements of the substrate's topography in any future comparisons of our model with experiments.

We conclude by noting that our model bears some similarities with the models presented in Ref [98, 99]. In particular, following Fuller and Tabor's [19] approach, Wei *et al*. [98] investigated the effect of roughness on adhesion hysteresis. However, there are significant differences between their models and ours. For example, Wei *et al.* assumed the asperities' radii of curvatures to be a constant, whereas in our model the asperities have different radii of curvatures depending on their heights. In Wei *et al*.'s model the asperity level contact is modeled using the JKR theory, whereas we model that interaction using the MD theory. Finally, Wei *et al* 's model does not capture the depth-dependent nature of the hysteretic energy loss. Our model provides a semi-analytical formula to estimate the depth-dependent energy loss.

Chapter 4

Surface roughness enhanced adhesion in adhesive elastic contact: Finite element simulation and analysis

4.1 Introduction

Adhesion has attracted significant attention due to its critical applications in the engineering field, such as sliding and rolling friction [100–102], wear and lubrication [103, 104], stiction failure in micro-electromechanical systems [105], head-disk interface of magnetic storage [106], and soft robotics [107]. Moreover, biological materials and tissues including gecko and spider's feet [108, 109], frog toe pad [110], and marine mussel [111] used for locomotion have aroused strong interest of the researchers to uncover the physical mechanisms of their fascinating adhesion properties. Many efforts have been devoted to create bio-inspired structures and materials with controllable, repeatable, and directional adhesion to a variety of surfaces [112–114]. For these reasons, there is a growing body of literatures to study the effect of surface roughness on adhesion and adhesive elastic contacts during the recent decades.

In this work, we propose an effective nonlinear body force field based finite element (FE) method to simulate the adhesive elastic contact and numerically investigate the effect of surface

roughness and adhesive interaction range on adhesion. In our simulations, the roughness is represented by the periodic undulations on the surface as in [34, 35]. The adhesive interaction between solids is modeled as an effective body force field using the generalized LJ potential. Our simulations capture the main features of the small-scale roughness induced elastic instability mechanism for the adhesion enhancement reported in [34–36, 72]. Moreover, it also captures the decreasing trend of adhesion as the surface roughness increases beyond a critical value. The decreasing trend can not be predicted by the analytical models proposed in [34–36], where the surface roughness is assumed to be small enough such that the solids are remained in full contact during a contact cycle. This assumption is no longer valid as the surface roughness becomes relatively large. Our simulations provide a critical evidence to the small-scale contact instability mechanism as a plausible explanation for DDH and reveal the underlying mechanism for the surface roughness enhanced adhesion.

It is noted that there exist several numerical approaches to model adhesive elastic contact, such as the cohesive zone modeling [115] and the surface traction formulation [18, 116–118]. Even though the two approaches have been widely used in modelling adhesive interaction, both have limitations. For example, the cohesive zone modeling needs a priori knowledge of the contact region, which is not suitable to model the entire contact process of two initially separated solids. On the other hand, the surface traction formulation is based on the *Derjaguin approximation* that the interaction energy per unit area between two solids with slightly curved surfaces is approximately equal to that between two parallel half-spaces [45, 119, 120]. This approximation holds only for the case that the curvature of the surface is very small and the distance between two surfaces is also small. By contrast, the nonlinear body force field employed here is an exact formulation based on the molecular potential of adhesive interaction, which does not rely on the *Derjaguin approximation* or need any predefined contact region as a priori knowledge. Therefore, it can be extended to model the adhesive elastic contact between a rigid half-space and an elastic solid with arbitrary surface topography.

This work is organized as follows. First, we present the adhesive elastic contact model and FE simulation setup based on the generalized LJ potential in §4.2. Next we analyze the effect of Tabor parameter on the pull-in and pull-off instabilities and determine the critical separation at which the

instability occurs in §4.3. Then we benchmark the simulations of adhesive contact between a rigid substrate and an elastic solid with smooth surface against the MD theory in §4.4. We discuss the effects of surface roughness and adhesive interaction range on adhesion and study the mechanisms of DDH and surface roughness dependent adhesion through the simulation results in §4.5. Finally, we conclude our work in §4.6.

4.2 Continuum model of adhesive elastic contact

4.2.1 Adhesion due to the generalized LJ potential

Considering that adhesion between solids origins from the intermolecular interactions [45], we assume the interaction between a pair of particles in two different solids can be described by the generalized LJ potential

$$V(r) = 4\varepsilon\left[-C_6\left(\frac{\sigma}{r}\right)^6 + C_{12}\left(\frac{\sigma}{r}\right)^{12}\right], \tag{4.1}$$

where ε and σ are the characteristic energy and distance, respectively, r is the distance between the two particles, and the constants $C_6, C_{12} \in \mathbb{R}^+$. Then we can derive the Depré work of adhesion between two solids based on the generalized LJ potential as follows.

Let us consider the interaction between two parallel half-spaces, which are separated at a distance ζ in the $\hat{e}_z$ direction, see Figure 4.1a. The interaction energy between a typical particle a in the top half-space and the infinitesimal volume dV around a typical particle b in the bottom half-space is $V(r)\rho_1 dV$, where the distance between the particles a and b is $r = \sqrt{\xi^2+\eta^2}$, and ρ_1 is the number of particles per unit volume of the bottom half-space. Then, with the assumption of additivity, the interaction energy between the particle a and the bottom half-space will be the sum of its interactions with all the particles in the bottom half-space. That is,

$$\mathscr{U}(d) = \int_d^\infty \int_0^\infty \int_0^{2\pi} V(r)\rho_1 \xi \, d\theta d\xi d\eta = 4\pi\varepsilon\rho_1\sigma^3\left[-\frac{C_6}{6}\left(\frac{\sigma}{d}\right)^3 + \frac{C_{12}}{45}\left(\frac{\sigma}{d}\right)^9\right]. \tag{4.2}$$

Here d is the distance from the particle a to the bottom half-space's surface. Consequently, the force

on the particle a due to its interaction with the bottom half-space is

$$F_{oh}(d) = \frac{d\mathscr{U}(d)}{dd} = 4\pi\varepsilon\rho_1\sigma^2\left[\frac{C_6}{2}\left(\frac{\sigma}{d}\right)^4 - \frac{C_{12}}{5}\left(\frac{\sigma}{d}\right)^{10}\right]. \tag{4.3}$$

Moreover, the interaction energy per unit area between two parallel half-spaces is

$$\mathscr{E}(\zeta) = \int_\zeta^\infty \mathscr{U}(d)\rho_2 dd = 4\pi\varepsilon\rho_1\rho_2\sigma^4\left[-\frac{C_6}{12}\left(\frac{\sigma}{\zeta}\right)^2 + \frac{C_{12}}{360}\left(\frac{\sigma}{\zeta}\right)^8\right], \tag{4.4}$$

where ρ_2 is the number of particles per unit volume of the top half-space. Thus, the force per unit area between the two half-spaces is

$$F_{hh}(\zeta) = \frac{d\mathscr{E}(\zeta)}{d\zeta} = 4\pi\varepsilon\rho_1\rho_2\sigma^3\left[\frac{C_6}{6}\left(\frac{\sigma}{\zeta}\right)^3 - \frac{C_{12}}{45}\left(\frac{\sigma}{\zeta}\right)^9\right]. \tag{4.5}$$

Due to the symmetry, both the forces F_{oh} and F_{hh} are in the $\hat{e}_z$ direction. The equilibrium distance between the two half-spaces, ζ_0, is determined by setting $F_{hh}(\zeta_0) = 0$. Thus, we obtain

$$\zeta_0 = \left(\frac{2C_{12}}{15C_6}\right)^{1/6}\sigma, \tag{4.6}$$

which denotes a characteristic length scale of adhesive interaction. The Dupré work of adhesion between two solids, w, is defined as the work done per unit area in order to separate them from their equilibrium distance to infinity [1, chap. 1]. Therefore, according to (4.4), we obtain the Dupré work of adhesion as

$$w = \mathscr{E}(\infty) - \mathscr{E}(\zeta_0) = \frac{C_6}{4}\left(\frac{2C_{12}}{15C_6}\right)^{1/6}\pi\varepsilon\rho_1\rho_2\sigma^4. \tag{4.7a}$$

In terms of the adhesive length scale ζ_0 and the Hamaker constant $A_\mathrm{H} = 4\pi^2\varepsilon\rho_1\rho_2\sigma^6$, (4.7a) can be rewritten as

$$w = \kappa A_\mathrm{H}/\zeta_0^2, \tag{4.7b}$$

where $\kappa = C_6/(16\pi)$.

4.2.2 Contact model and finite element simulation setup

Our model consists of the axisymmetric, adhesive contact between a linear elastic tip and a rigid, semi-infinite substrate. The (4.3) implies that the effect of adhesion between two solids is equivalent to exerting an effective body force on one solid induced by the other. Therefore, we model the contact interactions to be an effective body force given in (4.15) on the tip due to its interaction with the semi-infinite substrate. The equilibrium configuration of our contact problem is obtained by solving the governing equation (4.13) along with the constitutive law (4.12) and the contact law (4.15) through finite element method.

Geometry

Figure 4.1b shows the axisymmetric contact between the tip and substrate. We adopt a cylindrical coordinate system $(\hat{e}_r, \hat{e}_\theta, \hat{e}_z)$ in which the z-axis coincides with the symmetry axis of the tip. The substrate is a rigid body. It is fixed and occupies the region $\Omega := \{(r,\theta,z) \in \mathbb{R}^3 | r \geq 0, 0 \leq \theta \leq 2\pi, z \leq 0\}$. The tip is a linear, elastic material with Young's modulus E and Poisson's ratio ν. The reference configuration of the tip is the region $\mathscr{B}_0 \subset \mathbb{E}^3$, which is defined as

$$\mathscr{B}_0 := \{(r,\theta,z) \in \mathbb{R}^3 | r \leq r_0, 0 \leq \theta \leq 2\pi, z_s(r) \leq z \leq z_s(r) + h_0\}. \tag{4.8}$$

Here r_0 and h_0 are, respectively, the half-width and height of the tip; its radial profile

$$z_s(r) = z_0 + f(r) + A\rho\left(\frac{r}{\lambda}\right), \tag{4.9}$$

where z_0 is the gap between the tip and the substrate, $f(r)$ describes the large-scale surface topography of the tip, and the function ρ and parameters A and λ characterize its small-scale surface roughness. There are various models to describe the rough surface, including the random rough surface [24] and self-affine fractal rough surface [80]. For those models, the computational cost would be very high due to the extremely refined mesh to represent the surface features with a decent quality. For that reason, we idealize the rough surface profile to be a periodic undulation on the top of a smooth surface profile. Another merit of this periodic undulation model is that it will also

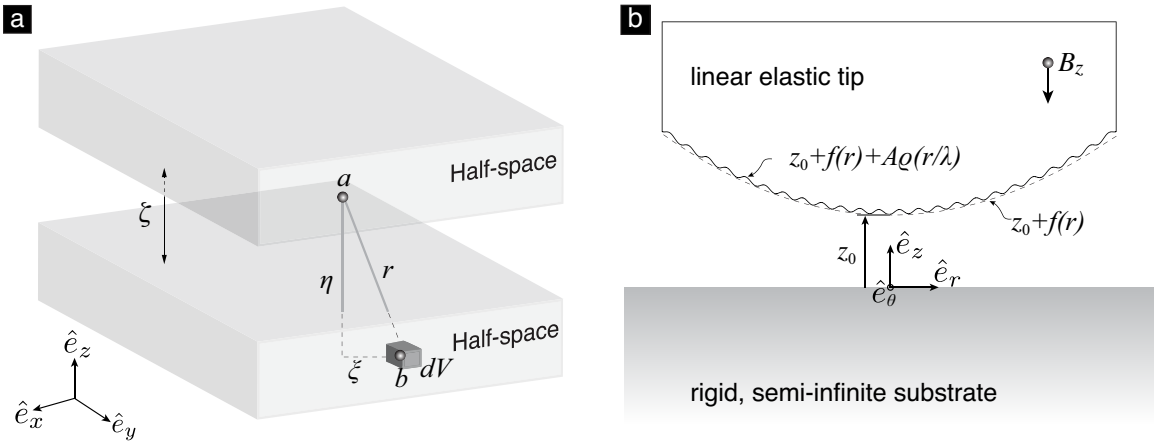

Figure 4.1: (a) The schematic of the interaction between two particles a and b in two parallel half-spaces. The distance between the two half-spaces is ζ. (b) The model setup of FE simulations of the axisymmetric adhesive contact between a linear elastic tip and a rigid, semi-infinite substrate. The elastic tip is subject to the body force $B_z\hat{e}_z$ due to its adhesive interaction with the rigid substrate.

allow us to compare our numerical results to analytical solutions of the adhesive contact problem in [34, 35]. For concreteness, we choose the tip's surface profile to be

$$z_s = z_0 + \frac{r^2}{2R} + A\left[1 - \cos\left(\frac{2\pi r}{\lambda}\right)\right], \tag{4.10}$$

in which the second term on the right side describes a parabola shape with a radius of curvature R at its apex, and the third term is a sinusoidal undulation with an amplitude A and a wave-length λ. To represent the small-scale roughness, we choose the parameters A and λ such that $A, \lambda \ll R$. We note that for the tip's surface given by (4.10) its RMS roughness is equal to its wavy amplitude A.

Material behavior

We use linear elastic and small deformation theory in our adhesive contact problem. Let $\boldsymbol{X} = (r, \theta, z)$ be the position of a material point of the tip in the reference configuration $\mathscr{B}_0$, and $\boldsymbol{u} = (u_r, u_\theta, u_z)$ be the corresponding displacement field. Note that $u_\theta = 0$ for the axisymmetric contact problem. The infinitesimal strain tensor is

$$\boldsymbol{\epsilon} = \frac{1}{2}(\nabla \boldsymbol{u} + (\nabla \boldsymbol{u})^{\mathrm{T}}). \tag{4.11}$$

Since we take the material of the tip to be linear elastic, the Cauchy stress tensor is

$$\boldsymbol{\sigma} = \frac{E}{1+\nu}\left[\boldsymbol{\epsilon} + \frac{\nu}{1-2\nu}\mathrm{Tr}(\boldsymbol{\epsilon})\boldsymbol{I}\right], \tag{4.12}$$

where $\boldsymbol{I}$ is the second-order identity tensor. The equilibrium configuration of the tip is obtained by solving the governing equation

$$\mathrm{Div}(\boldsymbol{\sigma}) + \boldsymbol{B} = 0, \quad \forall \boldsymbol{X} \in \mathscr{B}_0 \tag{4.13}$$

with boundary conditions

$$\boldsymbol{u} = \boldsymbol{u}^* \quad \text{on} \quad \Gamma_u, \tag{4.14a}$$

$$\boldsymbol{\sigma}\boldsymbol{n} = \boldsymbol{t}^* \quad \text{on} \quad \Gamma_s, \tag{4.14b}$$

where $\boldsymbol{B}$ is the body force, $\boldsymbol{n}$ is the surface normal, $\boldsymbol{u}^*$ is the specified displacement on boundary Γ_u, and $\boldsymbol{t}^*$ is the specified traction on boundary Γ_s. Due to the adhesive interaction of the tip with the substrate, the effect body force on the tip is $B_z\hat{\boldsymbol{e}}_z$, where

$$B_z(z,u_z) = \frac{A_H}{\pi\sigma^4}\left[\frac{C_6}{2}\left(\frac{\sigma}{z+u_z}\right)^4 - \frac{C_{12}}{5}\left(\frac{\sigma}{z+u_z}\right)^{10}\right]. \tag{4.15}$$

It can be seen from (4.15) that because of the nonlinear dependence of B_z on the displacement u_z, our adhesive contact problem (4.13)–(4.14) is highly nonlinear in nature.

Finite element simulation

The weak form for the approximation of the problem (4.13)–(4.14) by the FE formulation reads: Find $\boldsymbol{u} \in \mathscr{V}$ such that

$$a(\boldsymbol{u},\boldsymbol{v}) + b(\boldsymbol{u},\boldsymbol{v}) + L(\boldsymbol{v}) = 0, \quad \forall \boldsymbol{v} \in \hat{\mathscr{V}}, \tag{4.16}$$

where the vector-valued trial and test function spaces $\mathscr{V}$ and $\hat{\mathscr{V}}$ are defined as

$$\mathscr{V} = \{\boldsymbol{u} \in H^1(\mathscr{B}_0) : \boldsymbol{u} = \boldsymbol{u}^* \quad \text{on} \quad \Gamma_u\}, \tag{4.17a}$$

$$\hat{\mathscr{V}} = \{\boldsymbol{v} \in H^1(\mathscr{B}_0) : \boldsymbol{v} = \boldsymbol{o} \quad \text{on} \quad \Gamma_u\}, \tag{4.17b}$$

where $H^1(\mathscr{B}_0)$ is the Sobolev space and $\boldsymbol{o}$ is the null vector. The bilinear form a, nonlinear form b, and linear form L in (4.16) are

$$a(\boldsymbol{u},\boldsymbol{v}) = \int_\Omega \boldsymbol{\sigma}(\boldsymbol{u}) : \nabla \boldsymbol{v}\, dV, \quad b(\boldsymbol{u},\boldsymbol{v}) = -\int_\Omega \boldsymbol{B}(\boldsymbol{u}) \cdot \boldsymbol{v}\, dV, \quad L(\boldsymbol{v}) = -\int_{\Gamma_s} \boldsymbol{t}^* \cdot \boldsymbol{v}\, dA. \tag{4.18}$$

In the FE discretization, the mesh of the tip is constructed with 2D linear, triangular elements, and the substrate is modeled as a fixed, rigid half-space. In order to resolve the rapid change of the nonlinear body force field near the substrate, the mesh at the bottom of the tip should be very fine. Therefore, the mesh size in that region should be much smaller than the adhesive length scale ζ_0.

In the simulations, the boundary conditions are that the displacement of the tip's top surface is zero in the $\hat{\boldsymbol{e}}_r$ direction, while the displacement in the $\hat{\boldsymbol{e}}_z$ direction is prescribed and denoted as h_t. The top surface is moved towards the substrate up to a given distance $|h_{\min}|$ in a series of steps with small increments (loading phase), and then it is retracted back to its original position (unloading phase). The indentation depth h is defined as the top surface's displacement h_t plus a constant z_0. At a given indentation depth, we solve the nonlinear adhesive contact problem using the Newton-Raphson method. The initial guess for the first Newton-Raphson iteration in solving the nonlinear equation is taken to be the solution from the last converged loading step. After obtaining the equilibrium configuration, the contact force P is computed by integrating the stress σ_{zz} over the top surface of the tip. We remark that the definition of the contact radius a is not well-defined in the simulations, since the surfaces of the two solids can never make physical contact with each other. This is because the body force would go to infinity as the distance between the two surfaces becomes zero, which is not allowed physically. Therefore, we define an effective contact radius for the simulations as the width within which the distance between the two surfaces is smaller than σ.

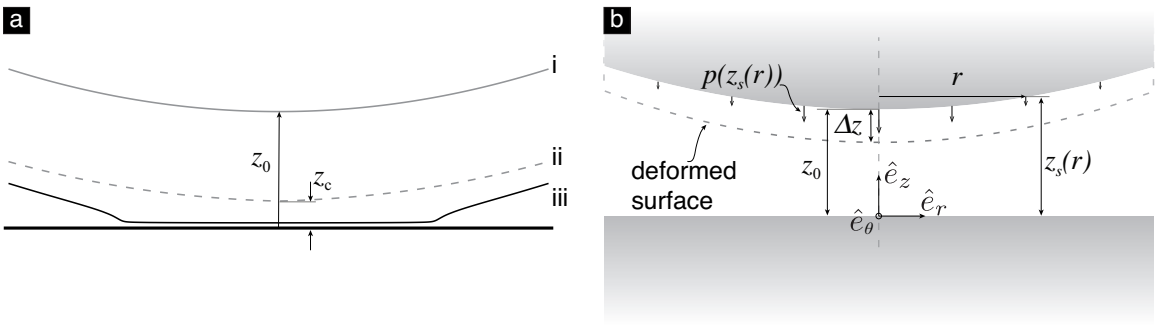

Figure 4.2: (a) The contact configurations of the tip during the contact with the substrate, where *i* is the reference configuration, *ii* and *iii* are the configurations just before and after the pull-in instability, respectively. (b) The surface displacement of the tip induced by the surface traction $p(z_s(r))$ due to its interaction with the substrate.

4.3 Effect of Tabor parameter on contact instabilities

As discussed in §4.1, during the loading phase of adhesive contact the tip is moved close to the substrate (Figure 4.2a.i–ii), and at a critical separation z_c, they would be brought into contact with the occurrence of a pull-in instability (Figure 4.2a.ii–iii). Similarly, during the unloading phase the tip would jump out of contact with the occurrence of a pull-off instability. In the following, we try to estimate the critical separation z_c at which the instability occurs in our adhesive contact model.

Consider that a smooth tip with a radial profile $z_s(r) = z_0 + r^2/(2R)$ is initially separated from the substrate at a distance z_0. With the *Derjaguin approximation*, we find from (4.5)–(4.7b) that the force per unit area on the tip surface (or surface traction) is $p(z_s(r))\hat{e}_z$, where

$$p(z_s(r)) = \frac{8w}{3(C_6C_{12})^{1/3}\zeta_0}\left[C_6\left(\frac{\zeta_0}{z_s(r)}\right)^3 - C_{12}\left(\frac{\zeta_0}{z_s(r)}\right)^9\right]. \tag{4.19}$$

To estimate z_c, we make the following two additional approximations. First, although the radial profile of the deformed tip before the occurrence of pull-in instability (Figure 4.2a.ii) is deviated from a perfect parabola, we still approximate it as a parabolic shape since the deformation is very small before the pull-in instability. Second, the curvature effect is negligible at the vicinity of the tip's bottom such that we can use the *Boussinesq* solution [121, chap. 5] of the surface displacement of a half-space due to a concentrated normal force to compute the surface displacement of the tip at $r = 0$ due to $p(z_s(r))$. Base on these three approximations, for a given separation z_0, we can obtain

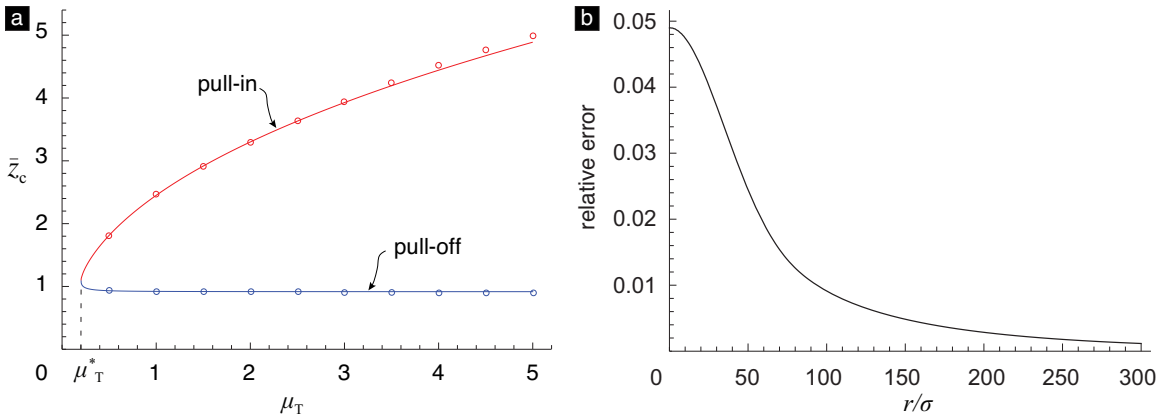

Figure 4.3: (a) The plot of the dimensionless critical separation $\bar{z}_c$ as a function of the Tabor parameter μ_T. The critical separations at the occurrences of pull-in and pull-off instabilities are marked using the red and blue colors, respectively, in which the solid lines denote the solutions of (4.23) and the circles are the results from FE simulations. (b) The relative error between the deformed radial profile of the tip just before the occurrence of an pull-in instability and its parabola approximation for $\mu = 5$.

the surface displacement of the tip at $r = 0$ as

$$\Delta z = \int_0^\infty \frac{(1-\nu^2)}{\pi E r} p(z_s(r)) 2\pi r \, dr. \tag{4.20}$$

After substituting the expression of $z_s(r)$ and (4.19) into (4.20) and evaluating the integration we have

$$\Delta z = \frac{\pi(1-\nu^2)}{\sqrt{2}(C_6 C_{12})^{1/3}} \frac{R^{1/2} w \zeta_0^2}{E z_0^{5/2}} \left[2C_6 - \frac{2145 C_{12}}{2048} \left(\frac{\zeta_0}{z_0} \right)^6 \right]. \tag{4.21}$$

At the critical separation z_c, an infinitesimal change of the displacement of the tip's top surface would result in a finite change of the separation Δz such that the tip and the substrate come into or jump out of contact. And that change of Δz is equal to the negative change of the separation z_0. Therefore, at the instability point, we have the following condition

$$\left. \frac{d\Delta z}{dz_0} \right|_{z_0 = z_c} = -1. \tag{4.22}$$

With the substitution of (4.21) into (4.22), the dimensionless critical separation $\bar{z}_c$ can be obtained from the roots of the following equation

$$\left(c_1 \bar{z}_0^{-7/2} - c_2 \bar{z}_0^{-19/2} \right) \mu_T^{3/2} = 1, \tag{4.23}$$

where $c_1 = 109395\sqrt{2}\pi C_{12}/(24576(C_6C_{12})^{1/3})$, $c_2 = 5\sqrt{2}\pi C_6/(2(C_6C_{12})^{1/3})$, $\bar{z}_0 = z_0/\zeta_0$, and μ_T is the Tabor parameter given in (1.8).

In the current work, unless otherwise stated, we choose $C_6 = 3$ and $C_{12} = 1$. Thus, $c_1 = 23.1$ and $c_2 = 13.7$. From (4.23) we find that there is no real root for $\mu_T < \mu_T^*$, and there exist one real root for $\mu_T = \mu_T^*$ and two real roots for $\mu_T > \mu_T^*$, where $\mu_T^* = 0.20155$. The physical meaning of the solution of (4.23) is as follows. When $\mu_T < \mu_T^*$, there is no occurrence of instability during the loading and unloading phases. This conclusion is consistent with our previous result in [64] that the instabilities would disappear as the adhesive interaction range $\zeta_0 \to \infty$ (or $\mu_T \to 0$). The reason is because the material of the tip is relative stiff such that the elastic strain energy of the tip is dominant over the adhesive interaction energy. Thus, the total energy function is convex and there is an unique energy minimizer. When $\mu_T > \mu_T^*$, the total energy function of the system becomes non-convex and the energy minimizer is not unique. In this case, there exist two critical separations. The larger and smaller ones, respectively, correspond to the distance at which the pull-in and pull-off instabilities occur. Figure 4.3a shows the dependence of $\bar{z}_c$ on μ_T. As can be seen, the two critical separations approach to each other as μ_T decreases, and become equal to 1.08258 for $\mu_T = \mu_T^*$. Moreover, the critical separation at the pull-in instability shows a strong dependence on μ_T while the one at the pull-off instability only changes slightly as μ_T varies. For the pull-in instability, $\bar{z}_c \approx \mu_T$. But for the pull-off instability, $\bar{z}_c \approx 1$. The different dependences of $\bar{z}_c$ for the pull-in and pull-off instabilities on μ_T are not surprising. On the one hand, it can be seen in Figure 4.2a.iii that the deformed tip after the pull-in instability shows a neck-like surface profile in the contact zone. As a rough estimation, the height of the "neck" just after the pull-in instability is approximately equal to the critical separation z_c. According to [17], the Tabor parameter μ_T represents the ratio of the height of the "neck", $(Rw^2/E^{*2})^{1/3}$, to the length scale of adhesive interaction, ζ_0. It implies that the ratio $\bar{z}_c/\mu_T$ at the pull-in instability should be of order unity. On the other hand, once the tip and the substrate are in contact, the separation between them is approximated to be the equilibrium distance ζ_0. Therefore, the critical separation $\bar{z}_c$ at the pull-off instability should be also of order unity and hardly changes with μ_T.

The theoretical analysis of the critical separation at the occurrence of contact instabilities have been verified through the FE simulations, as shown in Figure 4.3a. It can be seen that the analytical

and numerical results show a good agreement with each other. We find that the difference between them increases as μ_T increases. This is because that the approximation of neglecting the curvature effect at the vicinity of the tip's bottom surface is less accurate when the critical separation between the tip and the substrate becomes larger, which is the case for large μ_T. Moreover, we can examine the validation of the approximation that the deformed surface of the tip before the pull-in instability can be treated as a parabola by considering the difference between them. We define the relative error as

$$\mathrm{err}(r) = \frac{|z_0 + r^2/(2R) - z_{\mathrm{FEM}}(r)|}{z_{\mathrm{FEM}}(r)}, \tag{4.24}$$

where $z_{\mathrm{FEM}}(r)$ is the deformed radial profile of the tip before the pull-in instability from the FE simulation. Figure 4.3b shows the plot of the relative error $\mathrm{err}(r)$ at the point just before the occurrence of the pull-in instability for $\mu = 5$. It is found that the maximum error is less than 5% and is at the center of the tip. Therefore, the parabola approximation to the deformed surface of the tip is well justified.

4.4 Comparison with the Maguis-Dugdale theory

In this section, we present the results from the FE simulations of the axisymmetric adhesive contact between a rigid half-space and a paraboloidal tip with a smooth surface (i.e., $A = 0$). As a benchmark, we compare the contact force–indentation depth (P–h) curve and the contact force–contact radius (P–a) curve from the simulations with that predicted by the MD contact theory.

The MD theory describes the axisymmetric contact between two isotropic, homogeneous, linear elastic solids of Young's moduli and Poisson's ratios E_i and ν_i ($i = 1, 2$), respectively, see Figure 3.3a. The adhesive interactions are introduced using the *Dugdale cohesive zone* model [81]. As per this model, a surface material point experiences a traction only if its distance from the other solid in the direction normal to the surface is less than δ_0. Thus δ_0 denotes the range of the surface adhesive interaction, which are thought to arise from van der Waals type interactions between the surfaces. When the normal distance of the material point is less than δ_0 but non-zero then the traction experienced by it is purely tensile and of a fixed magnitude of σ_0, see Figures 3.3b–c. By defining σ_0 to be the maximum surface traction of (4.19), then it is related to w and ζ_0 as $\sigma_0 = w/(c_3\zeta_0)$,

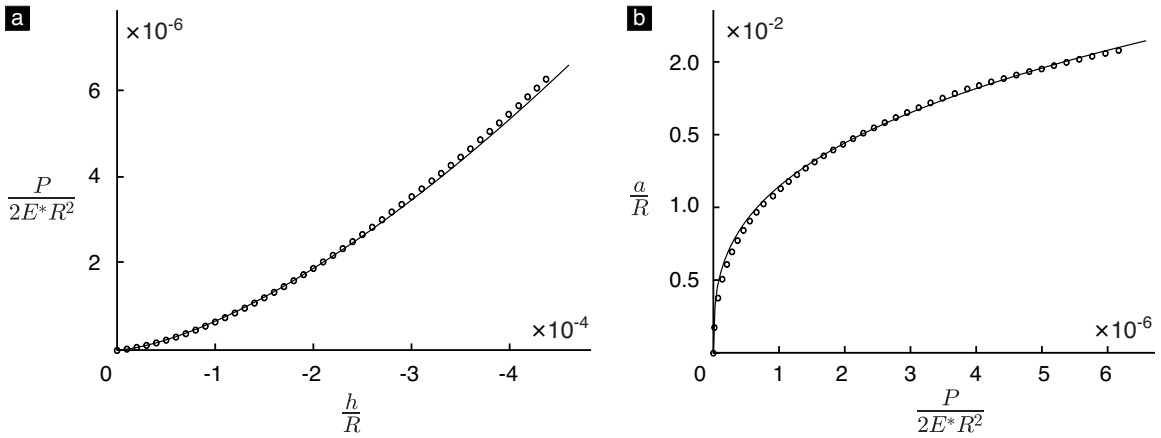

Figure 4.4: (a) The comparison of P–h curves and (b) the comparison of P–a curves computed from the adhesiveless contact simulations (circle) with that from the Hertz contact model (solid line). The theoretical curves are generated with $\ell = \chi = 0$ according to (3.3). In the simulation, we set $A = 0$, $R = 10$ μm, $E = 1.1$ MPa, $\nu = 0.25$. The parameters of the LJ potential are $C_6 = 0$, $C_{12} = 1$, $\sigma = 1$ nm, and $A_{\rm H} = 2 \times 10^{-21}$ J.

where $c_3 = 9\sqrt{3}C_{12}^{5/6}/(16C_6^{7/6})$. And it follows that $\delta_0 = c_3\zeta_0$. The contact process is governed by the two dimensionless parameters

$$\ell = \frac{\pi w}{E^* R} \quad \text{and} \quad \chi = \frac{w}{E^* \delta_0}. \tag{4.25}$$

The classical contact theory can be obtained from the MD theory by considering the different limit cases of ℓ and χ [64]. When $\ell > 0$, the MD theory asymptotes to the JKR and DMT theories, respectively, as $\chi \to \infty$ and 0. The JKR theory applies to compliant materials having a large work of adhesion, while the DMT theory applies to stiff materials having a small work of adhesion. When χ is any finite, fixed value, then as $\ell \to 0$ the MD theory asymptotes to the Hertz theory.

We first consider the adhesiveless elastic contact. This is accomplished in the simulations by only including the repulsive term of the LJ potential and setting $C_6 = 0$ in (4.15) to suppress the attractive interaction. In this case, the MD theory reduces to the Hertz theory. The relations among P, h, and a can be obtained by setting $\chi = 0$ in (3.3). Figure 4.4a and b, respectively, show the P–h and P–a curves that computed from the adhesiveless contact simulations. As a comparison, the analytical results by the Hertz theory are also shown in that figure. It can be seen that the numerical and analytical results nearly coincide, showing a good agreement with each other. Clearly there is no instability during the contact without adhesion.

Next we consider adhesion effect in the contact simulations, in which we choose $C_6 = 3$ in (4.15)

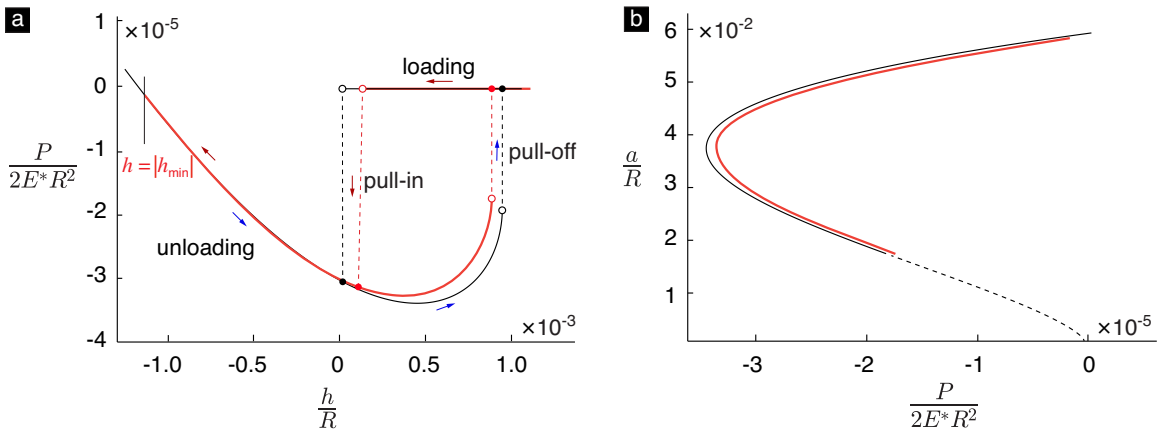

Figure 4.5: (a) The comparisons of P–h curve computed from the simulations (red lines) with that from the MD contact model (black lines). The pull-in and pull-off instabilities during the loading and unloading phase are marked as dashed lines on the curves, respectively. The dot and circle, respectively, indicate the stable and unstable equilibrium configurations. (b) The comparison of P–a curve computed from the simulations (red line) with that from the MD contact model (black lines), where the black dashed segment indicates unstable contact configurations as per the MD theory. The theoretical curves are generated with $\ell = 4.51 \times 10^{-5}$ and $\chi = 0.124$ according to (3.3). In the simulations, we use $A = 0$, $R = 5$ μm, $E = 4.4$ MPa, $\nu = 0.25$. The parameters of the LJ potential are $C_6 = 3$, $C_{12} = 1$, $\sigma = 1$ nm, and $A_{\mathrm{H}} = 2 \times 10^{-21}$ J.

to include the attractive interaction between the two solids. Figure 4.5a shows the P–h curve from a representative adhesive contact simulation with a smooth tip. It can be seen that a pair of pull-in and pull-off instabilities occurs during a contact cycle. The contact force after the pull-in instability is the same for the loading and unloading phases. The curve exhibits a single hysteresis loop induced by the contact instabilities. The resulted hysteretic energy loss is independent of the maximum indentation depth $|h_{\min}|$. This depth independent hysteresis is a consequence of the existence of two equilibrium configurations at the points between the pull-in and pull-off instabilities. One is that the solids are in contact and the other is that the solids are out of contact. The P–h curve as per the MD theory is also shown in Figure 4.5a as a comparison. As can be seen, the two curves match with each other quite well except at the points of pull-in and pull-off instabilities. The instabilities in the simulation occur earlier than the prediction of the MD theory. The P–a curve computed from the simulation also shows a good agreement with that of the MD theory, as shown Figure 4.5b.

The simulation captures some important features of the adhesive contact, such as the neck-like deformed shape of the tip and the stress concentration at the contact edges. For instance, Figure 4.6a shows the contour plot of the displacement u_z in the tip after the pull-in instability from the adhesive contact simulation. As can be seen, the deformed tip surface shows a neck-like radial profile in the contact zone (also see the deformed surface profile shown in Figure 4.2a.iii). Figure 4.6b shows the

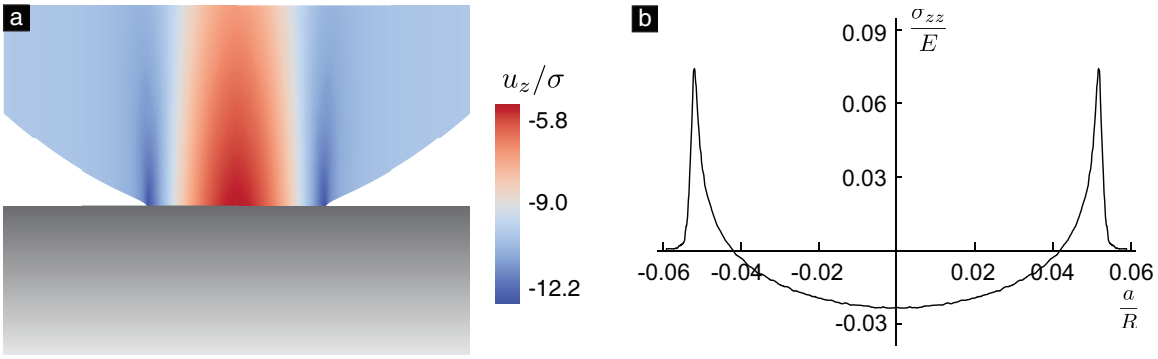

Figure 4.6: (a) The contour plot of the displacement u_z in the tip. (b) The distribution of normal stress σ_{zz} along the contacting interface. Note the stress concentration at the two contact edges. The corresponding *P*–*h* and *P*–*a* curves of the simulation are shown in Figure 4.5.

distribution of normal stress σ_{zz} along the contacting interface. (Since the tip's bottom surface is traction free, we plot the stress distribution at the position where σ_{zz} is maximum in tension). It can be seen that there exists significant stress concentration at two contact edges and the normal stress σ_{zz} is compressive in the center region but tensile near the contact edges due to adhesion, which are the same as in the classical adhesive contact model.

4.5 Depth-dependent hysteresis and surface roughness dependent adhesion

In this section, we study the effects of surface roughness and adhesive interaction range on adhesion by analyzing the results of contact simulations involving a paraboloidal tip with periodic undulations on its surface. The simulations reveal rich and interesting insights into the mechanics of adhesive contact between rough surfaces, which cannot be predicted by the theoretical models [34, 35]. We show that our simulations can capture DDH and that both adhesive force and hysteretic energy loss initially increase then decrease with increasing surface roughness. Furthermore, we discuss the mechanisms of DDH and surface roughness dependent adhesion.

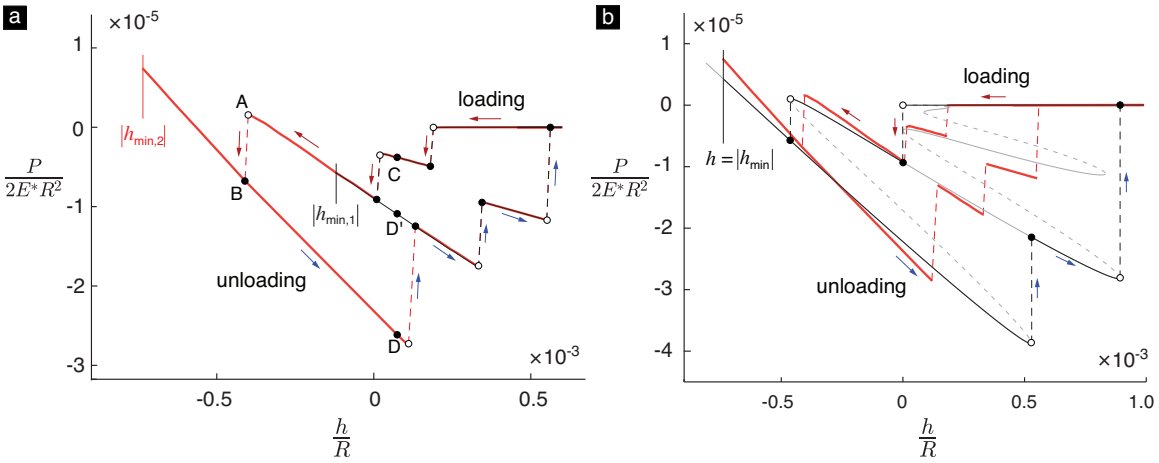

Figure 4.7: (a) The *P*–*h* curves from the contact simulation involving a tip having an moderate amount of roughness. The *P*–*h* curve during a contact cycle with a maximum indentation depth $|h_{\min,1}|/R = 1.5 \times 10^{-4}$ follows the loop marked as thin, black segments, while that with a maximum indentation depth $|h_{\min,2}|/R = 7.0 \times 10^{-4}$ follows the loop marked as thick, red segments. The dashed lines indicate the contact instabilities. The snapshots of equilibrium configurations at various stages of the contact process corresponding to the points marked as (A)–(D) are shown in Figure 4.8. (b) The comparison of *P*–*h* curves from the simulation (red) and the analytical solution of the wavy contact model (gray). The gray solid and dashed segments denote stable and unstable sets of equilibrium configurations, respectively. The measured curves are shown in thin black with solid and dashed segments, where the dashed one represents the contact instability. The parameters used in the simulation are $C_6 = 3$, $C_{12} = 1$, $\sigma = 1$ nm, $A_{\mathrm{H}} = 1.0 \times 10^{-21}$ J, $R = 10$ μm, $A = 1.25$ nm, $\lambda = 0.125$ μm, $E = 2.2$ MPa, and $\nu = 0.25$. The theoretical curves are generated with $\chi = 2.26 \times 10^{-5}$, $A/R = 1.25 \times 10^{-4}$, and $\lambda/R = 1.25 \times 10^{-2}$ according to (4.26). The dots and circles, respectively, mark stable and unstable configurations on the *P*–*h* curve in (a) and (b). For clarity, we do not mark the stable and unstable states for the simulation curves in (b).

4.5.1 Depth-dependent hysteresis

Figure 4.7 shows the representative *P*-*h* curves from a simulation having a moderate magnitude of roughness, $A/\lambda = 10^{-2}$, on the tip. As can be seen, there are multiple pull-in and pull-off instabilities (shown as dashed lines) during a contact cycle on the *P*-*h* curve. Each instability results in a sudden change in the contact force value. And after each instability the contact area grows or recedes across the surface asperities—the surface peaks on the tip's bottom surface—by a finite amount. For example, a pair of snapshots of the contact configuration just before and after the occurrence of an pull-in instability, which is marked as from (A) to (B) on the *P*-*h* curve in Figure 4.7a, is shown in Figure 4.8a and b, respectively. As can be seen, the contact area grows with a finite amount immediately after the pull-in instability. The pull-off instability leads the contact area to recede in a similar fashion but in the opposite direction.

We remark that the unstable contact area growth and recession across surface asperities are in some ways similar to the classical pull-in and pull-off instabilities as in the JKR model. However,

there are two important differences between them. First, the observed contact instabilities in simulations occur at the length scale of surface asperities, while the classical contact instabilities occur at a much larger length scale. As per the JKR theory, the radius of the contact area formed after the pull-in instability is $(2\pi Rw/E^*)^{1/3}$, where R is the radius of curvature of a smooth tip at its apex. For example, see the contact area formed shown in Figure 4.2a.iii. In contrast, the radius of the contact area formed after the pull-in instability across a surface asperity is on the order of $(2\pi R_a w/E^*)^{1/3}$ by approximating the surface asperity as a sphere, where R_a is the radius of the sphere. According to (4.10), we have $R_a = \lambda^2/(4\pi^2 A)$. Thus, the ratio of the contact radii for the surface asperity level contact instability and the classical one is $R_a/R = \lambda^2/(4\pi^2 AR)$, which is 0.0317 for the simulation shown in Figures 4.7 and 4.8. Second, as per the classical contact theories, there is always only a single pair of the pull-in and pull-off instabilities in any contact cycle. Whereas the surface asperity level contact instabilities can be multiple, and the number of such instabilities depends on the maximum indentation depth $|h_{\min}|$. For instance, the number of instabilities for a small $|h_{\min}|$ is less than that for a large $|h_{\min}|$, see Figure 4.7a. In fact, this is the precise mechanism through which the surface asperity level instabilities give rise to DDH. The total hysteretic energy loss in a contact cycle is the cumulative energy lost during all the contact instabilities. Therefore, the energy loss of DDH increases with $|h_{\min}|$ since more surface asperity level contact instabilities occur as $|h_{\min}|$ increases. Our simulations demonstrate that adhesion and surface roughness alone can induce DDH through a series of surface asperity level contact instabilities.

In Figure 4.7a, the *P-h* curves are different for the loading and the unloading phases. The contact forces are different because there exist many metastable states for the contact configuration at a given indentation depth due to the roughness and adhesion of the surface. In Figure 4.8c and d we show a pair of such metastable states, which are correspondingly marked as (C) and (D) on the *P-h* curves in Figure 4.7a. These metastable states have the same indentation depth but different contact regions. The system visits different metastable states during the loading and unloading phases. Consequently, we observe different contact forces at the same indentation depth during a contact cycle. Moreover, the states that are visited depend on the history of the contact process and the loading conditions. For instance, at a given indentation depth, the system visits the metastable state (D') during the unloading phase for the contact cycle with a maximum indentation depth

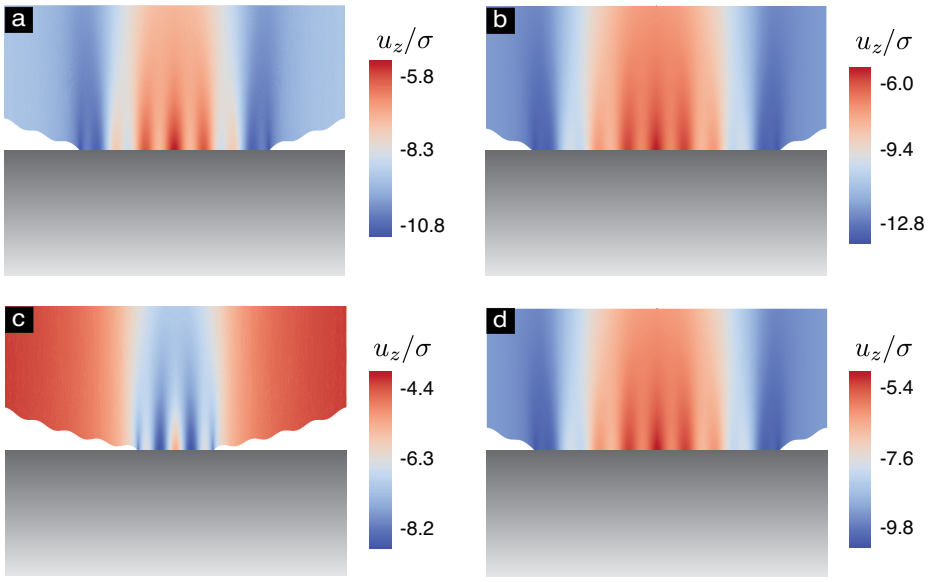

Figure 4.8: The equilibrium configurations at the points (A)–(D) marked on the P–h curves shown in Figure 4.7a with one-to-one correspondence. The snapshots (a) and (b) show the configurations of the tip just before and after the occurrence of an pull-in instability at $h/R = -4 \times 10^{-4}$. The snapshots (c) and (d) are two metastable configurations at the same indentation depth $h/R = 6 \times 10^{-5}$. The state (c) is visited during the loading phase and (d) during the unloading phase. Note the abrupt change in contact area from (a) to (b) due to the pull-in instability and the difference in the contact area between (c) and (d) at the same indentation depth.

$|h_{\min,1}|$, while it visits the metastable state (D) during the unloading phase for the contact cycle with a maximum indentation depth $|h_{\min,2}|$, see Figure 4.7a. The contact forces for these two metastable states are different. As a result, the hysteretic energy losses are also different for the two contact cycles with different maximum indentation depths—comparing the areas enclosed by the black and red curves in Figure 4.7a, which shows DDH.

Kesari *et al.* [35] and Guduru [34] have theoretically studied the axisymmetric, adhesive elastic contact problem between a half-space and a wavy tip—that has a moderate undulation on its bottom surface. In their theories, the adhesion was modeled by including an adhesion energy term for the contacting interface into the system's total potential energy. Thus, the adhesive interaction range as per this method is infinitely short. Furthermore, it was assumed in their models that the contact region remains simply connected during contact—the contact area always grows (resp. recedes) during the loading (resp. unloading) phase at the contact edge, such that the contact problem is theoretically attackable. According to [34, 35], the non-dimensional contact force $\bar{P}$ and indentation

depth $\bar{h}$ are given as

$$\bar{P} = \frac{2\bar{a}^3}{3} - \sqrt{2\chi\bar{a}^2} + \frac{\pi^2\bar{A}\bar{a}^2}{\bar{\lambda}} H_0\left(\frac{2\pi\bar{a}}{\bar{\lambda}}\right) - \frac{\pi\bar{A}\bar{a}}{2} H_1\left(\frac{2\pi\bar{a}}{\bar{\lambda}}\right), \tag{4.26a}$$

$$\bar{h} = \bar{a}^2 - \sqrt{2\chi\bar{a}} + \frac{\pi^2\bar{A}\bar{a}}{\bar{\lambda}} H_0\left(\frac{2\pi\bar{a}}{\bar{\lambda}}\right), \tag{4.26b}$$

where the definitions of $\bar{P}$, $\bar{a}$, $\bar{h}$, and χ are the same as given in §3.2.1, $\bar{A} = A/R$, $\bar{\lambda} = \lambda/R$, H_0 and H_1 denote Struve functions of zeroth and first oder, respectively.

The comparison of *P-h* curves of the adhesive contact with rough surface from the simulation and analytical solution is shown in Figure 4.7b. It can be seen that the simulation captures the multiple pull-in and pull-off instabilities as predicted by the theory. By closely examining the contact configurations during a contact cycle, we find that, for the simulation shown in Figure 4.7b, the contact area always grows and recedes at the contact edge during the loading and unloading phases, respectively. For example, see the contact area changes shown Figure 4.8. This observation is consistent with the assumption of contact area change made in [34, 35]. Nevertheless, we note that the adhesive force in the simulation is smaller than that predicted by the theory, and the contact instabilities occur earlier in the simulation. We believe these differences might result from the different approaches of modeling adhesion employed in them. That is, the adhesion is modeled based on the intermolecular potential whose adhesive interaction range is finite in the simulation, while the adhesion is modeled as an interfacial energy and the adhesive interaction range is infinitely short in the theoretical model.

4.5.2 Effects of surface roughness and adhesive interaction range on adhesion

We first investigated the effect of surface roughness on adhesion by tuning the wavy amplitude A in simulations. The adhesive force P_{adh} and hysteretic energy loss $\mathscr{H}$ are used as two critical metrics to quantify the effective adhesion, and are referred to as adhesive strength and toughness of the contacting interface, respectively. Figure 4.9a shows the *P–h* curves from three different adhesive contact simulations with $|h_{\min}|/R = 6 \times 10^{-4}$. In those simulations, all the parameters remain unchanged except for the wavy amplitude (or equivalently, the RMS roughness). It can be seen that surface roughness has an important effect on adhesive contact. As the roughness increases

(A/λ changes from 0 to 0.0075), the dimensionless adhesive force, $P_{\text{adh}}/(2E^*R^2)$, increases from 1.54×10^{-5} to 3.06×10^{-5}. However, for a larger roughness ($A/\lambda=0.02$), it drops to 1.93×10^{-5}. The dimensionless hysteretic energy loss, $\mathscr{H}/(2E^*R^3)$, changes from 2.93×10^{-9} to 12.43×10^{-9} to 7.7×10^{-9} as A/λ increases. Moreover, we performed simulations by varying the adhesive interaction range σ. The results are shown in Figure 4.9b. For all the simulations, we found that the effect of surface roughness on adhesion is consistent, and independent with σ. That is, P_{adh} and $\mathscr{H}$ can be increased by introducing a small roughness, but eventually they get reduced as the roughness becomes larger, which is reported in many adhesive contact experiments. We will discuss the rough effect on adhesion in detail later in this section.

The effect of adhesive interaction range σ on adhesion is more interesting. Figure 4.9b shows the plots of P_{adh} and $\mathscr{H}$ as a function σ. From (1.8) and (4.6) we know that the Tabor parameter μ_{T} decreases with σ. And we have shown in §4.3 that contact instability would disappear when μ_{T} is smaller than a critical value. Therefore, for the case of smooth surface (i.e., $A=0$), P_{adh} and $\mathscr{H}$ decrease monotonically and eventually disappear with increasing σ, see the plots with $A/\lambda=0$ in Figure 4.9b. For the case of rough surfaces (i.e., $A/\lambda=0.0075$ and 0.02), it is also observed that P_{adh} and $\mathscr{H}$ decrease when σ is in the large regime. The decreasing trend of P_{adh} and $\mathscr{H}$ with σ for both smooth and rough surfaces is consistent with our theoretical result in [64]. However, for the case of rough surface, our simulations additionally show that P_{adh} and $\mathscr{H}$ can be increased for small values of σ and achieve their maximum values before they drop when σ becomes larger, see the plots with $A/\lambda=0.0075$ and $A/\lambda=0.02$ in Figure 4.9b. Yet we did not find any experimental results or theoretical models of rough surface contact that can capture this initial trend of enhanced adhesion with increasing adhesive interaction range.

We identify two important non-dimensional parameters

$$\alpha=\frac{A^2}{\lambda(w/E^*)}\quad\text{and}\quad\beta=\frac{\sigma^2}{\lambda(w/E^*)},\tag{4.27}$$

where α and β represent the ratio of surface roughness and adhesive interaction range to the intrinsic adhesion length scale w/E^* of solid, respectively. We performed a systematic study of the effect of surface roughness and adhesive interaction range on adhesion by considering a wide range of α and

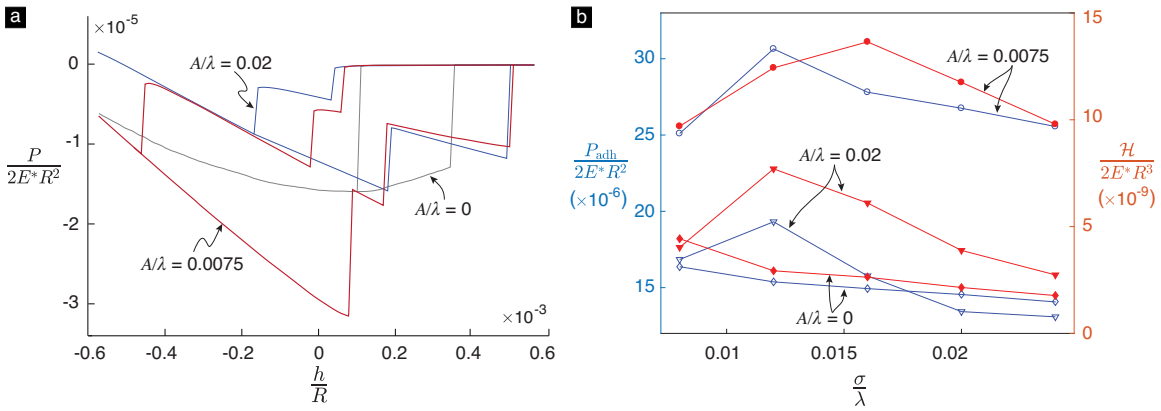

Figure 4.9: (a) The P–h curves of the contact simulations with three different wavy amplitudes. All the parameters are the same as those in Figure 4.7a except that $\sigma = 1.5$ nm and A changes from 0 to 0.9375 nm to 2.5 nm. (b) The plots of adhesive force P_{adh} and hysteretic energy loss $\mathscr{H}$ as a function of adhesive interaction range σ for different roughnesses.

β values in the simulations. The results are shown in Figure 4.10a and b where the 3D plots of P_{adh} and $\mathscr{H}$ as a function of α and β are presented, respectively. The biphasic dependence of P_{adh} and $\mathscr{H}$ on surface roughness and adhesive interaction range can be seen clearly. It implies that there exists an optimal combination of α and β such that the contacting interface achieves the maximum adhesive strength and toughness. The conditions corresponding to maximum adhesive strength and toughness are the same for the case shown in Figure 4.10, which are at $(\alpha, \beta) = (0.1741, 0.4457)$.

It is often believed that adhesion is typically reduced when the surface is rough, as detailed in §4.1. However, our simulations reveal that adhesion can be enhanced for small roughnesses before it gets reduced by the large roughness. The underlying mechanism of the surface roughness dependent adhesion can be inferred by examining the topology of the contact region. As an example, we show the contact configurations corresponding to the adhesive force P_{adh} during a contact cycle for four different roughness values in Figure 4.11. The corresponding $P_{\text{adh}}/(2E^*R^2)$ is also given. As A/λ changes from 0 to 0.03, P_{adh} first increases then decreases, and the maximum P_{adh} is achieved at $A/\lambda = 0.01$. For $A/\lambda \leq 0.01$, the contact region is simply connected and the real contact area increases with roughness. However, as $A/\lambda > 0.01$, the contact region becomes multiply connected and the real contact area begins to decrease. Therefore, the change in the trend of roughness effect on adhesion correlates with the transition of contact region from being simply connected to multiply connected. The maximum adhesive strength and toughness occur just before the contact region stops being simply connected. Meanwhile, the corresponding real contact area first increases then decreases with roughness, see Figure 4.11. Hence, our simulations provide a critical evidence for the

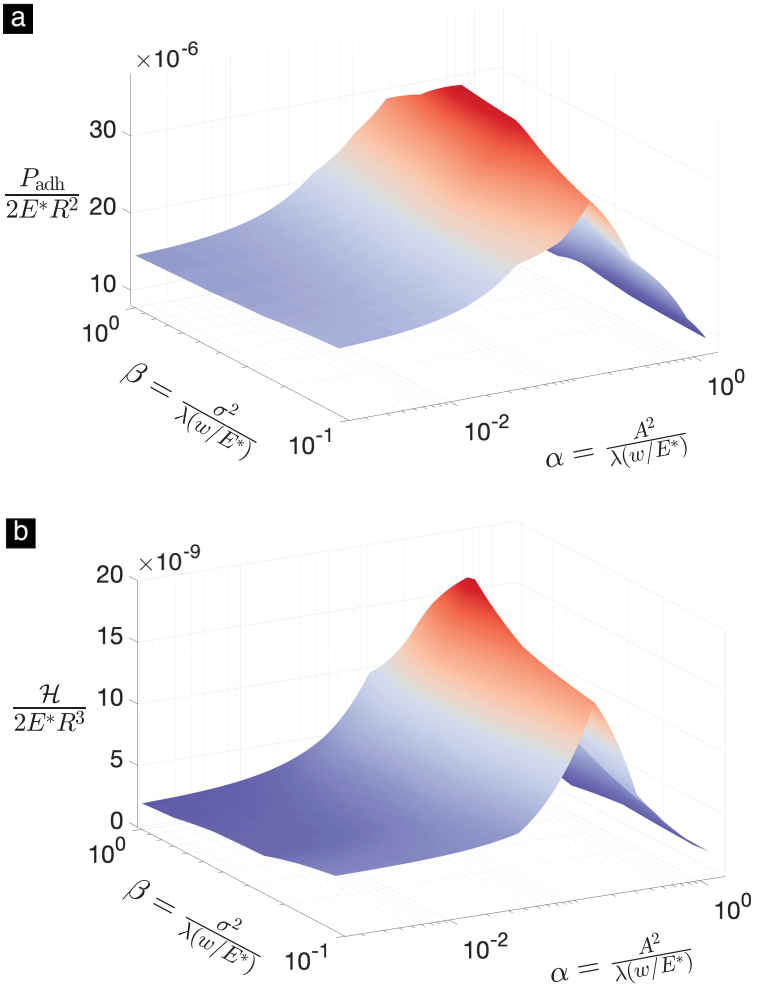

Figure 4.10: (a) The plot of adhesive force P_{adh} and (b) the plot of hysteretic energy loss $\mathscr{H}$ as a function of $\alpha = A^2/(\lambda w/E^*)$ and $\beta = \sigma^2/(\lambda w/E^*)$. The results are from contact simulations carried out with $|h_{\text{min}}|/R = 6 \times 10^{-4}$. All the parameters in the simulations are the same as those in Figure 4.7a except that A and σ are varied.

conjecture that the enhanced adhesion by small roughness is resulted from the increase of the real contact area. In addition to the change in real contact area, we remark that the enhanced adhesion is also related to the contact instabilities. As can be seen in Figure 4.9a, the multiple asperity level contact instabilities cause additional energy dissipation during contact as discussed in §4.5.1, giving rise to an enhanced effective adhesion.

When the tip's surface is not smooth but shows a certain roughness, it has to be elastically deformed to form an intimate contact with the substrate. This leads to a competition between the elastic strain energy penalty with the interfacial energy gained by forming the contacting interface due to adhesion. For small surface roughness, the elastic penalty is relatively small compared with the gained interfacial energy if a large contact area forms. However, as surface roughness increases,

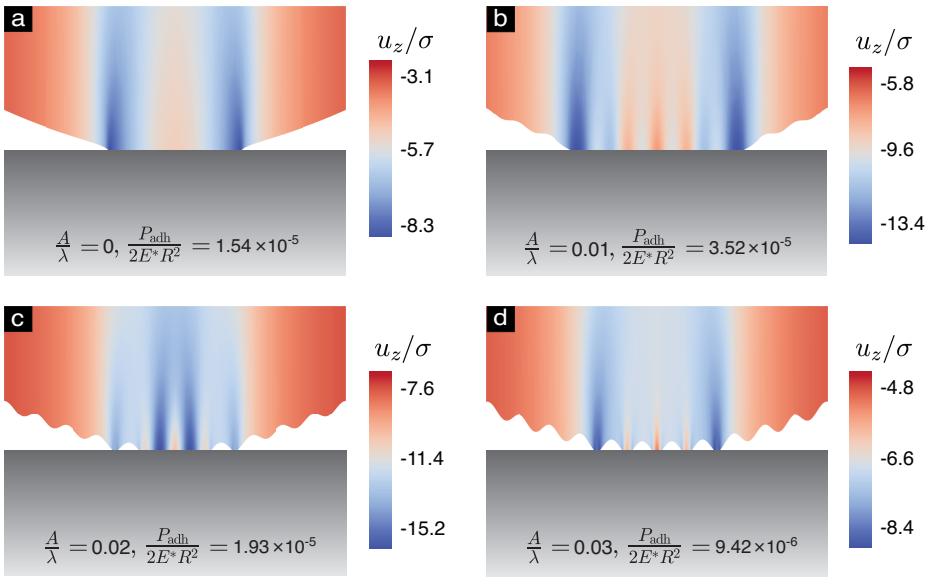

Figure 4.11: Effect of surface roughness on the topology of the contact region. (a–d) show the snapshots of contact configurations corresponding to the adhesive force P_{adh} during contact for different roughnesses marked along with the configurations. All the parameters in the simulations are the same as those in Figure 4.7a except that $\sigma = 1.5$ nm and in (a) $A = 0$, (b) $A = 1.25$ nm, (c) $A = 2.5$ nm, and (d) $A = 3.75$ nm.

a large amount of elastic energy has to be spent to create a full contact between the tip and the substrate, which is not energetically favorable for large roughness. Since it was assumed that the contact region is always simply connected during contact in the theoretical models [34, 35], they predicted the increased adhesion by roughness but cannot capture the decreasing effect of roughness on adhesion. The contact configuration of Figure 4.11d indicates that the mechanics of contact at large surface roughness should be better described by the asperity-type contact models.

4.6 Discussions and conclusions

It is noted that there is a significant body of literature discussing the *contact splitting* for enhanced adhesion by the fibrillar structures observed in many biological systems such as the gecko and spider's feet. Artz *et al.* [8] put forward contact splitting principle to illustrate the underlying mechanism of adhesion of fibrillar structures. They argued that, when a contact with a tip radius R branches into n sub-contacts, each has a sub-tip radius $R/\sqrt{n}$ as per self-similarity or R as per curvature invariance, the adhesive force would increase by a factor of $\sqrt{n}$ and n, respectively. Gao and Yao [122] showed that at the pull-off moment, a theoretical adhesive stress uniformly distributed

across the contact interface can be achieved with an optimal tip shape of the fiber when its diameter is down to nanoscale size. Here, our simulations of rough surface contact provide insights about another yet important effect of contact splitting—crack arrest and reinitiation. Figure 4.12a–c show the detachment of the tip with a small roughness from the substrate with two consecutive pull-off instabilities, while Figure 4.12d–f show the detachment with two consecutive pull-off instabilities for a large roughness. In the former case, it is found that the detachment of an asperity would trigger its neighboring asperity to immediately detach from the substrate, e.g., see Figure 4.12a–b and b–c. The reason behind this observation is that once an asperity detaches the strain energy released is immediately transfered to its adjacent asperity due to their strong coupling interaction, which favors the detachment process. However, for the large roughness case the mechanics of contact becomes asperity type. And the coupling interaction between asperities becomes weaker. The strain energy stored in the detached asperity is not enough to drive the next asperity to detach. Thus, we observe a one-by-one fashion of the detachment process in Figure 4.12d–f. In the fracture mechanics point of view, the interfacial crack gets arrested after propagation crossing an asperity and it needs more energy to reinitiate the crack. Similar argument can be applied to the adhesion of fibrillar structures, where the pull-off of a single fibril is unable to trigger the next fibril to detach from the surface. The additional energy needed for crack reinitiation of each fibril manifests as a better adhesion effect of the fibril structure.

In this work, we idealized the roughness to be a periodic undulation on the surface. Despite of the fact that most of the real surfaces in experiments are randomly rough, the simplified rough surface model employed in our simulations allows us to uncover the fundamental mechanisms of DDH and surface roughness dependent adhesion that are observed in many adhesive contact experiments. Our simulations provide direct evidences for the operation of the small-scale asperity level contact instability mechanism in DDH. The results also suggest that a full contact between rough surfaces is energetically favorable as long as the roughness is small enough, hence an enhanced adhesion can be obtained due to the increased real contact area.

We note that for the experiment that shows DDH and surface roughness enhanced adhesion, it often involves soft materials (< 1 MPa) with viscoelastic effect, such as soft rubber and high molecular weight PDMS. The viscoelastic property of the soft material enables it to creep and so confirm

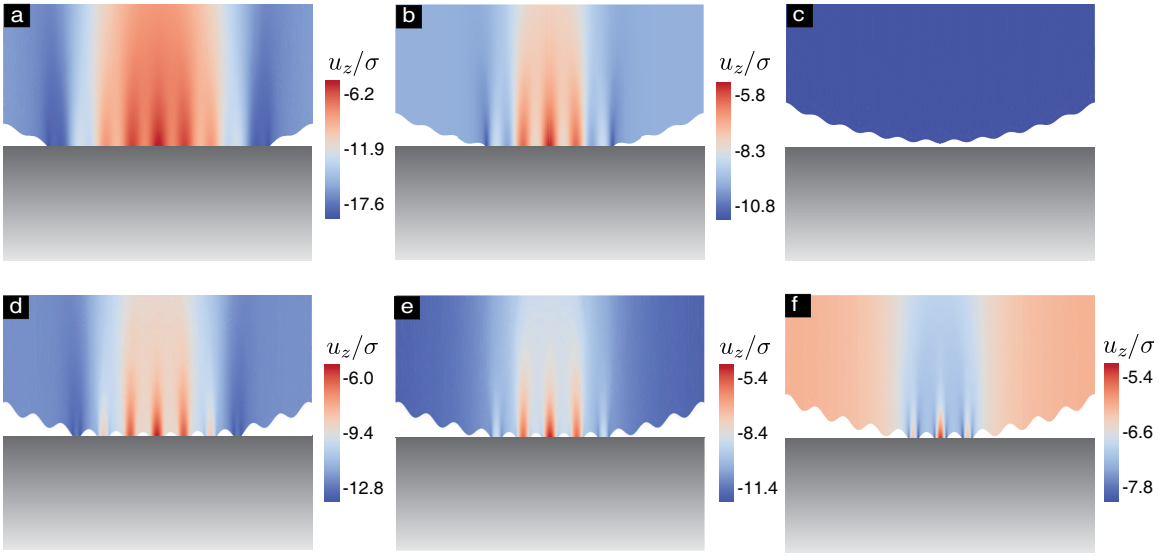

Figure 4.12: (a-b) and (b-c) show the contact configurations at two consecutive pull-off instabilities during the unloading phase for a wavy tip with $A = 1.25$ nm. (d-e) and (e-f) show the contact configurations at two consecutive pull-off instabilities during the unloading phase for a wavy tip with $A = 3.125$ nm. The parameters used in the simulations are the same as in Figure 4.9a.

to the rough surface, which results in a greater real contact area than the apparent one. Moreover, the stress relaxation around the contact points reduces the strain energy that will be released to assist in separation of surfaces during the unloading phase. However, the material's viscoelasticity is not considered in our contact model. We show that the effective adhesion is resulted from elastic contact instabilities that cause energy dissipation during contact. Although it has been long conjectured in previous studies that the increased adhesion by roughness is related to the increased real contact area, however, the role of small-scale contact instability is overlooked in them. Our results suggest that DDH and enhanced adhesion emerging at the large scale are the smeared out effect of small-scale elastic contact instabilities that take place at the asperity level due to adhesion and surface roughness.

Chapter 5

Multiple spring model for adhesion of biological fibriallar structures

5.1 Introduction

In contrast to the contact between smooth surfaces, it has been experimentally shown that the real contact area is much less than the apparent contact area for the adhesive elastic contact between rough surfaces [123, 124], resulting a weak adhesion. Therefore, it is necessary to increase the real contact area to enhance adhesion between rough surfaces and complete contact would be the most desirable for adhesion. In 1939, Westergaard [125] showed that a remote compressive pressure $p^* > \pi E^* \Delta/\lambda$ is needed to be applied to achieve a complete adhesiveless contact between a wavy rigid surface and an elastic half-space, where Δ and λ are the amplitude and wavelength of the wavy surface, respectively, E^* is the plane Young's modulus of the half-space. Based on the Westergaard solution, Johnson [90] showed that an elastic solid with wavy surface would spontaneously adhere to a flat surface with complete contact due to adhesion alone without applying remote force as long as the non-dimensional parameter $\sqrt{2\lambda w/(\pi^2 \Delta^2 E^*)} \geq 0.57$, where w is the work of adhesion. Taking $w = 50$ mJ/m^2, $E^* = 2$ GPa for a typical biological material composed of relative stiff components such as keratin [126], it requires that $\Delta < 40$ nm of a wavy surface with $\lambda = 100$ μm for the biological material to achieve a spontaneously complete contact with the wavy surface.

However, for most real rough surfaces, the roughness is much larger than 40 nm [127], which makes it difficult for the relatively stiff biological material to form intimate contact with the rough surface to achieve strong adhesion.

Many animals such insects, spiders, and lizards have developed an alternate strategy—fibrillar structures on their attachment pads—to achieve remarkable adhesion and easy release for locomotion on natural rough surfaces [8, 11, 12]. The biological fibrillar structures allow individual fibril to deform more easily to conform with the rough surface, which can give rise to larger contact area and strong adhesion for relative stiff biological materials, such as β-keratin protein in gecko's attachment pad that has an elastic Young's modulus of ≈ 2 GPa [126, 128]. Inspired by the biological fibrillar structures, considerable efforts have been made to create synthetic adhesive structures with pillar arrays of different terminal geometries through a variety of fabrication methodologies [114].

Analytical models based on adhesive elastic contact mechanics have been proposed to understand adhesion properties of fibrillar structures [8–10, 113, 129, 130]. Among those models, the critical mechanism is based on the principle of contact splitting—by which splitting contact into finer subcontacts—put forward by Arzt *et al.* [8]. According to Arzt *et al.*'s contact splitting principle, the adhesion force can be increased by $\sqrt{n}$ times through splitting up the contact with radius R into n subcontacts with radius $R/\sqrt{n}$ (self-similarity), or by n times through splitting up contact with fixed radius (curvature invariance). Arzt *et al.*'s contact splitting principle is based on the JKR theory in which the adhesive interaction range is infinitesimally short; whereas the adhesive interaction of biological fibrillar structure originates from the finite-ranged van der Waals forces [131]. Moreover, Arzt *et al.*'s contact splitting principle only applies to flat surface. Yet, there is a lack of model to understand adhesion of fibrillar structures on rough surfaces.

The aim of this work is to investigate the adhesion properties of fibrillar structures on rough surfaces. We consider gecko's adhesive pad as a paradigm and propose a multiple spring model for adhesion of biological fibrillar structures. In §5.2, we briefly summarize the hierarchical structures of a gecko's adhesive system. In §5.3, we model the adhesive interaction of the fibril structure using the LJ potential. Then in §5.4, we study the adhesion of individual fibril using a single spring model. In §5.5, we investigate the adhesion of fibrillar structure based on the multiple spring model and examine the effects of fibril stiffness and surface roughness and correlation length of rough

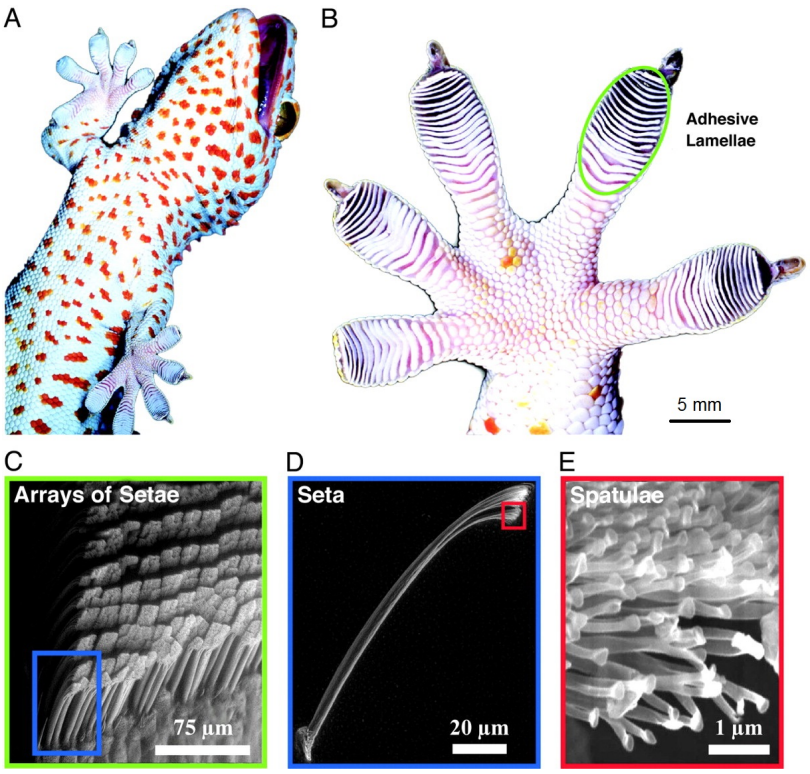

Figure 5.1: Hierarchical structure of the gecko adhesive system. (a) A gecko climbing on glass. (b) The sticky lamellae on gecko's toes. (c–e) Scanning electron microscope images of arrays of setae, a single seta, and arrays of branches and spatulae, respectively. Reproduced from Hansen *et al.* [135].

surface on adhesion. Finally, we conclude this work by discussing the principle of contact splitting for adhesion of fibril structures in §5.6.

5.2 Hierarchical structures of a gecko's toe

The structural hierarchy of the gecko adhesive system is shown in Figure 5.1 and its structural and mechanical properties are summarized in Table 5.1 [108, 126, 128, 131–136]. The attachment pad (toe) of a gecko's foot consist of an intricate hierarchical structure beginning with $\approx$ 20 rows of sticky lamellae which are 1–5 mm in length. Each lamella contains many setal arrays consisting of hundred of thousands of setae. It is estimated that there are $14,400$ setae per mm^2, or $200,000$ setae per toe. These setae are typically 30–130 μm in length and 5–10 μm in diameter. Each seta further splits into 100-1000 branches with terminal spatulae at the end. The branches have a length of 1–10 μm and a diameter of 0.1 μm. The spatula has a typical size of 0.2–0.5 μm in diameter and 5–10 nm in thickness.

5.3 Adhesion based on the Lennard-Jones potential

Autumn *et al.* [131] discovered that van der Waals forces are the primary mechanism of adhesion in gecko's setae. The Lennard-Jones (LJ) potential is often used to describe the van der Waals interactions between solids and to study adhesion of fibrillar structures [45], which has the form

$$V_{\mathrm{LJ}}(r) = 4\varepsilon\left[-\left(\frac{\sigma}{r}\right)^6 + \left(\frac{\sigma}{r}\right)^{12}\right], \tag{5.1}$$

where ε is the depth of the LJ potential well, σ is the distance at which the potential is zero, r is the distance between the molecules. The potential reaches its minimum $-\varepsilon$ at $2^{1/6}\sigma \approx 1.122\sigma$.

The interaction energy and force between a molecule and an half-space which interact via the LJ potential at a distance ζ are

$$\mathscr{U}(\zeta) = 4\pi\rho_s\varepsilon\sigma^3\left[-\frac{1}{6}\left(\frac{\sigma}{\zeta}\right)^3 + \frac{1}{45}\left(\frac{\sigma}{\zeta}\right)^9\right] \tag{5.2}$$

and

$$F_{\mathrm{mh}}(\zeta) = 4\pi\rho_s\varepsilon\sigma^2\left[\frac{1}{2}\left(\frac{\sigma}{\zeta}\right)^4 - \frac{1}{5}\left(\frac{\sigma}{\zeta}\right)^{10}\right], \tag{5.3}$$

respectively, where ρ_s is the molecular density of the half-space. The energy and force per unit area between two half-spaces separated at a distance d are

$$\mathscr{E}_{\mathrm{hh}}(d) = 4\pi\rho_s\rho_t\varepsilon\sigma^4\left[-\frac{1}{12}\left(\frac{\sigma}{d}\right)^2 + \frac{1}{360}\left(\frac{\sigma}{d}\right)^8\right] \tag{5.4}$$

and

$$F_{\mathrm{hh}}(d) = 4\pi\rho_s\rho_t\varepsilon\sigma^3\left[\frac{1}{6}\left(\frac{\sigma}{d}\right)^3 - \frac{1}{45}\left(\frac{\sigma}{d}\right)^9\right], \tag{5.5}$$

Table 5.1: Hierarchical structure of gecko's toe and its structural and mechanical properties.

	Size		Density	Adhesion force
	length	diameter		
lamella	1–5 mm	-	20 rows per toe	-
seta	30–130 μm	5–10 μm	14,400 per mm^2	20–40 μN
branch	1–10 μm	0.1 μm	100–1000 per seta	-
spatula	5–10-nm thick	0.2–0.5 μm	1 per branch	$\approx$ 10 nN

respectively, where ρ_t is the molecular density of the other half-space. The equilibrium distance between two half-spaces is found to be $Z_0 = (2/15)^{1/6}\sigma$ by setting $F_{\mathrm{hh}}(Z_0) = 0$. In terms of the *Hamaker* constant $A = 4\pi^2\rho_s\rho_t\varepsilon\sigma^6$, (5.4) and (5.5), respectively, become

$$\mathscr{E}_{\mathrm{hh}}(d) = \frac{A}{12\pi Z_0^2}\left[-\left(\frac{Z_0}{d}\right)^2 + \frac{1}{4}\left(\frac{Z_0}{d}\right)^8\right] \tag{5.6}$$

and

$$F_{\mathrm{hh}}(d) = \frac{A}{6\pi Z_0^3}\left[\left(\frac{Z_0}{d}\right)^3 - \left(\frac{Z_0}{d}\right)^9\right]. \tag{5.7}$$

The *Dupré* work of adhesion for a pair of solids is defined as the work done per unit area to separate a pair of surface from their equilibrium separation to infinity. Thus, according to (5.6) we obtain the *Dupré* work of adhesion as

$$w = \frac{A}{16\pi Z_0^2}. \tag{5.8}$$

Estimate the adhesive force of a single spatula Taking the typical value of the *Hamaker* constant of β-keratin to $A = 10^{-19}\,\mathrm{J}$, the equilibrium distance $Z_0 = 0.3\,\mathrm{nm}$ [133], we obtain the work of adhesion as $w = 22.1\,\mathrm{mJ/m^2}$. By assuming the spatula to be a spherical tip with radius of $R = 100\,\mathrm{nm}$, according to the JKR model, we obtain the adhesive force of a single spatula to be $3/2\pi wR = 10.4\,\mathrm{nN}$, which is very consistent with the experimental measured value [136].

5.4 Single spring model for adhesion of individual fibril

In this section, we derive the effective stiffness of the gecko's seta and investigate the individual fibril adhesion using the single spring model based on the LJ potential. We motivate our analysis by noting that gecko's toes make contact with substrate at a relative small angle between the seta and the substrate surface for attachment while it peels off at a relative large angle for detachment [128, 137]. We show the tilted angle of setal arrays plays an important role in the adhesion of the fibrillar structure, since it affects the stiffness of the setae and the stiffness has a significant effect on adhesion.

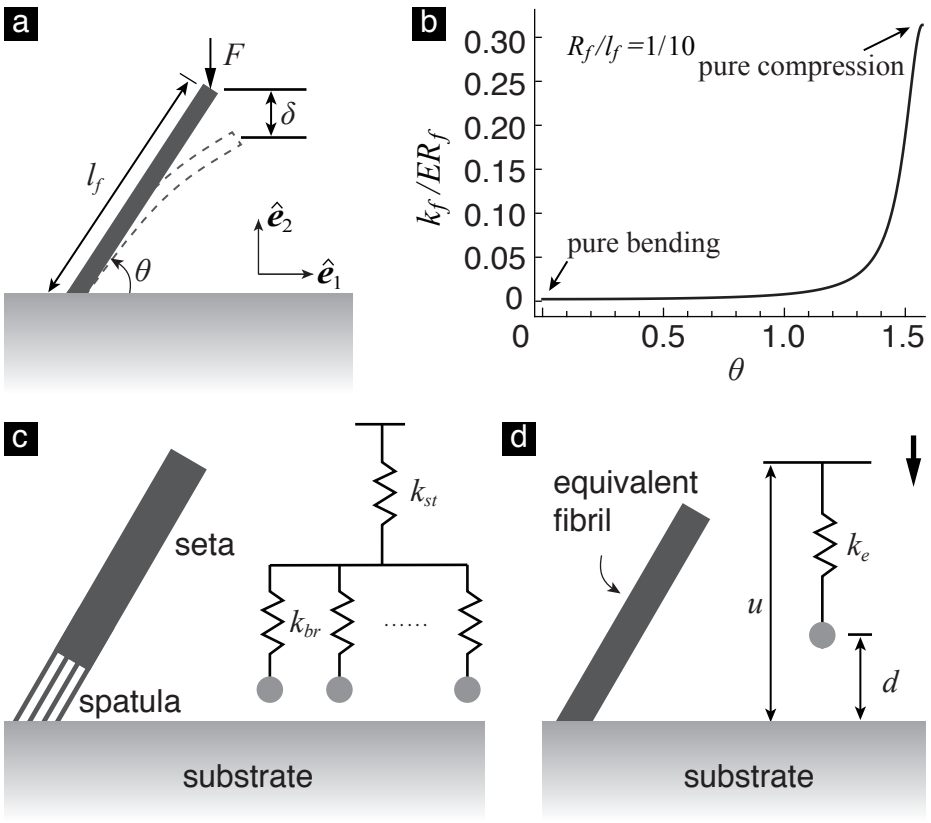

Figure 5.2: (a) An fibril extends away from its backing at an angle θ. (b) The variation of the stiffness of the tilted fibril as a function of θ. (c) The seta and spatulae can be modeled as a two-level spring system with different stiffnesses, k_{st} and k_{br} and (d) it is mechanically equivalent to a single fibril with an effective stiffness k_e.

5.4.1 Stiffness of a tilted fibril

We start with computing the stiffness of a single fibril that extends away from its backing at a angle θ and is subjected to a vertical force F in the $-\hat{e}_2$ direction at the end, see Figure 5.2a. The tilted fibril has a length l_f and a circular cross-section with radius R_f. The components of the external force perpendicular and tangential to the direction of the fibril, $F\cos\theta$ and $F\sin\theta$, give rise to bending and axial compressive deformation, δ_b and δ_c, respectively. Note that we do not consider the buckling of the fibril under the external force. Using the simple beam theory, we have

$$\delta_b = \frac{F\cos\theta l_f^3}{3EI}, \quad \delta_c = \frac{F\sin\theta l_f}{EA}, \tag{5.9}$$

where E is the elastic Young's modulus, $A = \pi R_f^2$ is the cross-section area, and $I = \pi R_f^4/4$ is the moment of inertia of the fibril. Thus, the total displacement of the fibril's top end in the $-\hat{e}_2$

direction is

$$\delta = \delta_b \cos\theta + \delta_c \sin\theta = \frac{F\cos^2\theta l_f^3}{3EI} + \frac{F\sin^2\theta l_f}{EA}. \tag{5.10}$$

Substituting the expression of A and I in the (5.10), and from the definition of the fibril's stiffness $k_f := F/\delta$, we obtain

$$k_f = \frac{\pi R_f^2 E}{l_f \sin^2\theta \left(1 + \frac{4l_f^2\cot^2\theta}{3R_f^2}\right)}. \tag{5.11}$$

Figure 5.2b plots the variation of the fibril's stiffness k_f with the tilted angle θ for $R_f/l_f = 1/10$. As can be seen, k_f increases monotonically from the value for pure bending to that for pure compression as θ changes from 0 to $\pi/2$. Therefore, the fibril is stiffest in compression ($\theta = 0$) and most compliant in bending ($\theta = \pi/2$).

5.4.2 Equivalent fibril for the seta-spatula adhesive system

As mentioned in §5.2 and Figure 5.1, the gecko's toe is characterized by the hierarchical structures. The seta and its substructure, branches and spatula, can be modeled as a two-level spring system with different stiffnesses for seta and branch, as shown in Figure 5.2c. According to (5.11), the stiffnesses of seta and branch, k_{st} and k_{br}, are given by

$$k_{st} = \frac{\pi R_{st}^2 E}{l_{st}\sin^2\theta\left(1 + \frac{4l_{st}^2\cot^2\theta}{3R_{st}^2}\right)}, \quad k_{br} = \frac{\pi R_{br}^2 E}{l_{br}\sin^2\theta\left(1 + \frac{4l_{br}^2\cot^2\theta}{3R_{br}^2}\right)}, \tag{5.12}$$

respectively, where R_{st} and R_{br} are the radius of the seta and the branch connected to spatula, respectively, l_{st} and R_{br} are their lengths, θ is the angle between the seta and the substrate, E is the elastic Young's modulus of β-keratin protein that composes setae.

We find that the two-level spring system shown in Figure 5.2c is mechanically equivalent to a single fibril with an effective stiffness k_e, as shown in Figure 5.2d. Suppose a seta contains n_{br} branches, then we can compute the effective stiffness of the equivalent fibril as

$$k_e = \left(\frac{n_{br}}{k_{st}} + \frac{1}{k_{br}}\right)^{-1}. \tag{5.13}$$

which is smaller than the branch's stiffness k_{br}.

5.4.3 Individual fibril adhesion

Let us consider the model shown in Figure 5.2d to study individual fibril adhesion. The fibril, which is modeled as a spring with stiffness k_e, interacts with a fixed, rigid half-space (substrate) below it via the LJ potential. The contact force between them is denoted as P. The distance from the top of the spring to the substrate is u, which is the controlled displacement in the model. The distance between the bottom of the spring and the substrate is d and is greater than zero. The top of the spring is first moved towards the substrate up to a given distance (loading phase) and then retracted back to its original position (unloading phase). From (5.4) we obtain the interaction energy between the fibril and the half-space as

$$\Pi_{\mathrm{LJ}}(d) = cwA_e\left[-\frac{1}{12}\left(\frac{\sigma}{d}\right)^2 + \frac{1}{360}\left(\frac{\sigma}{d}\right)^8\right], \tag{5.14}$$

where $c = 16(2/15)^{1/3} \approx 8.174$, and $A_e = \pi R_e^2$ is the cross-section area of the fibril with R_e the radius. The total potential energy of the system is

$$\Pi_{\mathrm{tot}}(u,d) = \frac{1}{2}k_e(u-d)^2 + cwA_e\left[-\frac{1}{12}\left(\frac{\sigma}{d}\right)^2 + \frac{1}{360}\left(\frac{\sigma}{d}\right)^8\right], \tag{5.15}$$

where the first term on the right hand side is the elastic energy of the spring.

Introducing the non-dimensional variables $\bar{u} = u/\sigma$, $\bar{d} = d/\sigma$, $\bar{k}_e = k_e\sigma^2/(cwA_e)$, $\bar{P} = P\sigma/(cwA_e)$, and $\bar{\Pi}_{\mathrm{tot}} = \Pi_{\mathrm{tot}}/(cwA_e)$, then we can re-write (5.15) as

$$\bar{\Pi}_{\mathrm{tot}}(\bar{u},\bar{d}) = \frac{1}{2}\bar{k}_e(\bar{u}-\bar{d})^2 - \frac{1}{12}\bar{d}^{-2} + \frac{1}{360}\bar{d}^{-8}. \tag{5.16}$$

For a fixed displacement $\bar{u}$, the distance $\bar{d}^*$ of equilibrium configuration, which minimizes the total potential energy $\bar{\Pi}_{\mathrm{tot}}$, is determined by

$$\left.\frac{\partial\bar{\Pi}_{\mathrm{tot}}}{\partial\bar{d}}\right|_{\bar{u}=\text{fixed}} = 0. \tag{5.17}$$

Then the equilibrium distance $\bar{d}^*$ is the positive solution of the following equation,

$$-\bar{k}_e(\bar{u}-\bar{d}^*)+\frac{1}{6}\bar{d}^{*-3}-\frac{1}{45}\bar{d}^{*-9}=0. \tag{5.18}$$

The non-dimensional equilibrium force

$$\bar{P}=\bar{k}_e(\bar{u}-\bar{d}^*). \tag{5.19}$$

The stability of the system can be investigated by examining the sign of the second derivative of $\bar{\Pi}_{\text{tot}}$ given by

$$\frac{\partial^2\bar{\Pi}_{\text{tot}}}{\partial\bar{d}^2}=\bar{k}_e-\frac{1}{2}\bar{d}^{*-4}+\frac{1}{5}\bar{d}^{*-10}. \tag{5.20}$$

For stable equilibrium, it requires $\partial^2\bar{\Pi}_{\text{tot}}/\partial\bar{d}^2>0$. We find there exist a critical stiffness $\bar{k}_{cr}=0.3$ such that the $\partial^2\bar{\Pi}_{\text{tot}}/\partial\bar{d}^2$ is always positive for $\bar{k}_e>\bar{k}_{cr}$ and hence the system is always stable. However, if $\bar{k}_e<\bar{k}_{cr}$, the sign of $\partial^2\bar{\Pi}_{\text{tot}}/\partial\bar{d}^2$ can change from positive to negative and vice versa, and the system would develop instabilities. We discuss these two cases in the following sections.

Stable case: $\bar{k}_e>\bar{k}_{cr}$

We first consider the stable case by taking $\bar{k}_e=2\bar{k}_{cr}$ as an example. Figure 5.3a–c show the plots of $\bar{\Pi}_{\text{tot}}$, $\partial\bar{\Pi}_{\text{tot}}/\partial\bar{d}$, and $\partial^2\bar{\Pi}_{\text{tot}}/\partial\bar{d}^2$ as a function of $\bar{d}$ for different $\bar{u}$, respectively. As can be seen, for each $\bar{u}$, there is a unique energy minimizer $\bar{d}^*$ corresponding to the solution of (5.18). $\partial\bar{\Pi}_{\text{tot}}/\partial\bar{d}$ has a unique zero, and the equilibrium is stable since $\partial^2\bar{\Pi}_{\text{tot}}/\partial\bar{d}^2$ is always positive. Considering a loading–unloading cycle with the displacement $\bar{u}$ first decreasing to a pre-specified value and then increasing, the equilibrium distance d^* for each $\bar{u}$ can be obtained through (5.18), which we plot in Figure 5.4a. The equilibrium force $\bar{P}$ is shown in Figure 5.4b. We find that the $\bar{d}^*$–$\bar{u}$ and $\bar{P}$–$\bar{u}$ curves for the loading and unloading phases overlap with each other, which indicates that there is no hysteresis during a loading–unloading cycle. We also plot the $\bar{d}^*$–$\bar{u}$ and $\bar{P}$–$\bar{u}$ curves for the case of $\bar{k}_e=\bar{k}_{cr}$. As can be seen, the loading and unloading processes are reversible for $\bar{k}_e\geq\bar{k}_{cr}$.

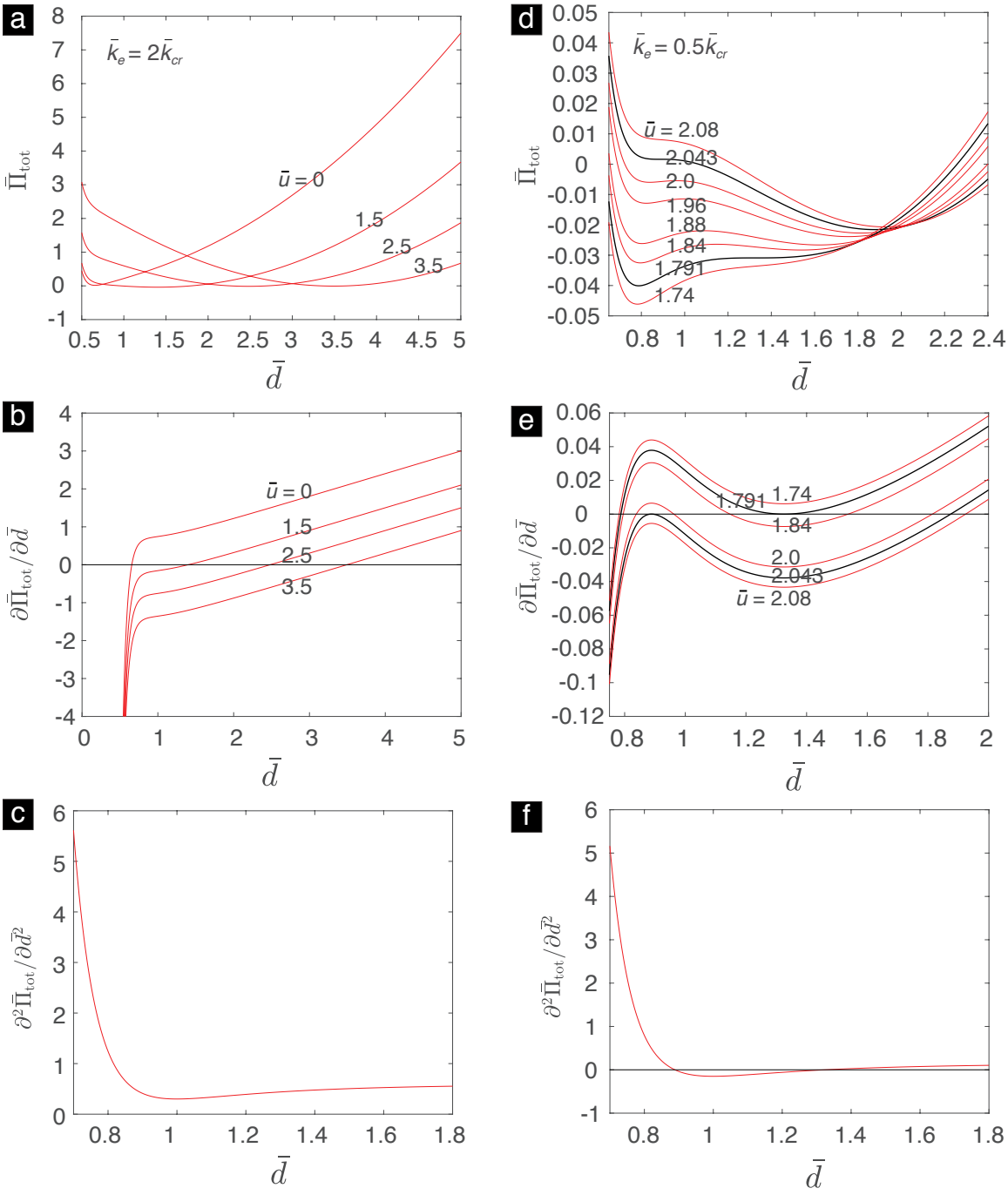

Figure 5.3: (a)–(c) show the plots of $\bar{\Pi}_{\rm tot}$, $\partial\bar{\Pi}_{\rm tot}/\partial\bar{d}$, and $\partial^2\bar{\Pi}_{\rm tot}/\partial\bar{d}^2$ as a function of $\bar{d}$ for different $\bar{u}$ in the case of $\bar{k}_e = 2\bar{k}_{cr}$, respectively. (d)–(f) show those plots for the case of $\bar{k}_e = 0.5\bar{k}_{cr}$.

Unstable case: $\bar{k}_e < \bar{k}_{cr}$

Next we consider the unstable case by taking $\bar{k}_e = 0.5\bar{k}_{cr}$ as an example. Figure 5.3d–f show the plots of $\bar{\Pi}_{\rm tot}$, $\partial\bar{\Pi}_{\rm tot}/\partial\bar{d}$, and $\partial^2\bar{\Pi}_{\rm tot}/\partial\bar{d}^2$ as a function of $\bar{d}$ for different $\bar{u}$, respectively. In the

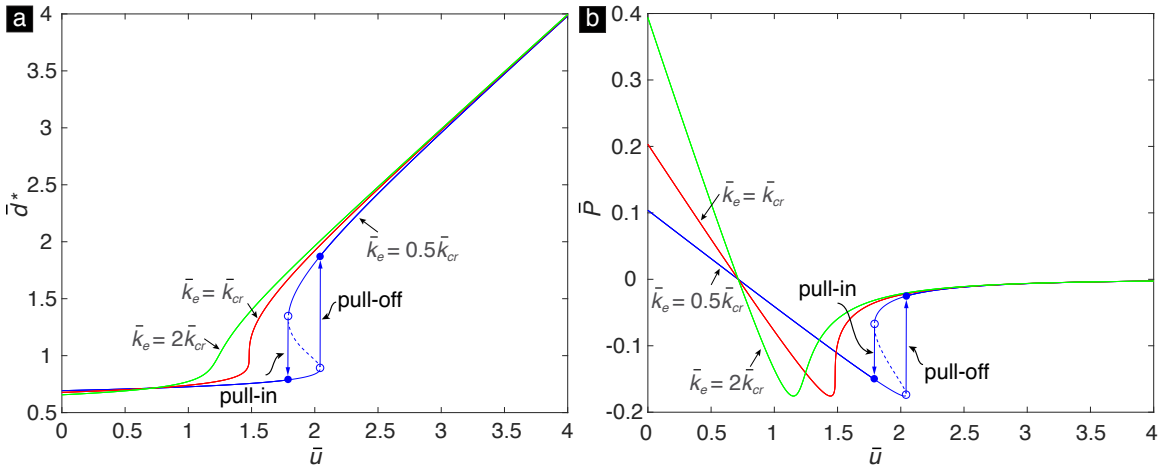

Figure 5.4: The plots of (a) equilibrium distance $\bar{d}^*$ and (b) force $\bar{P}$ as a function of displacement $\bar{u}$ during a loading–unloading cycle for $\bar{k}_e = 0.5\bar{k}_{cr}$, $\bar{k}_{cr}$, and $2\bar{k}_{cr}$. The circle and dot represent unstable and stable equilibriums, respectively.

loading phase, the displacement $\bar{u}$ decreases from a very large value. For example, at $\bar{u} = 2.08$, the energy minimizer $\bar{d}^*$ is unique, and the equilibrium is stable. On decreasing $\bar{u}$, the energy minimizer becomes non-unique for some displacements, e.g., $1.791 \leq \bar{u} \leq 2.043$. The larger minimizer becomes unstable once the second derivative becomes zero at $\bar{u} = 1.791$. This implies that the fibril would jump into contact with the substrate with the occurrence of a pull-in instability. The energy minimizer becomes unique again on further decreasing $\bar{u}$ for $\bar{u} < 1.791$.

In the unloading phase, with increasing $\bar{u}$ from the minimum specified value, the energy minimizer is unique and the equilibrium is stable. With further increase of $\bar{u}$, the energy minimizer becomes non-unique. However, the system will stay in the local minimum corresponding to the smaller minimizer, since there exists an energy barrier to switch to the other minimum corresponding to the larger minimizer. After the second derivative of $\bar{\Pi}_{\text{tot}}$ at the smaller minimizer becomes zero at $\bar{u} = 2.043$, the fibril would jump out of contact with the substrate with the occurrence of a pull-off instability. The energy minimizer becomes unique again on further increasing $\bar{u}$.

Because of the pull-in and pull-off instabilities, the equilibrium distance $\bar{d}^*$ during the loading and unloading phases are different for some displacements and the system exhibits hysteresis. This is clearly seen in Figure 5.4a which shows $\bar{d}^*$ as a function of the displacement $\bar{u}$ for $\bar{k}_s = 0.5\bar{k}_{cr}$. Outside of the pull-in and pull-off region, the $\bar{d}^*$–$\bar{u}$ curves for loading and unloading phases are overlapped. The evolution of equilibrium force shows a similar hysteretic behavior for $\bar{k}_s = 0.5\bar{k}_{cr}$, see Figure 5.4b.

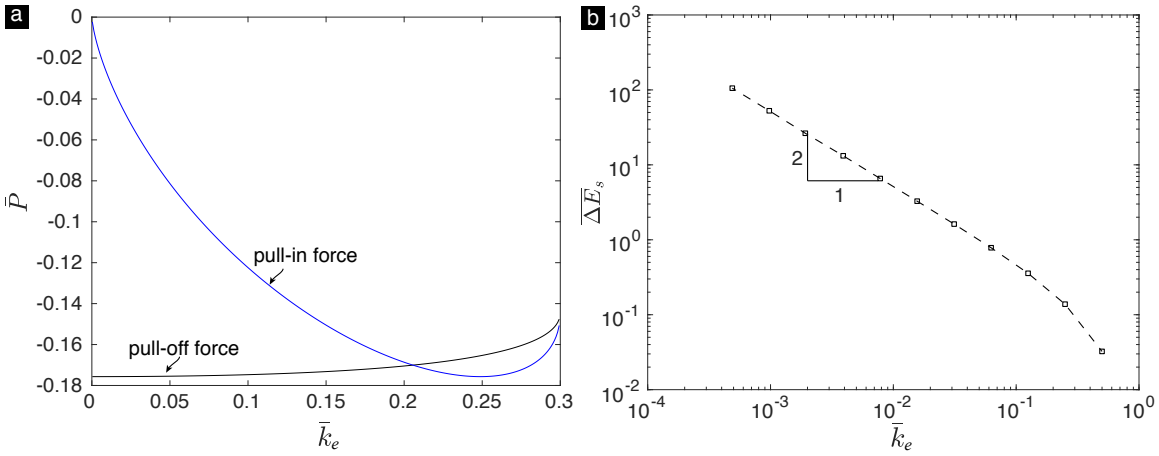

Figure 5.5: The plot of (a) the pull-in and pull-off forces and (b) hysteretic energy loss as a function of the fiber's effective stiffness $\bar{k}_e$.

Effect of $\bar{k}_e$ on pull-in and pull-off forces and hysteretic energy loss

The critical forces just after the occurrence of the pull-in instability and before the pull-off instability are referred to as pull-in and pull-off forces, respectively. We investigate the dependence of pull-in and pull-off forces on the stiffness $\bar{k}_e$ and show the results in Figure 5.5a. As can be seen, the magnitude of pull-in force initially increases and later then decreases with the stiffness. In contrast, the magnitude of pull-in force decreases monotonically with the stiffness. Figure 5.5b shows the variation of hysteretic energy loss, $\overline{\Delta E}_s$, as a function of $\bar{k}_e$ for a single fibril adhesion. It can be seen that $\overline{\Delta E}_s$ decreases as $\bar{k}_e$ increases. $\overline{\Delta E}_s$ becomes zero as $\bar{k}_e > \bar{k}_{cr} = 0.3$ since there is no instability.

As discussed in §5.4.1, the stiffness $\bar{k}_e$ of a fibril depends on the tilted angle θ. And it is found that the gecko's toe makes contact with substrate at a relative small angle between the seta and the substrate surface for attachment while it peels off at a relative large angle for detachment [128, 137]. The reason is because the equivalent fibril has a lower effective stiffness at a smaller tilted angle, leading to a higher pull-off force beneficial for attachment; while it has a higher effective stiffness at a larger tilted angel, leading to a lower pull-off force beneficial for detachment. Since the gecko's toe contains hundreds of thousands of setae and the substrate surface is often very rough, we shall examine the effect of stiffness on pull-off force in a more realistic way, which will be discussed in the next section.

5.5 Multiple spring model for adhesion of fibrillar structures

Based on the result of single fibril adhesion in §5.4.3, we discuss the multiple spring model for adhesive elastic contacts of the fibrillar structures with a rough substrate in this section. To begin with, we first present a general multiple spring model for adhesive contact of an elastic solid with a rigid rough substrate, see Figure 5.6. In this model, the elastic solid is represented by an assemble of elastic springs with identical stiffness k_e, and each spring is considered to interact with its neighbors using a coupled stiffness k_μ, which represents the shear deformation of the elastic solid. This model can be directly applied to investigate the adhesion of fibrillar structures by setting $k_\mu = 0$, i.e., ignoring the coupling effect between individual fibrils.

5.5.1 Model setup

We consider an ensemble system of $N \times M$ elastic springs sitting above a rigid substrate, which has an isotropic, randomly rough surface. Specifically, we consider that the height of the rough surface has a Gaussian probability distribution

$$p(z) = \frac{1}{\sqrt{2\pi}\sigma_{\text{rms}}} e^{-z^2/(2\sigma_{\text{rms}}^2)} \tag{5.21}$$

and the surface has a Gaussian auto-correlation function

$$R_{zz}(\delta) = \frac{\sigma_{\text{rms}}^2}{4\pi^2} e^{-\delta^2/L_c^2}, \tag{5.22}$$

where σ_{rms} is RMS roughness and L_c is the correlation length. A detailed discussion of the randomly rough surface and its numerical realizations can be found in Appendix C. The distance between the top of the springs and the mean plane of the substrate's rough surface is u, which is the controlled displacement in the model. Contact is determined by the LJ interaction of each spring with the substrate and the contact behavior of individual spring is discussed in detail in §5.4.3.

Let $\boldsymbol{d} = (d_1, d_2, ..., d_{MN})$ and $\boldsymbol{z} = (z_1, z_2, ..., z_{MN})$, where $d_i > 0$ is the distance between the i^{th} spring and the rough substrate and z_i is the height of the rough surface against the i^{th} spring. The

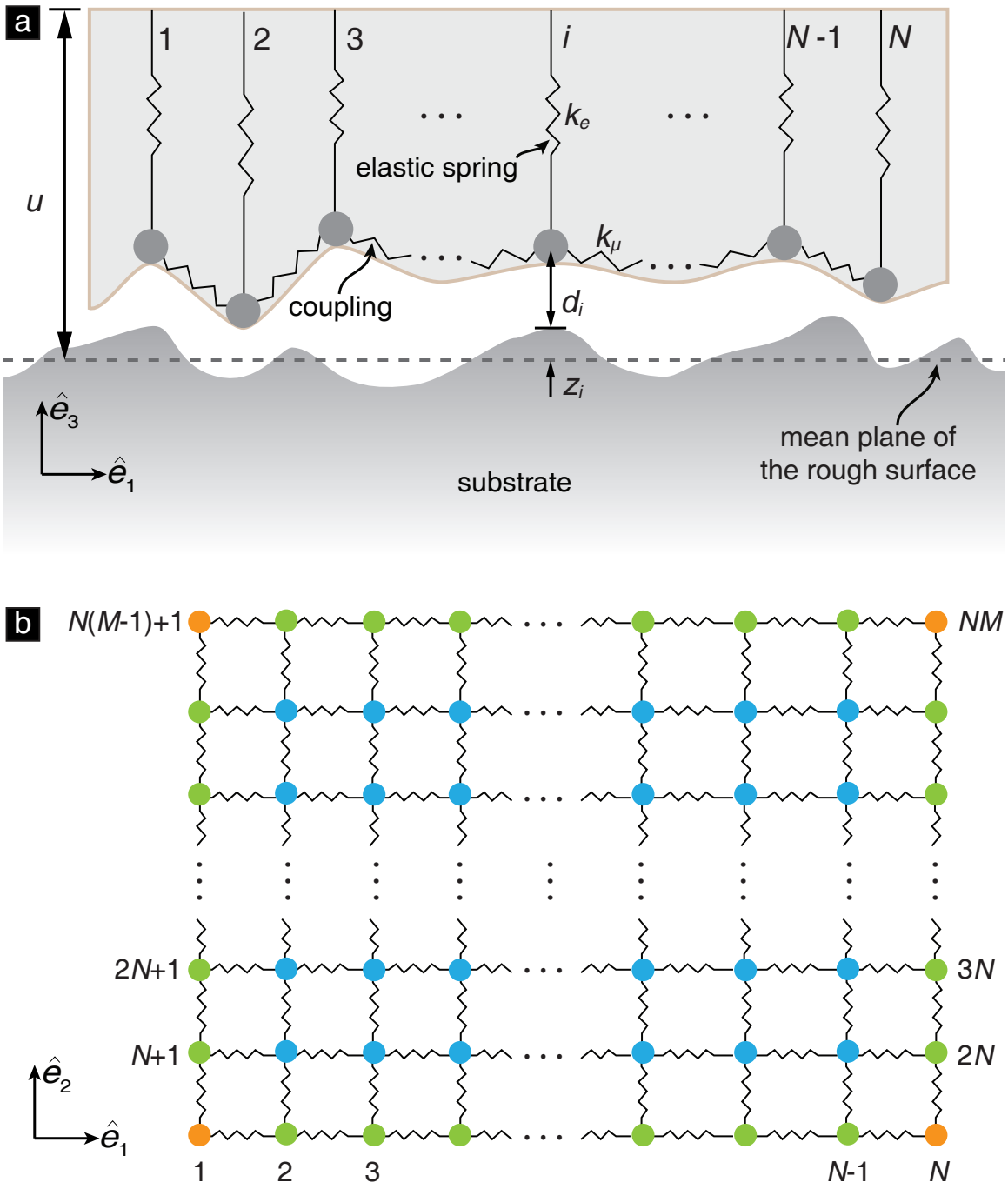

Figure 5.6: The adhesive contact between an elastic solid and a rigid rough substrate is represented by an assembly of coupled elastic springs. (a) Section view and (b) Top view of the system. In (b), Blue–interior springs; Yellow–corner springs; Green–edge springs.

stretch energy of the i^{th} spring is

$$\Pi_e^i(u, z_i, d_i) = \frac{1}{2} k_e (u - z_i - d_i)^2, \quad i \in \mathscr{I}, \tag{5.23}$$

where $\mathscr{I} = \{1,2,...,MN\}$. The coupling energy is

$$\Pi_{\mu}^{i} = \begin{cases} \frac{1}{2}k_{\mu}(z_{i+1} - z_i + d_{i+1} - d_i)^2 + \frac{1}{2}k_{\mu}(z_{i+N} - z_i + d_{i+N} - d_i)^2, & i \in \mathscr{I}_1, \\ \frac{1}{2}k_{\mu}(z_{i+1} - z_i + d_{i+1} - d_i)^2, & i \in \mathscr{I}_2, \\ \frac{1}{2}k_{\mu}(z_{i+N} - z_i + d_{i+N} - d_i)^2, & i \in \mathscr{I}_3, \end{cases} \tag{5.24}$$

where $\mathscr{I}_2 = \{MN - N + 1, MN - N + 2, ..., MN - 1\}$, $\mathscr{I}_3 = \{N, 2N, ..., (M-1)N\}$, and $\mathscr{I}_1 = \mathscr{I} \cap (\mathscr{I}_2 \cup \mathscr{I}_3 \cup \{MN\})$. Therefore, the total elastic energy is

$$\begin{aligned} \Pi_{\text{Etot}}(u, \boldsymbol{z}, \boldsymbol{d}) = &\sum_{i \in \mathscr{I}} \Pi_e^i(u, z_i, d_i) + \sum_{i \in \mathscr{I}_1} \Pi_{\mu}^i(u, z_i, d_i, z_{i+1}, d_{i+1}, z_{i+N}, d_{i+N}) \\ &+ \sum_{i \in \mathscr{I}_2} \Pi_{\mu}^i(u, z_i, d_i, z_{i+1}, d_{i+1}) + \sum_{i \in \mathscr{I}_3} \Pi_{\mu}^i(u, z_i, d_i, z_{i+N}, d_{i+N}). \end{aligned} \tag{5.25}$$

For the interaction energy, although the substrate surface is non-flat, we assume that the interaction energy between the fibril and the substrate per unit area can be approximated by (5.14) to the first order. Therefore, the interaction energy of the i^{th} spring with the substrate is

$$\Pi_{\text{LJ}}^i(d_i) = cwA_e f(d_i), \tag{5.26}$$

where

$$f(d_i) = -\frac{1}{12}\left(\frac{\sigma}{d_i}\right)^2 + \frac{1}{360}\left(\frac{\sigma}{d_i}\right)^8. \tag{5.27}$$

The total interaction energy of the system becomes

$$\Pi_{\text{LJtot}}(\boldsymbol{d}) = \sum_{i \in \mathscr{I}} \Pi_{\text{LJ}}^i(d_i) = cwA_e \sum_{i \in \mathscr{I}} f(d_i). \tag{5.28}$$

Thus, the total potential energy of the system is

$$\Pi_{\text{tot}}(u, \boldsymbol{d}, \boldsymbol{z}) = \Pi_{\text{Etot}}(u, \boldsymbol{d}, \boldsymbol{z}) + \Pi_{\text{LJtot}}(\boldsymbol{d}). \tag{5.29}$$

For a fixed displacement u, the equilibrium of the system requires that the first variation of the

Π_{tot} about the equilibrium distance d_i^* should be zero, i.e.,

$$< \delta\Pi_{\text{tot}}(d_i^*), \delta d_1, \delta d_2, ..., \delta d_{MN} >= \left(\frac{\partial \Pi_{\text{Etot}}}{\partial d_i}\Big|_{d_i=d_i^*} + \frac{\partial \Pi_{\text{LJtot}}}{\partial d_i}\Big|_{d_i=d_i^*} \right) \delta d_i = 0, \tag{5.30}$$

which gives a set of nonlinear equations

$$\frac{\partial \Pi_{\text{Etot}}}{\partial d_i} + \frac{\partial \Pi_{\text{LJtot}}}{\partial d_i} = 0, \tag{5.31}$$

to find d_i^* for $i = 1, 2, ..., MN$.

We use the Newton-Raphson method to find the equilibrium position d_i^* for a given displacement u. Suppose we have an initial guess d_i^k, where k denotes the iteration number, we want to correct this guess with an increment δd_i^k which leads $d_i^k + \delta d_i^k$ to satisfy (5.31). The correction δd_i^k is obtained by solving the linear equation system

$$\mathscr{A}_{ij} \delta d_i^k = b_j, \tag{5.32}$$

with

$$\begin{aligned} \mathscr{A}_{ij} &= K_{ij} + cwA_e f''(d_i^k)\delta_{ij}, \\ b_j &= -K_{ij}(d_i^k + z_i - u) - cwA_e f'(d_j^k), \end{aligned} \tag{5.33}$$

where δ_{ij} is the Kronecker delta function and

$$\begin{aligned} K_{i,i} &= k_e + 4k_\mu,\ K_{i,i-1} = K_{i,i+1} = K_{i,i-N} = K_{i,i+N} = -k_\mu,\ i \in \mathscr{I}_{\text{in}}, \\ K_{i,i} &= k_e + 3k_\mu,\ K_{i,i+1} = K_{i,i-N} = K_{i,i+N} = -k_\mu,\ i \in \mathscr{I}_{\text{lf}}, \\ K_{i,i} &= k_e + 3k_\mu,\ K_{i,i-1} = K_{i,i-N} = K_{i,i+N} = -k_\mu,\ i \in \mathscr{I}_{\text{rt}}, \\ K_{i,i} &= k_e + 3k_\mu,\ K_{i,i-1} = K_{i,i+1} = K_{i,i+N} = -k_\mu,\ i \in \mathscr{I}_{\text{bt}}, \\ K_{i,i} &= k_e + 3k_\mu,\ K_{i,i-1} = K_{i,i+1} = K_{i,i-N} = -k_\mu,\ i \in \mathscr{I}_{\text{tp}}, \\ K_{1,1} &= k_e + 2k_\mu,\ K_{1,2} = K_{i,N+1} = -k_\mu, \\ K_{N,N} &= k_e + 2k_\mu,\ K_{N,N-1} = K_{N,2N} = -k_\mu, \\ K_{MN-N+1,MN-N+1} &= k_e + 2k_\mu,\ K_{MN-N+1,MN-N+2} = K_{MN-N+1,MN-2N+1} = -k_\mu, \\ K_{MN,MN} &= k_e + 2k_\mu,\ K_{MN,MN-1} = K_{MN,MN-N} = -k_\mu, \end{aligned} \tag{5.34}$$

where $\mathscr{I}_{\text{lf}} = \{N+1, 2N+1, ..., (M-2)N+1\}$, $\mathscr{I}_{\text{rt}} = \{2N, 3N, ..., (M-1)N\}$, $\mathscr{I}_{\text{bt}} = \{2, 3, ..., N-1\}$, $\mathscr{I}_{\text{tp}} = \{(M-1)N+2, (M-1)N+3, ..., MN-1\}$, and $\mathscr{I}_{\text{in}} = \mathscr{I} \cap (\mathscr{I}_{\text{lf}} \cup \mathscr{I}_{\text{rt}} \cup \mathscr{I}_{\text{bt}} \cup \mathscr{I}_{\text{tp}} \cup \{1, N, MN-N+1, MN\})$. To guarantee that $d_i^k > 0$, we set d_i^k always to be positive in the Newton-Raphson iterations. We then update the guess $d_i^{k+1} = d_i^k + \delta d_i^k$, set $d_i^k \to d_i^{k+1}$, and continue to find the correction δd_i^k until it is smaller than a tolerance to meet the convergence criterion.

After obtaining the equilibrium distance d_i^*, we calculate the total contact force between the fibrillar structures and the rough surface as

$$P = \sum_{i=1}^{MN} k_e (u - d_i^*). \tag{5.35}$$

5.5.2 Numerical results and discussion

We apply the multiple spring model to study adhesion of fibrillar structures with rough surfaces by setting $k_\mu = 0$, which suppresses the coupling interaction between neighboring springs. We use the gecko's setae as an example to obtain a reasonable value for k_e in the numerical simulations. We compute the stiffness of the seta's branch as $k_e = \pi$ N/m from (5.11) by taking $E = 2$ GPa, $R_f = 50$ nm, $L_f = 5$ μm, $\theta = \pi/2$ and the critical stiffness is $k_{cr} = 0.3\pi c w R_e^2 = 5349.87$ N/m by taking $c = 8.174$, $w = 25$ mJ/m^2, $R_e = R_f$. We obtain $k_e/k_{cr} = 5.87 \times 10^{-4}$. Thus, we define an normalized effective stiffness as $\hat{k}_e := k_e/k_{cr} = 2^{-n}$ and vary n from 6 to 11 in the simulations to examine the effect of stiffness on adhesion, for which $\hat{k}_e$ changes from 1.56×10^{-2} to 4.88×10^{-4}.

In the simulations, we consider the total cross-section area of the fibrillar structures to be 100 μm $\times$ 100 μm, which consists of $N = M = 256$ branches (springs) in the $\hat{e}_1$ and $\hat{e}_2$ directions, respectively. This corresponds to a branch density of ≈ 6 μm^{-2}, which is consistent with the experimental observation in Figure 5.1e. We generate a series of rough surface samples with different RMS roughness σ_{rms} and correlation length L_c following the procedure in Appendix C. Some examples of those generated rough surfaces are shown in Figure C.1. The rough surface has a total area of 100 μm $\times$ 100 μm with a total of 256×256 grid points. We vary the normalized roughness of the substrate $\bar{\sigma}_{\text{rms}} = \sigma_{\text{rms}}/\sigma$ from 10 to 1500 and the normalized correlation length $\bar{L}_c = L_c/(100\ \mu\text{m})$ from 0.01 to 0.1, which correspond to a RMS roughness σ_{rms} from 3 nm to 450

nm and a correlation length L_c from 1 μm to 10 μm, respectively. To reduce the effect of randomness on the results due to the generation of substrate surface samples, we carry out the adhesive contact simulations of fibrillar structures over a total of 15 randomly rough surface samples for a given σ_{rms} and L_c. Then the results are averaged over the calculations of all samples for each rough surface.

Typical contact force–displacement curves

Figure 5.7 shows contact force–displacement (P–u) curves for stiffness $\hat{k}_e = 2^{-7}$ (i.e., $n = 7$) with various surface roughnesses. The hysteresis of the P–u curves manifests as the accumulation of hysteresis of individual springs during a loading–unloading cycle. At a large displacement, the interaction force between springs and the substrate is initially tensile. On further loading, springs close to the surface jump into contact with pull-in instabilities and are subsequently compressed. After reaching a minimum displacement, the system is unloaded and the springs remain in contact with the substrate until they reach their pull-off instability point and jump out of contact. Therefore, the force during unloading is different from loading, which gives hysteresis and energy loss. With further increasing u, the contact force decays to zero.

The effect of surface roughness $\bar{\sigma}_{\text{rms}}$ on the contact force–displacement curves can be clearly seen from Figure 5.7. As $\bar{\sigma}_{\text{rms}}$ increases, the compressive (positive) force increases during the loading phase and the maximum tensile (most negative) during the unloading phase decreases. Moreover, it takes a larger displacement for the contact force to decay to zero as $\bar{\sigma}_{\text{rms}}$ increases.

Effect of stiffness and roughness on adhesion efficiency

We define adhesion efficiency for the contact of fibrillar structures with rough surfaces as

$$\alpha_F = \frac{P_{max}}{MNP_m} \tag{5.36}$$

where P_{max} and P_m are the maximum tensile (most negative) forces for the fibrillar structures and the individual fiber (spring) during unloading, respectively. Figure 5.8 shows the effect of stiffness and roughness on adhesion efficiency. As can be seen, α_F decreases as $\bar{\sigma}_{\text{rms}}$ increases for a given stiffness. This trends is consistent with our previous finding that surface roughness is adverse to

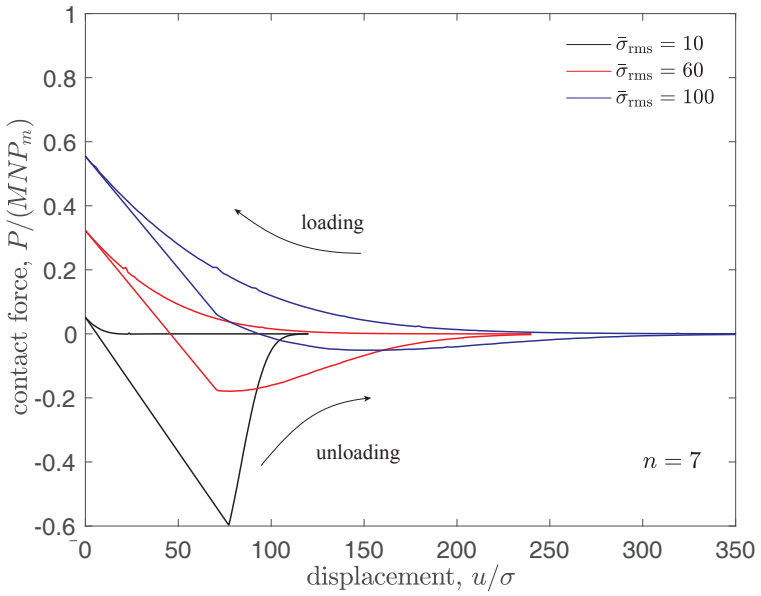

Figure 5.7: Contact force–displacement curves for $n = 7$ with different surface roughnesses.

adhesion.

The dependence of adhesion efficiency α_F on stiffness can shed some light on understanding the adhesion of gecko's toe as well as other similar fibrillar structures. As can be seen from Figure 5.8, for a given roughness surface, α_F increases as the stiffness, $\hat{k}_e = 2^{-n}$, becomes smaller (i.e., as n increases). Therefore, in order to enhance adhesion, there are two strategies employed in the design of gecko's adhesive toe. First, as shown in Figure 5.2b, the fibril's stiffness is decreased by tilting it to a lower angle with the substrate. Thus, the toe achieves a higher adhesion for attachment by making contact with substrate at a relative small angle between the seta and the substrate surface. Second, from (5.11) we find that the fibril's stiffness is decreased with increasing its length. However, the fibril's length cannot be as much longer as desired because of the bunching effect for the long fibers [138]. Therefore, as an alternative way, the gecko's toe evolves with a hierarchical structure, which can equivalently reduce the fibril's stiffness as seen from (5.13).

We use an empirical equation

$$\alpha_F = e^{-4\bar{\sigma}_{\rm rms}/2^n} \tag{5.37}$$

to describe the effect of stiffness and surface roughness on adhesion efficiency. It shows an exponential decay of α_F with $\bar{\sigma}_{\rm rms}$ and a larger α_F for a larger n (i.e., smaller stiffness $\hat{k}_e$). It is found that (5.37) matches well with the numerical data for $n = 6$, 7, and 8, but it deviates from the

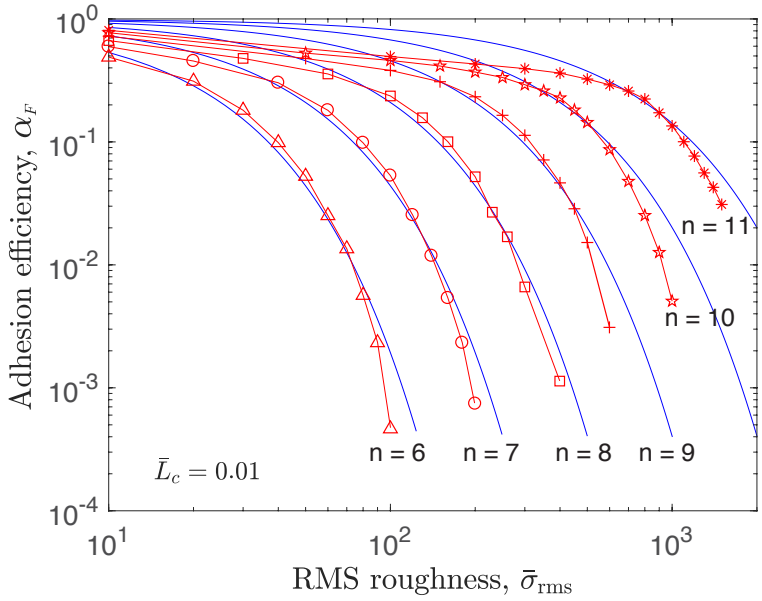

Figure 5.8: The effect of stiffness and roughness on adhesion efficiency. The stiffness is $\hat{k}_e = 2^{-n}$. The symbols denote the data from simulations and the solid lines are from (5.37).

numerical data for $n = 9$, 10, and 11.

Effect of correlation length on adhesion efficiency

We also studied the effect of correlation length L_c of the rough surface on adhesion efficiency. A representative result is shown in Figure 5.9, in which we calculate the adhesion efficiency α_F as a function of L_c for two different surface roughnesses, $\bar{\sigma}_{\rm rms} = 10$ and 50, with $n = 6$. The results are averaged over the calculations from a total of 15 randomly rough surface samples. It can be seen that there is no appreciable dependence of adhesion efficiency on the correlation length, although the uncertainty (error bar) increases for larger correlation length.

5.6 Discussion of contact splitting principle

Our multiple spring model can be used to study the contact splitting principle by considering the coupling between neighboring elastic springs. As a representative example, we show the effect of coupling stiffness in Figure 5.10–5.11 to discuss the principle of contact splitting for adhesion of fibrillar structure on rough surface. In the simulations corresponding to those results, we consider a total of $N = 256$ and $M = 1$ springs in the $\hat{e}_1$ and $\hat{e}_2$ directions, respectively. The contact simulations

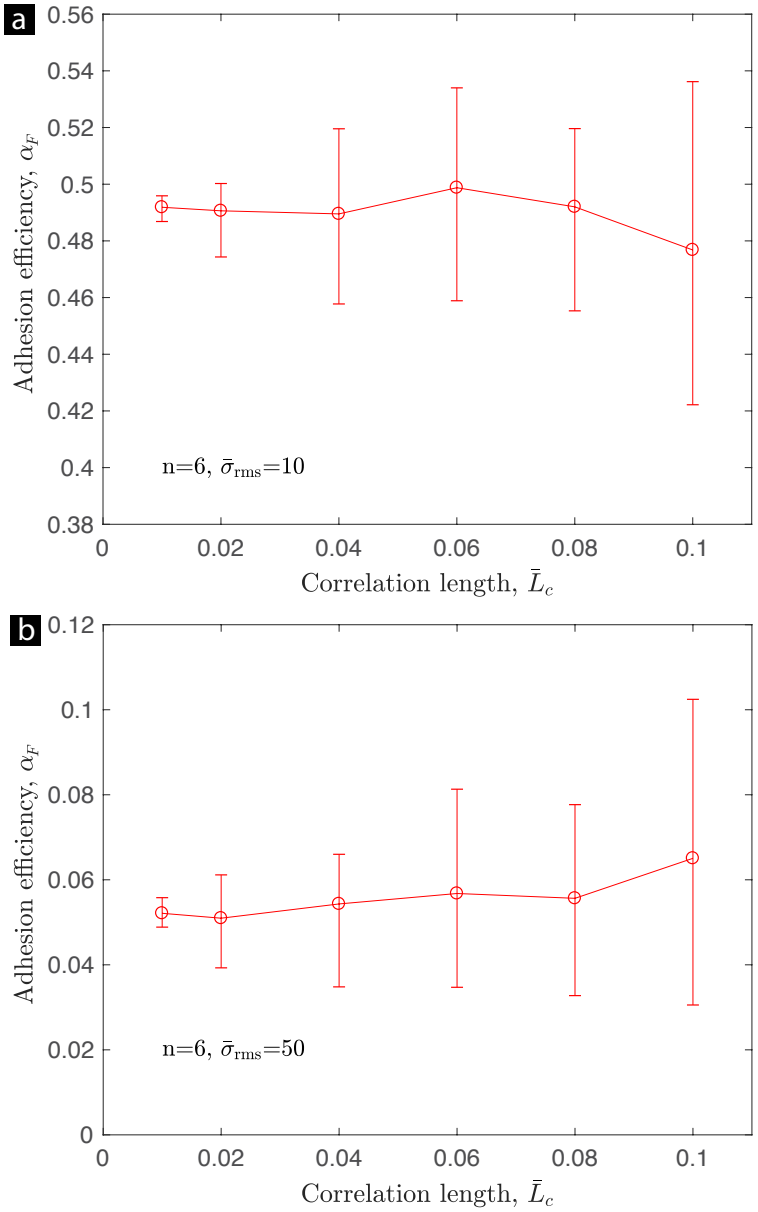

Figure 5.9: The dependence of adhesion efficiency α_F on correlation length L_c for surface roughness (a) $\bar{\sigma}_{\rm rms} = 10$ and (b) $\bar{\sigma}_{\rm rms} = 50$. The error bars are computed from the results averaged over the calculations from a total of 15 randomly rough surface samples.

are carried out with $\hat{k}_e = 2^{-10}$ (i.e., $n = 10$) on a rough surface with $\bar{\sigma}_{\rm rms} = 100$ and $\bar{L}_c = 0.01$. The normalized coupling stiffness $\hat{k}_\mu := k_\mu / k_{cr}$ is chosen to be 0, $2\hat{k}_e$, and $10\hat{k}_e$, which corresponds to no coupling, weak coupling, and strong coupling, respectively, between elastic springs.

Figure 5.10 shows the typical contact force–displacement curves for the three different coupling stiffnesses. As can be seen, both the adhesive (most negative) force and the hysteretic energy loss (area enclosed by the loading and unloading curves) decrease quickly as the coupling stiffness

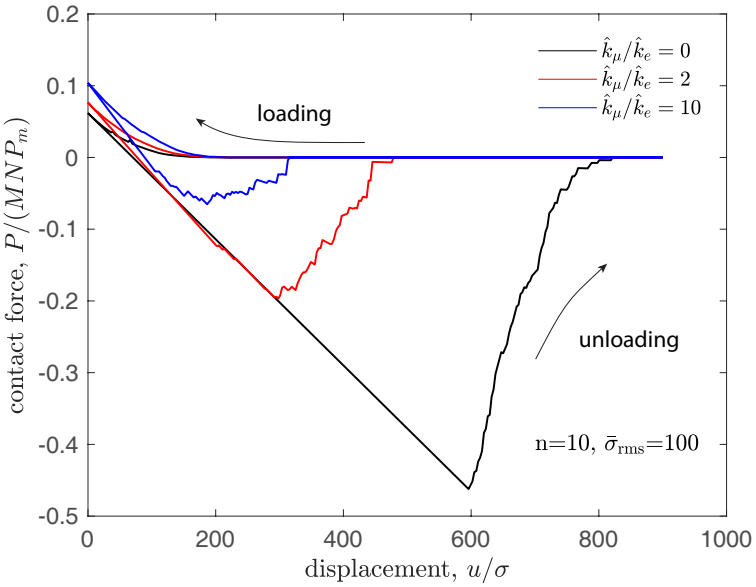

Figure 5.10: Contact force–displacement curves for different coupling stiffnesses.

increase. The results demonstrate that the contact splitting ($k_\mu = 0$) can significantly enhance the adhesion of fibrillar structure on rough surface.

We calculate the contact ratio, which is the ratio of the number of contacting springs to the total number of springs, during a loading and unloading cycle. It is related to contact area during the contact of fibrillar structure with rough surface. Figure 5.11 shows the variations of contact ratio during loading and unloading phases for the three different coupling stiffnesses, whose corresponding *P–u* curves are shown in Figure 5.10. For all three cases, it is found that the contact ratio during unloading phase is greater than that during loading phase at the same load step. Moreover, the contact ratio increases as the coupling stiffness decreases. The case of $\hat{k}_\mu = 0$ has the largest contact ratio, or equivalently, contact area. This indicates that the remarkable adhesion enhancement by contact splitting is due to the increase of contact area.

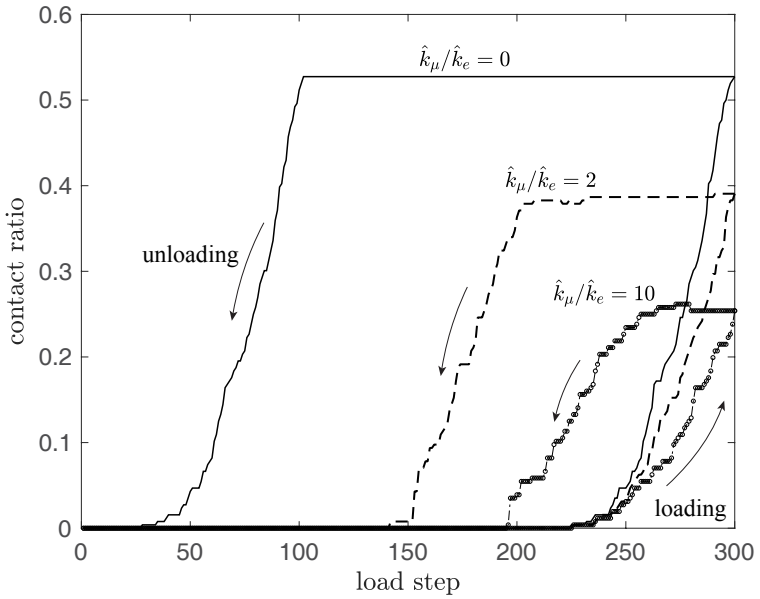

Figure 5.11: The variation of contact ratio during loading and unloading phases for different coupling stiffnesses. The corresponding contact force–displacement curves are shown in Figure 5.10.

Chapter 6

Interface toughening of thin film peeling from wavy substrates

6.1 Introduction

Adhesion between solid surfaces has been attracting a growing attention due to plentiful biomimetic applications of many biological species' adhesive pads on their feet, which endow them extraordinary adherence and climbing agility on natural surfaces. For instance, gecko can easily and reversibly stick to various rough surfaces, although it is well known that surface roughness is strongly averse to adhesion [19]. The remarkable attachment ability of geckos has been found to originate from the hierarchical fibrillar structure on their toe pads—which consists of thousands of elastic hairs called setae ($\sim$100 μm in length and $\sim$5 μm in diameter), each of which further splits into hundreds of finner fibrils ($\sim$10 μm in length and $\sim$0.1 μm in diameter) with a terminal 5–10 nm-thick thin film called spatula at each fibril's end [9, 139]. The spatulae constitute the primary adhesive elements of attachment pads evolved in gecko, which are shown to adhere to solid surfaces via van der Waals interactions [128, 131]. The hierarchical fibrillar structures are also commonly seen in many other biological species such as beetles, flies, and spiders [8, 140–144]. Inspired by those sticky attachment pads found in nature, a number of biomimetic adhesive structures consisting of arrays of polymer pillars terminated with spatula-like tips have been fabricated aiming to achieve a unique

combination of adhesion properties such as strength, reversibility, and directionality [112, 145, 146].

The biological fibrillar structure and its biomimetic counterpart detach from a solid's surface by peeling the terminal spatulae off, which is reminiscent of peeling a tape from a substrate. Therefore, many peeling models have been developed to understand the detachment mechanism and to optimize the adhesion of the fibrillar structure [128, 129, 147–150]. These models are a generalization of the Kendall's peeling model [151], which analyzes the peeling of a thin film from a rigid substrate first studied by Rivlin [152] and relates the peeling force to peeling angle and the work of adhesion. For example, Pesika *et al.* [147] presented a tape-peeling model based on the geometry of the peel zone that considers the effect of peel angle and friction on adhesion. Chen *et al.* [148] incorporated pre-tension effect of the thin film into the Kendall's peeling model. They found that the pre-tension significantly increases the peeling force at small peeling angles while decreasing it at large angles and the peeling force disappears beyond a critical peeling angle. Pugno [150] developed a multiple peeling model that contains multiple thin films adhered to a substrate with a common hinge when the peeling force is applied and accounts for large deformations and pre-stretching.

The peeling problem of a thin film from a substrate has been investigated extensively after the seminal work by Kendall [151]. For instance, Kim *et al.* [54, 153, 154] and Kinloch *et al.* [155] performed elasto-plastic analysis of the thin film peeling and computed the true interface adhesion based on energy balance approach. Wei and Hutchinson [156] analyzed the steady-state peeling of an elasto-plastic film bonded to an elastic substrate by using a cohesive zone model. Chen *et al.* [157] and Loukis *et al.* [158] determined the interface adhesion for a viscoelastic strip on a rigid substrate. Kendall [159] and Ghatak *et al.* [160] studied the peeling of heterogeneous thin film and found that the effective adhesion is increased compared with the homogeneous case. Xia *et al.* [161, 162] recently showed that the macroscale peeling behavior can be significantly affected by the microscale adhesive and elastic heterogeneities, which suggests a potential way to improve the interface adhesion.

Most of the previous work on peeling mechanics focused on smooth and flat substrates, but only a few works have been conducted to investigate the effect of interfacial topography on the peeling behavior [163, 164]. However, a number of researches demonstrate that the interfacical waviness has an important effect on the interface adhesion properties. For example, the use of

controlled interfacial geometry has been shown to be an effective way to enhance the interface adhesion and fracture toughness in ceramics and composites [165, 166]. Kesari *et al.* [35] developed an adhesive elastic contact theory to show that interfacial waviness at microscale can increase the effective interface adhesion in a sense that the inherent instabilities dissipate more energy during the attachment-detachment of contacting bodies. Furthermore, wavy interfaces are also found in biological materials such as woodpecker beaks [167] and cranial bones of rams [168]. These kinds of biological materials display outstanding strength and toughness owning to the deflection of crack propagation by their weak wavy interface and offer a prototype to develop bioinspired composites [169]. Therefore, it is important to study the effect of interface waviness on the peeling behavior, which could provide insights in improving the interface adhesion.

In this work, we investigate the peeling of an elastic soft thin film from a rigid wavy substrate. We obtain equilibrium of the peeling process by minimizing total potential energy of the system and examine stability of the equilibrium. We find that a series of snap-through instabilities occur during the peeling of thin film from wavy substrate surfaces under load control, resulting an apparent toughening of the thin film-wavy substrate interface. Furthermore, we show that the effective peeling force and work of adhesion of wavy substrates can be increased by several times compared to that of the flat substrate.

6.2 Wavy peeling model

In this section, we present our model involving the peeling of an elastic soft thin film from a rigid wavy substrate which has an arbitrary periodic surface. We derive the equilibrium configuration by minimizing the system's total potential energy and analyze its stability condition. Finally, we obtain the maximum peeling force and the effective work of adhesion during peeling.

6.2.1 Geometry

Figure 6.1 shows the geometry of our wavy peeling model. The substrate's surface profile is given by the function $y(x) = y_0 + \delta(x)$, where y_0 is a constant and $\delta(x) = A\lambda\rho(x/\lambda)$ describes the small-scale topography of the wavy surface, in which A is the aspect ratio of the surface and $\rho(x/\lambda) \in [-1,1]$ is

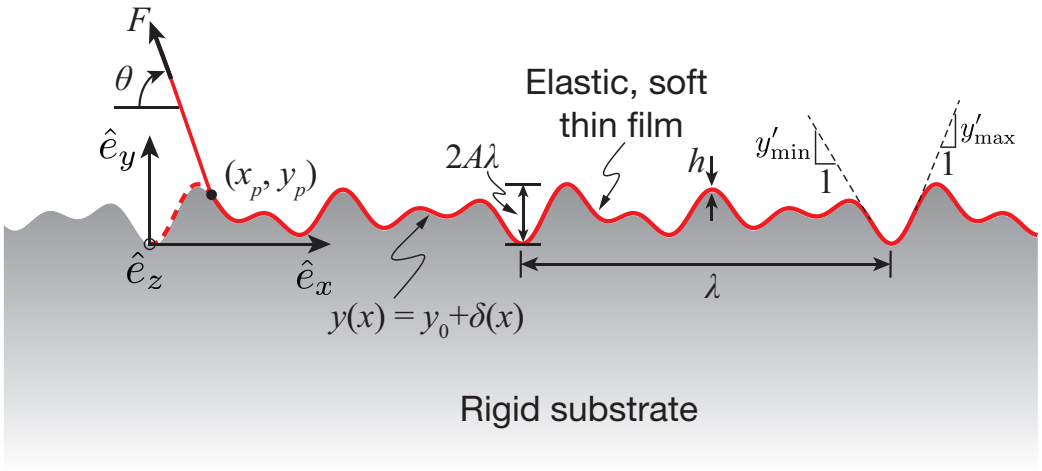

Figure 6.1: The schematic of peeling off an elastic, soft thin film from an rigid wavy substrate.

a non-constant periodic function with period λ. There is no condition for the function $\rho(x/\lambda)$ except that it is single-valued. The thin film's length is assumed to be long enough such that we can ignore the boundary effect. The elastic thin film has Young's modulus E, width b and thickness h and it is initially perfectly bonded to the substrate surface. Since we consider the thin film to be very soft (e.g., $E \leq 1$ MPa), we shall neglect the bending energy of the thin film due to its initial conformity to the wavy substrate. We consider that the peeling process is under load control. A peeling force F is applied on the left edge of the thin film at a constant angle $\theta \in [0, \pi]$ between the force and the $-\hat{e}_x$ direction. In our model, the peeling angle θ should be chosen to avoid contact between the peeled film and the substrate during the peeling process, which we refer to as the comparability condition. More specifically, the peeling angle should satisfy the condition $\tan\theta \geq |\min\{y'(x)\}|$ for $\theta \in [0, \pi/2]$ and $|\tan\theta| \geq \max\{y'(x)\}$ for $\theta \in [\pi/2, \pi]$, where y' denotes the first derivative of $y(x)$.

6.2.2 Equilibrium

We find the equilibrium configuration of the peeling process by minimizing the total potential energy of the system. We denote the coordinate of the peeling front as $(x_p, y(x_p))$. Then the peeled length of the thin film is

$$l_p = \int_0^{x_p} \sqrt{1 + y'(x)^2}\, dx. \tag{6.1}$$

Under the peeling force F, the tensile stress built up in the peeled thin film is $\sigma = F/(bh)$ and the elastic strain is $\varepsilon = \sigma/E$. Thus, the elastic strain energy stored in the peeled thin film is

$$\mathscr{E}_{el} = bh \int_0^{l_p} \frac{1}{2}\sigma\varepsilon \, dl = \frac{F^2 l_p}{2Ebh}. \tag{6.2}$$

Since the deformed length of the peeled thin film is $(1+\varepsilon)l_p$, the displacement of the point at which the force is applied, relative to the origin, to can be obtained as

$$\boldsymbol{u} = (-(1+\varepsilon)l_p \cos\theta + x_p)\,\hat{\boldsymbol{e}}_x + ((1+\varepsilon)l_p \sin\theta + y(x_p))\,\hat{\boldsymbol{e}}_y. \tag{6.3}$$

Therefore, the force potential is

$$\mathscr{E}_p = \boldsymbol{F}\cdot\boldsymbol{u} = -Fx_p\cos\theta + Fy(x_p)\sin\theta + F(1+\varepsilon)l_p, \tag{6.4}$$

where $\boldsymbol{F} = -F\cos\theta\hat{\boldsymbol{e}}_x + F\sin\theta\hat{\boldsymbol{e}}_y$.

We model adhesion between the thin film and the substrate following the approach in the JKR theory [14], in which the adhesion is modeled as an infinitesimal interaction and the adhesive energy is included in the system's total potential energy. According to the JKR theory, the potential energy from the adhesive interactions between the thin film and the substrate is

$$\mathscr{E}_s = l_p bw, \tag{6.5}$$

where w is the Dupré work of adhesion.

Therefore, the total potential energy of the system is

$$\begin{aligned}\mathscr{E}_{tot}(x_p) &= \mathscr{E}_{el} - \mathscr{E}_p - \mathscr{E}_s \\ &= -\left(\frac{F^2}{2Ebh} + F + bw\right)\int_0^{x_p}\sqrt{1+y'(x)^2}\,dx + Fx_p\cos\theta - Fy(x_p)\sin\theta.\end{aligned} \tag{6.6}$$

To obtain the equilibrium configuration, we locally minimize the total potential energy w.r.t. x_p. To

do this, we take the first-order derivative of $\mathscr{E}_{tot}$ w.r.t. x_p to be zero. Thus we have

$$\frac{d\mathscr{E}_{tot}}{dx_p} = -\left(\frac{F^2}{2Ebh} + F + bw\right)\sqrt{1+y'(x_p)^2} + F\cos\theta - Fy'(x_p)\sin\theta = 0. \tag{6.7}$$

Introducing the dimensionless parameter $\bar{F} = F/Ebh$ and $\bar{w} = w/Eh$, then we can rewrite (6.7) as

$$\frac{1}{2}\bar{F}^2 + \bar{F}\left[1 - \frac{\cos\theta - y'(x_p)\sin\theta}{\sqrt{1+y'(x_p)^2}}\right] + \bar{w} = 0. \tag{6.8}$$

By solving (6.8) we obtain two roots of the equation, of which one is positive and the other is negative. Since the force to peel the thin film should be tensile (positive), we obtain the non-dimensional peeling force as

$$\bar{F} = \sqrt{\left[\frac{\cos\theta - y'(x_p)\sin\theta}{\sqrt{1+y'(x_p)^2}} - 1\right]^2 + 2\bar{w}} + \frac{\cos\theta - y'(x_p)\sin\theta}{\sqrt{1+y'(x_p)^2}} - 1, \tag{6.9}$$

which is always positive. Furthermore, by letting $\phi = \tan^{-1}(y'(x_p))$, where $\phi \in [-\pi/2, \pi/2]$ is the angle of the surface's slope at the peeling front $(x_p, y(x_p))$, we can rewrite (6.9) as

$$\bar{F} = \sqrt{(\cos\theta_e - 1)^2 + 2\bar{w}} + \cos\theta_e - 1, \tag{6.10}$$

where we define $\theta_e = \theta + \phi$ as the equivalent peeling angle. It is in the range from 0 to π. The effect of the wavy surface's micro-scale topography is can be seen from the angle of the surface's slope ϕ in the equivalent peeling angle θ_e of (6.10). As can be seen, for a given peeling angle θ, the peeling force $\bar{F}$ is not constant since ϕ changes at different peeling front $(x_p, y(x_p))$. We note that the Kendall's result [151] can be recovered by setting $y'(x_p) = 0$ or $\phi = 0$, which gives the force of peeling a thin film from a flat substrate as

$$\bar{F}_{\text{flat}} = \sqrt{(\cos\theta - 1)^2 + 2\bar{w}} + \cos\theta - 1. \tag{6.11}$$

The force $\bar{F}_{\text{flat}}$ is constant for a given peeling angle θ. It is not surprising that (6.11) and (6.10) have the similar form, because at each local peeling front on the wavy substrate, the peeling can be viewed as the one on a flat substrate with an equivalent peeling angle θ_e.

6.2.3 Stability

An equilibrium configuration is said to be stable for $d^2\mathscr{E}_{tot}/dx_p^2 > 0$, neutral for $d^2\mathscr{E}_{tot}/dx_p^2 = 0$, and unstable for $d^2\mathscr{E}_{tot}/dx_p^2 < 0$. Using (6.6) we take second derivative of $\mathscr{E}_{tot}$ w.r.t. x_p to obtain

$$\frac{d^2\mathscr{E}_{tot}}{dx_p^2} = -Ebhy''(x_p)\left[\bar{F}\sin\theta + \frac{\left(\frac{\bar{F}^2}{2} + \bar{F} - \bar{w}\right)y'(x_p)}{\sqrt{1+y'(x_p)^2}}\right]. \tag{6.12}$$

Recall that $\phi = \tan^{-1}(y'(x_p))$, we have

$$\frac{d\phi}{dx_p} = \frac{\kappa(x_p)}{\sqrt{1+y'(x_p)^2}}, \tag{6.13}$$

where

$$\kappa(x_p) = \frac{y''(x_p)}{[1+y'(x_p)^2]^{3/2}} \tag{6.14}$$

is the curvature of substrate surface. With (6.8) and (6.13), (6.12) can be further simplified as

$$\frac{d^2\mathscr{E}_{tot}}{dx_p^2} = -F\kappa(x_p)[\sin\theta + y'(x_p)\cos\theta]\sqrt{1+y'(x_p)^2}. \tag{6.15}$$

Since the comparability condition requires that $\tan\theta \geq |\min\{y'(x_p)\}|$ for $\theta \in [0,\pi/2]$ and $|\tan\theta| \geq \max\{y'(x_p)\}$ for $\theta \in [\pi/2,\pi]$, thus $\sin\theta + y'(x_p)\cos\theta$ is always non-negative. Moreover, the peeling force is always positive and $1+y'(x_p)^2 \geq 1$. Therefore, $d^2\mathscr{E}_{tot}/dx_p^2$ is of the opposite sign as the surface curvature $\kappa(x_p)$.

With (6.13) and from (6.10) we obtain

$$\frac{d\bar{F}}{dx_p} = -\kappa(x_p)\sin\theta_e\sqrt{1+y'(x_p)^2}\left[1 - \frac{1-\cos\theta_e}{\sqrt{2\bar{w}+(1-\cos\theta_e)^2}}\right]. \tag{6.16}$$

Note that $1+y'(x_p)^2 \geq 1$, $\sin\theta_e \geq 0$ for $\theta_e \in [0,\pi]$, and the term inside the square bracket in (6.16) is positive, therefore, $d\bar{F}/dx_p$ is also of the opposite sign as the surface curvature $\kappa(x_p)$. Hence, from (6.15) and (6.16) we find that $d^2\mathscr{E}_{tot}/dx_p^2$ is of the same sign with $d\bar{F}/dx_p$. Therefore, it requires that $d^2\mathscr{E}_{tot}/dx_p^2$, or equivalently, $d\bar{F}/dx_p$, be greater than, equal to, and less than zero,

respectively, for stable, neutral, and unstable equilibrium configuration, which corresponds to negative, zero, and positive surface curvature $\kappa(x_p)$, respectively.

We find the maximum peeling force $\bar{F}_{\max}$ using (6.9) or (6.10). It can be shown from (6.10) that $\bar{F}$ monotonically decreases with increasing the equivalent peeling angle θ_e for $\theta_e \in [0,\pi]$. Therefore, the maximum peeling force is achieved when θ_e is minimum. (The minimum θ_e may or may not be equal to 0 depending on the peeling angle θ and surface slope ϕ.) Because the minimum equivalent peeling angle corresponds to the minimum slope of the surface, we have

$$\bar{F}_{\max} = \sqrt{\left[\frac{\cos\theta - y'_{\min}(x_p)\sin\theta}{\sqrt{1+y'_{\min}(x_p)^2}} - 1\right]^2 + 2\bar{w}} + \frac{\cos\theta - y'_{\min}(x_p)\sin\theta}{\sqrt{1+y'_{\min}(x_p)^2}} - 1. \tag{6.17}$$

We define the effective work of adhesion

$$\bar{w}_e = \frac{1}{2}\left[\cos(\theta+\phi_{\min}) - \cos\theta + \sqrt{(\cos(\theta+\phi_{\min})-1)^2 + 2\bar{w}}\right]^2 - \frac{1}{2}(\cos\theta - 1)^2, \tag{6.18}$$

where $\phi_{\min} = \tan^{-1}(y'_{\min}(x_p))$, so that we can rewrite (6.17) as

$$\bar{F}_{\max} = \sqrt{(\cos\theta - 1)^2 + 2\bar{w}_e} + \cos\theta - 1, \tag{6.19}$$

which has a similar form with (6.11). It can be seen from (6.18) that $\bar{w}_e$ depends on the peeling angle θ and the angle of the minimum slope $\phi_{\min}$.

6.3 Examples

In this section, we apply the results derived in §6.2 to investigate the peeling of a soft thin film from wavy substrates with sinusoidal and zigzag surface profiles.

6.3.1 Sinusoidal surface

For the substrate having a sinusoidal surface, the surface profile function is

$$y(x) = A\lambda[1 - \cos(2\pi x/\lambda)]. \tag{6.20}$$

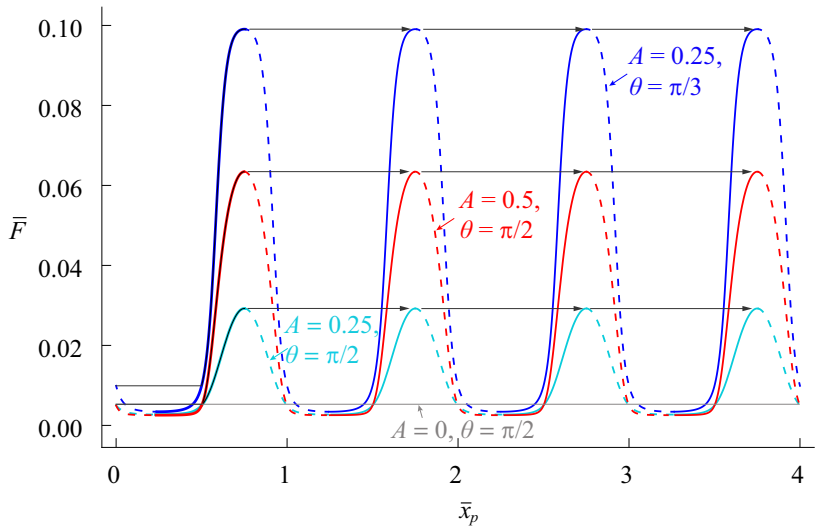

Figure 6.2: The plot of the peeling force $\bar{F}$ as a function of the abscissa of the peeling front $\bar{x}_p$ for different aspect ratio A and peeling angle θ in the case of the substrate with sinusoidal surfaces. For $A > 0$, the solid and dashed lines indicate stable and unstable equilibrium configurations, respectively. The thin black lines represent the measured forces with arrows indicating snap-through instabilities during peeling under load control. For $A = 0$, the solid line indicates the neutral equilibrium configuration.

The surface has a root-mean-square (RMS) roughness $A\lambda/\sqrt{2}$, which is proportion to the aspect ratio A of the surface. Let $\bar{y} = y/\lambda, \bar{x} = x/\lambda$, then $\bar{y} = A[1-\cos(2\pi\bar{x})]$. The minimum and maximum slope of this surface is $-2\pi A$ and $2\pi A$, respectively. The comparability condition requires that the peeling angle $\theta \in [\tan^{-1}(2\pi A), \pi - \tan^{-1}(2\pi A)]$ to avoid contact between the peeled thin film and the substrate.

Figure 6.2 shows the plot of peeling force $\bar{F}$ as a function of the abscissa of the peeling front $\bar{x}_p$ for different values of aspect ratio A and peeling angle θ. For those plots we choose the normalized work of adhesion $\bar{w} = 0.005$. For the peeling on a flat surface ($A = 0$), the peeling force is constant and the equilibrium is neutral. For the peeling on a sinusoidal surface ($A > 0$), it can be seen that the variation of the peeling force has the same period with the sinusoidal surface and the peeling force depends on the local curvature of the surface. According to the stability condition in §6.2, we mark the stable and unstable equilibrium configurations of peeling on wavy substrates with solid and dashed lines in Figure 6.2, respectively. For each combination of A and θ, a series of snap-through instabilities occur during the peeling on sinusoidal surface under load control, as indicated by black arrows. We define the effective peeling force as the maximum force during peeling. It is interesting to observe from Figure 6.2 that the maximum peeling force occurs not at the crest of the surface (where $\bar{x}_p = 1/2 + n$ with n being an integer), but at the point which has the minimum surface slope

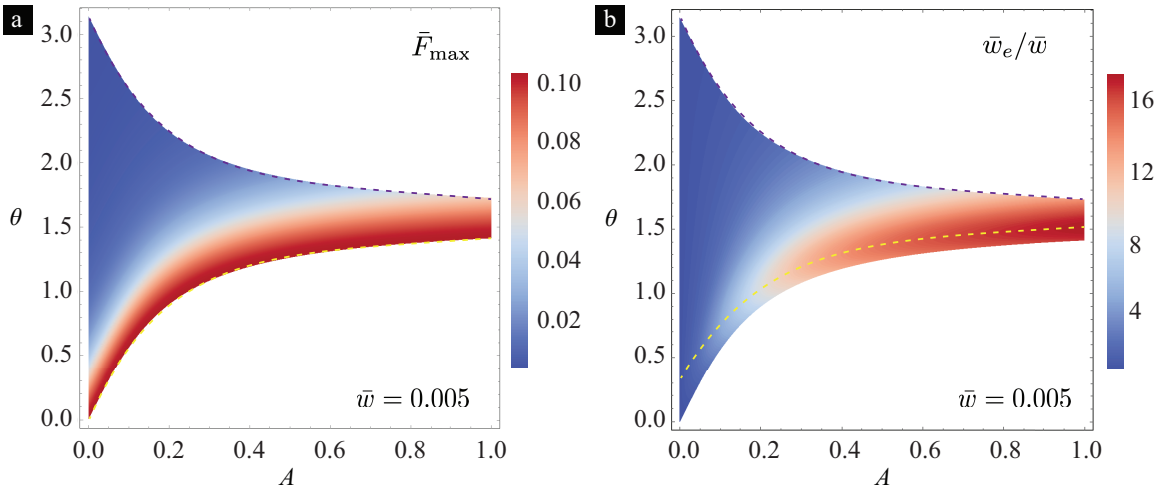

Figure 6.3: The contour plot of (a) effective peeling force $\bar{F}_{\max}$ and (b) effective work of adhesion $\bar{w}_e/\bar{w}$ as a function of the aspect ratio A and peeling angle θ with $\bar{w} = 0.005$ for the peeling on sinusoidal substrate surface. The purple and yellow dashed lines, respectively, indicate the minimum and maximum values of $\bar{F}_{\max}$ and $\bar{w}_e/\bar{w}$ for different θ at a given A.

($\bar{x}_p = 3/4 + n$). Moreover, at a given peeling angle, the maximum peeling force increases with the aspect ratio (or surface roughness). And at a given aspect ratio, the maximum peeling force decreases with peeling angle.

By taking $y'_{\min} = -2\pi A$ and $\phi_{\min} = -\tan^{-1}(2\pi A)$, we obtain the maximum peeling force from (6.17) as

$$\bar{F}_{\max} = \sqrt{\left(\frac{\cos\theta + 2\pi A\sin\theta}{\sqrt{1+4\pi^2A^2}} - 1\right)^2 + 2\bar{w}} + \frac{\cos\theta + 2\pi A\sin\theta}{\sqrt{1+4\pi^2A^2}} - 1 \tag{6.21}$$

and the effective work of adhesion from (6.18) as

$$\bar{w}_e = \frac{1}{2}\left[\cos(\theta - \tan^{-1}(2\pi A)) - \cos\theta + \sqrt{(\cos(\theta - \tan^{-1}(2\pi A)) - 1)^2 + 2\bar{w}}\right]^2 - \frac{1}{2}(\cos\theta - 1)^2. \tag{6.22}$$

The effects of peeling angle θ and aspect ratio A on the maximum peeling force (effective peeling force) $\bar{F}_{\max}$ and the effective work of adhesion $\bar{w}_e$ are shown in Figure 6.3a and b, respectively. Note that in generating the plot of Figure 6.3 we confine $\theta \in [\tan^{-1}(2\pi A), \pi - \tan^{-1}(2\pi A)]$, which is required by the compatibility condition. As can be seen, both $\bar{F}_{\max}$ and $\bar{w}_e$ increase with the aspect ratio A, which means that the adhesion can be effectively enhanced by introducing the geometrical waviness of the substrate surface. For a given aspect ratio, $\bar{F}_{\max}$ achieves its smallest value at

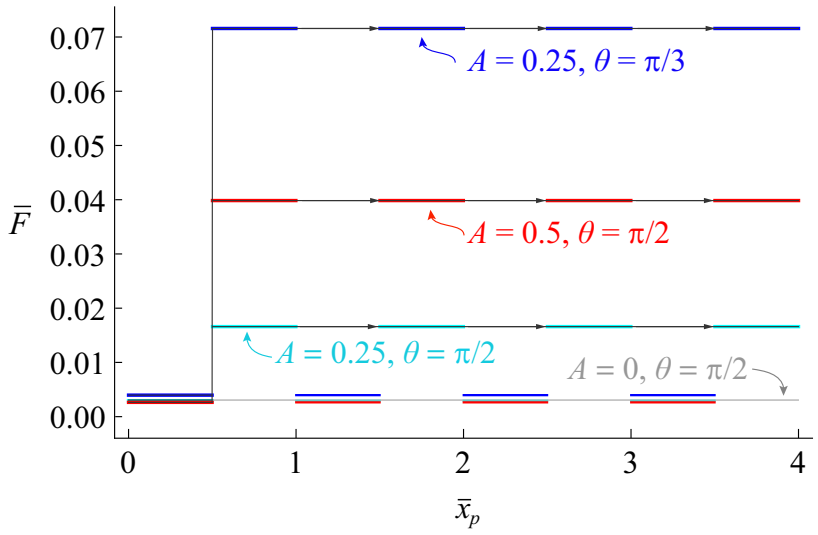

Figure 6.4: The plot of the peeling force $\bar{F}$ as a function of the abscissa of the peeling front $\bar{x}_p$ for different aspect ratio A and peeling angle θ in the case of the substrate with zigzag surface profile. The solid line indicates the neutral equilibrium configuration. The thin black lines represent the measured forces with arrows indicating snap-through instabilities during peeling under load control for $A > 0$.

$\theta = \pi - \tan^{-1}(2\pi A)$ and largest value at $\theta = \tan^{-1}(2\pi A)$, respectively. The effective work of adhesion $\bar{w}_e$ achieves its smallest value at $\theta = \pi - \tan^{-1}(2\pi A)$, whereas its largest value is obtained at

$$\theta \approx 0.5\pi \exp[1/(0.635 + 5.837A + 15.998A^2)]. \tag{6.23}$$

6.3.2 Zigzag surface

For the substrate with zigzag surface, the surface profile in one period is

$$y(x) = \begin{cases} 4Ax, & x \in [0, \lambda/2], \\ 4A\lambda(1 - x/\lambda), & x \in [\lambda/2, \lambda]. \end{cases} \tag{6.24}$$

In this case, the compatibility condition requires the peeling angle $\theta \in [\tan^{-1}(4A), \pi - \tan^{-1}(4A)]$. Figure 6.4 shows the plot of peeling force $\bar{F}$ as a function of the abscissa of the peeling front $\bar{x}_p$ for different values of aspect ratio A and peeling angle θ. For those plots we choose the normalized work of adhesion $\bar{w} = 0.005$. Note that the peeling process is in neutral equilibrium. For each combination of A and θ, a series of snap-through instabilities occur during the peeling on zigzag surface under load control, as indicated by black arrows. Moreover, at a given θ, $\bar{F}_{\max}$ increases

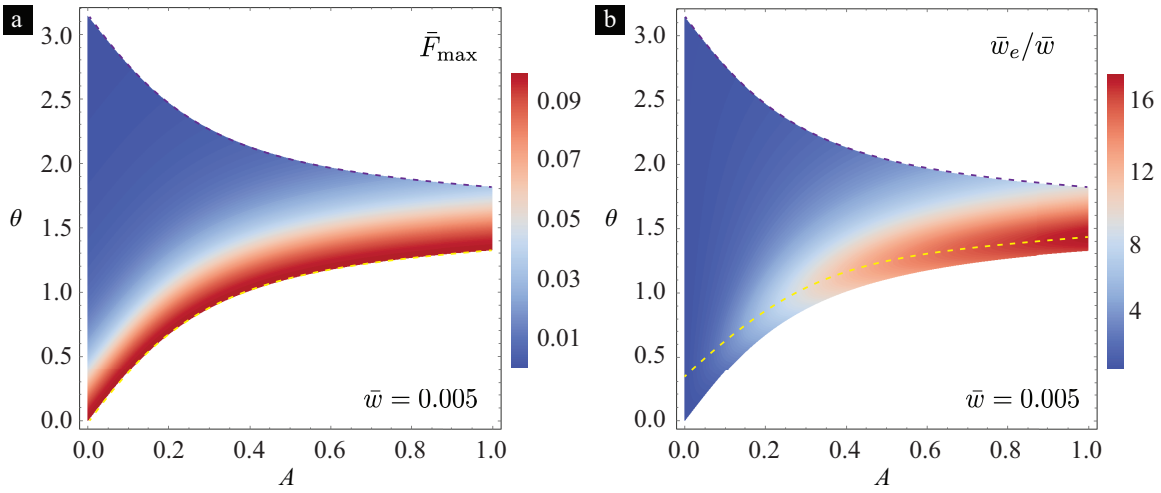

Figure 6.5: The contour plot of (a) effective peeling force $\bar{F}_{\max}$ and (b) effective work of adhesion $\bar{w}_e/\bar{w}$ as a function of the aspect ratio A and peeling angle θ with $\bar{w} = 0.005$ for the peeling on zigzag substrate surface. The purple and yellow dashed lines, respectively, indicate the minimum and maximum values of $\bar{F}_{\max}$ and $\bar{w}_e/\bar{w}$ for different θ at a given A.

with A. And at a given A, $\bar{F}_{\max}$ decreases with θ.

By taking $y'_{\min} = -4A$ and $\phi_{\min} = -\tan^{-1}(4A)$, we obtain the maximum peeling force as

$$\bar{F}_{\max} = \sqrt{\left(\frac{\cos\theta + 4A\sin\theta}{\sqrt{1+16A^2}} - 1\right)^2 + 2\bar{w}} + \frac{\cos\theta + 4A\sin\theta}{\sqrt{1+16A^2}} - 1 \tag{6.25}$$

and the effective work of adhesion as

$$\bar{w}_e = \frac{1}{2}\left[\cos(\theta - \tan^{-1}(4A)) - \cos\theta + \sqrt{(\cos(\theta - \tan^{-1}(4A)) - 1)^2 + 2\bar{w}}\right]^2 - \frac{1}{2}(\cos\theta - 1)^2. \tag{6.26}$$

The effects of peeling angle θ and aspect ratio A on $\bar{F}_{\max}$ and $\bar{w}_e$ are shown in Figure 6.5a and b, respectively. For a given aspect ratio, $\bar{F}_{\max}$ achieves its smallest value at $\theta = \pi - \tan^{-1}(4A)$ and largest value at $\theta = \tan^{-1}(4A)$, respectively; And $\bar{w}_e$ achieves its smallest value at $\theta = \pi - \tan^{-1}(4A)$, whereas its largest value is obtained at

$$\theta \approx 0.5\pi \exp[1/(0.631 + 3.786A + 6.306A^2)]. \tag{6.27}$$

6.4 Discussions

We find that a series of snap-through instabilities occur during peeling, resulting in an apparent toughening of the interface between the soft thin film and the substrate. The effective peeling force and work of adhesion increase significantly with the aspect ratio (or surface roughness) of substrate surface. The results suggest that interfacial adhesion can be enhanced by designing optimal interfacial topography.

Equation (6.17) for effective peeling force $\bar{F}_{\max}$ and (6.18) for effective work of adhesion $\bar{w}_e$ hold for the substrate with arbitrary periodic wavy surface. It is of interest to know how much of the enhancement can be achieved by introducing the surface waviness compared with the flat case. It is noted that the effective peeling force and work of adhesion mainly depend on the $y'_{\min}$ under a given peeling angle. For the surface profile described by $y(x) = y_0 + A\lambda\rho(x/\lambda)$, we have $y'_{\min} \propto A$. Let us consider two limiting cases of the aspect ratio, i.e., $A \to 0$ and $A \to \infty$ corresponding to the substrates with flat and highly oscillated steep surfaces, respectively. Assume that the peeling angle $\theta = \pi/2$, which guarantees no contact between the peeled thin film and the substrate. By limit analysis of (6.17), we obtain the asymptotic limit of the effective peeling force as

$$\bar{F}_{\max,\text{flat}} = \lim_{A\to 0} \bar{F}_{\max} = \sqrt{1+2\bar{w}} - 1 \sim \bar{w}, \tag{6.28a}$$

$$\bar{F}_{\max,\text{steep}} = \lim_{A\to \infty} \bar{F}_{\max} = \sqrt{2\bar{w}}, \tag{6.28b}$$

and define the enhancing efficiency of peeling force

$$\alpha = \frac{\bar{F}_{\max,\text{steep}}}{\bar{F}_{\max,\text{flat}}} = \frac{\sqrt{2\bar{w}}}{\sqrt{1+2\bar{w}}-1} \sim \sqrt{\frac{2}{\bar{w}}}. \tag{6.29}$$

The approximation in (6.28a) and (6.29) is reasonable when $\bar{w} \ll 1$, e.g., by taking $E = 1$ MPa, $h = 100\,\mu$m, and $w = 10\,\text{J/m}^{-2}$, we have $\bar{w} = 0.1$. We note that $\bar{F}_{\max,\text{steep}}$ is equal to the peeling force for the flat surface under the peeling angle $\theta = 0$, which is equivalent to the peeling on steep wavy substrate with $\theta = \pi/2$. Similarly, we obtain the asymptotic limit of effective work of adhesion

from (6.18) as

$$\bar{w}_{e,\text{flat}} = \lim_{A\to 0} \bar{w}_e = \bar{w}, \tag{6.30a}$$

$$\bar{w}_{e,\text{steep}} = \lim_{A\to \infty} \bar{w}_e = \bar{w} + \sqrt{2\bar{w}}, \tag{6.30b}$$

and define the enhancement efficiency of work of adhesion

$$\beta = \frac{\bar{w}_{e,\text{steep}}}{\bar{w}_{e,\text{flat}}} = 1 + \sqrt{\frac{2}{\bar{w}}}. \tag{6.31}$$

For $\bar{w} = 0.1$, we have $\alpha = 4.68$ and $\beta = 5.68$, which indicate a large enhancement of the peeling force and work of adhesion during the peeling on steep wavy surfaces.

Chapter 7

Conclusions and outlook

Fundamental understanding of the mechanics of elastic contact and adhesion of rough surfaces is important and desirable due to its wide applications in many engineering and biological fields. In this dissertation, we investigated several critical problems related to adhesive elastic contact with particular emphasis on the interplay of surface roughness and adhesion. The main findings of this dissertation are summarized as follows:

mf. i We improved the JKR theory by considering the effect of machine stiffness on interpreting contact force-indentation depth curves in adhesive elastic contact experiments. We performed stabilities analysis to investigated pull-in and pull-off instabilities under the influences of finite machine stiffness and showed that theoretical predictions of our model explain experimental measurements better than the JKR theory.

mf. ii Based on the MD theory and Nayak's theory of rough surface, we proposed a randomly rough surface contact model to study DDH in adhesive elastic contacts at large surface roughness. The computed energy loss of DDH from our model shows good consistency with the experiment result, which is predicted to decrease with roughness and increase with maximum indentation depth. Moreover, in the large roughness regime, the energy loss would fall off as the solids becomes stiffer or the range of adhesive interaction increases.

mf. iii We developed an effective, nonlinear body force based approach to simulate adhesive elastic contact using the realistic molecular potential. Our simulations provided a critical evidence

to the small-scale contact instability mechanism due to adhesion and roughness as a plausible explanation for DDH. An important feature of our nonlinear body force based simulation is that it shows the existence of two regimes: the small and large roughness regimes. The energy loss of DDH increases with roughness in the small roughness regime, whereas it decreases with roughness in the large roughness regime. These two regimes are demarcated by the surface topography and the bulk and surface material properties. The primary condition demarcating these two regimes, as seem from our simulations, is the nature of the contact region—as to whether it is simply-connected, or multiply-connected. The proposed approach for simulating adhesive elastic contact can be utilized to guide the design of surface topography to achieve reversible optimal adhesion strength.

mf. iv We investigated the principle of contact splitting for biological fibrillar structures and investigate their adhesion on rough surfaces through a multiple spring model. It is found that the remarkable adhesion enhancement by contact splitting is resulted from the increase of contact area. Moreover, the detachment of a single fibril is unable to trigger the next fibril to detach from the substrate. The additional energy needed for crack re-initiation of each fibril manifests as a better adhesion of the fibrillar structure.

mf. v We considered the quasi-static peeling of an elastic thin film from a rough substrate which it is perfectly adhering on. It is found that the effective peeling force and work of adhesion are significantly improved by surface roughness, resulting in an apparent toughening of the interface between thin film and substrate. The result suggests strategies to improve the adhesion of thin film-substrate systems in many micro- and nano-devices such as flexible and stretchable inorganic electronics.

Despite the achieved advances in this dissertation, there are several potential research topics that could be explored in the future. Those topics include:

pr. i In our randomly rough surface contact model, it is assumed that there is no interaction between surface asperities as in the GW model. This assumption greatly simplifies the calculation of the total contact force but ignores the fact that all asperities share the same substrate. Contact at the tallest asperities will deform the substrate and therefore reduce the heights of all other asperities by an amount that depends on the distance to the contacting asperity and

the response of the contacting asperity [170–173]. Therefore, the model can be improved more accurately by accounting for asperity interactions.

pr. ii Our randomly rough surface contact model applies to large surface roughness where the contact region is simply-connected, while the model in [35] applies to infinitesimally small surface roughness such that the contact region remains simply-connected. Our continuum simulations captures the transition of contact region from simply-connected to multiply-connected as surface roughness increases. Yet, currently there is no single theoretical model that applies to both small and large surface roughness regimes. Future efforts could be made to fill the gap in this direction.

pr. iii The proposed approach based on effective, nonlinear body force for simulating adhesive elastic contact can be extended to study the adhesion and roughness induced friction between two arbitrarily rough surfaces under transverse loading and obtain the effective (macro-scale) tribological properties, such as their effective friction and adhesion, as functions of the bulk and surface material properties and surface topography at a much small scale (micro-scale).

Appendix A

Supplementary Material: Effect of machine stiffness on interpreting contact force–indentation depth curves in adhesive elastic contact experiments

A.1 Solutions on the boundary of the domain $\mathcal{D}$

In this section we study the solutions as defined by (2.15) that lie on the boundary of the domain $\mathcal{D}$ of the function $\Pi(\cdot,\cdot;\Delta)$. Recall that the domain of $\Pi(\cdot,\cdot;\Delta)$ is the set $\mathcal{D} := \{(a,h) \in \mathbb{R}^2 \ : \ a \geq 0\}$. Therefore, the domain boundary $\partial\mathcal{D}$ is simply the set of points in $\mathbb{R}^2$ that are of the form $(0,h)$. As we will show, the solution points on $\partial\mathcal{D}$ could only exist in the form of $(0,\Delta)$ when $\Delta < 0$. At these points, there is no deformation of the elastic spring and the tip and the substrate are not in physical contact.

A.1.1 Points of the form $(0,h)$ where $h > 0$ cannot be solutions

A point of the form $(0,h)$ where $h > 0$ cannot be a solution to our contact mechanics problem. Given any $\delta > 0$, the neighborhood $B(0,h,\delta)$ of $(0,h)$ contains the point $(\delta/2,h)$. The value of $\Pi(\cdot,\cdot;\Delta)$

at $(\delta/2, h)$, as given by the first line in (2.13), is finite and smaller than its value at $(0,h)$. As can be determined by the third line of (2.13), it is also unbounded. That is, we are always able to find a point in the neighborhood of $(0,h)$, no matter how small the neighborhood's diameter, where the value of $\Pi(\cdot,\cdot;\Delta)$ is smaller than at $(0,h)$. Consequently, the point $(0,h)$ cannot be a solution.

A.1.2 A point (a,h) where $a = 0$ and $h < 0$ is a solution iff $\Delta < 0$ and $h = \Delta$

The difference in the value of $\Pi(\cdot,\cdot;\Delta)$ at a point $(0,h)$, where $h < 0$, and a neighboring point $(\delta a, h+\delta h)$, where $\delta a \geq 0$, can be expressed as

$$\Pi[\delta a, h+\delta h;\Delta] - \Pi[0,h;\Delta] = \mathcal{E}h^2\delta a + k_s\delta h(h-\Delta) + O(\|(\delta a,\delta h)\|^2) \tag{A.1.1}$$

in the limit of $(\delta a,\delta h) \to (0,0)$. Any sequence of points converging to $(0,h)$ where $h < 0$ can be expressed as $(\delta a_n, h+\delta h_n)_{n\in\mathbb{N}}$, where $\delta a_n \geq 0$ and the sequence $(\delta a_n,\delta h_n)$ converges to $(0,0)$. Consider the case $\Delta < 0$ and $h = \Delta$. It follows from (A.1.1) that there exists an $N \in \mathbb{N}$ such that for all $n > N$ the sign of the difference $\Pi[a_n,h_n;\Delta] - \Pi[0,h;\Delta]$ is the same as that of the leading order term $\mathcal{E}h^2\delta a_n$. Because both $\mathcal{E}$ and δa_n are positive, the leading order term is positive. This result implies that when $\Delta < 0$, the point $(0,\Delta)$ is always a solution.

Now consider the case $h \neq \Delta$ and the sequence of points $(a_n,h_n)_{n\in\mathbb{N}}$ where $a_n = 0$ and $h_n = h-(h-\Delta)/n$. This sequence of points also converge to $(0,h)$. It follows from (A.1.1) that there exists an $N \in \mathbb{N}$ such that for all $n > N$ the sign of the difference $\Pi[a_n,h_n;\Delta] - \Pi[0,h;\Delta]$ is the as same that of the term $-k_s(h-\Delta)^2/n$, which is negative because $k_s > 0$. Therefore, when $h \neq \Delta$, the point $(0,h)$ where $h < 0$ cannot be a solution. Therefore, it is implied that that a point of the form $(0,h)$ where $h < 0$ is a solution iff $\Delta < 0$ and $h = \Delta$.

A.1.3 The point $(a,h) = (0,0)$ cannot be a solution

In this section we show that the point $(a,h) = (0,0)$ cannot be a solution at any given Δ. We demonstrate this by showing that no matter how small δ is, there will always exist points in $B(0,0,\delta)$ where the value of $\Pi(\cdot,\cdot;\Delta)$ is smaller than its value at $(a,h) = (0,0)$. We begin by deriving an asymptotic series expansion for $\Pi(\cdot,\cdot;\Delta)$ in the limit $(a,h) \to 0$, with $a > 0$. In the limit $\tilde{a} \to 0$ we

know from (2.2) and (2.12) that

$$\chi(\tilde{a};h) = \frac{2h}{\pi} + \tilde{a}f'(0) + \frac{2\tilde{a}^2}{\pi}f''(0) + O(\tilde{a}^3), \tag{A.1.2}$$

where O is the Bachmann–Landau "Big-Oh" symbol. We then obtain

$$\chi(\tilde{a};h)^2 = \frac{4h^2}{\pi^2} + \frac{4ahf'(0)}{\pi} + a^2\left(\frac{8hf''(0)}{\pi^2} + f'(0)^2\right) + O(\tilde{a}^3). \tag{A.1.3}$$

After substituting (A.1.3) into (2.13) and simplifying, we determine that

$$\begin{aligned}\frac{\pi^2\mathcal{E}}{4}\int_0^a \chi(\tilde{a};h)^2\,d\tilde{a} =& \mathcal{E}h^2a + \frac{\pi}{2}\mathcal{E}hf'(0)a^2 \\ &+ \mathcal{E}\left(\frac{2}{3}hf''(0) + \frac{\pi^2}{12}f'(0)^2\right)a^3 + O(a^4).\end{aligned} \tag{A.1.4}$$

It follows that in the limit $(a,h) \to (0,0)$ with $a > 0$, the potential energy can be written as

$$\begin{aligned}\Pi(a,h;\Delta) =& \frac{1}{2}k_s\Delta^2 - k_s\Delta h + \frac{1}{2}k_sh^2 - \pi wa^2 \\ &+ \mathcal{E}h^2a + \frac{\pi}{2}\mathcal{E}f'(0)ha^2 + \mathcal{E}\frac{\pi^2}{12}f'(0)^2a^3 + O(\|(a,h)\|^4).\end{aligned} \tag{A.1.5}$$

When $(a,h) = (0,0)$ the value of $\Pi(\cdot,\cdot;\Delta)$ equals $k_s\Delta^2/2$. Taking this into account, it follows from (A.1.5) that in the limit $(a,h) \to (0,0)$ with $a > 0$,

$$\Pi(a,h;\Delta) - \Pi(0,0;\Delta) = -k_s\Delta h + \frac{1}{2}k_sh^2 - \pi wa^2 + O(\|(a,h)\|^3). \tag{A.1.6}$$

First consider the case $|\Delta| \neq 0$. In this case, using (A.1.6), we can express that

$$\Pi(a,h;\Delta) - \Pi(0,0;\Delta) = -k_s\Delta h + O(\|(a,h)\|^2) \tag{A.1.7}$$

in the limit $(a,h) \to (0,0)$ with $a > 0$. The asymptotic expansion given by (A.1.7) holds for all sequences $(a_n,h_n)n \in \mathbb{N}$ converging to $(0,0)$ in which $a_n > 0$. An example of such a sequence is $(|\Delta|/n, \Delta/n)n \in \mathbb{N}$. In this sequence, it follows from (A.1.7) and the definition of $O(\cdot)$ that there exists an $N \in \mathbb{N}$ such that for all $n > N$ the sign of $\Pi(a_n,h_n;\Delta) - \Pi(0,0;\Delta)$ is the same as that

of $-k_s\Delta^2/n$. Since $k_s > 0$, this result implies that no matter how small we choose δ there will always exist a point in $B(0,0,\delta)$ where the value of $\Pi(\cdot,\cdot;\Delta)$ is smaller than its value at the point $(a,h) = (0,0)$. This proves that when $|\Delta| \neq 0$, the point $(a,h) = (0,0)$ cannot be a solution.

Now let us consider the case $|\Delta| = 0$. For this case, using (A.1.6), we can express

$$\Pi(a,h;\Delta) - \Pi(0,0;\Delta) = \frac{1}{2}k_s h^2 - \pi w a^2 + O(\|(a,h)\|^3). \tag{A.1.8}$$

Consider the sequence $(a_n,h_n)_{n\in\mathbb{N}}$ when $a_n = |\Delta|/n$ and $h_n = 0$. Note that this is an admissible sequence since $a_n > 0$ for all n. For this sequence, it follows from (A.1.8) and the definition of $O(\cdot)$ that there exists an $N \in \mathbb{N}$ such that for all $n > N$ the sign of $\Pi(a_n,h_n;\Delta) - \Pi(0,0;\Delta)$ is the same as that of $-\pi w\Delta^2/n^2$. Since $w > 0$, this result implies that no matter how small we choose δ there will always exist a point in $B(0,0,\delta)$ where the value of $\Pi(\cdot,\cdot;\Delta)$ is smaller than its value at the point $(a,h) = (0,0)$. Hence, even in the case $|\Delta| = 0$, the point $(a,h) = (0,0)$ cannot be a solution.

A.2 Sign of $\chi(a;h)$

We take the negative root of $\chi(a^\circ;h^\circ)$ from (2.16b). This is because a negative sign implies tensile tractions close to the contact periphery, whereas a positive sign implies a compressive tractions close to the contact periphery. Adhesion indicates an attractive interaction between the surfaces. Thus, for the case of adhesive contact, the traction in a region close enough to the contact periphery has to be tensile when in equilibrium. The proof is as follows. According to [71], the surface traction of the elastic half-space is

$$\begin{aligned} t_z(r,z=0;h) &= -\frac{\mathcal{E}}{2r}\frac{d}{dr}\int_r^a \frac{\chi(\tilde{a};h)\tilde{a}}{\sqrt{\tilde{a}^2-r^2}}\,d\tilde{a} \\ &= -\frac{\mathcal{E}}{2r}\frac{d}{dr}\left[\chi(a;h)\sqrt{a^2-r^2} - \int_r^a \chi'(\tilde{a};h)\sqrt{\tilde{a}^2-r^2}\,d\tilde{a}\right] \\ &= -\frac{\mathcal{E}}{2r}\left[-\chi(a;h)\frac{r}{\sqrt{a^2-r^2}} + r\int_r^a \chi'(\tilde{a};h)\sqrt{\tilde{a}^2-r^2}\,d\tilde{a}\right] \\ &= \frac{\mathcal{E}}{2}\left[\frac{\chi(a;h)}{\sqrt{a^2-r^2}} - \int_r^a \chi'(\tilde{a};h)\sqrt{\tilde{a}^2-r^2}\,d\tilde{a}\right], \end{aligned} \tag{A.2.1}$$

where $\chi'(a;h) = \partial\chi(\tilde{a};h)/\partial\tilde{a}$. Let $a = a^\circ$, $h = h^\circ$, and $r = (1-\varepsilon)a^\circ$, where $\varepsilon \to 0^+$. After substituting, (A.2.1) becomes

$$t_z((1-\varepsilon)a^\circ;h^\circ) = \frac{\mathcal{E}}{2a^\circ}\left[\frac{\chi(a^\circ;h^\circ)}{\sqrt{2\varepsilon}} + O(\sqrt{\varepsilon})\right]. \tag{A.2.2}$$

If the traction close to the contact periphery has to be negative (or tensile traction according to the convention of [71]), then it requires that $\chi(a^\circ;h^\circ) < 0$, i.e.,

$$\chi(a^\circ;h^\circ) = -\sqrt{\frac{8a^\circ w}{\pi\mathcal{E}}}. \tag{A.2.3}$$

Another reason why $\chi(a^\circ;h^\circ) < 0$ is that the surfaces should not intersect with each other outside of the contact region. The displacement discontinuity outside the contact region $[\tilde{u}]_z$ is [1]

$$[\tilde{u}_z(r;h)] = -\int_a^r \frac{\chi(\tilde{a};h)}{\sqrt{r^2-\tilde{a}^2}}\,d\tilde{a}. \tag{A.2.4}$$

Let $a = a^\circ$, $h = h^\circ$, and $r = (1+\varepsilon)a^\circ$, as $\varepsilon \to 0^+$. Then, (A.2.4) becomes

$$\begin{aligned}[\tilde{u}_z((1+\varepsilon)a^\circ;h^\circ)] &= -\int_{a^\circ}^{(1+\varepsilon)a^\circ} \frac{\chi(\tilde{a};h^\circ)}{\sqrt{((1+\varepsilon)a^\circ)^2-\tilde{a}^2}}\,d\tilde{a} \\ &= -\chi(a^\circ;h^\circ)\sqrt{2\varepsilon} + O(\varepsilon).\end{aligned} \tag{A.2.5}$$

Because the surfaces do not intersect, this implies that $[\tilde{u}]_z > 0$ outside the contact region. Therefore it requires that $\chi(a^\circ;h^\circ) < 0$.

A.3 Second order necessary and sufficient conditions on interior solution points

In A.3.1 we present the general form of the second order necessary condition on an interior solution point (a^*,h^*), and a second order sufficient condition that a stationary point (a°,h°) needs to satisfy in order for it to be an interior solution point. Recall that a stationary point (a°,h°) is an interior point that is also a root of the function (2.21). These conditions are given in terms of the second partial

derivatives of $\Pi(\cdot,\cdot;\Delta)$. We derive expressions for the second partial derivatives of $\Pi(\cdot,\cdot;\Delta)$ at a stationary point in A.3.2. In A.3.3 we make use of those expressions to particularize and simplify the general conditions that we present in A.3.1. In this section we take (a^*,h^*) to denote an interior solution point.

A.3.1 General second order necessary and sufficient conditions from optimization theory

It can be shown that $\Pi(\cdot,\cdot;\Delta)$ is twice continuously differentiable on $\text{int}(\mathcal{D})$. Therefore, it follows from standard nonlinear optimization theory that a second order necessary condition on (a^*,h^*) is that the value of its corresponding quadratic form is always non-negative. The quadratic form corresponding to a point (a,h) is the function $Q(\cdot,\cdot;a,h):\mathbb{R}^2\backslash(0,0)\to\mathbb{R}$, where

$$Q(x,y;a,h) := x^2\frac{\partial^2\Pi}{\partial a^2}(a,h;\Delta)+2xy\frac{\partial^2\Pi}{\partial a\partial h}(a,h;\Delta)+y^2\frac{\partial^2\Pi}{\partial h^2}(a,h;\Delta). \tag{A.3.1}$$

The quadratic form $Q(\cdot,\cdot;a^*,h^*)$ is always non-negative iff

$$\frac{\partial^2\Pi}{\partial h^2}(a^*,h^*;\Delta)\geq 0, \tag{A.3.2a}$$

$$\frac{\partial^2\Pi}{\partial a^2}(a^*,h^*;\Delta)\frac{\partial^2\Pi}{\partial h^2}(a^*,h^*;\Delta)-\frac{\partial^2\Pi}{\partial a\partial h}(a^*,h^*;\Delta)^2\geq 0, \tag{A.3.2b}$$

$$\frac{\partial^2\Pi}{\partial a^2}(a^*,h^*;\Delta)\geq 0. \tag{A.3.2c}$$

According to optimization theory, a sufficient condition for a stationary point (a°,h°) to be an interior solution point is that the value of its corresponding quadratic form must always be positive. The quadratic form corresponding to (a°,h°), namely $Q(\cdot,\cdot;a^\circ,h^\circ)$, is always positive iff

$$\frac{\partial^2\Pi}{\partial a^2}(a^\circ,h^\circ;\Delta)\frac{\partial^2\Pi}{\partial h^2}(a^\circ,h^\circ;\Delta)-\frac{\partial^2\Pi}{\partial a\partial h}(a^\circ,h^\circ;\Delta)^2>0, \tag{A.3.3a}$$

$$\frac{\partial^2\Pi}{\partial a^2}(a^\circ,h^\circ;\Delta)>0. \tag{A.3.3b}$$

A.3.2 Second order partial derivatives of $\Pi(\cdot,\cdot;\Delta)$ at an interior solution point

After differentiating (2.17) with respect to a and h, we find that

$$\frac{\partial^2\Pi}{\partial a^2}(a,h;\Delta) = \frac{\pi^2\mathcal{E}}{2}\chi(a;h)\frac{\partial\chi(a;h)}{\partial a} - 2\pi w, \tag{A.3.4a}$$

$$\frac{\partial^2\Pi}{\partial a\partial h}(a,h;\Delta) = \frac{\pi^2\mathcal{E}}{2}\chi(a;h)\frac{\partial\chi(a;h)}{\partial h}, \tag{A.3.4b}$$

$$\frac{\partial^2\Pi}{\partial h^2}(a,h;\Delta) = \frac{\pi^2\mathcal{E}}{2}\int_0^a\left\{\left(\frac{\partial\chi(\tilde{a};h)}{\partial h}\right)^2 + \chi(\tilde{a};h)\frac{\partial^2\chi(\tilde{a};h)}{\partial h^2}\right\}d\tilde{a} + k_s. \tag{A.3.4c}$$

It follows from (2.12) that

$$\frac{\partial\chi(\tilde{a};h)}{\partial h} = \frac{2}{\pi}. \tag{A.3.5}$$

In light of (A.3.5), (A.3.4) is reduced to

$$\frac{\partial^2\Pi}{\partial a^2}(a,h;\Delta) = \frac{\pi^2\mathcal{E}}{2}\chi(a;h)\frac{\partial\chi(a;h)}{\partial a} - 2\pi w, \tag{A.3.6a}$$

$$\frac{\partial^2\Pi}{\partial a\partial h}(a,h;\Delta) = \pi\mathcal{E}\chi(a;h), \tag{A.3.6b}$$

$$\frac{\partial^2\Pi}{\partial h^2}(a,h;\Delta) = 2\mathcal{E}a + k_s. \tag{A.3.6c}$$

Equation (A.3.6) gives the second partial derivatives of $\Pi(\cdot,\cdot;\Delta)$ at any interior point (a,h). Using (A.3.6) we next evaluate the second partial derivatives of $\Pi(\cdot,\cdot;\Delta)$ at a stationary point (a°,h°). To simply these derivatives, we first recall an important result discussed in §2.2.3, which is that

$$\chi(a^\circ;h^\circ) = -\sqrt{\frac{8a^\circ w}{\pi\mathcal{E}}}. \tag{A.3.7}$$

We first substitute (a,h) in (A.3.6) with (a°,h°). In the resulting equation, we then substitute $\chi(a^\circ;h^\circ)$ with the expression on the right side of (A.3.7). After simplifying, we determine that

$$\frac{\partial^2\Pi}{\partial a^2}(a^\circ,h^\circ;\Delta) = -\sqrt{2\pi^3 a^\circ \mathcal{E} w}\frac{\partial\chi(a;h)}{\partial a}\bigg|_{(a^\circ,h^\circ)} - 2\pi w, \tag{A.3.8a}$$

$$\frac{\partial^2\Pi}{\partial a\partial h}(a^\circ,h^\circ;\Delta) = -\sqrt{8\pi a^\circ \mathcal{E} w}, \tag{A.3.8b}$$

$$\frac{\partial^2\Pi}{\partial h^2}(a^\circ,h^\circ;\Delta) = 2\mathcal{E}a^\circ + k_s. \tag{A.3.8c}$$

Recall that by definition (a°,h°) is a root of the function (2.21). The application of the *Implicit function theorem* to function (2.21) infers the existence of the function $\hbar$, which is defined in (2.22). Additionally, it implies that

$$\frac{\partial\chi(a;h)}{\partial a}\bigg|_{(a^\circ,h^\circ)} = -\sqrt{\frac{2w}{\pi a^\circ \mathcal{E}}} - \frac{2}{\pi}\hbar'(a^\circ). \tag{A.3.9}$$

We can then simplify (A.3.8a) to

$$\frac{\partial^2\Pi}{\partial a^2}(a^\circ,h^\circ;\Delta) = \hbar'(a^\circ)\sqrt{8\pi a^\circ \mathcal{E} w}. \tag{A.3.10}$$

In summary, the second partial derivatives of $\Pi(\cdot,\cdot;\Delta)$ at an interior solution point are

$$\frac{\partial^2\Pi}{\partial a^2}(a^\circ,h^\circ;\Delta) = \hbar'(a^\circ)\sqrt{8\pi a^\circ \mathcal{E} w}, \tag{A.3.11a}$$

$$\frac{\partial^2\Pi}{\partial a\partial h}(a^\circ,h^\circ;\Delta) = -\sqrt{8\pi a^\circ \mathcal{E} w}, \tag{A.3.11b}$$

$$\frac{\partial^2\Pi}{\partial h^2}(a^\circ,h^\circ;\Delta) = 2a^\circ\mathcal{E} + k_s. \tag{A.3.11c}$$

A.3.3 Simplified second order necessary and sufficient conditions

A second order sufficiency condition for stationary points

It follows from (A.3.11c) that $\partial^2\Pi/\partial h^2(a^\circ,h^\circ;\Delta) > 0$ at all stationary points, since at any stationary point $a^\circ > 0$ and by construction $\mathcal{E}$ and k_s are positive. Therefore, if (a°,h°) satisfies the inequality (A.3.3a), then it also satisfies the inequality (A.3.3b). Therefore, in order for a point to be a solution point, the only non-redundant sufficient condition on (a°,h°) is given by (A.3.3a). It follows from

(A.3.11) that a stationary point (a°, h°) satisfies the sufficient condition (A.3.3a) iff

$$g(a^\circ) = \hbar'(a^\circ) - \frac{\sqrt{8\pi a^\circ \mathcal{E} w}}{2a^\circ \mathcal{E} + k_s} > 0. \tag{A.3.12}$$

A second order necessary condition for interior solution points

Since an interior solution point is also a stationary point (§2.2.3), then we obtain from (A.3.11) that

$$\frac{\partial^2 \Pi}{\partial a^2}(a^*, h^*; \Delta) = \hbar'(a^*)\sqrt{8\pi a^* \mathcal{E} w}, \tag{A.3.13a}$$

$$\frac{\partial^2 \Pi}{\partial a \partial h}(a^*, h^*; \Delta) = -\sqrt{8\pi a^* \mathcal{E} w}, \tag{A.3.13b}$$

$$\frac{\partial^2 \Pi}{\partial h^2}(a^*, h^*; \Delta) = 2a^* \mathcal{E} + k_s. \tag{A.3.13c}$$

The necessary condition (A.3.2a) does not lead to any additional conditions on the interior solution point (a^*, h^*). This is because it follows from (A.3.13c) that at any interior solution point $\partial^2 \Pi / \partial h^2(a^*, h^*; \Delta) > 0$, since at any interior solution point $a^* > 0$ and by construction $\mathcal{E}$ and k_s are positive.

It follows from (A.3.13) that the necessary condition (A.3.2b) holds iff $g(a^*) \geq 0$. The function g is defined in (2.23). If (a^*, h^*) satisfies the necessary condition (A.3.2b), then it also satisfies the necessary condition (A.3.2c). This is because if $\hbar'(a^*)$ is non-negative, then (A.3.13a) would imply that the necessary condition (A.3.2c) is satisfied.

If (a^*, h^*) satisfies the necessary condition (A.3.2b), then

$$g(a^*) = \hbar'(a^*) - \frac{\sqrt{8\pi a^* \mathcal{E} w}}{2a^* \mathcal{E} + k_s}$$

is non-negative and

$$\hbar'(a^*) \geq \frac{\sqrt{8\pi a^* \mathcal{E} w}}{2a^* \mathcal{E} + k_s}. \tag{A.3.14}$$

At any interior solution point, a^* is positive. By construction, $\mathcal{E}$ and k_s are positive and w is non-negative, thus (A.3.14) implies that $\hbar'(a^*)$ is non-negative.

A.4 Fitting contact experimental data to theory

In §2.4 we apply our model given in §2.3.1 to the experiments of Sun *at al.* [58] and Notbohm *et al.* [59]. It follows from (2.31b) and (2.32b) that the measured indentation depth, h, and the contact force, P, in those experiments should satisfy

$$h = F(P;\hat{a},\hat{P}), \tag{A.4.1}$$

where

$$F(P;\hat{a},\hat{P}) := \frac{4^{2/3}\hat{a}^2}{R}\left[\left(\frac{1+\sqrt{1+P/\hat{P}}}{2}\right)^{4/3} - \frac{2}{3}\left(\frac{1+\sqrt{1+P/\hat{P}}}{2}\right)^{1/3}\right],$$

and

$$\hat{a} := (9\pi w R^2/8\mathcal{E})^{1/3}, \tag{A.4.2a}$$

$$\hat{P} := 3\pi w R/2. \tag{A.4.2b}$$

Say (h_i,P_i), $i=1,2,...,n$, where n is a positive integer, is a sequence of indentation depth–contact force measurements. An estimate of the mismatch between the theory and experimental results can be

$$S(\hat{a},\hat{P}) := \sum_{i=1}^{n} r_i(\hat{a},\hat{P})^2, \tag{A.4.3}$$

where

$$r_i(\hat{a},\hat{P}) := h_i - F(P_i;\hat{a},\hat{P}), \tag{A.4.4}$$

and $i=1,2,...,n$. We take the best values for the parameters $\hat{a}$ and $\hat{P}$ to be those at which S attains its minimum. Denoting the best fit values of $\hat{a}$ and $\hat{P}$ as $\hat{a}^*$ and $\hat{P}^*$, respectively, a necessary condition that S attains its minimum at $(\hat{a}^*,\hat{P}^*)$ is that

$$\frac{\partial S}{\partial \hat{a}}(\hat{a}^*,\hat{P}^*) = 0, \tag{A.4.5a}$$

$$\frac{\partial S}{\partial \hat{P}}(\hat{a}^*,\hat{P}^*) = 0. \tag{A.4.5b}$$

We obtain $\hat{a}^*$ and $\hat{P}^*$ by numerically solving (A.4.5a)–(A.4.5b), which are a pair of coupled, nonlinear algebraic equations. The best fit values for w and $\mathcal{E}$ are then obtained by simultaneously solving (A.4.2a)–(A.4.2b) for w and $\mathcal{E}$ after first replacing in them $\hat{a}$ and $\hat{P}$ with their respective best fit values and R with its experimentally reported value.

Appendix B

Supplementary Material: Depth-dependent hysteresis in adhesive elastic contacts at large surface roughness

B.1 RMS roughness, PSD function, and spectral moments

For a rough surface whose height is described by the topography function $z : \mathbb{R}^2 \to \mathbb{R}$, its RMS roughness can be computed as

$$\sigma_{\text{rms}} = \left[\frac{1}{L_1 L_2} \int_0^{L_1} \int_0^{L_2} z(x_1, x_2)^2 \, dx_1 dx_2 \right]^{1/2}, \tag{B.1.1}$$

where L_1 and L_2 are the widths of a rectangular, nominal contact region in the $\hat{e}_1$ and $\hat{e}_2$ directions, respectively. The auto-correlation function corresponding to z can be defined as

$$R(x_1, x_2) = \lim_{L_1, L_2 \to \infty} \frac{1}{L_1 L_2} \int_0^{L_1} \int_0^{L_2} z(x_1', x_2') z(x_1' + x_1, x_2' + x_2) \, dx_1' dx_2'. \tag{B.1.2}$$

The rough surface's PSD function $C : \mathbb{R}^2 \to \mathbb{R}$ is the Fourier transform of R, i.e.,

$$C(q_1, q_2) = \int_{-\infty}^{\infty} \int_{-\infty}^{\infty} R(x_1, x_2) e^{-i(x_1 q_1 + x_2 q_2)} \, dx_1 dx_2, \tag{B.1.3}$$

where q_1, $q_2 \in \mathbb{R}$ are termed the wavevector components and i is the imaginary number $\sqrt{-1}$. Alternatively, the PSD function can also be computed as

$$C(q_1, q_2) = \lim_{L_1, L_2 \to \infty} \left[\frac{1}{L_1 L_2} \int_0^{L_1} \int_0^{L_2} z(x_1, x_2) e^{-i(x_1 q_1 + x_2 q_2)} \, dx_1 dx_2 \right]^2. \tag{B.1.4}$$

The PSD function's spectral moments are defined as

$$m_{kl} = \frac{1}{4\pi^2} \int_{-\infty}^{\infty} \int_{-\infty}^{\infty} C(q_1, q_2) q_1^k q_2^l \, dq_1 dq_2, \tag{B.1.5}$$

where k, $l \in \mathbb{N}$. In isotropic surfaces, the PSD function only depends on the wavenumber $q = \sqrt{q_1^2 + q_2^2}$. In this case, the isotropic PSD function C^{iso} is defined as

$$C^{\text{iso}}(q) := \frac{1}{2\pi} \int_0^{2\pi} C(q\cos\theta, q\sin\theta) \, d\theta. \tag{B.1.6}$$

Furthermore, for isotropic surfaces $m_{kl} = m_{lk}$. Therefore, Nayak [75] introduced the spectral moments $m_n := m_{n0} = m_{0n}$, $n = 0$, 2, and 4. These moments can be computed from C^{iso} as

$$\begin{aligned} m_n &= \int_0^{\infty} \int_0^{2\pi} C^{\text{iso}}(q) (q\sin\theta)^n q \, d\theta dq, \\ &= \frac{2\sqrt{\pi}\Gamma((1+n)/2)}{\Gamma(1+n/2)} \int_0^{\infty} q^{n+1} C^{\text{iso}}(q) \, dq, \end{aligned} \tag{B.1.7}$$

where Γ is the Gamma function.

In practice, the topography function z is measured only at a discrete set of points that are positioned on a rectangular grid. The points are equally spaced with intervals $\Delta x_1 = L_1/N_1$ and $\Delta x_2 = L_2/N_2$ in the $\hat{e}_1$ and $\hat{e}_2$ directions, respectively. The positive integers N_1 and N_2 denote the total number of points in the two directions, respectively. We denote the values of z measured at the discrete set of points as $\tilde{z}(m,n)$, $m = 0, 1, ..., N_1 - 1$ and $n = 0, 1, ..., N_2 - 1$. In concurrence with our definition of z, the datum in the $\hat{e}_3$ direction is chosen such that these discrete set of values have

a zero mean. Assuming that the surface topography is periodic with periodicities L_1 and L_2 in the $\hat{e}_1$ and $\hat{e}_2$ directions, respectively, we compute the discrete Fourier transform of $\tilde{z}(m,n)$ as

$$Z(k,l) = \Delta x_1 \Delta x_2 \sum_{m=0}^{N_1-1} \sum_{n=0}^{N_2-1} \tilde{z}(m,n) e^{-i2\pi(mk/N_1 + nl/N_2)}, \tag{B.1.8}$$

where $k = 0, 1, ..., N_1 - 1$ and $l = 0, 1, ..., N_2 - 1$. It can be shown using (B.1.4) that

$$C(q_k, q_l) \approx \tilde{C}(q_k, q_l) := \frac{|Z(k,l)|^2}{L_1 L_2}, \tag{B.1.9}$$

where $q_k = 2\pi k/L_1$ and $q_l = 2\pi l/L_2$ are termed the discrete wavevector components, and $\tilde{C}$ is called the discrete PSD function. Similarly, using (B.1.6) it can be shown that

$$C^{\text{iso}}(q) \approx \tilde{C}^{\text{iso}}(q), \tag{B.1.10}$$

where the value $\tilde{C}^{\text{iso}}(q)$ is obtained by averaging the value of $\tilde{C}$ over all pairs (q_k, q_l) for which $\sqrt{q_k^2 + q_l^2} = q$. The ordinates of the discrete set of points shown in Figure 3.7d of the main text are the values of the function $\tilde{C}^{\text{iso}}$. We assume that the PSD function in the experiments is the continuous, power-law PSD function given in (3.16) of the main text. We choose the parameters defining the power law PSD function in such a way so as to make the function's values as close as possible to the values of $\tilde{C}^{\text{iso}}$.

B.2 Nominal contact area as per the JKR theory

For computing the nominal contact area ΔA_c in Kesari *et al.*'s experiments, we ignore the roughness of both the tip and the substrate and model the loading branch of the experiments using the JKR theory. The indentation depth, h, and the contact radius a, in the loading phase of the experiments are then related as

$$\bar{h} = -\bar{a}^2 + (2\ell_{\text{JKR}}\bar{a})^{1/2}, \tag{B.2.1}$$

where $\bar{h} = h/R_t$, $\bar{a} = a/R_t$, and $\ell_{\text{JKR}} = \pi w/E^* R_t$. The parameters w, E^*, and R_t are defined in the Theory section of the main text. We denote the radii of the contact regions in the loading phase of

the experiment when $\bar{h} = 0$ and $\bar{h}_{\min}$ as $\bar{a}_0$ and $\bar{a}_{h_{\min}}$, respectively, where $\bar{h}_{\min} := h_{\min}/R_t$. In terms of these radii the contact areas $A_c^{h_{\min}}$ and A_c^0, defined in the section of Theory of the main text, are $\pi\bar{a}_{h_{\min}}^2 R_t^2$ and $\pi\bar{a}_0^2 R_t^2$, respectively. It follows then from (3.10) of the main text and (B.2.1) that

$$\Delta A_c = \pi R_t^2 |\bar{h}_{\min}| \left[1 + \frac{(2\ell_{\rm JKR}\bar{a}_{h_{\min}})^{1/2} - (2\ell_{\rm JKR})^{2/3}}{\bar{a}_{h_{\min}}^2 - (2\ell_{\rm JKR}\bar{a}_{h_{\min}})^{1/2}} \right]. \tag{B.2.2}$$

By fitting the loading branch of the the experimental P–h curves shown in Figure 3.2a of the main text to the JKR theory we found that $w = 20$ mJ/m^2 and $E^* = 0.75$ MPa. Recall that the radius of the glass bead (tip) in the experiments is $R_t = 25\ \mu$m. Thus, we have $\ell_{\rm JKR} = 3.35 \times 10^{-3}$. In the experiments $|h_{\min}|$ ranges from 0 to 1500 nm. For this variation in $h_{\min}$, we found numerically from (B.2.1) that $\bar{a}$ varies from 0.189 to 0.327. Consequently, the term in the square bracket in (B.2.2) varies from 1.19 to 1.33, which has a variation of only $\sim 10\%$. Therefore, we approximate this term as 1.26, and from (B.2.2) we obtain that

$$\Delta A_c \approx 4R_t|h_{\min}|. \tag{B.2.3}$$

B.3 The RMS roughness of the glass bead

In Table B.1 we report the RMS roughness of four glass beads. As can be noted, the beads' RMS roughness ranges from 2.59 nm to 12.14 nm. The RMS roughness of the glass beads is 6.41 ± 4.18 nm (mean $\pm$ standard deviation). Figure B.1 shows a microscope image taken during the AFM topography measurements. The AFM cantilever (white beam in Figure B.1) in those measurements has an atomically sharp, silicon nitride tip. These beads (dark spheres in Figure B.1) were sampled from the same population as from which the bead used in the experiments reported by Kesari *et al.* [27] was taken. The surface topography of the bead that is labelled as Bead #3 in Table B.1 is shown in Figures 3.7a–b.

Table B.1: The RMS Roughness of the glass beads.

Bead #	1	2	3	4
RMS roughness (nm)	6.68	2.59	12.14	4.21

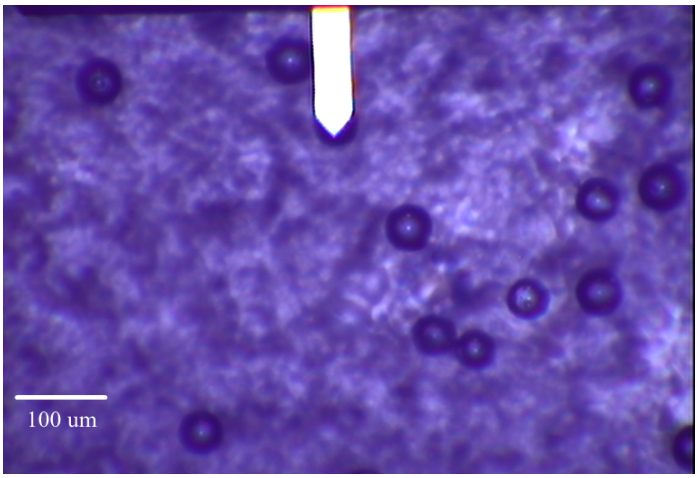

Figure B.1: Silicon cantilever on the top of a 50 μm-diameter bead in double-sided Scotch Tape.

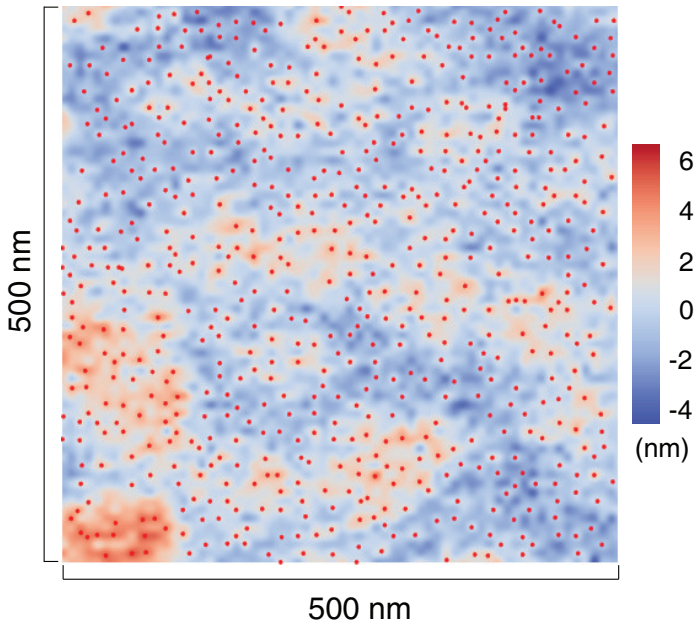

Figure B.2: The local peaks (red dots) over a partial region of the Si mold's rough surface. The color denotes the height of the surface.

B.4 The average of the distance between each asperity and its nearest neighbor on the Si mold's surface

Figure B.2 shows a representative region of the Si mold's surface which is shown in Figure 3.7c. We identified all the local peaks of the asperities over the Si mold's rough surface in Figure 3.7c. The local peak is defined as the highest point around a neighbor region, as shown in red dots of Figure B.2. We calculate the average of the distance between each asperity and its nearest neighbor

to be 17 nm. This value is very consistent with the correlation length ($L = 20.1$ nm) of the Si mold's rough surface that is obtained from the PSD fitting of the surface power spectrum.

Appendix C

Supplementary Material: Multiple spring model for adhesion of biological fibriallar structures

C.1 Generation of randomly rough surfaces

Surface topography measurements using contact methods (stylus instruments, AFM, etc. [174]) and optical non-contact methods (interferometry, deflectometry, etc. [175]) have shown that a wide range of natural and synthetic rough surfaces show characteristics of self-affine scaling, called as self-affine fractal surfaces [85]. As per Archard's model [176], the underlying picture is that roughness consists of asperities, which are covered with smaller asperities, which in turn are covered with even smaller asperities. A self-affine fractal surface has the property that the statistical properties of the surface are invariant if part of the surface is magnified.

Rough surfaces are also characterized as a stochastic process [75, 177, 178]. In the random process description of rough surfaces, there are two important statistical functions: the probability density function (PDF) of surface height which is typically Gaussian and the auto-correlation function (ACF) which describes the spatial features of roughness. The ACF is often taken to be an exponential form or a Gaussian.

We adopt the stochastic characterization of rough surfaces. Furthermore, we assume that the rough surface is homogeneous and isotropic. That is, the PDF characterizing the different geometric features of the asperities does not depend on the location or the orientation of the surface. We only consider the Gaussian ACF here, which is given as

$$R_{zz}(\delta_x,\delta_y)=\mathrm{E}\{z(x,y)z(x+\delta_x,y+\delta_y)\}=\sigma_{\mathrm{rms}}^2 e^{-(\delta_x^2/L_{cx}^2+\delta_y^2/L_{cy}^2)}, \tag{C.1.1}$$

where $\mathrm{E}\{\cdot\}$ denotes the expectation, L_{cx} and L_{cy} are the correlation lengths in the $\hat{e}_1$ and $\hat{e}_2$ directions, respectively. If the surface is isotropic, then its ACF becomes

$$R_{zz}(\delta)=\frac{\sigma_{\mathrm{rms}}^2}{4\pi^2}e^{-\delta^2/L_c^2}, \tag{C.1.2}$$

where $\delta=\sqrt{\delta_x^2+\delta_y^2}$, $L_c=L_{cx}=L_{cy}$. The PSD function is 2π times the zeroth-order Hankel transform of $R_{zz}(\delta)$ in the symmetric case, i.e.,

$$C(q)=2\pi\int_0^\infty R_{zz}(\delta)J_0(\delta q)\delta d\delta=\frac{\sigma_{\mathrm{rms}}^2 L_c^2}{4\pi}e^{-L_c^2q^2/4}, \tag{C.1.3}$$

where q is the wave-number and J_0 is the zeroth-order Bessel function of the first kind.

In this Appendix, we describe the numerical procedure of generation of randomly rough surfaces which are used to study adhesive elastic contacts. This procedure is based on the method proposed by Hu and Tonder [179]. The approach is to first generate a set of uncorrelated Gaussian random numbers for the surface heights and then apply a linear filter to it. The weights of the linear filter are chosen such that the final surface heights have the prescribed ACF.

Our purpose is to generate a discrete three-dimension randomly rough surface with a Gaussian PDF and a Gaussian ACF. Let M and N denotes the total grid points in the $\hat{e}_1$ and $\hat{e}_2$ directions, respectively. We consider the surface heights at the grid points to have a Gaussian distribution and choose the mean surface height as the datum to measure the surface height in the $\hat{e}_3$ direction. For a given RMS roughness, σ_{rms}, (i.e., standard deviation) of the surface, we generate a set of

uncorrelated random numbers for the surface heights, $\zeta(I,J)$, with the Gaussian distribution

$$p(\zeta) = \frac{1}{\sqrt{2\pi}\sigma_{\text{rms}}} e^{-\frac{\zeta^2}{2\sigma_{\text{rms}}^2}}. \tag{C.1.4}$$

The pair (I,J) indicates the indices of the grid points in the $\hat{e}_x$ and $\hat{e}_y$ directions, respectively, where $I = 1,2,...,M$ and $J = 1,2,...,N$. Then we apply a linear filter to obtain the final surface heights as

$$z(I,J) = \sum_{k=0}^{m-1}\sum_{l=0}^{n-1} h(k,l)\zeta(I-k,J-l), \tag{C.1.5}$$

where $h(k,l)$ is the coefficient of the linear filter with finite response of lengths m and n. If we take the Fourier transform of the two sides of (C.1.5), we obtain

$$Z(q_x,q_y) = H(q_x,q_y)A(q_x,q_y), \tag{C.1.6}$$

where $Z(q_x,q_y)$ and $A(q_x,q_y)$ are the discrete Fourier transforms of the input and output sequences, respectively, and $H(q_x,q_y)$ is the transfer function or frequency response given by

$$H(q_x,q_y) = \sum_{k=-m/2+1}^{m/2-1}\sum_{l=-n/2+1}^{n/2-1} h(k,l)e^{-ikq_x}e^{-ilq_y}. \tag{C.1.7}$$

where $q_x = 2\pi r/m$, $r = -m/2+1,...,0,...,m/2-1$, $q_y = 2\pi s/n$, and $s = -n/2+1,...,0,...,n/2-1$.

In the discrete form, the ACF of a stationary random process $z(I,J)$ is defined as

$$R_{zz}(k,l) = \mathrm{E}\{z(I,J)z(I+k,J+l)\}. \tag{C.1.8}$$

If the process is assumed to be ergodic, then we have

$$R_{zz}(k,l) = \frac{1}{MN}\sum_{I=0}^{M-1}\sum_{J=0}^{N-1} z(I,J)z(I+k,J+l) \tag{C.1.9}$$

as $M,N \to \infty$. The PSD function of $z(I,J)$, which is the discrete Fourier transform of $R(k,l)$, is given by

$$C_{zz}(q_x,q_y) = \frac{1}{mn}\sum_{k=-m/2+1}^{m/2-1}\sum_{l=-n/2+1}^{n/2-1} R_{zz}(k,l)e^{-ikq_x}e^{-ilq_y}. \tag{C.1.10}$$

Let $C_{\zeta\zeta}(q_x,q_y)$ be the PSD function of $\zeta(I,J)$, then the relation between $C_{zz}(q_x,q_y)$ and $C_{\zeta\zeta}(q_x,q_y)$ for a linear filter is

$$C_{zz}(q_x,q_y) = |H(q_x,q_y)|^2 C_{\zeta\zeta}(q_x,q_y). \tag{C.1.11}$$

Since $\zeta(I,J)$ is a set of uncorrelated random numbers, its PSD function $C_{\zeta\zeta}(q_x,q_y)$ must be a constant. We set this constant to be one. This will change the RMS roughness of the finally generated surface, which can be fixed later by a proper scaling of the surface heights. Thus, from (C.1.11), we have

$$H(q_x,q_y) = C_{zz}(q_x,q_y)^{1/2}. \tag{C.1.12}$$

The filter coefficient $h(k,l)$ is obtained by taking the inverse Fourier transform of $H(q_x,q_y)$,

$$h(k,l) = \frac{1}{mn} \sum_{r=-m/2+1}^{m/2-1} \sum_{s=-n/2+1}^{n/2-1} H(q_x,q_y) e^{ikq_x} e^{ilq_y}. \tag{C.1.13}$$

Therefore, the generation of a randomly rough surface with a Gaussian PDF and a specified ACF can be achieved by the following procedures.

1. For a given ACF $R(k,l)$, compute its PSD function $C_{zz}(q_x,q_y)$ with (C.1.10).
2. Determine the transfer function $H(q_x,q_y)$ with (C.1.12).
3. Obtain the filter coefficients $h(k,l)$ with (C.1.13).
4. Generate a set of uncorrelated random numbers $\zeta(I,J)$ with the Gaussian distribution.
5. Obtain the surface height $z(I,J)$ with (C.1.5).
6. Scale the surface heights to obtain the desired RMS roughness of the surface.

Figure C.1 shows the realization of a series of rough surfaces with a Gaussian PDF and a Gaussian ACF of surface heights. The RMS roughness of the surface is $\sigma_{\text{rms}} = 10$, and the correlation lengths are $L_c = 0.01, 0.02, 0.04, 0.06, 0.08, 0.1$ for the generated surfaces shown in Figure C.1a–f, respectively.

Figure C.2a and b shows the comparison of numerical and analytical PSDs for the generated

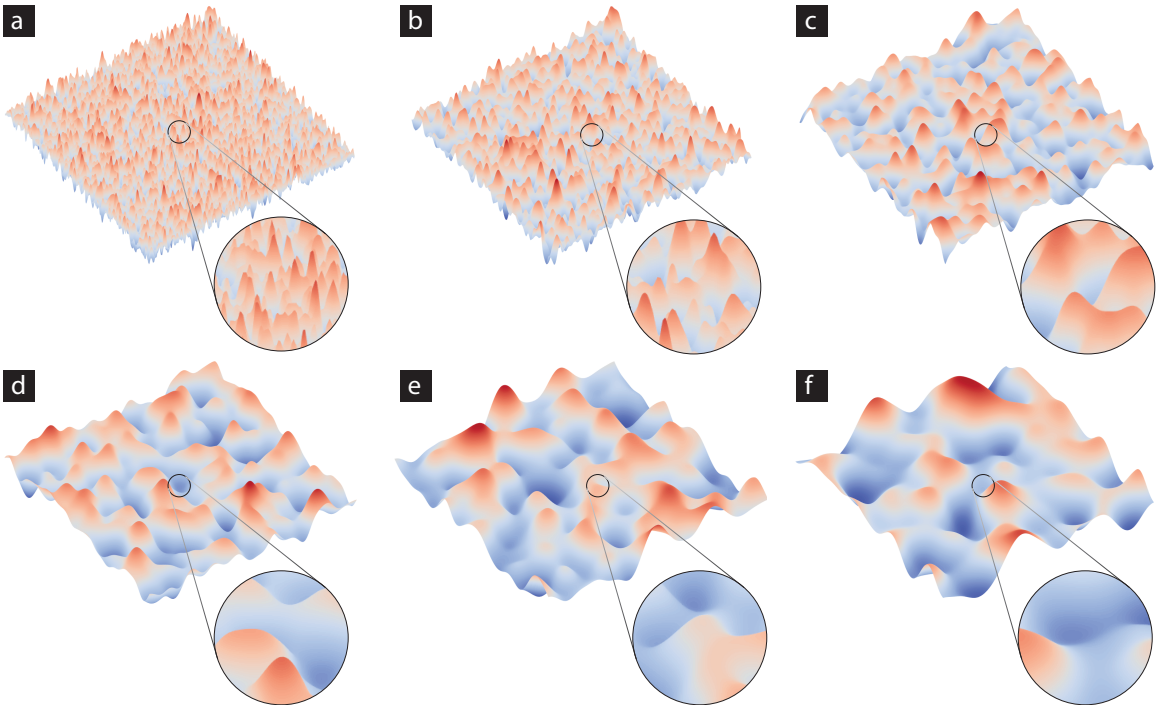

Figure C.1: The generated rough surface samples with $\sigma_{\text{rms}} = 10$. The correlation lengths in (a)–(f) are $L_c = 0.01, 0.02, 0.04, 0.06, 0.08, 0.1$, respectively.

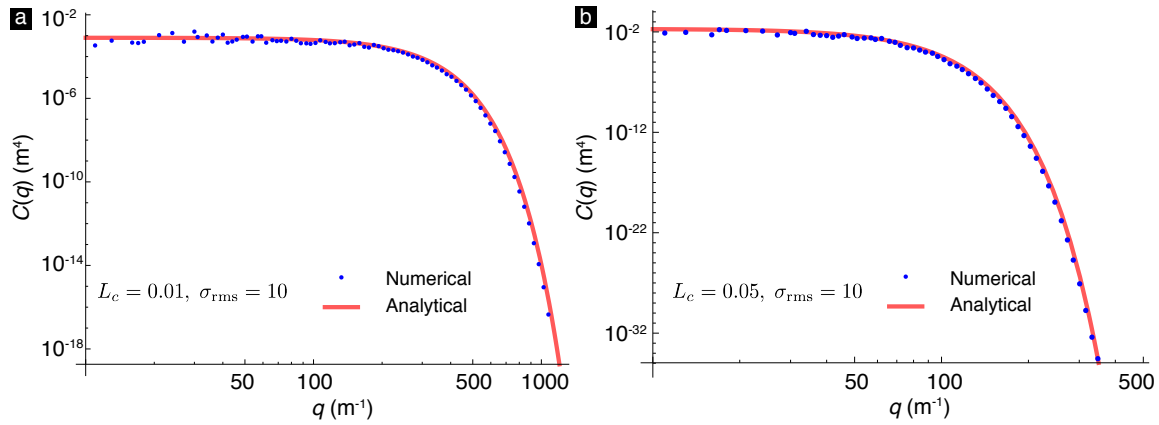

Figure C.2: The comparison of numerical and analytical PSDs for the generated rough surface with $\sigma_{\text{rms}} = 10$, $L_c = 0.01$ and $\sigma_{\text{rms}} = 10$, $L_c = 0.05$, respectively.

rough surface with $\sigma_{\text{rms}} = 10$, $L_c = 0.01$ and $\sigma_{\text{rms}} = 10$, $L_c = 0.05$, respectively. The match between numerical and analytical PSDs demonstrates that the generated surface has the specified ACF.

Bibliography

[1] D. Maugis. *Contact adhesion and rupture of elastic solids*. Solid State Sciences. Springer, 2000.

[2] D. M. Tanner, N. F. Smith, L. W. Irwin, W. P. Eaton, K. S. Helgesen, J. J. Clement, W. M. Miller, S. L. Miller, M. T. Dugger, J. A. Walraven, and K. A. Peterson. MEMS reliability: Infrastructure, test structures, experiments, and failure modes. Technical report, Sandia National Labs., Albuquerque, NM (US); Sandia National Labs., Livermore, CA (US), 2000.

[3] M. A. Meitl, Z.-T. Zhu, V. Kumar, K. J. Lee, X. Feng, Y. Y. Huang, I. Adesida, R. G. Nuzzo, and J. A. Rogers. Transfer printing by kinetic control of adhesion to an elastomeric stamp. *Nature Materials*, 5(1):33–38, 2006.

[4] C. Linghu, S. Zhang, C. Wang, and J. Song. Transfer printing techniques for flexible and stretchable inorganic electronics. *npj Flexible Electronics*, 2(1):26, 2018.

[5] R. Aghababaei, D. H. Warner, and J.-F. Molinari. Critical length scale controls adhesive wear mechanisms. *Nature communications*, 7:11816, 2016.

[6] I. Hutchings and P. Shipway. *Tribology: Friction and wear of engineering materials*. Butterworth-Heinemann, 2017.

[7] V. S. Deshpande, M. Mrksich, R. M. McMeeking, and A. G. Evans. A bio-mechanical model for coupling cell contractility with focal adhesion formation. *Journal of the Mechanics and Physics of Solids*, 56(4):1484–1510, 2008.

[8] E. Arzt, S. Gorb, and R. Spolenak. From micro to nano contacts in biological attachment devices. *Proceedings of the National Academy of Sciences*, 100(19):10603–10606, 2003.

[9] H. Gao, X. Wang, H. Yao, S. Gorb, and E. Arzt. Mechanics of hierarchical adhesion structures of geckos. *Mechanics of Materials*, 37(2-3):275–285, 2005.

[10] C.-Y. Hui, N. Glassmaker, T. Tang, and A. Jagota. Design of biomimetic fibrillar interfaces: 2. mechanics of enhanced adhesion. *Journal of The Royal Society Interface*, 1(1):35–48, 2004.

[11] L. F. Boesel, C. Greiner, E. Arzt, and A. Del Campo. Gecko-inspired surfaces: A path to strong and reversible dry adhesives. *Advanced Materials*, 22(19):2125–2137, 2010.

[12] R. D. O'Rorke, T. W. SteelE, and H. Taylor. Bioinspired fibrillar adhesives: A review of analytical models and experimental evidence for adhesion enhancement by surface patterns. *Journal of Adhesion Science and Technology*, 30(4):362–391, 2016.

[13] H. Hertz. Uber die beruhrung fester elastischer korper. *Journal fur die Reine und Angewandte Mathematik*, 92:156–171, 1882.

[14] K. Johnson, K. Kendall, and A. Roberts. Surface energy and the contact of elastic solids. *Proceedings of the Royal Society of London A: Mathematical, Physical and Engineering Sciences*, 324(1558):301–313, 1971.

[15] B. V. Derjaguin, V. M. Muller, and Y. P. Toporov. Effect of contact deformations on the adhesion of particles. *Journal of Colloid and Interface Science*, 53(2):314–326, 1975.

[16] D. Maugis. Adhesion of spheres: The JKR-DMT transition using a Dugdale model. *Journal of Colloid and Interface Science*, 150(1):243–269, 1992.

[17] D. Tabor. Surface forces and surface interactions. *Journal of Colloid and Interface Science*, 58(1):2–13, 1977.

[18] V. Muller, V. Yushchenko, and B. Derjaguin. On the influence of molecular forces on the deformation of an elastic sphere and its sticking to a rigid plane. *Journal of Colloid and Interface Science*, 77(1):91–101, 1980.

[19] K. Fuller and D. Tabor. The effect of surface roughness on the adhesion of elastic solids. *Proceedings of the Royal Society of London. A. Mathematical and Physical Sciences*, 345(1642):327–342, 1975.

[20] J. M. Levins, T. K. Vanderlick, et al. Impact of roughness on the deformation and adhesion of a rough metal and smooth mica in contact. *Journal of Physical Chemistry*, 99(14):5067–5076, 1995.

[21] R. Quon, R. Knarr, and T. Vanderlick. Measurement of the deformation and adhesion of rough solids in contact. *The Journal of Physical Chemistry B*, 103(25):5320–5327, 1999.

[22] Y. I. Rabinovich, J. J. Adler, A. Ata, R. K. Singh, and B. M. Moudgil. Adhesion between nanoscale rough surfaces: II. measurement and comparison with theory. *Journal of Colloid and Interface Science*, 232(1):17–24, 2000.

[23] G. Briggs and B. Briscoe. Effect of surface roughness on rolling friction and adhesion between elastic solids. *Nature*, 260(5549):313–315, 1976.

[24] J. Greenwood and J. Williamson. Contact of nominally flat surfaces. *Proceedings of the Royal Society of London A: Mathematical, Physical and Engineering Sciences*, 295(1442):300–319, 1966.

[25] K. Fuller and A. Roberts. Rubber rolling on rough surfaces. *Journal of Physics D: Applied Physics*, 14(2):221, 1981.

[26] H.-C. Kim and T. P. Russell. Contact of elastic solids with rough surfaces. *Journal of Polymer Science Part B: Polymer Physics*, 39(16):1848–1854, 2001.

[27] H. Kesari, J. C. Doll, B. L. Pruitt, W. Cai, and A. J. Lew. Role of surface roughness in hysteresis during adhesive elastic contact. *Philosophical Magazine Letters*, 90(12):891–902, 2010.

[28] Y. Rahmawan, C.-M. Chen, and S. Yang. Recent advances in wrinkle-based dry adhesion. *Soft Matter*, 10(28):5028–5039, 2014.

[29] E. P. Chan, E. J. Smith, R. C. Hayward, and A. J. Crosby. Surface wrinkles for smart adhesion. *Advanced Materials*, 20(4):711–716, 2008.

[30] D. Martina, C. Creton, P. Damman, M. Jeusette, and A. Lindner. Adhesion of soft viscoelastic adhesives on periodic rough surfaces. *Soft Matter*, 8(19):5350–5357, 2012.

[31] S. Vajpayee, K. Khare, S. Yang, C.-Y. Hui, and A. Jagota. Adhesion selectivity using rippled surfaces. *Advanced Functional Materials*, 21(3):547–555, 2011.

[32] C. S. Davis, D. Martina, C. Creton, A. Lindner, and A. J. Crosby. Enhanced adhesion of elastic materials to small-scale wrinkles. *Langmuir*, 28(42):14899–14908, 2012.

[33] I. S. Kwon, G. Tang, P.-J. Chiang, and C. J. Bettinger. Texture-dependent adhesion in polydopamine nanomembranes. *ACS Applied Materials & Interfaces*, 2018.

[34] P. Guduru. Detachment of a rigid solid from an elastic wavy surface: Theory. *Journal of the Mechanics and Physics of Solids*, 55(3):445–472, 2007.

[35] H. Kesari and A. J. Lew. Effective macroscopic adhesive contact behavior induced by small surface roughness. *Journal of the Mechanics and Physics of Solids*, 59(12):2488–2510, 2011.

[36] Q. Li and K.-S. Kim. Micromechanics of rough surface adhesion: A homogenized projection method. *Acta Mechanica Solida Sinica*, 22(5):377–390, 2009.

[37] P. Guduru and C. Bull. Detachment of a rigid solid from an elastic wavy surface: Experiments. *Journal of the Mechanics and Physics of Solids*, 55(3):473–488, 2007.

[38] P. Silberzan, S. Perutz, E. J. Kramer, and M. K. Chaudhury. Study of the self-adhesion hysteresis of a siloxane elastomer using the JKR method. *Langmuir*, 10(7):2466–2470, 1994.

[39] G. Choi, S. Kim, and A. Ulman. Adhesion hysteresis studies of extracted poly (dimethylsiloxane) using contact mechanics. *Langmuir*, 13:6333–6338, 1997.

[40] J. Pickering, D. Van Der Meer, and G. Vancso. Effects of contact time, humidity, and surface roughness on the adhesion hysteresis of polydimethylsiloxane. *Journal of Adhesion Science and Technology*, 15(12):1429–1441, 2001.

[41] Y. Chen, C. Helm, and J. Israelachvili. Molecular mechanisms associated with adhesion and contact angle hysteresis of monolayer surfaces. *Journal of Physical Chemistry*, 95:10736–10746, 1991.

[42] M. Giri, D. B. Bousfield, and W. Unertl. Dynamic contacts on viscoelastic films: Work of adhesion. *Langmuir*, 17(10):2973–2981, 2001.

[43] U. Landman, W. Luedtke, N. A. Burnham, and R. J. Colton. Atomistic mechanisms and dynamics of adhesion, nanoindentation, and fracture. *Science*, 248(4954):454–461, 1990.

[44] K. Kendall. *Molecular adhesion and its applications: The sticky universe*. Springer US, 2001.

[45] J. N. Israelachvili. *Intermolecular and surface forces (revised third edition)*. Academic press, 2011.

[46] T. Eisner and D. J. Aneshansley. Defense by foot adhesion in a beetle (hemisphaerota cyanea). *Proceedings of the National Academy of Sciences*, 97(12):6568–6573, 2000.

[47] G. Huber, S. N. Gorb, N. Hosoda, R. Spolenak, and E. Arzt. Influence of surface roughness on gecko adhesion. *Acta Biomaterialia*, 3(4):607–610, 2007.

[48] J. M. Bullock and W. Federle. Beetle adhesive hairs differ in stiffness and stickiness: In vivo adhesion measurements on individual setae. *Naturwissenschaften*, 98(5):381–387, 2011.

[49] J. O. Wolff and S. N. Gorb. Surface roughness effects on attachment ability of the spider philodromus dispar (araneae, philodromidae). *Journal of Experimental Biology*, 215(1):179–184, 2012.

[50] F. Frost, S. N. Gorb, and J. O. Wolff. Adhesion and friction in hunting spiders: The effect of contact splitting on their attachment ability. *Zoologischer Anzeiger*, 273:231–239, 2018.

[51] K. Friedrich. *Friction and wear of polymer composites*, volume 1. Elsevier, 2012.

[52] R. S. Bradley. The cohesive force between solid surfaces and the surface energy of solids. *The London, Edinburgh, and Dublin Philosophical Magazine and Journal of Science*, 13(86):853–862, 1932.

[53] K. Kendall. The adhesion and surface energy of elastic solids. *Journal of Physics D: Applied Physics*, 4(8):1186, 1971.

[54] J. Kim, K. Kim, and Y. Kim. Mechanical effects in peel adhesion test. *Journal of Adhesion Science and Technology*, 3(1):175–187, 1989.

[55] T. Cohen, C. U. Chan, and L. Mahadevan. Competing failure modes in finite adhesive pads. *Soft Matter*, 14(10):1771–1779, 2018.

[56] J. Hinkley. A blister test for adhesion of polymer films to SiO_2. *The Journal of Adhesion*, 16(2):115–125, 1983.

[57] Z. Cao, P. Wang, W. Gao, L. Tao, J. Suk, R. Ruoff, D. Akinwande, R. Huang, and K. Liechti. A blister test for interfacial adhesion of large-scale transferred graphene. *Carbon*, 69:390–400, 2014.

[58] Y. Sun, B. Akhremitchev, and G. C. Walker. Using the adhesive interaction between atomic force microscopy tips and polymer surfaces to measure the elastic modulus of compliant samples. *Langmuir*, 20(14):5837–5845, 2004.

[59] J. Notbohm, B. Poon, and G. Ravichandran. Analysis of nanoindentation of soft materials with an atomic force microscope. *Journal of Materials Research*, 27(1):229–237, 2012.

[60] N. Bouchonville, M. Meyer, C. Gaude, E. Gay, D. Ratel, and A. Nicolas. AFM mapping of the elastic properties of brain tissue reveals kpa μm^{-1} gradients of rigidity. *Soft Matter*, 12(29):6232–6239, 2016.

[61] D. M. Ebenstein and K. J. Wahl. A comparison of JKR-based methods to analyze quasi-static and dynamic indentation force curves. *Journal of Colloid and Interface Science*, 298(2):652–662, 2006.

[62] D. Ahn and K. R. Shull. JKR studies of acrylic elastomer adhesion to glassy polymer substrates. *Macromolecules*, 29(12):4381–4390, 1996.

[63] D. M. Ebenstein and L. A. Pruitt. Nanoindentation of biological materials. *Nano Today*, 1(3):26–33, 2006.

[64] W. Deng and H. Kesari. Depth-dependent hysteresis in adhesive elastic contacts at large surface roughness. *Scientific Reports*, 9(1):1639, 2019.

[65] K. Takahashi, R. Mizuno, and T. Onzawa. Influence of the stiffness of the measurement system on the elastic adhesional contact. *Journal of Adhesion Science and Technology*, 9(11):1451–1464, 1995.

[66] F. Yang. Load–displacement relation in adhesion measurement. *Journal of Physics D: Applied Physics*, 36(19):2417, 2003.

[67] I. Argatov, Q. Li, R. Pohrt, and V. L. Popov. Johnson–Kendall–Roberts adhesive contact for a toroidal indenter. *Proceedings of the Royal Society A: Mathematical, Physical and Engineering Sciences*, 472(2191):20160218, 2016.

[68] E. Willert, Q. Li, and V. L. Popov. The JKR-adhesive normal contact problem of axisymmetric rigid punches with a flat annular shape or concave profiles. *Facta Universitatis, Series: Mechanical Engineering*, 14(3):281–292, 2016.

[69] V. L. Popov, R. Pohrt, and Q. Li. Strength of adhesive contacts: Influence of contact geometry and material gradients. *Friction*, 5(3):308–325, 2017.

[70] I. N. Sneddon. The relation between load and penetration in the axisymmetric Boussinesq problem for a punch of arbitrary profile. *International Journal of Engineering Science*, 3(1):47–57, 1965.

[71] H. Kesari and A. J. Lew. Adhesive frictionless contact between an elastic isotropic half-space and a rigid axi-symmetric punch. *Journal of Elasticity*, 106(2):203–224, 2012.

[72] W. Deng and H. Kesari. Molecular statics study of depth-dependent hysteresis in nano-scale adhesive elastic contacts. *Modelling and Simulation in Materials Science and Engineering*, 25(5):055002, 2017.

[73] D. C. Lin and F. Horkay. Nanomechanics of polymer gels and biological tissues: A critical review of analytical approaches in the hertzian regime and beyond. *Soft Matter*, 4(4):669–682, 2008.

[74] M. K. Chaudhury and G. M. Whitesides. Direct measurement of interfacial interactions between semispherical lenses and flat sheets of poly(dimethylsiloxane) and their chemical derivatives. *Langmuir*, 7(5):1013–1025, 1991.

[75] P. R. Nayak. Random process model of rough surfaces. *Journal of Tribology*, 93(3):398–407, 1971.

[76] Z. Song and K. Komvopoulos. Adhesive contact of an elastic semi-infinite solid with a rigid rough surface: Strength of adhesion and contact instabilities. *International Journal of Solids and Structures*, 51(6):1197–1207, 2014.

[77] W. Cheng, P. Dunn, and R. Brach. Surface roughness effects onmicroparticle adhesion. *The Journal of Adhesion*, 78(11):929–965, 2002.

[78] W. Chang, I. Etsion, and D. B. Bogy. An elastic-plastic model for the contact of rough surfaces. *Journal of tribology*, 109(2):257–263, 1987.

[79] S. Yashima, V. Romero, E. Wandersman, C. Frétigny, M. Chaudhury, A. Chateauminois, and A. Prevost. Normal contact and friction of rubber with model randomly rough surfaces. *Soft Matter*, 11(5):871–881, 2015.

[80] B. N. Persson. Theory of rubber friction and contact mechanics. *The Journal of Chemical Physics*, 115(8):3840–3861, 2001.

[81] D. S. Dugdale. Yielding of steel sheets containing slits. *Journal of the Mechanics and Physics of Solids*, 8(2):100–104, 1960.

[82] K.-S. Kim, R. McMeeking, and K. Johnson. Adhesion, slip, cohesive zones and energy fluxes for elastic spheres in contact. *Journal of the Mechanics and Physics of Solids*, 46(2):243–266, 1998.

[83] B. Bhushan. *Principles and applications of tribology*. John Wiley & Sons, 2013.

[84] G. Franceschetti and D. Riccio. *Scattering, natural surfaces, and fractals*. Academic Press, 2006.

[85] T. D. Jacobs, T. Junge, and L. Pastewka. Quantitative characterization of surface topography using spectral analysis. *Surface Topography: Metrology and Properties*, 5(1):013001, 2017.

[86] R. Gavrila, A. Dinescu, and D. Mardare. A power spectral density study of thin films morphology based on AFM profiling. *Raman J Inf Sci Technol*, 10:291–300, 2007.

[87] Y. Gong, S. T. Misture, P. Gao, and N. P. Mellott. Surface roughness measurements using power spectrum density analysis with enhanced spatial correlation length. *The Journal of Physical Chemistry C*, 120(39):22358–22364, 2016.

[88] A. Milling and S. Biggs. Direct measurement of the depletion force using an atomic force microscope. *Journal of Colloid and Interface Science*, 170(2):604–606, 1995.

[89] M. A. Bevan and D. C. Prieve. Direct measurement of retarded van der Waals attraction. *Langmuir*, 15(23):7925–7936, 1999.

[90] K. L. Johnson. The adhesion of two elastic bodies with slightly wavy surfaces. *International Journal of Solids and Structures*, 32(3):423–430, 1995.

[91] F. Hua, Y. Sun, A. Gaur, M. A. Meitl, L. Bilhaut, L. Rotkina, J. Wang, P. Geil, M. Shim, J. A. Rogers, et al. Polymer imprint lithography with molecular-scale resolution. *Nano Letters*, 4(12):2467–2471, 2004.

[92] A. Jagota, D. Paretkar, and A. Ghatak. Surface-tension-induced flattening of a nearly plane elastic solid. *Physical Review E*, 85(5):051602, 2012.

[93] D. Paretkar, X. Xu, C.-Y. Hui, and A. Jagota. Flattening of a patterned compliant solid by surface stress. *Soft Matter*, 10(23):4084–4090, 2014.

[94] R. W. Style, A. Jagota, C.-Y. Hui, and E. R. Dufresne. Elastocapillarity: Surface tension and the mechanics of soft solids. *Annual Review of Condensed Matter Physics*, 8:99–118, 2017.

[95] C. Jalbert, J. T. Koberstein, I. Yilgor, P. Gallagher, and V. Krukonis. Molecular weight dependence and end-group effects on the surface tension of poly (dimethylsiloxane). *Macromolecules*, 26(12):3069–3074, 1993.

[96] N. Nadermann, C.-Y. Hui, and A. Jagota. Solid surface tension measured by a liquid drop under a solid film. *Proceedings of the National Academy of Sciences*, 110(26):10541–10545, 2013.

[97] Q. Xu, K. E. Jensen, R. Boltyanskiy, R. Sarfati, R. W. Style, and E. R. Dufresne. Direct measurement of strain-dependent solid surface stress. *Nature Communications*, 8(1):555, 2017.

[98] Z. Wei, M.-F. He, and Y.-P. Zhao. The effects of roughness on adhesion hysteresis. *Journal of Adhesion Science and Technology*, 24(6):1045–1054, 2010.

[99] B. Zappone, K. J. Rosenberg, and J. Israelachvili. Role of nanometer roughness on the adhesion and friction of a rough polymer surface and a molecularly smooth mica surface. *Tribology Letters*, 26(3):191, 2007.

[100] N. Maeda, N. Chen, M. Tirrell, and J. Israelachvili. Adhesion and friction mechanisms of polymer-on-polymer surfaces. *Science*, 297(5580):379–382, 2002.

[101] M. Urbakh, J. Klafter, D. Gourdon, and J. Israelachvili. The nonlinear nature of friction. *Nature*, 430(6999):525–528, 2004.

[102] S. Hulikal, K. Bhattacharya, and N. Lapusta. Collective behavior of viscoelastic asperities as a model for static and kinetic friction. *Journal of the Mechanics and Physics of Solids*, 76:144–161, 2015.

[103] B. Bhushan, J. N. Israelachvili, and U. Landman. Nanotribology: friction, wear and lubrication at the atomic scale. *Nature*, 374(6523):607–616, 1995.

[104] T. D. Jacobs and R. W. Carpick. Nanoscale wear as a stress-assisted chemical reaction. *Nature nanotechnology*, 8(2):108–112, 2013.

[105] R. Maboudian. Adhesion and friction issues associated with reliable operation of MEMS. *MRS Bulletin*, 23(6):47–51, 1998.

[106] A. Y. Suh and A. A. Polycarpou. Adhesive contact modeling for sub-5-nm ultralow flying magnetic storage head-disk interfaces including roughness effects. *Journal of Applied Physics*, 97(10):104328, 2005.

[107] S. Kim, C. Laschi, and B. Trimmer. Soft robotics: A bioinspired evolution in robotics. *Trends in Biotechnology*, 31(5):287–294, 2013.

[108] K. Autumn, Y. A. Liang, S. T. Hsieh, W. Zesch, W. P. Chan, T. W. Kenny, R. Fearing, and R. J. Full. Adhesive force of a single gecko foot-hair. *Nature*, 405(6787):681–685, 2000.

[109] D. Labonte and W. Federle. Scaling and biomechanics of surface attachment in climbing animals. *Phil. Trans. R. Soc. B*, 370(1661):20140027, 2015.

[110] W. Federle, W. Barnes, W. Baumgartner, P. Drechsler, and J. Smith. Wet but not slippery: Boundary friction in tree frog adhesive toe pads. *Journal of The Royal Society Interface*, 3(10):689–697, 2006.

[111] H. Lee, N. F. Scherer, and P. B. Messersmith. Single-molecule mechanics of mussel adhesion. *Proceedings of the National Academy of Sciences*, 103(35):12999–13003, 2006.

[112] M. Kamperman, E. Kroner, A. del Campo, R. M. McMeeking, and E. Arzt. Functional adhesive surfaces with "gecko" effect: The concept of contact splitting. *Advanced Engineering Materials*, 12(5):335–348, 2010.

[113] A. Jagota and C.-Y. Hui. Adhesion, friction, and compliance of bio-mimetic and bio-inspired structured interfaces. *Materials Science and Engineering: R: Reports*, 72(12):253–292, 2011.

[114] D. Brodoceanu, C. Bauer, E. Kroner, E. Arzt, and T. Kraus. Hierarchical bioinspired adhesive surfacesa review. *Bioinspiration & Biomimetics*, 11(5):051001, 2016.

[115] R. D. Campilho, M. D. Banea, J. Neto, and L. F. da Silva. Modelling adhesive joints with cohesive zone models: Effect of the cohesive law shape of the adhesive layer. *International Journal of Adhesion and Adhesives*, 44:48–56, 2013.

[116] J. Q. Feng. Contact behavior of spherical elastic particles: A computational study of particle adhesion and deformations. *Colloids and Surfaces A: Physicochemical and Engineering Aspects*, 172(1-3):175–198, 2000.

[117] J.-J. Wu. Numerical simulation of the adhesive contact between a slightly wavy surface and a half-space. *Journal of Adhesion Science and Technology*, 26(1-3):331–351, 2012.

[118] Z. Song and K. Komvopoulos. Adhesion-induced instabilities in elastic and elastic–plastic contacts during single and repetitive normal loading. *Journal of the Mechanics and Physics of Solids*, 59(4):884–897, 2011.

[119] B. V. Derjaguin. Untersuchungen über die reibung und adhäsion, iv. *Colloid & Polymer Science*, 69(2):155–164, 1934.

[120] J. Greenwood. Adhesion of elastic spheres. *Proceedings of the Royal Society of London A: Mathematical, Physical and Engineering Sciences*, 453(1961):1277–1297, 1997.

[121] A. F. Bower. *Applied mechanics of solids*. CRC press, 2009.

[122] H. Gao and H. Yao. Shape insensitive optimal adhesion of nanoscale fibrillar structures. *Proceedings of the National Academy of Sciences*, 101(21):7851–7856, 2004.

[123] A. I. Bennett, K. L. Harris, K. D. Schulze, J. M. Urueña, A. J. McGhee, A. A. Pitenis, M. H. Müser, T. E. Angelini, and W. G. Sawyer. Contact measurements of randomly rough surfaces. *Tribology Letters*, 65(4):134, 2017.

[124] R. Sahli, G. Pallares, C. Ducottet, I. B. Ali, S. Al Akhrass, M. Guibert, and J. Scheibert. Evolution of real contact area under shear and the value of static friction of soft materials. *Proceedings of the National Academy of Sciences*, 115(3):471–476, 2018.

[125] H. M. Westergaard. Bearing pressures and cracks. *Trans AIME, J. Appl. Mech.*, 6:49–53, 1939.

[126] K. Autumn, C. Majidi, R. Groff, A. Dittmore, and R. Fearing. Effective elastic modulus of isolated gecko setal arrays. *Journal of Experimental Biology*, 209(18):3558–3568, 2006.

[127] T. R. Thomas. *Rough surfaces, 2nd Edition*. Imperial College Press, 1999.

[128] Y. Tian, N. Pesika, H. Zeng, K. Rosenberg, B. Zhao, P. McGuiggan, K. Autumn, and J. Israelachvili. Adhesion and friction in gecko toe attachment and detachment. *Proceedings of the National Academy of Sciences*, 103(51):19320–19325, 2006.

[129] B. Chen, P. Wu, and H. Gao. Hierarchical modelling of attachment and detachment mechanisms of gecko toe adhesion. *Proceedings of the Royal Society A: Mathematical, Physical and Engineering Sciences*, 464(2094):1639–1652, 2008.

[130] B. Aksak, C.-Y. Hui, and M. Sitti. The effect of aspect ratio on adhesion and stiffness for soft elastic fibres. *Journal of The Royal Society Interface*, 8(61):1166–1175, 2011.

[131] K. Autumn, M. Sitti, Y. A. Liang, A. M. Peattie, W. R. Hansen, S. Sponberg, T. W. Kenny, R. Fearing, J. N. Israelachvili, and R. J. Full. Evidence for van der waals adhesion in gecko setae. *Proceedings of the National Academy of Sciences*, 99(19):12252–12256, 2002.

[132] H. H. Schleich and W. Kästle. Ultrastrukturen an gecko-zehen (reptilia: sauria: gekkonidae). *Amphibia-Reptilia*, 7(2):141–166, 1986.

[133] Y. A. Liang, K. Autumn, S. T. Hsieh, W. Zesch, W. Chan, R. Fearing, R. Full, and T. W. Kenny. Adhesion force measurements on single gecko setae. In *Technical Digest of the 2000 Solid-State Sensor and Actuator Workshop*, volume 2000, pages 33–38, 2000.

[134] W. Sun, P. Neuzil, T. S. Kustandi, S. Oh, and V. D. Samper. The nature of the gecko lizard adhesive force. *Biophysical Journal*, 89(2):L14–L17, 2005.

[135] W. R. Hansen and K. Autumn. Evidence for self-cleaning in gecko setae. *Proceedings of the National Academy of Sciences*, 102(2):385–389, 2005.

[136] G. Huber, S. N. Gorb, R. Spolenak, and E. Arzt. Resolving the nanoscale adhesion of individual gecko spatulae by atomic force microscopy. *Biology Letters*, 1(1):2–4, 2005.

[137] K. Autumn, A. Dittmore, D. Santos, M. Spenko, and M. Cutkosky. Frictional adhesion: a new angle on gecko attachment. *Journal of Experimental Biology*, 209(18):3569–3579, 2006.

[138] C. Hui, A. Jagota, Y.-Y. Lin, and E. Kramer. Constraints on microcontact printing imposed by stamp deformation. *Langmuir*, 18(4):1394–1407, 2002.

[139] B. Persson and S. Gorb. The effect of surface roughness on the adhesion of elastic plates with application to biological systems. *The Journal of Chemical Physics*, 119(21):11437–11444, 2003.

[140] S. N. Gorb. The design of the fly adhesive pad: distal tenent setae are adapted to the delivery of an adhesive secretion. *Proceedings of the Royal Society of London. Series B: Biological Sciences*, 265(1398):747–752, 1998.

[141] S. Niederegger, S. Gorb, and Y. Jiao. Contact behaviour of tenent setae in attachment pads of the blowfly calliphora vicina (Diptera, Calliphoridae). *Journal of Comparative Physiology A*, 187(12):961–970, 2002.

[142] S. Niederegger and S. N. Gorb. Friction and adhesion in the tarsal and metatarsal scopulae of spiders. *Journal of Comparative Physiology A*, 192(11):1223–1232, 2006.

[143] T. Eimüller, P. Guttmann, and S. Gorb. Terminal contact elements of insect attachment devices studied by transmission X-ray microscopy. *Journal of Experimental Biology*, 211(12):1958–1963, 2008.

[144] M. Varenberg, N. M. Pugno, and S. N. Gorb. Spatulate structures in biological fibrillar adhesion. *Soft Matter*, 6(14):3269–3272, 2010.

[145] A. del Campo, C. Greiner, I. Álvarez, and E. Arzt. Patterned surfaces with pillars with controlled 3D tip geometry mimicking bioattachment devices. *Advanced Materials*, 19(15):1973–1977, 2007.

[146] S. Gorb, M. Varenberg, A. Peressadko, and J. Tuma. Biomimetic mushroom-shaped fibrillar adhesive microstructure. *Journal of The Royal Society Interface*, 4(13):271–275, 2007.

[147] N. S. Pesika, Y. Tian, B. Zhao, K. Rosenberg, H. Zeng, P. McGuiggan, K. Autumn, and J. N. Israelachvili. Peel-zone model of tape peeling based on the gecko adhesive system. *The Journal of Adhesion*, 83(4):383–401, 2007.

[148] B. Chen, P. Wu, and H. Gao. Pre-tension generates strongly reversible adhesion of a spatula pad on substrate. *Journal of The Royal Society Interface*, 6(35):529–537, 2008.

[149] R. A. Sauer. The peeling behavior of thin films with finite bending stiffness and the implications on gecko adhesion. *The Journal of Adhesion*, 87(7-8):624–643, 2011.

[150] N. M. Pugno. The theory of multiple peeling. *International Journal of Fracture*, 171(2):185–193, 2011.

[151] K. Kendall. Thin-film peeling-the elastic term. *Journal of Physics D: Applied Physics*, 8(13):1449, 1975.

[152] R. Rivlin. The effective work of adhesion. *Paint Technol.*, 9:215–218, 1944.

[153] K.-S. Kim and J. Kim. Elasto-plastic analysis of the peel test for thin film adhesion. *Journal of Engineering Materials and Technology*, 110(3):266–273, 1988.

[154] K. S. Kim and N. Aravas. Elastoplastic analysis of the peel test. *International Journal of Solids and Structures*, 24(4):417–435, 1988.

[155] A. Kinloch, C. Lau, and J. Williams. The peeling of flexible laminates. *International Journal of Fracture*, 66(1):45–70, 1994.

[156] Y. Wei and J. W. Hutchinson. Interface strength, work of adhesion and plasticity in the peel test. *International Journal of Fracture*, 93(1):315–333, 1998.

[157] H. Chen, X. Feng, Y. Huang, Y. Huang, and J. A. Rogers. Experiments and viscoelastic analysis of peel test with patterned strips for applications to transfer printing. *Journal of the Mechanics and Physics of Solids*, 61(8):1737–1752, 2013.

[158] M. Loukis and N. Aravas. The effects of viscoelasticity in the peeling of polymeric films. *The Journal of Adhesion*, 35(1):7–22, 1991.

[159] K. Kendall. Control of cracks by interfaces in composites. *Proceedings of the Royal Society of London A: Mathematical, Physical and Engineering Sciences*, 341(1627):409–428, 1975.

[160] A. Ghatak, L. Mahadevan, J. Y. Chung, M. K. Chaudhury, and V. Shenoy. Peeling from a biomimetically patterned thin elastic film. *Proceedings of the Royal Society of London A: Mathematical, Physical and Engineering Sciences*, 460(2049):2725–2735, 2004.

[161] S. Xia, L. Ponson, G. Ravichandran, and K. Bhattacharya. Toughening and asymmetry in peeling of heterogeneous adhesives. *Physical Review Letters*, 108(19):196101, 2012.

[162] S. Xia, L. Ponson, G. Ravichandran, and K. Bhattacharya. Adhesion of heterogeneous thin films–I: Elastic heterogeneity. *Journal of the Mechanics and Physics of Solids*, 61(3):838–851, 2013.

[163] A. Ghatak. Peeling off an adhesive layer with spatially varying topography and shear modulus. *Physical Review E*, 89(3):032407, 2014.

[164] Z. Peng and S. Chen. Peeling behavior of a thin-film on a corrugated surface. *International Journal of Solids and Structures*, 60:60–65, 2015.

[165] T.-S. Oh, J. Rödel, R. Cannon, and R. Ritchie. Ceramic/metal interfacial crack growth: Toughening by controlled microcracks and interfacial geometries. *Acta Metallurgica*, 36(8):2083–2093, 1988.

[166] R. Ritchie. Mechanisms of fatigue crack propagation in metals, ceramics and composites: role of crack tip shielding. *Materials Science and Engineering: A*, 103(1):15–28, 1988.

[167] N. Lee, M. F. Horstemeyer, H. Rhee, B. Nabors, J. Liao, and L. N. Williams. Hierarchical multiscale structure–property relationships of the red-bellied woodpecker (melanerpes carolinus) beak. *Journal of The Royal Society Interface*, 11(96):20140274, 2014.

[168] C. R. Jaslow and A. A. Biewener. Strain patterns in the horncores, cranial bones and sutures of goats (capra hircus) during impact loading. *Journal of Zoology*, 235(2):193–210, 1995.

[169] M. Mirkhalaf, A. K. Dastjerdi, and F. Barthelat. Overcoming the brittleness of glass through bio-inspiration and micro-architecture. *Nature Communications*, 5, 2014.

[170] C.-D. Yeo, R. R. Katta, J. Lee, and A. A. Polycarpou. Effect of asperity interactions on rough surface elastic contact behavior: Hard film on soft substrate. *Tribology International*, 43(8):1438–1448, 2010.

[171] L. Afferrante, G. Carbone, and G. Demelio. Interacting and coalescing Hertzian asperities: A new multiasperity contact model. *Wear*, 278:28–33, 2012.

[172] A. I. Vakis. Asperity interaction and substrate deformation in statistical summation models of contact between rough surfaces. *Journal of Applied Mechanics*, 81(4):041012, 2014.

[173] H. Song, A. Vakis, X. Liu, and E. Van der Giessen. Statistical model of rough surface contact accounting for size-dependent plasticity and asperity interaction. *Journal of the Mechanics and Physics of Solids*, 106:1–14, 2017.

[174] C. Y. Poon and B. Bhushan. Comparison of surface roughness measurements by stylus profiler, afm and non-contact optical profiler. *Wear*, 190(1):76–88, 1995.

[175] P. de Groot. Principles of interference microscopy for the measurement of surface topography. *Advances in Optics and Photonics*, 7(1):1–65, 2015.

[176] J. Archard. Elastic deformation and the laws of friction. *Proceedings of the Royal Society of London. Series A. Mathematical and Physical Sciences*, 243(1233):190–205, 1957.

[177] M. S. Longuet-Higgins. The statistical analysis of a random, moving surface. *Philosophical Transactions of the Royal Society of London. Series A, Mathematical and Physical Sciences*, 249(966):321–387, 1957.

[178] D. J. Whitehouse and J. Archard. The properties of random surfaces of significance in their contact. *Proceedings of the Royal Society of London. A. Mathematical and Physical Sciences*, 316(1524):97–121, 1970.

[179] Y. Hu and K. Tonder. Simulation of 3-D random rough surface by 2-D digital filter and fourier analysis. *International Journal of Machine Tools and Manufacture*, 32(1-2):83–90, 1992.